Holocene Ice Sheet Dynamics and Detrital Provenance Shifts Along the West Greenland Margin

Recorded by Radiogenic Isotopes (Sr, Nd, Pb)

Dissertation

zur Erlangung des Doktorgrades der Naturwissenschaften
(Dr. rer. nat.)

im Fachbereich Geowissenschaften
der Universität Bremen

vorgelegt von

Lina Madaj

MARUM—Zentrum für Marine Umweltwissenschaften

Bremen, April 2021

Erstgutachterin:	Prof. Dr. Simone A. Kasemann Universität Bremen
Zweitgutachter:	Prof. Dr. Cristiano M. Chiessi University of São Paulo
Datum des Promotionskolloquiums:	24. September 2021

Versicherung an Eides Statt / *Affirmation in lieu of an oath*

gem. § 5 Abs. 5 der Promotionsordnung vom 18.06.2018 /
according to § 5 (5) of the Doctoral Degree Rules and Regulations of 18 June, 2018

Ich / I, Lina Madaj

versichere an Eides Statt durch meine Unterschrift, dass ich die vorliegende Dissertation selbständig und ohne fremde Hilfe angefertigt und alle Stellen, die ich wörtlich dem Sinne nach aus Veröffentlichungen entnommen habe, als solche kenntlich gemacht habe, mich auch keiner anderen als der angegebenen Literatur oder sonstiger Hilfsmittel bedient habe und die zu Prüfungszwecken beigelegte elektronische Version (PDF) der Dissertation mit der abgegebenen gedruckten Version identisch ist. / *With my signature I affirm in lieu of an oath that I prepared the submitted dissertation independently and without illicit assistance from third parties, that I appropriately referenced any text or content from other sources, that I used only literature and resources listed in the dissertation, and that the electronic (PDF) and printed versions of the dissertation are identical.*

Ich versichere an Eides Statt, dass ich die vorgenannten Angaben nach bestem Wissen und Gewissen gemacht habe und dass die Angaben der Wahrheit entsprechen und ich nichts verschwiegen habe*. / I affirm in lieu of an oath that the information provided herein to the best of my knowledge is true and complete.*

Die Strafbarkeit einer falschen eidesstattlichen Versicherung ist mir bekannt, namentlich die Strafandrohung gemäß § 156 StGB bis zu drei Jahren Freiheitsstrafe oder Geldstrafe bei vorsätzlicher Begehung der Tat bzw. gemäß § 161 Abs. 1 StGB bis zu einem Jahr Freiheitsstrafe oder Geldstrafe bei fahrlässiger Begehung. / *I am aware that a false affidavit is a criminal offence which is punishable by law in accordance with § 156 of the German Criminal Code (StGB) with up to three years imprisonment or a fine in case of intention, or in accordance with § 161 (1) of the German Criminal Code with up to one year imprisonment or a fine in case of negligence.*

_____ _____

Ort / *Place*, Datum / *Date* Unterschrift / *Signature*

To my dad,

whose secret wish of me doing a PhD one day, written in a Christmas email to a family friend was the actual spark that made me seriously consider going on this journey.

And to Sean, who was this family friend.

It always seems impossible until it is done.

Nelson Mandela

Preface

This thesis has been submitted to the Faculty of Geosciences of the University of Bremen in order to receive the degree of Doctor of Natural Sciences (Dr. rer. Nat.). The PhD project was part of the DFG funded International Research Training Group ArcTrain *"Processes and impacts of climate change in the North Atlantic Ocean and the Canadian Arctic"*. The research described in the following chapters was conducted under the supervision of Prof. Dr. Simone A. Kasemann at the Isotope Geochemistry Lab of MARUM—Center for Marine Environmental Sciences and the Faculty of Geosciences, University of Bremen, Germany. A minor part of the research has been completed in the framework of a research residence under the supervision of the project partner Claude Hillaire-Marcel at GEOTOP - Centre de recherche en géochimie et géodynamique, Université du Québec à Montréal, Canada. This thesis was written as a cumulative thesis, including three manuscripts in preparation for submission to scientific journals. A short summary of all included chapters is given below.

Chapter 1 represents the introduction into the research topic and area. The chapter summarises the aim of the study, scientific motivation and importance of current Arctic research with regards to the development of the Greenland Ice Sheet in the past and how that serves future predictions.

Chapter 2 summarises the applied methodology, included sample material and laboratory results. An overview of the application of radiogenic isotopes in provenance studies is given.

Chapter 3 contains the first manuscript *Radiogenic Isotopes Reveal Neoglacial Provenance Shift and Ice Advance in Southwest Greenland*. The manuscript deals with a marine record in the northeast Labrador Sea revealing late Holocene provenance shifts.

Chapter 4 presents the second manuscript, entitled *Northwestern Greenland Ice Sheet Dynamics traced by radiogenic isotopes*. Three marine records represent Holocene detrital sediment contribution and variations onto the west Greenland shelf along a south-north transect.

Chapter 5 introduces the third manuscript *Radiogenic Isotope Signatures of Holocene Sediments from Kane Basin: Linkage with the Re-opening and Evolution of Nares Strait.* The marine record in the focus of this manuscript identifies two major radiogenic isotope clusters and corresponding source regions in connection to deglaciation processes in Nares Strait, northernmost Greenland.

Chapter 6 summarises the results of the three aforementioned manuscripts. It further provides the overall and combined conclusions of this thesis work and an outlook into future research.

Table of Contents

List of Abbreviations 1
List of Included Figures 2
Abstract 5
Kurzfassung 7
1. Introduction 13
1.1. Scientific Motivation - Why should we care about the Arctic? 13
1.1.1. The importance of ice sheets and glaciers in the climate system 14
1.1.2. The Greenland Ice Sheet – Recent developments 15
1.2. Introduction into the Research Area 16
1.2.1. Baffin Bay 16
1.2.2. Labrador Sea 18
1.3. Greenland Ice Sheet History since the Last Glacial Maximum 19
1.4. Recent Studies and Research Aim 20
1.5. Overview of Own Research 21
1.6. References 23
2. Methodology and Results 37
2.1. Radiogenic Isotopes as Tracers for Palaeoclimatological and Palaeoceanographic Changes 37
2.1.1. Radiogenic Isotopes Strontium, Neodymium and Lead 37
2.1.1.1. Strontium 37
2.1.1.2. Neodymium 38
2.1.1.3. Lead 38
2.2. Sedimentary Archives of Ice-Sheet Dynamics 39
2.2.1. Provenance Approach 41
2.2.2. Greenland Geology Overview 42
2.3. Analytical Procedures and Results 44
2.3.1. Age Chronology 44
2.3.2. Isotope analysis 44
2.3.2. X-Ray Diffraction 50
2.4. References 54
3. Radiogenic Isotopes Reveal Neoglacial Provenance Shift and Ice Advance in Southwest Greenland 63
Abstract 63
3.1. Introduction 63

3.1.1. Holocene History of the southwestern Greenland Ice Sheet 64
3.1.2. Provenance Studies 65
3.2. Regional Setting and Research Area 66
3.2.1. Southern Greenland Geology 66
3.2.2. Labrador Sea 67
3.3. Material and Methods 67
3.3.1. Core Description and Age Chronology 67
3.3.2. Radiogenic Isotope Analysis 68
3.3.3. Mineralogical x-ray Diffraction 68
3.4. Results and Interpretation 69
3.4.1. Radiogenic Isotope Records 69
3.4.2. Mineralogy 70
3.4.3. Detrital Sediment Provenance 71
3.5. Discussion 72
3.5.1. Early to Mid Holocene Ice-Sheet Retreat 72
3.5.2. Ice-sheet advance – late Holocene 73
3.6. Conclusions 77
3.7. Acknowledgements 78
3.8. References 78
4. Northwestern Greenland Ice Sheet Dynamics traced by radiogenic isotopes 87
Abstract 87
4.1. Introduction 87
4.2. Regional Setting and Research Area 89
4.2.1. Northern Greenland Ice Sheet History 91
4.3. Material and Methods 91
4.3.1. Core Description and Age Chronology 91
4.3.2. Radiogenic Isotope Analysis 92
4.3.3 Mineralogical x-ray diffraction 93
4.4. Results and Interpretation 93
4.4.1. GeoTÜ SL170 – Midwest Greenland Slope 93
4.4.2. GeoB19927-3 - Upernavik Trough 94
4.4.3. GeoB19946-4 – Northern Melville Bay 96
4.4.4. Detrital Sediment Provenance 97
4.5. Discussion 98
4.5.1. Deglacial Period 99
4.5.2. Holocene Thermal Maximum 101

4.5.3 Neoglacial Period 102
4.6. Conclusions 103
4.7. Acknowledgements 104
4.8. References 105
5. Radiogenic Isotope Signatures of Holocene Sediments from Kane Basin: Linkage with the Re-opening and Evolution of Nares Strait 115
Abstract 115
5.1. Introduction 115
5.2. Regional Setting and Research Area 116
5.2.1. Current Setting 116
5.2.2. Past Setting 118
5.3. Material and Methods 118
5.3.1. Core Description and Age Chronology 118
5.3.2. Isotope Ratio Measurements 119
5.4. Results 120
5.4.1. Radiogenic Isotope Records 120
5.4.2. Detrital Sediment Provenance 121
5.5. Discussion 121
5.5.1. Deglacial Period and Holocene Thermal Maximum (~9.0 – 7.5 ka BP) 122
5.5.2. Post- and Neoglacial Period (~7.5 – 0 ka BP) 125
5.5.3. Detrital Sediment Clusters 126
5.6. Conclusions 127
5.7. Acknowledgements 127
5.8. References 128
6. Conclusions and Outlook 135
6.1. References 137
7. Acknowledgements 143
8. Appendices 151
8.1. Radiogenic Isotope Data 151
8.2. Mineralogical Data (XRD) 163
8.3. Elemental Composition (ICP-OES, ICP-MS) 166
8.4. Radiogenic Isotope Data for Standard Reference Material 167
8.5. Radiogenic Isotope Data for Geological Terrains 168
8.6. References 172

List of Abbreviations

AB	Archean Block
AMOC	Atlantic Meridional Overturning Circulation
CAA	Canadian Arctic Archipelago
CHUR	Chondritic Uniform Reservoir
CMB	Committee-Melville Belt
EGC	East Greenland Current
GIC	Glaciers and Ice Caps
GIS	Greenland Ice Sheet
HTM	Holocene Thermal Maximum
IC	Irminger Current
IIS	Innuitian Ice Sheet
IRD	Ice Rafted Debris
ka BP	1000 years before present
KMB	Ketilidian Mobile Belt
LGM	Last Glacial Maximum
LIA	Little Ice Age
LIS	Laurentide Ice Sheet
LSW	Labrador Sea Water
NADW	North Atlantic Deep Water
Nd	Chemical Symbol: Neodymium
NMB	Nagssugtoqidian Mobiel Belt
NOW	North Water Polynya
Pb	Chemical Symbol: Lead
RMB	Rinkian Mobile Belt
Sr	Chemical Symbol: Strontium
TIMS	Thermal Ionization Mass Spectrometer
WGC	West Greenland Current
WGMC	West Greenland Mineral Clusters
XRD	X-ray Diffraction
XRF	X-ray Fluorescence

List of Included Figures

Chapter 1

Figure 1.1: Map of the research entire area with simplified present-day surface current circulation pattern and locations mentioned in text 17

Chapter 2

Figure 2.1: Map of the entire research area with simplified present-day surface current circulation pattern and locations of all sediment cores included into this study 41
Figure 2.2: Geological map of Greenland with isotopic signatures of main geological terrains included into this study and present day Baffin Bay and Labrador Sea surface circulation pattern 43
Figure 2.3: Flow chart of leaching procedure for decarbonisation, FeMn leaching and hot-acid digestion to receive the siliciclastic detrital sediment fraction 45
Figure 2.4: Isotopic composition of FeMn leachates of gravity cores GeoB19905-1, GeoB19927-3 and GeoB19946-4 47
Figure 2.5: Elemental composition of leachates of gravity core GeoB19927-3 47
Figure 2.6: Isotopic composition of gravity core GeoB19905-1 of all three sediment fractions: bulk, decarbonised (dc), detrital (dt) 49
Figure 2.7: Isotopic composition of gravity core GeoB19927-3 of all three sediment fractions: bulk, decarbonised (dc), detrital (dt) 49
Figure 2.8: Isotopic composition of gravity core GeoB19946-4 of all three sediment fractions: bulk, decarbonised (dc), detrital (dt) 50
Figure 2.9: Isotopic composition of gravity core AMD14-Kane2B of all three sediment fractions: bulk, decarbonised (dc), detrital (dt) 50
Figure 2.10: Isotopic composition of box core GeoB19965-2A of all three sediment fractions: bulk, decarbonised (dc), detrital (dt) 51
Figure 2.11: Detailed overall mineralogical composition of gravity cores GeoB19905-1, GeoB19927-3 and GeoB19946-4 52
Figure 2.12: Mineralogical composition of the bulk sediment fraction of gravity core GeoB19905-1 53
Figure 2.13: Mineralogical composition of the bulk sediment fraction of gravity core GeoB19927-3 54
Figure 2.14: Mineralogical composition of the bulk sediment fraction of gravity core GeoB19946-4 54

Chapter 3

Figure 3.1: Map of the research area in the Labrador Sea with simplified ocean current system and close-up on southern Greenland geological terrains 66
Figure 3.2: Radiogenic isotope records of the siliciclastic detrital sediment fraction of gravity core GeoB19905-1 69
Figure 3.3: Mineralogical composition of the bulk sediment fraction of gravity core GeoB19905-1 70

Figure 3.4: Provenance plot for radiogenic isotope composition of the siliciclastic detrital sediment fraction of gravity core GeoB19905-1 and isotopic ranges of the main southern Greenland geological terrains for $^{87}Sr/^{86}Sr$ versus εNd and $^{206}Pb/^{204}Pb$ versus $^{207}Pb/^{204}Pb$. 71
Figure 3.5: Close-up of Sr and Nd isotopic data of gravity core GeoB19905-1 ……..74
Figure 3.6: Distribution of KMB and AB stream sediment data for each isotope system: εNd $^{87}Sr/^{86}Sr$ and $^{206}Pb/^{204}Pb$ ……75

Chapter 4

Figure 4.1: Overview map of research area, main ocean surface currents and core locations of the study in northeastern Baffin Bay ……90
Figure 4.2: Radiogenic isotope records of siliciclastic detrital sediment fraction of gravity core GeoTÜ SL170 ……94
Figure 4.3: Radiogenic isotope records of siliciclastic detrital sediment fraction of gravity core GeoB19927-3 ……95
Figure 4.4: Mineralogical composition of gravity core GeoB19927-3 ……95
Figure 4.5: Radiogenic isotope records of siliciclastic detrital sediment fraction of gravity core GeoB19946-4 ……96
Figure 4.6: Mineralogical composition of gravity core GeoB19946-4 …… 97
Figure 4.7: Provenance plots for radiogenic isotope composition of the siliciclastic detrital sediment fraction of gravity cores GeoTÜ SL170, GeoB19927-3 and GeoB19946-4 and isotopic ranges of the main Greenland geological terrains for $^{87}Sr/^{86}Sr$ versus εNd and $^{206}Pb/^{204}Pb$ versus $^{207}Pb/^{204}Pb$ ……98

Chapter 5

Figure 5.1: Area map of Baffin Bay and Nares Strait and their present-day surface current patterns. Core location of gravity core AMD14-Kane2B and main northern Greenland and Ellesmere Island geological terrains ……117
Figure 5.2: Radiogenic isotope records of the siliciclastic detrital sediment fraction of gravity core AMD14-Kane2B ……120
Figure 5.3: Provenance plots of radiogenic isotope composition of the siliciclastic detrital sediment fraction from gravity core AMD14-Kane2B and isotopic ranges of the main Greenland and Ellesmere Island geological terrains for $^{87}Sr/^{86}Sr$ versus εNd and $^{206}Pb/^{204}Pb$ versus $^{207}Pb/^{204}Pb$ …… 121
Figure 5.4: Close-up into Sr – Nd and Pb provenance plot for gravity core AMD14-Kane2B data …… 124

Abstract

Due to the effect of Arctic Amplification the Arctic is currently warming at least twice as fast as the rest of the planet. Seasonal sea-ice extent has been alarmingly declining in the past decade. Glaciers and ice caps along the Greenland coast and in the Canadian Arctic have been losing mass on an accelerated rate during the past century. As the global climate system is a complex system connecting different regions via atmospheric transport, changes in Arctic climate patterns are affecting the climate and weather conditions in the lower latitudes. The Greenland Ice Sheet as well as glaciers and ice caps in the Canadian Arctic are the largest freshwater storages on the northern hemisphere and expected to be among the highest contributors to global sea level rise. Freshwater input through meltwater discharge is not only affecting sea level rise but further influencing deep water formation in the Labrador Sea and the subpolar North Atlantic and hence global ocean circulation and climate patterns.

To be able to sufficiently predict future developments of the Greenland Ice Sheet with respect to mass loss and resulting impacts on the global climate, data from past climate and Greenland Ice Sheet extents are crucially important. The Holocene spanning the last period of the deglaciation after the Last Glacial Maximum culminating in the Holocene Thermal Maximum when atmospheric temperatures were warmer and glacier and ice-sheet extent smaller than today represents the closest analogue to current atmospheric warming and Greenland Ice Sheet mass loss. The wide west Greenland shelf of Baffin Bay and Labrador Sea hosts thick marine sediments archiving around ten thousand years of this past climate and ice-sheet history.

Siliciclastic detrital material discharged into Baffin Bay and the Labrador Sea via meltwater and erosion can be separated from those sedimentary archives and traced back to its source region. Radiogenic isotopes (Sr, Nd, Pb) label the source regions of those sediments by fingerprinting the isotopic composition of the prevailing bedrock. Hence, they can be used as reliable provenance tracers. Retreating land-ice masses expose bedrock that before was not subject to erosion, influencing the isotopic signatures delivered into the surrounding ocean. Based on this theory, radiogenic isotopes can record changes in siliciclastic detrital sediment provenance and hence, indirectly trace ice-sheet dynamics.

The overall aim of this thesis work is to reconstruct changes in detrital sediment provenance along the west Greenland shelf to gain new insights into Holocene Greenland Ice Sheet dynamics and ocean current-induced sediment transport. Sedimentary archives from three main research areas (eastern Labrador Sea, northeastern Baffin Bay, and Kane Basin, central Nares Strait) record obvious shifts in sediment provenance throughout the Holocene. Those shifts coincide with major regional climatic changes in the research area. Generally, all records reveal the local bedrock as the main source region of detrital material and distal-sourced material transported along the coast via the West Greenland Current as a secondary source. Although the proportion of distal sourced material appears to be small, changes in West Greenland Current strength have been recorded in the isotopic composition.

In southwestern Greenland and the Labrador Sea radiogenic isotope records reveal a shift towards a higher proportion of the local Archean Block in the late Holocene caused by Neoglacial ice advance and a reduction in West Greenland Current speed delivering less material from southern most Greenland. Farther north in the Upernavik region, midwest Greenland coast, the isotopic composition marks a change with the transition from early to mid

Holocene caused by increased West Greenland Current strength and the opening of Vaigat Strait which enabled erosion and transport of freshly exposed basalts from the Disko Bay area due to ice-sheet retreat. This basalt input is, however, not transported all the way to northernmost Melville Bay (northern Baffin Bay) where the detrital sediment composition is clearly dominated by contribution of the local Committee-Melville Belt without any significant provenance changes throughout the Holocene. Farthest north, the sedimentary record from Kane Basin records provenance shifts that confirm the opening of Nares Strait around 8.3 ka BP. This event is followed by an increased delivery of carbonate-rich detrital sediments from northern Ellesmere Island due to the newly established gateway of Arctic Ocean water transporting sediments from further north to the core location.

Additionally determined mineralogical composition of the sedimentary records along the west Greenland coast supports the interpretation drawn from the radiogenic isotopic composition. Furthermore, it points out the additional value of radiogenic isotopes through variations only visible in isotopic composition but not in the mineralogical composition. Further comparison to other studies from the region based on different tracers confirms the reliability and sufficient application of radiogenic isotopes in provenance studies as well as the advantage of multi-proxy approaches in paleoclimatological studies.

Overall, this study highlights the advantages and reliability of radiogenic isotopes in provenance studies with regards to reconstructions of ice-sheet dynamics. The combination of the three isotopic systems (Sr, Nd, Pb) enables source region determination with a higher probability compensating for overlapping signatures within individual isotopic systems. The transect of sedimentary records along the west Greenland coast identifies clearly distinguishable isotopic ranges for the different Greenland bedrock terrains, qualifying this approach for further high-resolution investigation in past Greenland Ice Sheet development.

Kurzfassung

Durch den Effekt der Arktischen Verstärkung (Arctic Amplification) erwärmt sich die Arktis derzeit mindestens doppelt so schnell wie der Rest des Planeten. Innerhalb des letzten Jahrzehnts verzeichnete die saisonale Meereisausdehnung einen alarmierend rückläufigen Trend. Die Gletscher und Eiskappen entlang der grönländischen Küste und in der kanadischen Arktis haben innerhalb des letzten Jahrhunderts zunehmend an Masse verloren. Da das globale Klimasystem ein komplexes System ist, welches die unterschiedlichen Regionen der Erde über atmosphärische Transportwege miteinander verbindet, beeinflussen klimatische Veränderungen in der Arktis das Klima und die Wetterbedingungen in den gemäßigten Breiten ausschlaggebend. Der grönländische Eisschild und die Gletscher und Eiskappen in der kanadischen Arktis sind die größten Speicher von Süßwasser in der nördlichen Hemisphäre und tragen voraussichtlich mit am stärksten zum globalen Meeresspiegelanstieg bei. Süßwassereintrag durch Schmelzwasser dieser Landeismassen wirkt sich allerdings nicht nur auf den Meeresspiegelanstieg aus, sondern beeinflusst auch die Tiefenwasserbildung in der Labradorsee und im subpolaren Nordatlantik und somit die globale Ozeanzirkulation sowie das globale Klima.

Um die zukünftige Entwicklung des grönländisches Eisschildes in Bezug auf dessen Massenverlust und die daraus resultierenden Auswirkungen auf das globale Klima hinreichend vorhersagen zu können, sind Daten über vergangene Klimabedingungen und die Ausdehnung des grönländischen Eisschildes von essentieller Bedeutung. Das Holozän schließt die letzte Periode des Eisrückganges nach dem letzten glazialen Maximum ein, der im Holozänen Optimum (Holocene Thermal Maximum) seinen Höhepunkt findet, als atmosphärische Temperaturen wärmer und die Ausdehnung der Gletscher und des Eisschildes geringer waren als heute. Damit stellt das Holozän das nächste Analogon zur gegenwärtigen globalen Erwärmung und dem Massenverlust des grönländischen Eisschildes dar. Der breite westgrönländische Schelf der Baffin Bucht und Labradorsee beherbergt meterdicke, marine Sedimente, die etwa zehntausend Jahre dieser vergangenen Klima- und Eisschildgeschichte archivieren.

Siliziklastisches, detritisches Material, das durch Schmelzwasser und Erosion in die Baffin Bucht und Labradorsee eingetragen wird, kann aus diesen Sedimentarchiven isoliert und zu seinen Herkunftsregionen zurückverfolgt werden. Radiogene Isotope (Sr, Nd, Pb) kennzeichnen die Herkunftsregion dieser Sedimente mit spezifischen Isotopenzusammensetzungen des anstehenden Grundgesteins und dienen daher als verlässliche Herkunftsmarker. Sich zurückziehende Landeismassen legen Gesteinsschichten frei, die zuvor nicht der Erosion ausgesetzt waren, was sich auf die Isotopensignaturen auswirkt, die in den umgebenden Ozean gelangen. Basierend auf dieser Theorie können radiogene Isotope Veränderungen in der Provenienz von detritischen Sedimenten aufzeichnen und somit können indirekte Rückschlüsse auf vergangene Gletscher- und Eisbewegungen gezogen werden.

Das übergeordnete Ziel dieser Dissertation ist es, Veränderungen in den Provenienzen detritischer Sedimente entlang des westgrönländischen Schelfs zu rekonstruieren, um neue Erkenntnisse über Eisbewegungen des grönländischen Eisschildes im Holozän und den durch die Meeresströmung induzierten Sedimenttransport zu gewinnen. Sedimentkerne aus drei Hauptuntersuchungsgebieten (der östlichen Labradorsee, der nordöstlichen Baffin Bay und dem Kane Basin in der zentralen Nares-Straße) zeigen deutliche Verschiebungen der

Sedimentprovenienzen innerhalb des Holozäns. Diese Verschiebungen überschneiden sich mit bekannten regionalen klimatischen Veränderungen im Forschungsgebiet. Generell deuten die erhobenen Daten darauf hin, dass das lokale Grundgestein die Hauptquelle für den Eintrag von detritischem Material auf dem westgrönländischen Schelf ist und Material, welches über den Westgrönlandstrom entlang der Küste transportiert worden ist, eine sekundäre Quelle darstellt. Obwohl der Anteil an weittransportiertem Material gering zu sein scheint, sind Änderungen in der Stärke des Westgrönlandstroms aus der Isotopenzusammensetzung zu erkennen.

Im Südwesten Grönlands und in der Labradorsee zeigen die Messungen radiogener Isotope eine Verschiebung zu einem höheren Anteil des lokalen Archaischen Blocks (Archean Block) im späten Holozän. Diese wurde durch den neoglazialen Eisvorstoß verursacht sowie durch eine gleichzeitige Verringerung der Geschwindigkeit des Westgrönlandstroms, der weniger Material aus Südgrönland transportiert. Weiter nördlich in der Region Upernavik, an der mittelwestlichen Küste Grönlands, markiert die Isotopenzusammensetzung eine Veränderung während des Übergangs vom frühen zum mittleren Holozän, herbeigeführt durch eine Verstärkung des Westgrönlandstroms und die Öffnung der Vaigat-Straße, die aufgrund des Eisschildrückzuges die Erosion und den Transport von freigelegten Basalten aus dem Gebiet der Diskobucht ermöglichte. Dieser Basalteintrag wird jedoch nicht bis in die nördlichste Melville-Bucht (nördliche Baffinbucht) transportiert, wo die detritische Sedimentzusammensetzung eindeutig von Sedimenteinträgen des lokalen Committee-Melville Gürtels dominiert wird, ohne ersichtliche signifikante Veränderung innerhalb der Provenienz während des Holozäns. Der nördlichste Sedimentkern aus dem Kane Basin verzeichnet eine Provenienzverschiebung, die die Öffnung der Nares-Straße um 8,3 ka BP und eine damit verstärkte Anlieferung von karbonatreichen, detritischen Sedimenten von der nördlichen Ellesmere-Insel bestätigen. Dieser Transport von karbonatreichem Material wurde erst möglich durch die Wiedereinstellung vom Oberflächenstrom aus dem Arktischen Ozean nach der Öffnung der Nares-Straße, der detritische Sedimente von weiter nördlichen Gebieten der Ellesmere-Insel zur Kernlokation transportiert.

Eine zusätzliche Untersuchung der mineralogischen Zusammensetzung der Sedimentkerne entlang der westgrönländischen Küste unterstützt die aus der radiogenen Isotopenzusammensetzung gezogene Interpretation. Desweiteren wird durch Variationen, die aus der mineralogischen Zusammensetzung nicht ersichtlich sind, der Mehrwert der radiogenen Isotope sichtbar, die diese Variationen anzeigen. Auch der Vergleich mit weiteren Studien aus der Region, die auf unterschiedlichen Tracern basieren, bestätigt die Zuverlässigkeit der Anwendung von radiogenen Isotopen in Provenienzstudien, sowie den Vorteil von Multi-Proxy-Ansätzen in paläoklimatologischen Studien.

Insgesamt unterstreicht diese Studie die Vorteile und Zuverlässigkeit von radiogenen Isotopen in Provenienzstudien im Hinblick auf Gletscher- und Eisschildbewegungen. Die Kombination der drei Isotopensysteme (Sr, Nd, Pb) ermöglicht die Bestimmung der Herkunftsregion mit einer höheren Wahrscheinlichkeit, da regional überlappende Isotopensignaturen einzelner Isotopensysteme kompensiert werden. Das Profil von Sedimentkernen entlang der westgrönländischen Küste identifiziert klar unterscheidbare Isotopensignaturen der verschiedenen grönländischen Gesteinsformationen. Diese klare Unterscheidung qualifiziert diese Methode für weitere hochauflösende Untersuchungen der vergangenen Entwicklung des grönländischen Eisschildes.

CHAPTER ONE

Introduction

Why should we care about the Arctic?

1. Introduction

1.1. Scientific Motivation - Why should we care about the Arctic?

The Arctic, a place that is often hidden on the upper edge of world maps, is one of the most sensible environments of this planet. It is not just the Arctic Ocean that has been increasingly catching attention due to declining sea-ice extent and concentration over the past years (e.g. Grosfeld et al., 2016; Notz & Stroeve, 2018; Vaughan et al., 2013). The Arctic is most often defined as the entire area above the Arctic Circle at 66°33'N, including major land areas and native peoples in Canada, Russia, Alaska (USA), Norway, Finland, Sweden and Greenland (Denmark). It is home to a variety of regional-restricted species, land and water-based, such as polar bears, reindeer, walruses, hooded seals, sea-birds, fish and essential microorganisms such as algae, but also home to mysterious and sparsely studied animals such as narwhales and the Greenland shark. A large number of these animals is today classified as *vulnerable* by the *International Union for Conservation of Nature and Natural Resources*. A reason for this development is the declining extent of sea ice and the lengthening of the period from spring sea ice retreat to fall sea ice advance. Over the past 3.5 decades this time interval from retreat to advance has increased by three to nine weeks in most regions over the Arctic which has a significant influence on marine mammal life history and habitat (Stern & Laidre, 2016). Polar bears are especially impacted as with declining sea-ice extent and freezing periods their hunting grounds are shrinking.

But why is the Arctic so important? – What happens in the Arctic doesn't stay in the Arctic.

The past summer of 2020 has been recorded as a historical low in July sea-ice extent and the second lowest September extent after the record year of 2012 (Grosfeld et al., 2016; Spreen et al., 2008). A decline in Arctic perennial sea-ice extent has been recorded over the past decades (Comiso, 2012; Nghiem et al., 2007). Since 1979 Arctic September sea-ice extent has been declining with a rate of more than 11% per decade (Polyakov et al., 2012). The perennial sea ice is also becoming younger with only 15% being older than two years in 2010 compared to 50-60% in the 1980s, which is fostering further decline in coming years (Comiso, 2012; Maslanik et al., 2007; Polyakov et al., 2012). The ongoing decline in sea-ice extent is generally the most pronounced indicator of our planet's changing climate. With ongoing climate change, the Arctic has been found to warm more than twice as fast as the rest of the planet (e.g. Jansen et al., 2020; Screen et al., 2012). This process is called Arctic Amplification and is caused by interplay of several drivers, spanning from local drivers such as ocean-atmosphere heat transfer during the transition from melting to freezing season to atmospheric heat and moisture transport from the tropics through teleconnection (e.g. Ding et al., 2014; Goosse et al., 2018; Screen et al., 2012; Serreze & Francis, 2006; Svendsen et al., 2018). The contribution of these drivers to actual Polar and Arctic Amplification is still debated (Stuecker et al., 2018). It is, however, known that for this century projections of Polar Amplification in the Arctic is stronger than in the Antarctic (Hugues Goosse et al., 2018; Serreze & Francis, 2006). Not only the Arctic Ocean is warming, most prominent annual mean surface and tropospheric warming since 1979 has been attributed to Greenland and north eastern Canada, almost twice as much as Arctic mean warming (Ding et al., 2014). Ding et al. (2014) attribute around half of the

current enhanced warming to the general uniform warming in the entire Arctic caused by anthropogenic forcing and the other half to the enhance heat transport from the tropical pacific. According to climate models, with increasing anthropogenic CO_2 emissions, the Arctic Ocean will most likely be ice-free (sea ice area $<10^6$ km^2) for the first time in September before 2050 (Notz et al., 2020; Notz & Stroeve, 2018). What happens in the arctic does not stay in the Arctic, as the climate system is a complex system and connected via atmospheric transport, changes in the Arctic are as well affecting the climate and weather conditions in the lower latitudes leading to increased frequencies of extreme weather events (Francis & Vavrus, 2012; Jung et al., 2015; 2014), such as recently observed severe winters.

1.1.1. The importance of ice sheets and glaciers in the climate system

Ice sheets, glaciers and ice caps store the majority of freshwater on this planet and keep it from heating up by reflecting solar insolation and therefore making up a major part to the earth's albedo, simply the sum of all solar radiation reflected from a surface. Therefore the Arctic functions as the natural refrigerator of the planet and its development is of crucial importance for other parts of the planet. Ice-albedo feedback is playing an important role in global climate change (e.g. Kashiwase et al., 2017; Forster et al., 2007; Lemke et al., 2007) as variations in albedo caused by changes in land-ice cover can influence the Earth's radiation budged (cf. Luthcke et al., 2013).

The earth's three biggest storages of freshwater are the Antarctic Ice Sheet, the Greenland Ice Sheet (GIS) and the glaciers and ice caps (GIC) in the Canadian Arctic (e.g. Gardner et al., 2011; Radić & Hock, 2010) and thereby two of the most important freshwater storages are located in the Arctic. Freshwater is not only stored in these ice masses but released via meltwater discharge. Recent observations report increased mass loss at a number of well known glaciers and ice streams, such as Helheim Glacier, the largest glacier in southeast Greenland or Jakobshavn Isbræ, the largest and most productive ice stream in western Greenland (e.g. Andresen et al., 2012; Bjørk et al., 2012; Holland et al., 2008). Increased air temperatures lead to increased melting, which lowers the ice sheet's surface elevation and exposes the ice to lower atmosphere and higher temperatures which further increases melting (Church et al., 2013; Edwards et al., 2014). This is one of the major positive feedback mechanisms influencing GIS melt, especially in contrary to the Antarctic Ice Sheet where surface temperatures are low and this mechanism becomes insignificant (Hugues Goosse et al., 2018). Glacier and ice-sheet mass balance is therefore an important measure of enhanced climate change. Mass balance parameters comprise amongst others accumulations of snow and ice, calving at marine-based margins and basal melting (e.g. Simon et al., 2014) but the overall prediction of these processes is far from simple, due to the amount of unknown variables in specifying the stress boundary conditions at the base and the seaward margin (cf. Vaughan & Arthern, 2007). GIC in the Canadian Arctic and Greenland are among the highest contributors to sea level rise until 2100 (Radić et al., 2014).

Not only is the sea level rising through major contribution of freshwater into the ocean, major ocean currents can also be affected which might have a significant influence on the global climate. The temperature, salinity and wind driven global ocean conveyer belt led by the Atlantic Meridional Overturning Circulation (AMOC) has its starting point in the North Atlantic through the formation of North Atlantic Deep Water (NADW). Around 30 Sv of NADW are transported out of the Labrador Sea via the deep Western Boundary Current (Zantopp et al., 2017). The formation of NADW is steered by the sinking of dense and cold water. Significantly

higher contribution of low salinity fresh and colder water through increased meltwater discharge can have a crucial influence on this deepwater formation and therefore the global ocean circulation. Major freshwater contributions are entering the north Atlantic through Baffin Bay and Labrador Sea, originating from the Arctic Ocean and in form of meltwater from the GIS and the GIC in the Canadian Arctic Archipelago (CAA) and Baffin Island. Not just the declining Arctic Ocean sea-ice concentration but also the increasing mass loss of the Greenland Ice Sheet became a symbol of global climate change (Weidick et al., 2012). Current global glacier retreat is unusual for the entire Holocene and the retreat within the past 100 to 150 years can no longer be explained by natural changes and is attributed to the anthropogenic global temperature increase (Solomina et al., 2016; Vaughan et al., 2013). Current temperatures and melting rates in the Canadian Arctic resemble those of the Holocene Thermal Maximum (HTM) with increased melting rates of GIC since the past ~30 years (Fisher et al., 2012; Lecavalier et al., 2017).

1.1.2. The Greenland Ice Sheet – Recent developments

Greenland is considered the largest island in the world. Today 81% of its 2,166,000 km^2 are covered by a large ice sheet leaving only a small coastal fringe of 0 to 300 km of ice-free bedrock (Dawes, 2009a). The continental shelf encompasses more than twice the area of the ice-free land of Greenland, around 830,000 km^2 (Dawes, 2009a). The maximum elevation at its summit is 3.2 km and 2.8 km at the secondary elevation maximum in southern Greenland. Estimated ice volume of the GIS adds up to 2,960,000 km^3 (Bamber et al., 2013). Since 2003 the GIS has lost around 244 ± 6 Gt/yr on average with an increasing rate of -28 ± 9 Gt/yr^2 (Harig & Simons, 2016), and even more since 2011, average -269 ± 51 Gt/yr (McMillan et al., 2016), which is around one order of magnitude higher than the combined estimated mass loss from Ellesmere, Axel Heiberg, Devon and Baffin Island GIC, which sums up to -37 ± 6 Gt/yr (Jacob et al., 2012). In comparison, mass loss of the Antarctic Ice Sheet was significantly smaller during the same time period: -81 ± 26 Gt/yr (Luthcke et al., 2013). Between 2011 and 2014 the southwestern GIS sector has lost about 41% and the northwestern around 24%, making western Greenland losing the majority of mass (McMillan et al., 2016).

Increased and continuous GIS mass loss (Castro de la Guardia et al., 2015; Harig & Simons, 2012, 2016; Jacob et al., 2012; Rignot et al., 2011; Solomina et al., 2015) was observed to be a response to increased summer air temperature and summer melt season extent (Luthcke et al., 2013) but also to increased sea surface temperatures of the surrounding ocean basins (Hanna et al., 2013; Holland et al., 2008). The GIS mass balance has been clearly identified as being sensible to atmospheric warming, including influences trough changes in North Atlantic Oscillation (Hanna et al., 2008). However, the rate of this sensitivity and the expected response of the GIS to global warming contains ongoing uncertainties (cf. Hanna et al., 2013; McFarlin et al., 2018). Greenland temperatures are predicted to increase between 1 and 8°C by 2100 (Hanna et al., 2008). The GIS has been estimated to be the major contributor to present global sea level rise (Church et al., 2013; Harig & Simons, 2012; Jacob et al., 2012; McFarlin et al., 2018; Rignot et al., 2011), with a potential of 7.42 ± 0.05 m above modern global sea level (Morlighem et al., 2017).

Due to the major role ice sheets, glaciers and ice caps play in the current debate of climate change and the fact that the prediction of their development is rather complex, we cannot exclusively rely on present-day observations through satellites and weather stations, but have to take a look at past developments to feed and improve climate models in order to make more

confident predictions for the future (Notz & Stroeve, 2018; Simon et al., 2014; Weidick et al., 2012). Models deliver general trends but have been found to underlie uncertainties in detecting smaller scale fluctuations or overestimate ice-sheet movements on a more regional trend (Larsen et al., 2015; Levy et al., 2017). To fill these missing gaps further actual geological and palaeoceanographical data is needed. Holocene records are essentially important for past climate reconstructions as most prior records of past interglacial and ice-sheet dynamics have been overprinted or lost due to glacial erosion (e.g. Long et al., 2009; McFarlin et al., 2018; Vaughan & Arthern, 2007; Weidick et al., 2012). Especially, as during the past in the process of the deglaciation after the Last Glacial Maximum (LGM) and the following Holocene Thermal Maximum the expansion of the GIS and GIC were even smaller than today. Also mean global temperature have not yet reached the maximum of the early-mid Holocene (for the period 2000-2009), but exceeded temperatures during ~75% of the past Holocene temperatures (Marcott et al., 2013). Northern Greenland air temperatures are now at their highest since the past 6.8 to 7.8 ka (Lecavalier et al., 2017).

The aim of this thesis work is to emphasize the importance of past GIS development and ice-sheet dynamics with a focus on the (north)western GIS margin and add to the recently growing number of contribution from this area. Especially the (south)western Greenland margin has been found to be particularly sensitive to long-term climate change (Larsen et al., 2014) and the northwestern GIS has been found object to increased mass loss (Luthcke et al., 2013), both are expected to increase in the future (McFarlin et al., 2018). Past ice-sheet dynamics will be indirectly traced by changes in detrital sediment provenance from marine records collected along the West Greenland shelf. To increase the comparability of studies, locations from the entire west Greenland margin have been included to point out differences based on comparable data and to define different endmembers of material transported from and into these different regions. As it has been found that the Arctic is not behaving as a single climatological unit (Kaufman et al., 2004; McKay et al., 2018), studies on a bigger regional scale are highly sufficient and promising.

1.2. Introduction into the Research Area

Andrews and Funder (1985) described the Baffin Bay region as 'one of the most important sources of paleoenvironmental data in the entire Northern Hemisphere'. Baffin Bay has been highlighted as one of the most important areas for ice-sheet dynamics as it was bordered by three major ice sheets during the LGM and recorded lots of those ice streaming activities within its sediments (Simon et al., 2014).

1.2.1. Baffin Bay

Bordered by Greenland in the east and the Canadian Arctic Archipelago and Baffin Island in the west, Baffin Bay is a large marine embayment compassing roughly 1400 by 550 km, around 690000 km^2 (e.g. Simon et al., 2014; Tang et al., 2004). The Bay resulted from an extension of the North Atlantic - Labrador Shelf Sea rift system (MacLean et al., 1990; Simon et al., 2014), which is why the prevailing geology on both sides is similar (Dawes, 2009a, 2009b; Jackson & Berman, 2000; Le Pichon et al., 1977). The bay is presently characterized by a counter-clockwise surface current gyre, transporting warmer Atlantic sourced waters northwards along the West Greenland coast and mixing in the northern part of the bay with Arctic sourced fresh water, travelling south again along the Baffin Island coast (Figure 1.1). This way Baffin Bay represents an important pathway of Arctic Ocean freshwater through Labrador Sea into the North Atlantic. The warmer more saline waters travelling north originate from the cold and

fresh East Greenland Current (EGC) transporting Arctic Ocean freshwater along the East Greenland coast and merging with warmer and more saline waters from the Irminger Current when travelling around Cape Farewell, the southern tip of Greenland (e.g. Fratantoni & Pickart, 2007; Myers et al., 2009). Those waters make their way north as the West Greenland Current (WGC). A major part of the WGC is turning west around 61°N into Labrador Sea, leaving the remaining current notably slower travelling through Davis Strait into Baffin Bay (Cuny et al., 2002; Fratantoni & Pickart, 2007; Myers et al., 2009). The WGC is continuing north along the West Greenland coast where it freshens on the way due to freshwater input through meltwater discharge and outlet glaciers and hence losing parts of its Atlantic influence (Buch, 2002; Myers et al., 2009). Atlantic water can however, be traced as far north as Thule (Funder, 1990). Arctic waters enter through Jones Sound, Lancaster Sound and Nares Strait, spilling over sills at 120 m, 125 m (Barrow Strait) and 250m (Kane Basin) depth, respectively (Tang et al., 2004). These Arctic waters merge with the WGC and travel south along the CAA and Baffin Island coast, leaving Baffin Bay through Davis Strait and continuing along the Labrador coast. Arctic water entering through Nares Strait and the CAA is however also penetrating on the west Greenland shelf, at least in Melville Bay and Uummannaq Trough (e.g. Sheldon et al., 2016).

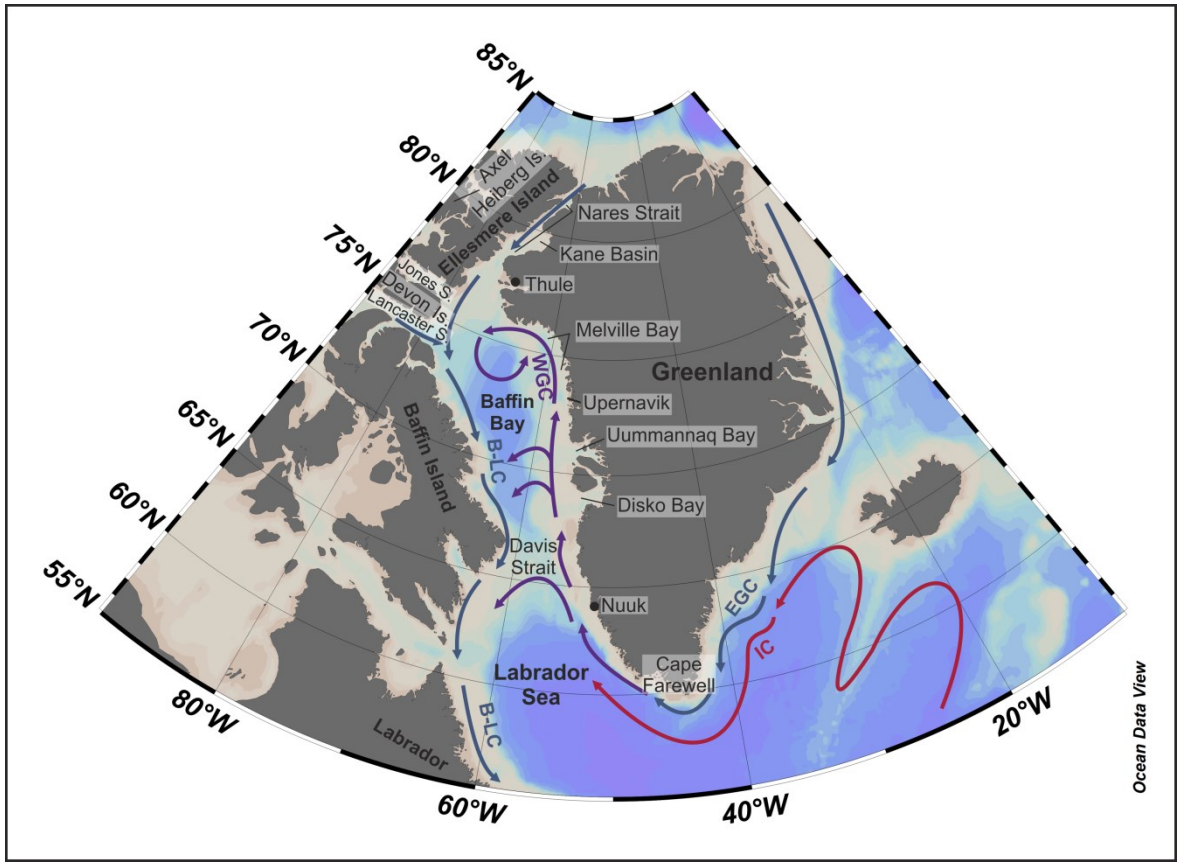

Figure 1.1: Map of the research area with simplified present-day surface current circulation pattern and locations mentioned in text. Map created with Ocean Data View (Schlitzer, 2020).

The Baffin Bay hydrography can be roughly summarized into three water mass layers: cold and fresh surface water (0 to 150-300 m), warmer and more saline intermediate water (150-300 to 1200-1300 m), both originating from WGC, and cold slightly fresher deep-water (1300 to bottom) (cf. Aksu, 1983; Tang et al., 2004). However, there is always a lens of seasonal freshwater due to sea-ice melt and glacial runoff (Stordal & Wasserburg, 1986). The bay is almost completely ice-covered most of the year, with sea-ice forming from October onwards

and growing continuously from northwest to south and only ice-free in August and September (Tang et al., 2004). This so-called west-ice is first year ice formed in northern Baffin Bay in September and continuously growing southwards along the northwestern Greenland coast (Buch, 2002) reaching its maximum in March only leaving eastern Davis Strait partly ice-free (Tang et al., 2004).

The West Greenland shelf is sloping into Baffin Basin, an abyssal plain with maximum water depth of 2300 m (Aksu, 1983; Tang et al., 2004). The shelf spans around 250 km in width and is much wider than the counterpart along the Canadian Baffin Island coast (Aksu & Piper, 1987). Both shelf sides are characterised by major ice streams and cross-shelf troughs, discharging and accumulating regional and distal transported marine and detrital sediments (Batchelor & Dowdeswell, 2014). Those troughs represent most likely former locations of marine-terminating ice streams during the quaternary (Batchelor & Dowdeswell, 2014).

The West Greenland coast is further shaped by a number of marine embayments influencing the Baffin Bay hydrography and representing the most efficient source areas for iceberg calving. The majority of Baffin Bay icebergs calve from outlet glaciers along the West Greenland coast north of 68°N, with Disko Bay and Uummannaq Bay being the most efficient calving areas (Tang et al., 2004). Generally, larger icebergs drift northwards and smaller ones southwards and through Davis Strait into the North Atlantic, making Baffin Bay an important iceberg source area, especially as the northern pathway is blocked by an ice arch in Kane Basin, Nares Strait (Tang et al., 2004).

North of Disko Bay, Melville Bay represents the final and major turning area of the WGC. The Bay is a heavily glaciated area around 70 km north of Upernavik Trough (Briner et al., 2013). Its shelf is characterised by three major cross-shelf troughs, as well as multiple fast-flowing glaciers and ice streams (Bennike, 2008; Briner et al., 2013). Today about 27% of the western GIS drain into Melville Bay (Rignot & Kanagaratnam, 2006).

1.2.2. Labrador Sea

The Labrador Sea, the coldest and freshest basin in the subpolar North Atlantic, is presently characterised by a counter-clockwise surface current gyre (Yashayaev, 2007). The surface circulation pattern comprises of the westwards flowing branch of the WGC and the Arctic Ocean sourced waters from the Baffin Island Current (e.g. Mao et al., 2014) and leaving the Labrador Sea as the Labrador Current, the main pathway for equatorwards freshwater (Yashayaev, 2007). The coastal waters of Labrador Sea are influenced by seasonal variations in meltwater input from the GIS (Castelao et al., 2019), with the majority of freshwater and sea ice being delivered into Labrador Sea from Baffin Bay through Davis Strait (Tang et al., 2004). However, the majority of GIS meltwater reaching the interior of Labrador Sea and influencing salinity and stratification patterns originates from southeast Greenland, whereas the southwest Greenland meltwater gets mainly transported northwards into Baffin Bay (Castelao et al., 2019; Luo et al., 2016). Occasionally sea ice from east Greenland gets transported through the EGC into Labrador Sea (Grosfeld et al., 2016; Spreen et al., 2008). The current circulation pattern and the full appearance of Labrador Sea water establish around 3 ka BP (e.g. de Vernal & Hillaire-Marcel, 2000; Fagel et al., 2004). Also, surface and deeper water masses are currently warming, the Labrador Sea has been observed to be nearly 18°C warmer at 1500 m depth than 20 years ago (Zantopp et al., 2017).

1.3. Greenland Ice Sheet History since the Last Glacial Maximum

Greenland glaciation was mainly controlled by a decrease in atmospheric carbon dioxide during the late Pliocene (Lunt et al., 2008). Glaciations are generally influenced by changes in the planet's energy budget, because an increase in thermal contrast between the poles and the equator leads to the development of land ice cover (Budyko, 1969).

The Greenland Ice Sheet is the last remaining ice sheet on the northern Hemisphere. During the LGM around 20 ka ago it was connected via the southeastern sector of the Innuitian Ice Sheet (IIS) to the northeastern sector of the Laurentide Ice Sheet (LIS), both covering major parts of the north American continent (England et al., 2006). In the process of the deglaciation those ice sheets retreated on different rates discharging meltwater and sediments into the enclosed Baffin Bay and Labrador Sea (Jackson et al., 2017). The LIS and IIS retreated slowly until 7.5 ka BP, leaving only some glaciers and ice caps throughout the island of CAA and Baffin Island (England et al., 2006). The IIS started to retreat from east to west around 11.6 ka ago, leaving only island-based ice caps on Ellesmere Island by 9 ka BP and the sea penetrating the eastern CAA by 8.5 ka (England et al., 2006) The deglaciation and separation history of the IIS and GIS is documented by meltwater channels and moraines throughout Nares Strait (England et al., 2006).

In the process of the deglaciation following the LGM the GIS itself has also been retreating asynchronous along the west Greenland coast which has been documented in several studies and investigated in a variety of modelling studies of different generations with ongoing improvements (Lecavalier et al., 2014; Tarasov & Peltier, 2003). During the LGM the entire west Greenland shelf has been covered by the GIS which retreated towards the mid shelf until around the Younger Dryas and fully retreated to its current position by 8.4 ka BP in Melville Bay, northernmost Baffin Bay (Slabon et al., 2016). In midwest Greenland the GIS retreated from the shelf between ~11.3 ka BP (Corbett et al., 2013), ~9.9 ka BP (Briner et al., 2013) and ~9.5 ka BP (Bennike, 2000) in the Upernavik region, ~70 km south of Melville Bay. At Uummannaq Trough the GIS was in retreat from its offshore position during the LGM by around 15 ka BP (Sheldon et al., 2016a) and 14.8 ka BP and around 13.8 ka BP in the Disko Bay (Ó Cofaigh et al., 2013). In southern Greenland the GIS started to retreat from the outer coast between ~11.4 and 10.4 ka BP (Larsen et al., 2014) reaching its minimum position around ~4 ka BP (Larsen et al., 2015) and its current position around 2.2 ka BP (Kaplan et al., 2002; Larsen et al., 2011). The ice-sheet retreat from the shelf during the early Holocene might have been accelerated through incoming warmer Atlantic-sourced waters (Knutz et al., 2011; Larsen et al., 2014) after the establishment of the WGC before 14 ka BP (Sheldon et al., 2016a). While the northwestern GIS margin reached its current position comparably early (Lecavalier et al., 2014), ice-sheet fluctuations exceeding its current outlines have been documented in southern Greenland (Larsen et al., 2015, 2011; Levy et al., 2018).

Today the GIS leaves 100-125 km of revealed Greenland bedrock in the Nuuk region, southern Greenland (Weidick et al., 2012) and only a small fringe of ice-free bedrock in Northern Greenland, making land-based geological records marking the complete deglaciation of Melville Bay and northernmost Greenland relatively sparse (Bennike, 2008; Young & Briner, 2015). The ice sheet drains through several ice streams and glaciers entering fjords along the coast (e.g. Weidick et al., 2012). Based on mass-balance calculations Melville Bay currently drains around 27% of the GIS, which is a comparably large proportion considering that the

entire West Greenland sector drains 43%, with Jakobshavn Isbræ draining around 7% (Rignot & Kanagaratnam, 2006).

1.4. Recent Studies and Research Aim

Over the past decades a variety of studies have been conducted, including marine and lacustrine sedimentary archives, ice cores, morphological as well as modelling studies to reconstruct past Greenland climate and environmental conditions, sea-ice extent and ice-sheet dynamics in the Baffin Bay and Labrador Sea area.

The majority of studies from the Baffin Bay and Labrador Sea area concentrate around southern Greenland and the Labrador Sea as well as the Disko Bay area. Southern Greenland fjords, lakes and marine archives as well as morphological evidences have been studied for Holocene climate and circulation patterns and ice-sheet development (e.g. Kaplan et al., 2002; Larsen et al., 2015, 2017; Levy et al., 2017; Møller et al., 2006; Seidenkrantz et al., 2007; Weiser et al., 2021). The Disko Bay (e.g. Allan et al., 2018; Ouellet-Bernier et al., 2014; Perner et al., 2012; Seidenkrantz et al., 2013) and Uummannaq area (e.g. Philipps et al., 2018; Rignot et al., 2016; Sheldon et al., 2016) have been, amongst others, subject to studies of past ocean circulation, sea-surface conditions as well as the development of local ice streams such as the well-known Jakobshavn Isbræ. In comparisons to southern Greenland and the Disko Bay area studies from northern Baffin Bay are comparably sparse. A number of studies has been focused on the North Water polynya (NOW), one of the largest polynyas in the Northern Hemisphere located in northwestern Baffin Bay and a prominent area to study productivity and sea-ice patterns and air-sea interactions (e.g. April et al., 2019; Barber et al., 2001; Lalande et al., 2009; Marchese et al., 2017; Moore & Våge, 2018). Due to the position of the GIS margin in Melville Bay close to the coast, land-based studies on GIS deglaciation are limited (Bennike, 2008; Young & Briner, 2015) and have only recently been complimented by high-resolution swath bathymetry studies (Freire et al., 2015; Slabon et al., 2018a, 2018b; Slabon et al., 2016). Even more recently further studies on marine sedimentary archives from the Melville Bay and Upernavik area investigated past oceanic and sea-ice conditions and sediment delivering regimes with regards to ice-sheet dynamics (Caron et al., 2020, 2019a, 2019b; Giraudeau et al., 2019; Hansen et al., 2020; Saini et al., 2020). Farther north in Nares Strait, one of three pathways of Arctic Ocean water into Baffin Bay, morphological studies have been conducted to define the timing of the re-opening of the strait after it was blocked by the GIS and IIS during the LGM (England, 1999; Zreda et al., 1999). The re-opening of Nares Strait formerly dated to around 7.5 ka BP (England, 1999) has been recently discussed and suggested to be adapted to dates between 9 and 8.3 ka BP (Ceperley et al., 2020; Georgiadis et al., 2018; Jennings et al., 2011, 2019).

However, the majority of studies conducted on marine sedimentary archives along the west Greenland margin are based on micropaleontological and palynological, as well as common geochemical proxies, stable isotope tracers or biomarkers, dealing with overall climatological and oceanographic changes. To trace ice-sheet dynamics from marine records, compensating for morphological overprints land-based studies are prone to (Long et al., 2009; Weidick et al., 2012) and regional differences that are often not detected or overestimated in climate models (Larsen et al., 2015; Levy et al., 2017) sediment pathways of detrital sediments onto the west Greenland shelf have to be identified. Provenance studies defining source regions of detrital sediments can be a powerful tool to trace these pathways and has been done on Baffin Bay marine sediments based on mineralogical and geochemical composition (Andrews et al., 2015,

2018; Caron et al., 2020; Giraudeau et al., 2019). Andrews et al. (2015) combined mineralogical data with data of radiogenic isotopes Sr and Nd, identifying significant differences between eastern and western Greenland surface sediment composition. They point out that the additional and independently analysed radiogenic isotopes strongly reinforce the results of the mineralogical composition (Andrews et al., 2015). Still, the amount of studies applying radiogenic isotopes in provenance studies to track ice-sheet dynamics is relatively sparse and can be mainly summarised by two studies investigating southern Greenland Ice Sheet extent during the last interglacial (Colville et al., 2011) and Marine Isotope Stage 11 (Reyes et al., 2014) as well as studies throughout Baffin Bay and the subpolar North Atlantic defining IRD sources of the surrounding ice sheets during Heinrich Events (Benson et al., 2003; Farmer et al., 2003).

In order to take advantage of the high-resolution Holocene sedimentary records of the west Greenland shelf and the reliability of radiogenic isotopes in provenance studies with regards to ice-sheet dynamics (Colville et al., 2011; Reyes et al., 2014) this thesis work is introducing Holocene radiogenic isotope records along the west Greenland coast. The overall aim is to investigate the still underrepresented potential of radiogenic isotopes and their specific application in west Greenland provenance differentiation. By analysing Holocene records of combined radiogenic isotopes strontium, neodymium and lead along a south to north transect along the west Greenland shelf and Nares Strait, spatio-temporal differences in isotopic composition will be used to tackle the following questions:

(1) How is the isotopic composition changing over time and does it indicate specific detrital provenance changes linked to Greenland Ice Sheet dynamics?
(2) Are there major regional differences in Greenland Ice Sheet development throughout the Holocene?
(3) How reliable are the combined radiogenic isotope records of Sr, Nd and Pb in the discrimination of different Greenland detrital sediment sources?
(4) Are there general advantages of radiogenic isotope based provenance studies in comparison to those based on mineralogical composition?

1.5. Overview of Own Research

This thesis work aims to identify provenance changes of siliciclastic detrital sediment for indirect reconstruction of ice-sheet dynamics throughout the Holocene. Three research areas have been chosen to identify the spatial distribution of these changes along the west Greenland coast. The results of each research area were summarised in separate manuscripts (chapters 3-5) in preparation for scientific journals. The study outline and conceptual ideas of this PhD project were devised by Simone A. Kasemann and Lina Madaj in close consultation with Friedrich Lucassen, Claude Hillaire-Marcel, Dierk Hebbeln and Rüdiger Stein (all thesis committee members).

The sample material for manuscripts one and two (chapters 3-4) was obtained during research cruise *MSM44* on board *RV Maria S .Merian* (Dorschel et al., 2015) and provided by the MARUM GeoB core repository at the University of Bremen, Germany. Independently from this thesis work, Lina Madaj participated in research cruise *MSM44* and supported the ship's crew and scientific party during retrieving and handling of the included sedimentary archives. The sampling of gravity core GeoB19905-1 was conducted by Jens Weiser, GeoB19927-3 was jointly sampled by Lina Madaj, Sabrina Hohmann, Jeetendra Saini and Jens Weiser (all IRTG

ArcTrain), GeoB19946-4 was sampled by Lina Madaj. Box core samples of GeoB19965-2A were taken by Jens Weiser.

The sample material for manuscript three (chapter 5) was obtained during *ArcticNet* expedition (Leg 1b) on board *CCGS Amundsen* in 2014 (Tremblay et al., 2014). Gravity core (Calypso Square) AMD14-Kane2B has been directly subsampled on board. Samples included into manuscript three have been provided by Myriam Caron, Institut des sciences de la mer de Rimouski, GEOTOP, Université du Québec à Rimouski, Canada.

Samples of GeoB19927-3 and GeoB19965-2A were freeze-dried by Volker Diekamp, MARUM, University of Bremen. Samples of GeoB19905-1, GeoB19946-4 and AMD14-Kane2B were oven-dried by Lina Madaj. Subsequent analysis of radiogenic isotopes (including sample preparation) and the corresponding measurements for all included samples were done by Lina Madaj at the Isotope Geochemistry Lab of MARUM, University of Bremen, Germany.

Additional mineralogical analysis through x-ray diffraction (XRD) on samples of all GeoB-cores was conducted at GEOTOP, Centre de recherche en géochimie et géodynamique, Université du Québec à Montréal (UQÀM), Canada. The sample preparation was done by Lina Madaj with support from Michel Preda, GEOTOP-UQÀM. Michel Preda conducted the XRD measurements, while closely explaining analytical steps and procedures to Lina Madaj.

In the following a short summary of each manuscript and the corresponding contributions are provided.

Manuscript 1 (Chapter 3)

Radiogenic Isotopes Reveal Neoglacial Provenance Shift and Ice Advance in Southwest Greenland

(L. Madaj, C. Hillaire-Marcel, F. Lucassen and S. A. Kasemann)

This manuscript summarises the results of the radiogenic isotope and XRD analyses of gravity core GeoB19905-1. Radiogenic isotope analysis (sample preparation, analysis and measurements) was done by Lina Madaj as well as the sample preparation for XRD analysis. The XRD analysis itself was performed by Michel Preda, GEOTOP-UQÀM. The original manuscript draft was written by Lina Madaj. All co-authors contributed to preceding data discussion and provided improving input on the manuscript's text and content. All figures were compiled by Lina Madaj. The record reveals shifts towards increased local detrital sediment input onto the southwest Greenland shelf during the transition into the mid and late Holocene. Those shifts are most likely connected to a reduction in West Greenland Current speed, transporting less distal material to the core location. The shift at the transition into the late Holocene is more pronounced than the first one, identified by a significant shift towards unradiogenic Nd isotopes and connected to increased local erosion cause by Neoglacial ice advance.

Manuscript 2 (Chapter 4)

Northwestern Greenland Ice Sheet Dynamics traced by radiogenic isotopes

(L. Madaj, V. Kirillova, F. Lucassen, C. Hillaire-Marcel and S. A. Kasemann)

This manuscript summarises the results of the radiogenic isotope and XRD analyses of gravity cores GeoB19927-3 and GeoB19946-4. Box corer GeoB19965-2A serves as additional reference data for source region identification. Radiogenic isotope analysis of the aforementioned sedimentary archives (sample preparation, analysis and measurements) was done by Lina Madaj who also prepared these samples for XRD analysis. The XRD analysis itself was performed by Michel Preda, GEOTOP-UQÀM. Additional radiogenic isotope data of core GeoTÜ SL170 was provided (prepared, analysed and measured) by Valeriia Kirillova within the frame work of her PhD thesis (Kirillova, 2017). The manuscript and all included figures were prepared by Lina Madaj. All co-authors contributed to data discussion and interpretation and provided feedback on the manuscript. All three gravity core records identify local west Greenland sources corresponding to their latitude. While along the coast of Greenland provenance shifts through activation and deactivation of sources can be reconstructed, the northernmost west Greenland ice margin appeared to be stable with respect to detrital provenances.

Manuscript 3 (Chapter 5)

Radiogenic Isotope Signatures of Holocene Sediments from Kane Basin: Linkage with the Re-opening and Evolution of Nares Strait

(L. Madaj, F. Lucassen, C. Hillaire-Marcel and S. A. Kasemann)

This manuscript summarises the results of the radiogenic isotope analysis of gravity core AMD14-Kane2B. Radiogenic isotope analysis (sample preparation, analysis and measurements) was done by Lina Madaj. The original manuscript was constructed and written by Lina Madaj, who also compiled all included figures and main interpretational ideas. All co-authors contributed to data discussion and interpretation and provided feedback on the manuscript. The record identifies two isotopic clusters, an Inglefield Land source (northern Greenland) and an Ellesmere Island source (Canadian Arctic Archipelago), the main two source regions of material discharged into Kane Basin, Nares Strait. The identification of both sources being predominant during different times of the Holocene supports the theory of the final opening of Nares Strait in the process of the deglaciation after the Last Glacial Maximum.

1.6. References

Aksu, A. E. (1983). Holocene and Pleistocene Dissolution Cycles in Deep-Sea Cores of Baffin Bay and Davis Strait: Palaeoceanographic Implications. Marine Geology, 53, 331–348.

Aksu, A. E., & Piper, J. W. (1987). Late Quaternary sedimentation in Baffin Bay. Canadian Journal of Earth Sciences, 24, 1833–1846.

Allan, E., Vernal, A., Knudsen, M. F., Hillaire-Marcel, C., Moros, M., Ribeiro, S., … Seidenkrantz, M. (2018). Late Holocene sea-surface instabilities in the Disko Bugt area, west Greenland, in phase with δ18O-oscillations at Camp Century. Paleoceanography and Paleoclimatology. https://doi.org/10.1002/2017PA003289

Andresen, C. S., Straneo, F., Ribergaard, M. H., Bjørk, A. A., Andersen, T. J., Kuijpers, A., … Ahlstrøm, A. P. (2012). Rapid response of Helheim Glacier in Greenland to climate variability over the past century. Nature Geoscience, 5(1), 37–41. https://doi.org/10.1038/ngeo1349

Andrews, J. T. & Funder S. (1985). Introduction to Quaternary Studies. In: J. T. Andrews (Ed.) Quaternary Environments: Eastern Canadian Arctic, Baffin Bay and Western Greenland. Allen & Unwin, Boston.

Andrews, J. T., Bjork, A. A., Eberl, D. D., Jennings, A. E., & Verplanck, E. P. (2015). Significant differences in late Quaternary bedrock erosion and transport : East versus West Greenland ~ 70 ° N – evidence from the mineralogy of offshore glacial marine sediments. Journal of Quaternary Science, 30(5), 452–463. https://doi.org/10.1002/jqs.2787

Andrews, J. T., Klein, A. J., Jenner, K. A., Jennings, A. E., & Campbell, C. (2018). The variability of Baffin Bay seafloor sediment mineralogy: The identification of discrete glacial sediment sources and application to Late Quaternary downcore analysis. Canadian Journal of Earth Sciences, 55(6), 620–639. https://doi.org/10.1139/cjes-2017-0223

April, A., Montpetit, B., & Langlois, D. (2019). Linking the Open Water Area of the North Open Water Polynya to Climatic Parameters using a Multiple Linear Regression Prediction Model. Atmosphere - Ocean, 57(2), 91–100. https://doi.org/10.1080/07055900.2019.1598332

Bamber, J. L., Griggs, J. A., Hurkmans, R. T. W. L., Dowdeswell, J. A., Gogineni, S. P., Howat, I., … Steinhage, D. (2013). A new bed elevation dataset for Greenland. Cryosphere, 7(2), 499–510. https://doi.org/10.5194/tc-7-499-2013

Barber, D. G., Hanesiak, J. M., Chan, W., & Piwowar, J. (2001). Sea-ice and meteorological conditions in Northern Baffin Bay and the North Water polynya between 1979 and 1996. Atmosphere - Ocean, 39(3), 343–359. https://doi.org/10.1080/07055900.2001.9649685

Batchelor, C. L., & Dowdeswell, J. A. (2014). The physiography of High Arctic cross-shelf troughs. Quaternary Science Reviews, 92, 68–96. https://doi.org/10.1016/j.quascirev.2013.05.025

Bennike, O. (2000). Palaeoecological studies of Holocene lake sediments from west Greenland. Palaeogeography, Palaeoclimatology, Palaeoecology, 155(3–4), 285–304. https://doi.org/10.1016/S0031-0182(99)00121-2

Bennike, O. (2008). An early Holocene Greenland whale from Melville Bugt, Greenland. Quaternary Research, 69(1), 72–76. https://doi.org/10.1016/j.yqres.2007.10.004

Benson, L., Barber, D., Andrews, J. T., Taylor, H., & Lamothe, P. (2003). Rare-earth elements and Nd and Pb isotopes as source indicators for Labrador Sea clay-size sediments during Heinrich event 2. Quaternary Science Reviews, 22(8–9), 881–889. https://doi.org/10.1016/S0277-3791(03)00011-8

Bjørk, A. A., Kjær, K. H., Korsgaard, N. J., Khan, S. A., Kjeldsen, K. K., Andresen, C. S., … Funder, S. (2012). An aerial view of 80 years of climate-related glacier fluctuations in southeast Greenland. Nature Geoscience, 5(6), 427–432. https://doi.org/10.1038/ngeo1481

Briner, J. P., Håkansson, L., & Bennike, O. (2013). The deglaciation and neoglaciation of upernavik isstrøm, greenland. Quaternary Research (United States), 80(3), 459–467. https://doi.org/10.1016/j.yqres.2013.09.008

Buch, E. (2002). Present oceanographic conditions in Greenland Waters. Danish Meteorological Institute, Scientific report.

Budyko, M. I. (1969). The effect of solar radiation variations on the climate of the Earth. Tellus, 21(5), 611–619. https://doi.org/10.3402/tellusa.v21i5.10109

Caron, M., Montero-Serrano, J. C., St-Onge, G., & Rochon, A. (2020). Quantifying Provenance and Transport Pathways of Holocene Sediments From the Northwestern Greenland Margin.

Paleoceanography and Paleoclimatology, 35(5), 1–23. https://doi.org/10.1029/2019PA003809

Caron, M., Rochon, A., Montero-Serrano, J. C., & St-Onge, G. (2019b). Evolution of sea-surface conditions on the northwestern Greenland margin during the Holocene. Journal of Quaternary Science, 34(7), 569–580. https://doi.org/10.1002/jqs.3146

Caron, M., St-Onge, G., Montero-Serrano, J. C., Rochon, A., Georgiadis, E., Giraudeau, J., & Massé, G. (2019a). Holocene chronostratigraphy of northeastern Baffin Bay based on radiocarbon and palaeomagnetic data. Boreas, 48(1), 147–165. https://doi.org/10.1111/bor.12346

Castelao, R. M., Luo, H., Oliver, H., Rennermalm, A. K., Tedesco, M., Bracco, A., … Medeiros, P. M. (2019). Controls on the Transport of Meltwater From the Southern Greenland Ice Sheet in the Labrador Sea. Journal of Geophysical Research: Oceans, 124(6), 3551–3560. https://doi.org/10.1029/2019JC015159

Castro de la Guardia, L., Hu, X., & Myers, P. G. (2015). Greenland Ice Sheet melt increases Baffin Bay heat content on the west Greenland shelf. Geophysical Research Letters, n/a-n/a. https://doi.org/10.1038/nature05320

Ceperley, E. G., Marcott, S. A., Reusche, M. M., Barth, A. M., Mix, A. C., Brook, E. J., & Caffee, M. (2020). Widespread early Holocene deglaciation, Washington Land, northwest Greenland. Quaternary Science Reviews, 231, 106181. https://doi.org/10.1016/j.quascirev.2020.106181

Church, J. A., Clark, P. U., Cazenave, A., Gregory, J. M., Jevrejeva, S., Levermann, A., … Unnikrishnan, A. S. (2013). Sea Level Change. In: Climate Change 2013: The Physical Science Basis. Contribution of Working Group I to the Fifth Assessment Report of the Intergovernmental Panel on Climate Change [Stocker, T.F., D. Qin, G.-K. Plattner, M. Tignor, S.K. Allen, J. Boschung, A. Nauels, Y. Xia, V. Bex and P.M. Midgley (eds.)]. Cambridge University Press, Cambridge, United Kingdom and New York, NY, USA.

Colville, E. J., Carlson, A. E., Beard, B. L., Hatfield, R. G., Stoner, J. S., Reyes, A. V, & Ullman, D. J. (2011). Sr-Nd-Pb isotope evidence for ice-sheet presence on southern Greenland during the Last Interglacial. Science, 333(6042), 620–623. https://doi.org/10.1126/science.1204673

Comiso, J. C. (2012). Large decadal decline of the arctic multiyear ice cover. Journal of Climate, 25(4), 1176–1193. https://doi.org/10.1175/JCLI-D-11-00113.1

Corbett, L. B., Bierman, P. R., Graly, J. A., Neumann, T. A., & Rood, D. H. (2013). Constraining landscape history and glacial erosivity using paired cosmogenic nuclides in upernavik, northwest greenland. Bulletin of the Geological Society of America, 125(9–10), 1539–1553. https://doi.org/10.1130/B30813.1

Cuny, J., Rhines, P. B., Niiler, P. P., & Bacon, S. (2002). Labrador Sea boundary currents and the fate of the Irminger Sea Water. Journal of Physical Oceanography, 32(2), 627–647. https://doi.org/10.1175/1520-0485(2002)032<0627:LSBCAT>2.0.CO;2

Dawes, P R. (2009). The bedrock geology under the Inland Ice: the next major challenge for Greenland mapping. Geological Survey of Denmark and Greenland Bulletin, 17, 57–60.

Dawes, Peter R. (2009). Precambrian - Palaeozoic geology of Smith Sound, Canada and Greenland: Key constraint to palaeogeographic reconstructions of northern Laurentia and the North Atlantic region. Terra Nova, 21(1), 1–13. https://doi.org/10.1111/j.1365-3121.2008.00845.x

De Vernal, A., & Hillaire-Marcel, C. (2000). Sea-ice cover, sea-surface salinity and halo-/thermocline structure of the northwest North Atlantic: Modern versus full glacial

conditions. Quaternary Science Reviews, 19(1–5), 65–85. https://doi.org/10.1016/S0277-3791(99)00055-4

Ding, Q., Wallace, J. M., Battisti, D. S., Steig, E. J., Gallant, A. J. E., Kim, H. J., & Geng, L. (2014). Tropical forcing of the recent rapid Arctic warming in northeastern Canada and Greenland. Nature, 509(7499), 209–212. https://doi.org/10.1038/nature13260

Dorschel, B., Afanasyeva, V., Bender, M., Dreutter, S., Eisermann, H., Gebhardt, A. C., … Wangner, D. J. (2015). Past Greenland Ice Sheet dynamics, Palaeoceanography and Plankton Ecology in the Northeast Baffin Bay Cruise No. MSM44 30. MARIA S. MERIAN-Berichte, 148.

Edwards, T., Fettweis, X., Gagliardini, O., Gillet-Chaulet, F., Goelzer, H., Gregory, J., … Ritz, C. (2014). Probabilistic parameterisation of the surface mass balance–elevation feedback in regional climate model simulations of the Greenland ice sheet. The Cryosphere, 8, 181–194. https://doi.org/10.5194/tc-8-181-2014

England, J., Atkinson, N., Bednarski, J., Dyke, A. S., Hodgson, D. A., & Ó Cofaigh, C. (2006). The Innuitian Ice Sheet: configuration, dynamics and chronology. Quaternary Science Reviews, 25(7–8), 689–703. https://doi.org/10.1016/j.quascirev.2005.08.007

England, John. (1999). Coalescent Greenland and Innuitian ice during the Last Glacial Maximum: Revising the Quaternary of the Canadian High Arctic. Quaternary Science Reviews, 18(3), 421–456. https://doi.org/10.1016/S0277-3791(98)00070-5

Fagel, N., Hillaire-Marcel, C., Humblet, M., Brasseur, R., Weis, D., & Stevenson, R. (2004). Nd and Pb isotope signatures of the clay-size fraction of Labrador Sea sediments during the Holocene: Implications for the inception of the modern deep circulation pattern. Paleoceanography, 19(3). https://doi.org/10.1029/2003PA000993

Farmer, G. L., Barber, D., & Andrews, J. (2003). Provenance of Late Quaternary ice-proximal sediments in the North Atlantic : Nd , Sr and Pb isotopic evidence. Earth and Planetary Science Letters, 209, 227–243. https://doi.org/10.1016/S0012-821X(03)00068-2

Fisher, D., Zheng, J., Burgess, D., Zdanowicz, C., Kinnard, C., Sharp, M., & Bourgeois, J. (2012). Recent melt rates of Canadian arctic ice caps are the highest in four millennia. Global and Planetary Change, 84–85, 3–7. https://doi.org/10.1016/j.gloplacha.2011.06.005

Forster, P., V. Ramaswamy, P. Artaxo, T. Berntsen, R. Betts, D.W. Fahey, J. Haywood, J. Lean, D.C. Lowe, G. Myhre, J. Nganga, R. Prinn, G. Raga, M. Schulz and R. Van Dorland, 2007: Changes in Atmospheric Constituents and in Radiative Forcing. In: Climate Change 2007: The Physical Science Basis. Contribution of Working Group I to the Fourth Assessment Report of the Intergovernmental Panel on Climate Change [Solomon, S., D. Qin, M. Manning, Z. Chen, M. Marquis, K.B. Averyt, M.Tignor and H.L. Miller (eds.)]. Cambridge University Press, Cambridge, United Kingdom and New York, NY, USA.

Francis, J. A., & Vavrus, S. J. (2012). Evidence linking Arctic amplification to extreme weather in mid-latitudes. Geophysical Research Letters, 39(6), 1–6. https://doi.org/10.1029/2012GL051000

Fratantoni, P. S., & Pickart, R. S. (2007). The western North Atlantic shelfbreak current system in summer. Journal of Physical Oceanography, 37(10), 2509–2533. https://doi.org/10.1175/JPO3123.1

Freire, F., Gyllencreutz, R., Greenwood, S. L., Mayer, L., Egilsson, A., Thorsteinsson, T., & Jakobsson, M. (2015). High resolution mapping of offshore and onshore glaciogenic features in metamorphic bedrock terrain, Melville Bay, northwestern Greenland. Geomorphology, 250, 29–40. https://doi.org/10.1016/j.geomorph.2015.08.011

Gardner, A. S., Moholdt, G., Wouters, B., Wolken, G. J., Burgess, D. O., Sharp, M. J., … Labine, C. (2011). Sharply increased mass loss from glaciers and ice caps in the Canadian Arctic Archipelago. Nature, 473(7347), 357–360. https://doi.org/10.1038/nature10089

Georgiadis, E., Giraudeau, J., Martinez, P., Lajeunesse, P., St-Onge, G., Schmidt, S., & Massé, G. (2018). Deglacial to postglacial history of Nares Strait, Northwest Greenland: A marine perspective from Kane Basin. Climate of the Past, 14(12), 1991–2010. https://doi.org/10.5194/cp-14-1991-2018

Giraudeau, J., Georgiadis, E., Caron, M., Martinez, P., Saint-Onge, G., Billy, I., … Massé, G. (2019). A high-resolution elemental record of post-glacial lithic sedimentation in Upernavik Trough, western Greenland: history of ice-sheet dynamics and ocean circulation changes over the last 9 100 years. Paleoceanography and Paleoclimatology, 191(April 2019), 1–37. https://doi.org/10.1016/j.gloplacha.2020.103217

Goosse, H., Kay, J. E., Armour, K. C., Bodas-Salcedo, A., Chepfer, H., Docquier, D., … Vancoppenolle, M. (2018). Quantifying climate feedbacks in polar regions. Nature Communications, 9(1). https://doi.org/10.1038/s41467-018-04173-0

Grosfeld, K., Treffeisen, R., Asseng, J., Bartsch, A., Bräuer, B., Fritzsch, B., … Weigelt, M. (2016). Online Sea-Ice Knowledge and Data Platform <www.meereisportal.de>. Polarforschung, 85(2), 143–155. https://doi.org/10.2312/polfor.2016.011

Hanna, E., Huybrechts, P., Steffen, K., Cappelen, J., Huff, R., Shuman, C., … Griffiths, M. (2008). Increased runoff from melt from the Greenland Ice Sheet: A response to global warming. Journal of Climate, 21(2), 331–341. https://doi.org/10.1175/2007JCLI1964.1

Hanna, E., Jones, J. M., Cappelen, J., Mernild, S. H., Wood, L., Steffen, K., & Huybrechts, P. (2013). The influence of North Atlantic atmospheric and oceanic forcing effects on 1900-2010 Greenland summer climate and ice melt/runoff. International Journal of Climatology, 33(4), 862–880. https://doi.org/10.1002/joc.3475

Hansen, K. E., Giraudeau, J., Wacker, L., & Pearce, C. (2020). Reconstruction of Holocene oceanographic conditions in the Northeastern Baffin Bay. Climate of the Past Discussions, (January), 1–34.

Harig, C., & Simons, F. J. (2012). Mapping Greenland's mass loss in space and time. Proceedings of the National Academy of Sciences of the United States of America, 109(49), 19934–19937. https://doi.org/10.1073/pnas.1206785109

Harig, C., & Simons, F. J. (2016). Ice mass loss in Greenland, the Gulf of Alaska, and the Canadian Archipelago: Seasonal cycles and decadal trends. Geophysical Research Letters, 43(7), 3150–3159. https://doi.org/10.1002/2016GL067759

Holland, D. M., Thomas, R. H., de Young, B., Ribergaard, M. H., & Lyberth, B. (2008). Acceleration of Jakobshavn Isbræ triggered by warm subsurface ocean waters. Nature Geoscience, 1(10), 659–664. https://doi.org/10.1038/ngeo316

Jackson, G. D., & Berman, R. G. (2000). Precambrian metamorphic and tectonic evolution of northern Baffin Island, Nunavut, Canada. Canadian Mineralogist, 38(2), 399–421. https://doi.org/10.2113/gscanmin.38.2.399

Jackson, R., Carlson, A. E., Hillaire-Marcel, C., Wacker, L., Vogt, C., & Kucera, M. (2017). Asynchronous instability of the North American-Arctic and Greenland ice sheets during the last deglaciation. Quaternary Science Reviews, 164, 140–153. https://doi.org/10.1016/j.quascirev.2017.03.020

Jacob, T., Wahr, J., Pfeffer, W. T., & Swenson, S. (2012). Recent contributions of glaciers and ice caps to sea level rise. Nature, 482(7386), 514–518. https://doi.org/10.1038/nature10847

Jansen, E., Christensen, J. H., Dokken, T., Nisancioglu, K. H., Vinther, B. M., Capron, E., … Stendel, M. (2020). Past perspectives on the present era of abrupt Arctic climate change. Nature Climate Change, 10(August), 714–721. https://doi.org/10.1038/s41558-020-0860-7

Jennings, A E, Sheldon, C., Cronin, T., Francus, P., Stoner, J. S., & Andrews, J. (2011). The Holocene History of Nares Strait. Oceanography, 24(3), 26–41. https://doi.org/10.5670/oceanog.2011.52

Jennings, Anne E., Andrews, J. T., Oliver, B., Walczak, M., & Mix, A. (2019). Retreat of the Smith Sound Ice Stream in the Early Holocene. Boreas, 48(4), 825–840. https://doi.org/10.1111/bor.12391

Jung, T., Doblas-Reyes, F., Goessling, H., Guemas, V., Bitz, C., Buontempo, C., … Yang, S. (2015). Polar lower-latitude linkages and their role in weather and climate prediction. Bulletin of the American Meteorological Society, 96(11), ES197–ES200. https://doi.org/10.1175/BAMS-D-15-00121.1

Jung, T., Kasper, M. A., Semmler, T., & Serrar, S. (2014). Arctic influence on subseasonal midlatitude prediction. Geophysical Research Letters, 41(10), 3676–3680. https://doi.org/10.1002/2014GL059961

Kaplan, M. R., Wolfe, A. P., & Miller, G. H. (2002). Holocene Environmental Variability in Southern Greenland Inferred from Lake Sediments. Quaternary Research, 58(2), 149–159. https://doi.org/10.1006/qres.2002.2352

Kashiwase, H., Ohshima, K. I., Nihashi, S., & Eicken, H. (2017). Evidence for ice-ocean albedo feedback in the Arctic Ocean shifting to a seasonal ice zone. Scientific Reports, 7(1), 1–10. https://doi.org/10.1038/s41598-017-08467-z

Kaufman, D. S., Ager, T. A., Anderson, N. J., Anderson, P. M., Andrews, J. T., Bartlein, P. J., … Wolfe, B. B. (2004). Holocene thermal maximum in the western Arctic (0-180°W). Quaternary Science Reviews, 23(5–6), 529–560. https://doi.org/10.1016/j.quascirev.2003.09.007

Kirillova, V. (2017). Radiogenic isotopes on the marine sediments from the Baffin Bay: implications for the sediment supply during the last deglaciation. Dissertation, University of Bremen, Germany.

Knutz, P. C., Sicre, M. A., Ebbesen, H., Christiansen, S., & Kuijpers, A. (2011). Multiple-stage deglacial retreat of the southern Greenland Ice Sheet linked with Irminger Current warm water transport. Paleoceanography, 26(3), 1–18. https://doi.org/10.1029/2010PA002053

Lalande, C., Forest, A., Barber, D. G., Gratton, Y., & Fortier, L. (2009). Variability in the annual cycle of vertical particulate organic carbon export on Arctic shelves: Contrasting the Laptev Sea, Northern Baffin Bay and the Beaufort Sea. Continental Shelf Research, 29(17), 2157–2165. https://doi.org/10.1016/j.csr.2009.08.009

Larsen, N. K., Funder, S., Kjær, K. H., Kjeldsen, K. K., Knudsen, M. F., & Linge, H. (2014). Rapid early Holocene ice retreat in West Greenland. Quaternary Science Reviews, 92, 310–323. https://doi.org/10.1016/j.quascirev.2013.05.027

Larsen, N. K., Kjær, K. H., Lecavalier, B., Bjørk, A. A., Colding, S., Huybrechts, P., … Olsen, J. (2015). The response of the southern Greenland ice sheet to the Holocene thermal maximum. Geology, 43(4), 291–294. https://doi.org/10.1130/G36476.1

Larsen, N. K., Kjær, K. H., Olsen, J., Funder, S., Kjeldsen, K. K., & Nørgaard-Pedersen, N. (2011). Restricted impact of Holocene climate variations on the southern Greenland Ice Sheet. Quaternary Science Reviews, 30(21–22), 3171–3180. https://doi.org/10.1016/j.quascirev.2011.07.022

Larsen, N. K., Strunk, A., Levy, L. B., Olsen, J., Bjørk, A., Lauridsen, T. L., … Davidson, T. A. (2017). Strong altitudinal control on the response of local glaciers to Holocene climate change in southwest Greenland. Quaternary Science Reviews, 168, 69–78. https://doi.org/10.1016/j.quascirev.2017.05.008

Le Pichon, X., Sibuet, J.-C., & Francheteau, J. (1977). The fit of the continents around the North Atlantic Ocean. Tectonophysics, 38(3–4), 169–209. https://doi.org/10.1016/0040-1951(77)90210-4

Lecavalier, B. S., Fisher, D. A., Milne, G. A., Vinther, B. M., Tarasov, L., Huybrechts, P., … Dyke, A. S. (2017). High Arctic Holocene temperature record from the Agassiz ice cap and Greenland ice sheet evolution. Proceedings of the National Academy of Sciences, 114(23), 5952–5957. https://doi.org/10.1073/pnas.1616287114

Lecavalier, B. S., Milne, G. A., Simpson, M. J. R., Wake, L., Huybrechts, P., Tarasov, L., … Larsen, N. K. (2014). A model of Greenland ice sheet deglaciation constrained by observations of relative sea level and ice extent. Quaternary Science Reviews, 102, 54–84. https://doi.org/10.1016/j.quascirev.2014.07.018

Lemke, P., J. Ren, R.B. Alley, I. Allison, J. Carrasco, G. Flato, Y. Fujii, G. Kaser, P. Mote, R.H. Thomas and T. Zhang, 2007: Observations: Changes in Snow, Ice and Frozen Ground. In: Climate Change 2007: The Physical Science Basis. Contribution of Working Group I to the Fourth Assessment Report of the Intergovernmental Panel on Climate Change [Solomon, S., D. Qin, M. Manning, Z. Chen, M. Marquis, K.B. Averyt, M. Tignor and H.L. Miller (eds.)]. Cambridge University Press, Cambridge, United Kingdom and New York, NY, USA.

Levy, L. B., Larsen, N. K., Davidson, T. A., Strunk, A., Olsen, J., & Jeppesen, E. (2017). Contrasting evidence of Holocene ice margin retreat, south-western Greenland. Journal of Quaternary Science, 32(5), 604–616. https://doi.org/10.1002/jqs.2957

Levy, L. B., Kelly, M. A., Applegate, P. A., Howley, J. A., Virginia, R. A., Levy, L. B., … Howley, J. A. (2018). Middle to late Holocene chronology of the western margin of the Greenland Ice Sheet : A comparison with Holocene temperature and precipitation records. Arctic, Antarctic, and Alpine Research, 50(1), 1–12. https://doi.org/10.1080/15230430.2017.1414477

Long, A. J., Woodroffe, S. A., Dawson, S., Roberts, D. H., & Bryant, C. L. (2009). Late Holocene relative sea level rise and the Neoglacial history of the Greenland ice sheet. Journal of Quaternary Science, 24(4), 345–359. https://doi.org/10.1002/jqs

Luo, H., Castelao, R. M., Rennermalm, A. K., Tedesco, M., Bracco, A., Yager, P. L., & Mote, T. L. (2016). Oceanic transport of surface meltwater from the southern Greenland ice sheet. Nature Geoscience, 9(7), 528–532. https://doi.org/10.1038/ngeo2708

Luthcke, S. B., Sabaka, T. J., Loomis, B. D., Arendt, A. A., McCarthy, J. J., & Camp, J. (2013). Antarctica, Greenland and Gulf of Alaska land-ice evolution from an iterated GRACE global mascon solution. Journal of Glaciology, 59(216), 613–631. https://doi.org/10.3189/2013JoG12J147

Mao, L., Piper, D. J. W., Saint-Ange, F., Andrews, J. T., & Kienast, M. (2014). Provenance of sediment in the Labrador Current: A record of hinterland glaciation over the past 125 ka. Journal of Quaternary Science, 29(7), 650–660. https://doi.org/10.1002/jqs.2736

Marchese, C., Albouy, C., Tremblay, J. É., Dumont, D., D'Ortenzio, F., Vissault, S., & Bélanger, S. (2017). Changes in phytoplankton bloom phenology over the North Water (NOW) polynya: a response to changing environmental conditions. Polar Biology, 40(9), 1721–1737. https://doi.org/10.1007/s00300-017-2095-2

Maclean B, Williams GL, Srivastava SP. 1990. Geology of Baffin Bay and Davis Strait. In Geology of Canada No.2: Geology of the continental margin of eastern Canada, Keen MJ, Williams GL (eds). Geological Survey of Canada: 293–348.

Marcott, S. A., Shakun, J. D., Clark, P. U., & Mix, A. C. (2013). A Reconstruction of Regional and Global Temperature for the Past 11,300 Years. Science - Reports, 339(March), 1198–1202.

Maslanik, J. A., Fowler, C., Stroeve, J., Drobot, S., Zwally, J., Yi, D., & Emery, W. (2007). A younger, thinner Arctic ice cover: Increased potential for rapid, extensive sea-ice loss. Geophysical Research Letters, 34(24), 2004–2008. https://doi.org/10.1029/2007GL032043

McFarlin, J. M., Axford, Y., Osburn, M. R., Kelly, M. A., Osterberg, E. C., & Farnsworth, L. B. (2018). Pronounced summer warming in northwest Greenland during the Holocene and Last Interglacial. Proceedings of the National Academy of Sciences, 115(25), 6357–6362. https://doi.org/10.1073/pnas.1720420115

McKay, N. P., Kaufman, D. S., Routson, C. C., Erb, M. P., & Zander, P. D. (2018). The Onset and Rate of Holocene Neoglacial Cooling in the Arctic. Geophysical Research Letters, 45(22), 12,487-12,496. https://doi.org/10.1029/2018GL079773

McMillan, M., Leeson, A., Shepherd, A., Briggs, K., Armitage, T. W., Hogg, A., … Gilbert, L. (2016). A high-resolution record of Greenland mass balance. Geophysical Research Letters, 43, 7002–7010. https://doi.org/10.1007/978-3-642-41714-6_130721

Møller, H. S., Jensen, K. G., Kuijpers, A., Aagaard-Sørensen, S., Seidenkrantz, M., Prins, M., … Mikkelsen, N. (2006). Late-Holocene environment and climatic changes in Ameralik Fjord , southwest Greenland : evidence from the sedimentary record. The Holocene, 16(5), 685–695. https://doi.org/10.1191/0959683606hl963rp

Moore, G. W. K., & Våge, K. (2018). Impact of model resolution on the representation of the air–sea interaction associated with the North Water Polynya. Quarterly Journal of the Royal Meteorological Society, 144(714), 1474–1489. https://doi.org/10.1002/qj.3295

Morlighem, M., Williams, C. N., Rignot, E., An, L., Arndt, J. E., Bamber, J. L., … Zinglersen, K. B. (2017). BedMachine v3: Complete Bed Topography and Ocean Bathymetry Mapping of Greenland From Multibeam Echo Sounding Combined With Mass Conservation. Geophysical Research Letters, 44(21), 11,051-11,061. https://doi.org/10.1002/2017GL074954

Myers, P. G., Donnelly, C., & Ribergaard, M. H. (2009). Structure and variability of the West Greenland Current in Summer derived from 6 repeat standard sections. Progress in Oceanography, 80(1–2), 93–112. https://doi.org/10.1016/j.pocean.2008.12.003

Nghiem, S. V., Rigor, I. G., Perovich, D. K., Clemente-Colón, P., Weatherly, J. W., & Neumann, G. (2007). Rapid reduction of Arctic perennial sea ice. Geophysical Research Letters, 34(19), 1–6. https://doi.org/10.1029/2007GL031138

Notz, D., Dörr, J., Bailey, D. A., Blockley, E., Bushuk, M., Boldingh, J., … Vancoppenolle, M. (2020). Arctic Sea Ice in CMIP6. Geophysical Research Letters, 47(10). https://doi.org/10.1029/2019GL086749

Notz, D., & Stroeve, J. (2018). The Trajectory Towards a Seasonally Ice-Free Arctic Ocean. Current Climate Change Reports, 4(4), 407–416. https://doi.org/10.1007/s40641-018-0113-2

Ó Cofaigh, C., Dowdeswell, J. A., Jennings, A. E., Hogan, K. A., Kilfeather, A., Hiemstra, J. F., … Moros, M. (2013). An extensive and dynamic ice sheet on the west greenland shelf during the last glacial cycle. Geology, 41(2), 219–222. https://doi.org/10.1130/G33759.1

Ouellet-Bernier, M.-M., de Vernal, A., Hillaire-Marcel, C., & Moros, M. (2014). Paleoceanographic changes in the Disko Bugt area, West Greenland, during the Holocene. The Holocene, 24(11), 1573–1583. https://doi.org/10.1177/0959683614544060

Perner, K., Moros, M., Jennings, A. E., Lloyd, J. M., & Knudsen, K. L. (2012). Holocene palaeoceanographic evolution off West Greenland. The Holocene, 23(3), 374–387. https://doi.org/10.1177/0959683612460785

Philipps, W., Briner, J. P., Bennike, O., Schweinsberg, A., Beel, C., & Lifton, N. (2018). Earliest Holocene deglaciation of the central Uummannaq Fjord system, West Greenland. Boreas, 47, 311–325. https://doi.org/10.1111/bor.12270

Polyakov, I. V., Walsh, J. E., & Kwok, R. (2012). Recent changes of Arctic multiyear sea ice coverage and the likely causes. Bulletin of the American Meteorological Society, 93(2), 145–151. https://doi.org/10.1175/BAMS-D-11-00070.1

Radić, V., Bliss, A., Beedlow, A. C., Hock, R., Miles, E., & Cogley, J. G. (2014). Regional and global projections of twenty-first century glacier mass changes in response to climate scenarios from global climate models. Climate Dynamics, 42, 37–58.

Radić, V., & Hock, R. (2010). Regional and global volumes of glaciers derived from statistical upscaling of glacier inventory data. Journal of Geophysical Research: Earth Surface, 115(1), 1–10. https://doi.org/10.1029/2009JF001373

Reyes, A. V, Carlson, A. E., Beard, B. L., Hatfield, R. G., Stoner, J. S., Winsor, K., … Ullman, D. J. (2014). South Greenland ice-sheet collapse during Marine Isotope Stage 11. Nature, 510(7506), 525–528. https://doi.org/10.1038/nature13456

Rignot, E., Fenty, I., Xu, Y., Cai, C., Velicogna, I., Cofaigh, C., … Duncan, D. (2016). Bathymetry data reveal glaciers vulnerable to ice-ocean interaction in Uummannaq and Vaigat glacial fjords, west Greenland. Geophysical Research Letters, 43(6), 2667–2674. https://doi.org/10.1002/2016GL067832

Rignot, E., Velicogna, I., Van Den Broeke, M. R., Monaghan, A., & Lenaerts, J. (2011). Acceleration of the contribution of the Greenland and Antarctic ice sheets to sea level rise. Geophysical Research Letters, 38(5), 1–5. https://doi.org/10.1029/2011GL046583

Rignot, Eric, & Kanagaratnam, P. (2006). Changes in the Velocity Structure of the Greenland Ice Sheet. Science, 311, 986–990.

Saini, J., Stein, R., Fahl, K., Weiser, J., Hebbeln, D., & Hillaire, C. (2020). Holocene variability in sea ice and primary productivity in the northeastern Baffin Bay. Arktos. https://doi.org/10.1007/s41063-020-00075-y

Schlitzer, R. (2020). Ocean Data View, odv.awi.de, 2020.

Screen, J. A., Deser, C., & Simmonds, I. (2012). Local and remote controls on observed Arctic warming. Geophysical Research Letters, 39(10), 1–5. https://doi.org/10.1029/2012GL051598

Seidenkrantz, M. S., Aagaard-Sørensen, S., Sulsbrück, H., Kuijpers, A., Jensen, K. G., & Kunzendorf, H. (2007). Hydrography and climate of the last 4400 years in a SW Greenland fjord: Implications for Labrador Sea palaeoceanography. The Holocene, 17(3), 387–401. https://doi.org/10.1177/0959683607075840

Seidenkrantz, Marit Solveig, Ebbesen, H., Aagaard-Sørensen, S., Moros, M., Lloyd, J. M., Olsen, J., … Kuijpers, A. (2013). Early Holocene large-scale meltwater discharge from Greenland documented by foraminifera and sediment parameters. Palaeogeography, Palaeoclimatology, Palaeoecology, 391, 71–81. https://doi.org/10.1016/j.palaeo.2012.04.006

Serreze, M. C., & Francis, J. A. (2006). The arctic amplification debate. Climatic Change, 76(3–4), 241–264. https://doi.org/10.1007/s10584-005-9017-y

Sheldon, C., Jennings, A., Andrews, J. T., Ó Cofaigh, C., Hogan, K., Dowdeswell, J. A., & Seidenkrantz, M. S. (2016a). Ice stream retreat following the LGM and onset of the west Greenland current in Uummannaq Trough, west Greenland. Quaternary Science Reviews, 147, 27–46. https://doi.org/10.1016/j.quascirev.2016.01.019

Sheldon, C., Jennings, A., Andrews, J. T., Ó Cofaigh, C., Hogan, K., Dowdeswell, J. A., & Seidenkrantz, M. S. (2016b). Ice stream retreat following the LGM and onset of the west Greenland current in Uummannaq Trough, west Greenland. Quaternary Science Reviews, 147, 27–46. https://doi.org/10.1016/j.quascirev.2016.01.019

Simon, Q., Hillaire-Marcel, C., St-Onge, G., & Andrews, J. T. (2014). North-eastern Laurentide, western Greenland and southern Innuitian ice stream dynamics during the last glacial cycle. Journal of Quaternary Science, 29(1), 14–26. https://doi.org/10.1002/jqs.2648

Slabon, P., Dorschel, B., Jokat, W., & Freire, F. (2018a). Bedrock morphology reveals drainage network in northeast Baffin Bay. Geomorphology, 303, 133–145. https://doi.org/10.1016/j.geomorph.2017.11.024

Slabon, P., Dorschel, B., Jokat, W., & Freire, F. (2018b). Submarine geomorphology of northeast Baf fi n Bay and its implications for local paleo-ice sheet dynamics. Geomorphology, 318, 88–100. https://doi.org/10.1016/j.geomorph.2018.06.007

Slabon, P., Dorschel, B., Jokat, W., Myklebust, R., Hebbeln, D., & Gebhardt, C. (2016). Greenland ice sheet retreat history in the northeast Baffin Bay based on high-resolution bathymetry. Quaternary Science Reviews, 154, 182–198. https://doi.org/10.1016/j.quascirev.2016.10.022

Solomina, O. N., Bradley, R. S., Hodgson, D. A., Ivy-Ochs, S., Jomelli, V., Mackintosh, A. N., … Young, N. E. (2015). Holocene glacier fluctuations. Quaternary Science Reviews, 111, 9–34. https://doi.org/10.1016/j.quascirev.2014.11.018

Solomina, O. N., Bradley, R. S., Jomelli, V., Geirsdottir, A., Kaufman, D. S., Koch, J., … Yang, B. (2016). Glacier fluctuations during the past 2000 years. Quaternary Science Reviews, 149, 61–90. https://doi.org/10.1016/j.quascirev.2016.04.008

Spreen, G., Kaleschke, L., & Heygster, G. (2008). Sea ice remote sensing using AMSR-E 89-GHz channels. Journal of Geophysical Research: Oceans, 113(2), 1–14. https://doi.org/10.1029/2005JC003384

Stern, H. L., & Laidre, K. L. (2016). Sea-ice indicators of polar bear habitat. Cryosphere, 10(5), 2027–2041. https://doi.org/10.5194/tc-10-2027-2016

Stordal, M. C., & Wasserburg, G. J. (1986). Neodymium isotopic study of Baffin Bay water : sources of REE from very old terranes. Earth and Planetary Science Letters, 77, 259–272.

Stuecker, M. F., Bitz, C. M., Armour, K. C., Proistosescu, C., Kang, S. M., Xie, S. P., … Jin, F. F. (2018). Polar amplification dominated by local forcing and feedbacks. Nature Climate Change, 8(12), 1076–1081. https://doi.org/10.1038/s41558-018-0339-y

Svendsen, L., Keenlyside, N., Bethke, I., Gao, Y., & Omrani, N. E. (2018). Pacific contribution to the early twentieth-century warming in the Arctic. Nature Climate Change, 8(9), 793–797. https://doi.org/10.1038/s41558-018-0247-1

Tang, C. C. L., Ross, C. K., Yao, T., Petrie, B., DeTracey, B. M., & Dunlap, E. (2004). The circulation, water masses and sea-ice of Baffin Bay. Progress in Oceanography, 63(4), 183–228. https://doi.org/10.1016/j.pocean.2004.09.005

Tarasov, L., & Peltier, W. R. (2003). Greenland glacial history, borehole constraints, and Eemian extent. Journal of Geophysical Research: Solid Earth, 108(B3), 1–20. https://doi.org/10.1029/2001jb001731

Tremblay, J.-E. et al. (2014). ArcticNet Expedition Report Leg 1b – Baffin Bay and the Canadian Arctic Archipelago. Chalut K. & Merzouk A. (editors), ArcticNet – Amundsen Science Program, Université Laval, Canada.

Vaughan, D. G., & Arthern, R. (2007). Why Is It Hard to Predict the Future of Ice Sheets? Science - Perspectives, 315(March), 1503–1505.

Vaughan, D. G., Comiso, J. C., Allison, I., Carrasco, J., Kaser, G., Kwok, R., … Zhang, T. (2013). Observations: Cryosphere. In: Climate Change 2013: The Physical Sci- ence Basis. Contribution of Working Group I to the Fifth Assessment Report of the Intergovernmental Panel on Climate Change [Stocker, T.F., D. Qin, G.-K. Plattner, M. Tignor, S.K. Allen, J. Boschung, A. Nauels, Y. Xia, V. Bex and P.M. Midgley (eds.)]. Cambridge University Press, Cambridge, United Kingdom and New York, NY, USA.

Weidick, A., Bennike, O., Citterio, M., & Nørgaard-pedersen, N. (2012). Neoglacial and historical glacier changes around Kangersuneq fjord in southern West Greenland. Geological Survey of Denmark and Greenland Bulletin, 27, 1–68.

Weiser, J., Titschack, J., McCave, I. N., Lochte, A. A., Saini, J., Stein, R., & Hebbeln, D. (2021). Atlantic water inflow to Labrador Sea and its interaction with ice sheet dynamics during the Holocene. Quaternary Science Reviews, 4545(4545), 4545–1. https://doi.org/10.1016/j.quascirev.2021.106833

Yashayaev, I. (2007). Hydrographic changes in the Labrador Sea, 1960-2005. Progress in Oceanography, 73(3–4), 242–276. https://doi.org/10.1016/j.pocean.2007.04.015

Young, N. E., & Briner, J. P. (2015). Holocene evolution of the western Greenland Ice Sheet: Assessing geophysical ice-sheet models with geological reconstructions of ice-margin change. Quaternary Science Reviews, 114, 1–17. https://doi.org/10.1016/j.quascirev.2015.01.018

Zantopp, R., Fischer, J., Visbeck, M., & Karstensen, J. (2017). Journal of Geophysical Research : Oceans transports at the exit of the Labrador Sea. Journal of Geophysical Research: Oceans, 122, 1724–1748. https://doi.org/10.1002/2016JC012271.Received

Zreda, M., England, J., Phillips, F., Elmore, D., & Sharma, P. (1999). Unblockingof the Nares Strait by Greenland and Ellesmere ice-sheet retreat 10,000 years ago. Letter to Nature, 398, 139–142. https://doi.org/10.1038/246170a0

CHAPTER TWO

Methodology and Results

2. Methodology and Results

2.1. Radiogenic Isotopes as Tracers for Palaeoclimatological and Palaeoceanographic Changes

Radiogenic isotopes have been proven to serve as reliable provenance tracers based on their ability to reflect the isotopic signatures of their continental source regions. Based on different erosion processes terrigenous siliciclastic detritus carrying these isotopic signatures reaches the ocean where it can be locally deposited or transported farther away. Particles dissolved in the water column further have the ability to label the water masses they are carried in, which in turn can therefore be traced back to its source region and distinguished from other water masses (Frank, 2002; van de Flierdt & Frank, 2010). In the past a variety of studies took advantage of radiogenic isotopes in their application as provenance tracers to define source regions of detrital material and reconstruct transport pathways and water mass evolution on different time scales throughout the wider Arctic and subpolar north Atlantic region (e.g. Fagel et al., 2014; Haley et al., 2008; Laukert et al., 2017; Maccali et al., 2018; Werner et al., 2014).

Strontium (Sr), neodymium (Nd) and lead (Pb) are amongst the most common radiogenic isotopes used in the framework of provenance studies and form the base of this study.

2.1.1. Radiogenic Isotopes Strontium, Neodymium and Lead

Radiogenic isotopes are those at the end of a radioactive decay cascade. The principals of radioactive decay are that a so-called parent isotope is spontaneously decaying into one or different daughter isotopes by discharging different ways of energy in the form of nuclear particles (helium nuclei, electrons, (anti)neutrinos, positrons, photons) along a decay cascade. Based on the different ways of particle emissions, radioactive decay can be separated into alpha (α), beta (β) and gamma (γ) decay. The final isotopes at the end of these decay cascades are radiogenic isotopes. Generally, radiogenic isotopes can be used within provenance studies to identify source regions and transport pathways of various environmental cycles, reconstruct temporal and spatial changes within these systems and for dating of the formation of rocks and minerals (e.g. Banner, 2004).

2.1.1.1. Strontium

Sr has four common isotopes ^{84}Sr, ^{86}Sr, ^{87}Sr, and ^{88}Sr, with natural abundances of 0.56%, 9.86%, 7.0% and 82.58%, respectively. Radiogenic ^{87}Sr originates from beta decay of radioactive ^{87}Rb, with a half-life of 48.8 Ga:

$$^{87}Rb \rightarrow {}^{87}Sr + \beta^{-}$$

Sr isotope signatures are documented as ratios of radiogenic ^{87}Sr and the primordial ^{86}Sr. The main input sources for Sr into the ocean are weathering of continental bedrock (via rivers and glacial activity), hydrothermal vents and dissolution of marine carbonates (e.g. Banner, 2004; Frank, 2002). These different pathways contribute different isotopic Sr signatures to the ocean, where they form a uniform global ocean seawater value due to the average deep-water residence time of Sr of several million years, which exceeds the global ocean mixing time of around 1500 years (Broecker & Peng, 1982). This seawater signature depends on the aforementioned input of Sr which may be altered by a combination of long-term processes such as shifts in tectonic uplift, continent constellations, climatic and sea level variations amongst other (Banner, 2004). Therefore the ^{87}Sr/^{86}Sr composition in the ocean has not been constant

throughout the Phanerozoic and can be used as a dating method for marine authigenic sediments through comparison with the $^{87}Sr/^{86}Sr$ seawater curve by Burke et al. (1982). The present-day value for $^{87}Sr/^{86}Sr$ dissolved in seawater representing marine carbonates is 0.70917 (Henderson et al., 1994). $^{87}Sr/^{86}Sr$ signatures have to be interpreted with caution when continental weathering is involved as they inherit a tendency to change with grain size, fine-grained sediments have a tendency to provide more radiogenic $^{87}Sr/^{86}Sr$ signatures (Tütken et al., 2002). The isotopic signatures of Greenland bedrock range between 0.70 and 0.84 (Colville et al., 2011; Reyes et al., 2014; Figure 2.2).

2.1.1.2. Neodymium

Nd is one of the light rare earth elements. Nd has the following seven isotopes (natural abundances in brackets): ^{142}Nd (27.2%), ^{143}Nd (12.2%), ^{144}Nd (23.8%), ^{145}Nd (8.3%), ^{146}Nd (17.2%), ^{148}Nd (5.7%) and ^{150}Nd (5.6%). Radiogenic ^{143}Nd originates from ^{147}Sm which has a half-life of 106 Ga. The radioactive decay of ^{147}Sm is based on alpha decay:

$$^{147}Sm \rightarrow {}^{143}Nd + \alpha$$

The main input source of Nd into the ocean is erosion of continental bedrock. Nd has an average deep-water residence time of 600 – 2000 years which is on the order of or shorter than the global mixing time and therefore Nd can be used as a tracer for different water masses (e.g. Frank, 2002; van de Flierdt & Frank, 2010). Isotopic values of radiogenic Nd are measured as a ratio to the stable and natural occurring ^{144}Nd. To compensate for the resulting small numbers and differences in the corresponding ratio, the results will be normalised to the ancient Chondritic Uniform Reservoir (CHUR) value of 0.512638 as defined by Jacobsen & Wasserburg (1980). These values are widely presented in the ε_{Nd} notation:

$$\varepsilon_{Nd} = \left[\frac{^{143}Nd/^{144}Nd_{sample}}{^{143}Nd/^{144}Nd_{CHUR}} - 1\right] x\ 10^4$$

As ^{147}Sm is a common component of rock building minerals, the $^{143}Nd/^{144}Nd$ signature is dependent on the age and predominant Sm/Nd ratio of the corresponding rocks. Generally, unradiogenic ε_{Nd} values indicate origin of older rocks while more radiogenic values point to younger source regions. The Archean to Paleoproterozoic rocks of Greenland range between -41 and –15 while the Paleogene basalts of Disko Island, midwest Greenland, range between -4 and 10 (Colville et al., 2011; Reyes et al., 2014); Figure 2.2). The comparably short ocean residence time of Nd makes it not only a reliable tracer of detrital sediment sources but also of water masses. Different water masses tend to inhibit the ε_{Nd} signatures of the surrounding continents and therefore can be traced back to their origin and differentiated among each other, directly measured in seawater or recorded in marine carbonates (including shells), fish teeth and ferromanganese nodules or sediment grain coatings (e.g. Blaser et al., 2016; Gutjahr et al., 2007; Laukert, et al., 2017; Martin & Haley, 2000). Especially, in the Labrador Sea area, radiogenic Nd has been widely used as such a tracer due to the distinct ε_{Nd} signatures of Labrador Sea and Baffin Bay water (Blanckenburg & Nägler, 2001; Filippova et al., 2017; Stordal & Wasserburg, 1986). Unlike Sr Nd seems to be a grain-size independent tracer (Tütken et al., 2002).

2.1.1.3. Lead

The most common Pb isotopes are the natural occurring isotope ^{204}Pb (1.4%), the three radiogenic isotopes ^{206}Pb (24.1%), ^{207}Pb (22.1%), ^{208}Pb (52.4%) and the radioactive isotope

^{210}Pb (traces). Pb is primarily transported into the oceans through erosion of continental bedrock (mainly ^{206}Pb) and secondary through hydrothermal vents (mainly ^{207}Pb) (Frank, 2002). Pb isotopes have an average residence time in the Atlantic of around 50 years and between 200 and 400 years in the Pacific Ocean, which makes them sufficient water mass tracers, due to their residence time being shorter than the global ocean mixing time (e.g. Frank, 2002). Radiogenic ^{206}Pb, ^{207}Pb, and ^{208}Pb originate from radioactive uranium ^{238}U and ^{235}U, and thorium ^{232}Th with half lives of 4.47 Ga, 704 Ma and 14 Ga, respectively. The decay follows the following decay cascades through alpha and beta decay:

$$^{238}U \rightarrow {}^{206}Pb + \alpha + \beta^-$$

$$^{235}U \rightarrow {}^{207}Pb + \alpha + \beta^-$$

$$^{232}Th \rightarrow {}^{208}Pb + \alpha + \beta^-$$

The Archean and Paleoproterozoic rocks of Greenland compose of ^{206}Pb/^{204}Pb between 14 and 24 (Colville et al., 2011; Reyes et al., 2014; Figure 2.2).

2.2. Sedimentary Archives of Ice-Sheet Dynamics

This study aims to reconstruct detrital provenance changes and ice-sheet dynamics along a south to north transect of the west Greenland coast, from the Labrador Sea to Kane Basin in central Nares Strait. In total, five sediment cores are included into this study, divided into three main research areas: Labrador Sea, Upernavik and Melville Bay, Nares Strait (Figure 2.1, Table 2.1). Additionally, a box core has been analysed to compensate for missing reference values of geological background data (Table 2.2).

Table 2.1: Gravity cores included into this thesis work. Cruise reports MSM09 (Rhein et al., 2013), ArcticNet 2014 (Tremblay et al., 2014), MSM44 (Dorschel et al., 2015); CCGS = Canadian Coast Guard Ship

	GeoB19905-1	**GeoTÜ SL170**	**GeoB19927-3**	**GeoB19946-4**	**AMD14-Kane2B**
Core ID in Cruise Report	MSM44/331-1	MSM09/455-13	MSM44/353-3	MSM44/372-4	AMD14-KANE2b
Sampling Date	01 July 2015, 09:19 UTC	04 Sep 2008 19:09 UTC	08 July 2015 18:20 UTC	14 July 2015 18:01 UTC	04 Aug 2014 20:45 UTC -4
Latitude	64°21.68'N	68°58.15'N	73°35.26'N	75°49.99'N	79°30.91'N
Longitude	52°57.70'W	59°23.58'W	58°05.66'W	62°30.98'W	70°49.74'W
Water Depth [m]	485	1340	932	718	220
Recovery Depth [cm]	1045	600	1147	1372	425
Sampling Device	Gravity core	Gravity core	Gravity core	Gravity core	Calypso square
Scientific Cruise	MSM44	MSM09 Leg. 2	MSM44	MSM44	ArcticNet Leg. 1b
Research Vessel	*RV Maria S. Merian*	*RV Maria S. Merian*	*RV Maria S. Merian*	*RV Maria S. Merian*	*CCGS Amundsen*

Gravity cores GeoB19905-1, GeoB19927-3, GeoB19946-4 and box core GeoB19965-2A were provided by the GeoB Core Repository at MARUM—Center for Marine Environmental Sciences, University of Bremen. Samples from calypso core AMD14-Kane2B were taken and provided by Myriam Caron, Université du Québec à Rimouski, Canada. Data for gravity core GeoTÜ SL170

has been obtained by Valeriia Kirillova in the framework of her PhD thesis (Kirillova, 2017) and is included in the second manuscript of this thesis for data comparison and publication (chapter 4). As the data of GeoTÜ SL170 has not been obtained in the frame work of this PhD project it is not further included into this chapter.

Table 2.2: Box core included into this thesis work. Cruise report MSM44 (Dorschel et al., 2015).

	Core ID in Cruise Report	**Sampling Date**	**Coordinates**	**Water Depth and Recovery**	**Scientific Cruise and Research Vessel**
GeoB19965-2A	MSM44/391-2	22 July 2015 11:59 UTC	74°23.51'N 56°35.70'W	640 m 63 cm	MSM 44 *RV Maria S. Merian*

As Baffin Bay is a semi enclosed bay with its only connection to the Atlantic Ocean through Labrador Sea and thick layers of Holocene sediments on both sides of the shelves it represents an excellent area for palaeoclimatological studies. Detrital sediments delivering radiogenic isotope signatures of their corresponding source regions onto the west Greenland shelf are mainly transported by erosion through glacier activity, meltwater discharge and the West Greenland Current (WGC) as well as icebergs and sea ice. The Greenland west coast is currently draining around 43% of the Greenland Ice Sheet (GIS) dominated by a number of fast flowing glaciers and ice streams such as the well-known Jakobshavn Isbræ and the Upernavik ice stream, draining ~7% and ~2%, respectively (Eric Rignot & Kanagaratnam, 2006). Glaciers along the west coast north of 68°N are producing the majority of icebergs in Baffin Bay with Disko Bay and Uummannaq Bay being the most productive areas from where they mainly get transported farther north via the WGC (Tang et al., 2004). The WGC is the eastern component of the counter-clockwise surface current gyre characterising ocean circulation in Baffin Bay, with the Baffin – Labrador Current forming the western part (Figure 2.1). The relatively warm and saline Atlantic-sourced water of the WGC freshens on its way north through meltwater discharge along the west Greenland coast (Buch, 2002; Myers et al., 2009) collecting and transporting material discharged along the way. Sea ice might be a secondary but not neglectable transport pathway within Baffin Bay. It is seasonally forming in the northwest of Baffin Bay growing towards the south with the sea-ice border in eastern Davis Strait, leaving eastern Labrador Sea ice-free (Tang et al., 2004).

Different transport pathways generally favour different grain sizes being transported based on energy efficiency. Clay-size fractions are usually analysed for the reconstruction of deep ocean currents as they represent far-travelled material (e.g. Fagel et al., 2004; Fagel et al., 2002) while for meltwater discharge representing local erosion without influence of possible iceberg transport the silt–size fraction is commonly used (e.g. Colville et al., 2011; Reyes et al., 2014). The sand-size fraction can be used as a proxy for ice rafted debris (IRD) as they are too large to be carried by meltwater plumes and rather indicate ice-berg transport (e.g. Andresen et al., 2012). In the framework of this study tracing past ice-sheet dynamics of the western GIS all transport pathways will be considered and hence the bulk grain-size faction will be used for analysis in order to receive an overall signal of combined transport mechanisms within the research area. The general grain-size distribution of the included gravity cores is comparably fine and mainly compost of hemipelagic (clayey) mud and silty clay with occasional sandy layers towards the bottom of the records (chapters 3-5; Caron et al., 2019; Dorschel et al., 2015; Georgiadis et al., 2018; Saini et al., 2020; Weiser et al., 2021). Thus the general sediment grain-

size composition points towards an overall transport regime of meltwater discharge, local erosion (e.g. Colville et al., 2011; Reyes et al., 2014) and ocean currents, reducing the likelihood of possible bias of far-travelled material through IRD. The same approach has been followed by Kirillova (2017) for analysis of gravity core GeoTÜ SL170.

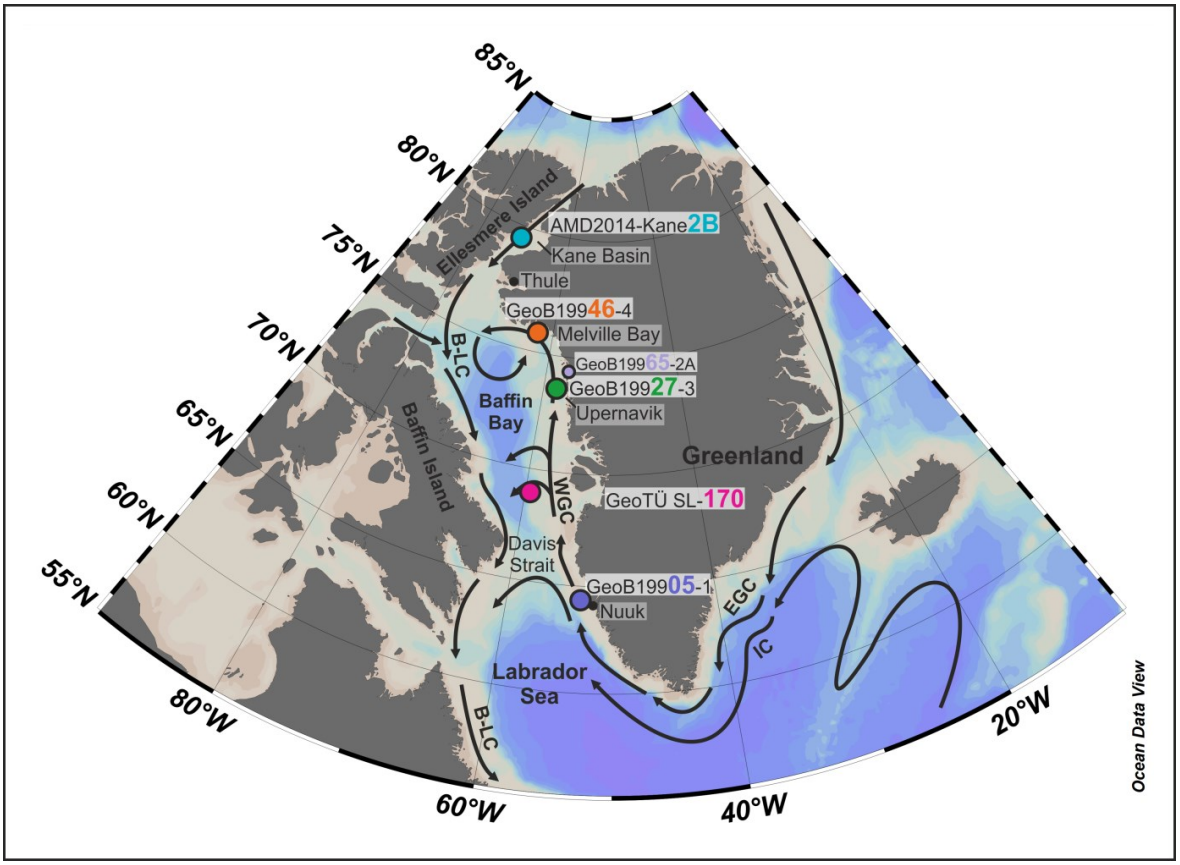

Figure 2.1: Map of the research area with simplified present-day surface current circulation pattern and locations of all sediment cores included into this study. EGC = East Greenland Current, IC = Irminger Current, WGC = West Greenland Current, B-LC = Baffin – Labrador Current. Map created with Ocean Data View (Schlitzer, 2020).

2.2.1. Provenance Approach

During rock formation a specific isotopic composition is imprinted on the resulting rock based on energetic properties and the isotopic composition and availability of different isotopes during the process and its corresponding time in Earth's history (cf. Dickin, 2005). Therefore, different rocks carry different signatures of radiogenic isotopes, especially with regards to age. Through erosion processes these signatures are transported into the surrounding oceans and hence yield information on the corresponding source regions of the discharged material. By newly added sources though freshly exposed bedrock caused by ice-sheet and glacier retreat or the deactivation of those sources through ice advance, the isotopic composition delivered into the oceans might change and provide indirect links on ice-sheet dynamics.

The studies closest to the approach of this study are the aforementioned ones by Colville et al., (2011) and Reyes et al. (2014) who applied radiogenic isotopes to investigate southern GIS presence during the Last Interglacial and southern GIS collapse during Marine Isotope Stage 11, respectively. By analyzing radiogenic isotopes in the detrital silt fraction from Eirik Drift sediments Reyes et al. (2014) proved that only a small residual ice dome remained over southernmost Greenland as decreased meltwater and sediment flux into the ocean led to an almost absence of specific isotopic signatures of the respective end member. Those studies are

based on the comparison of isotopic signatures in the detrital sediment fraction of the sample material to those of stream sediments collected along the southwest Greenland coast. The stream sediments represent fine-grained glaciofluvial sediments from meltwater streams and are supplemented by few glaciolacustrine sediments from ice-marginal lakes and debris entrained in icebergs near calving glacier margins (Reyes et al., 2014). All stream sediments were deposited in low energy environments along streams draining the local geology and therefore represent the isotopic composition actually delivered to the ocean rather than bedrock samples that might contain a bias towards certain rock types (Colville et al., 2011, supplement). Colville et al. (2011) followed the stream sediment approach as the use of isotopic composition of bedrock samples can yield complications because they might over-represent specific rock and mineral types analysed for petrologic or tectonic evolution instead of general isotopic composition on a lateral extent. In comparison of stream sediment data with weighted average rock data Colville et al. (2011, supplement) found mainly agreements in Nd isotopic signatures and slight disagreements in Sr and Pb isotopic composition for certain southern Greenland bedrock terrains. Based on these findings this PhD study will follow the same approach of using stream sediment data as isotopic background values for the geological terrains where the data are available. Additionally, some available bedrock data display large isotopic ranges, causing major overlaps between different sources and therefore do not serve the purpose of source region differentiation. However, data availability depends on the conducted studies and is comparably sparse in northern Greenland. Therefor the isotopic reference data for the different Greenland geological terrains used in this study is a combination of stream sediment and rock data. While the available stream sediments cover the entire southern Greenland margin, for the Rinkian Belt only Sr and Nd isotopic signatures based on rock data are available and for the Committee-Melville-Belt no radiogenic isotope data could be found at all (Figure 2.2). To compensate for the missing data surface sediment data (GeoB19965-2A) from a fjord in northwestern Greenland was added as well as data from Baffin Island. Due to the origin of Baffin Bay from the extension of the North Atlantic - Labrador Shelf Sea rift system (MacLean et al., 1990; Simon et al., 2014), the geology on both sides of the bay is similar (Jackson & Berman, 2000; Le Pichon et al., 1977) and isotopic composition has been found to be chemically comparable (cf. Jackson & Berman, 2000).

2.2.2. Greenland Geology Overview

Greenland holds some of the oldest rocks on Earth with Archean Rocks in southern and northern Greenland and Paleoproterozoic rocks in midwest Greenland (Figure 2.2) (e.g. Dawes, 2009a). The only comparably young rocks that can be found in west Greenland occur in the Disko Bay area, which contains Paleaogene basalts and intrusions (e.g. Dawes, 2009a). The main geological terrains discussed in this study are from south to north: the Ketilidian Mobile Belt (KMB), the Archean Block (AB), the Nagssugtoqidian Mobile Belt (NMB), Disko Island (DI), the Rinkian Mobiel Belt (RMB) and the Committee-Mobile Belt (CMB). Apart from the Paleaogene basalts on Disko Island those geological units are dominated by granites and orthogneisses with occasional supracrustal belts and intrusions (AB) and metagreywackes (RMB) (e.g. Colville et al., 2011; Connelly et al., 2006; Dawes, 2006; Grocott & McCaffrey, 2017; Kalsbeek et al., 1998). Based on their different geological composition and ages these bedrock terrains are composed of different radiogenic isotope signatures (Figure 2.2) which will be delivered into Labrador Sea and Baffin Bay and allowing for the source region determination that this study is based upon.

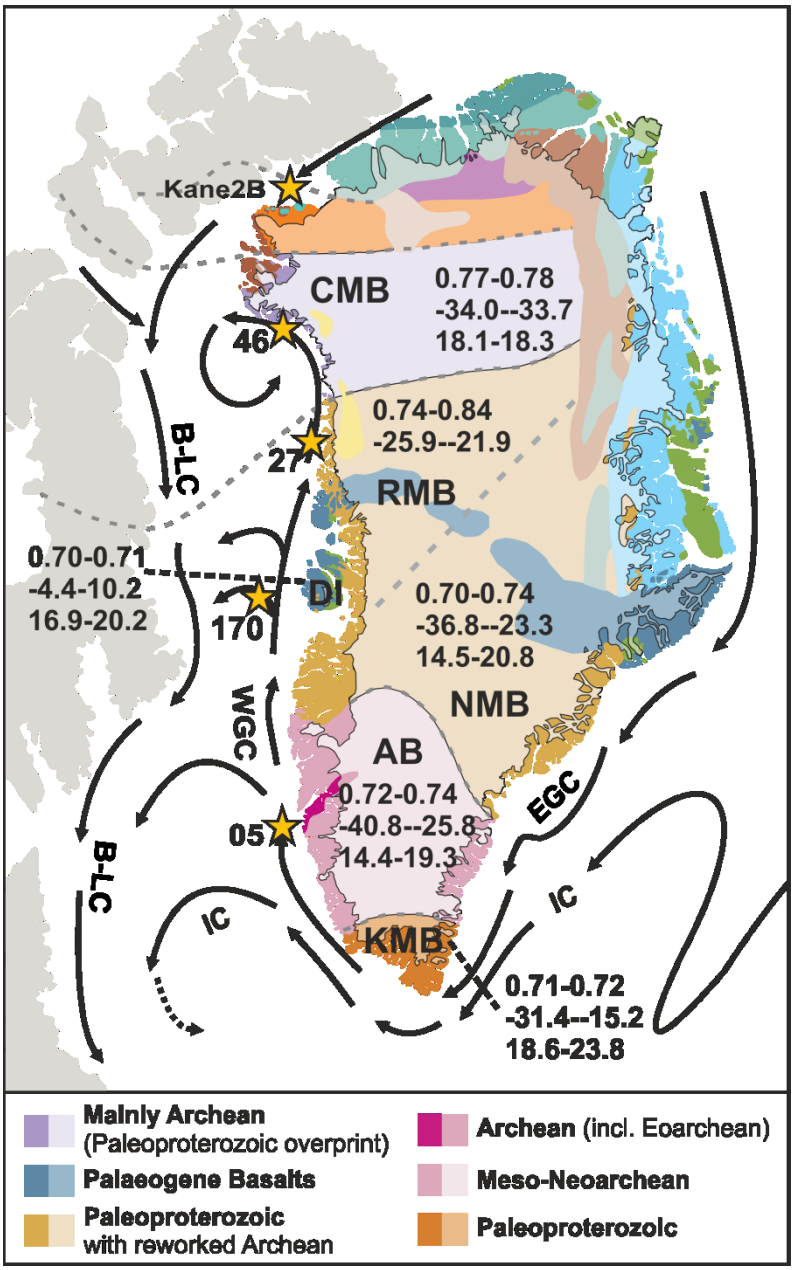

Figure 2.2: Geological map of Greenland with isotopic signatures of main geological terrains included into this study and present day Baffin Bay and Labrador Sea surface circulation pattern. Lighter shaded areas indicate the current extent of the Greenland Ice Sheet, dashed grey line represents the border between NMB and RMB (Dahl-Jensen et al., 2003). KMB = Ketilidian Mobile Belt, AB = Archean Block, NMB = Nagssugtoqidian Mobile Belt, DI = Disko Island, RMB = Rinkian Mobile Belt, CMB = Committee-Melville Belt (map adapted from Dawes, 2009a); EGC = East Greenland Current, WGC = West Greenland Current, B-LC = Baffin – Labrador Current, IC = Irminger Current. Isotopic background data: KMB, AB, NMB: Colville et al., 2011; Reyes et al., 2014, DI: Larsen & Pedersen, 2009, RMB: Kalsbeek et al., 1998, CMB: this study. Yellow stars mark the location of the sediment cores included in this study.

The major part of these bedrock terrains is presently covered by the massive GIS. In the Nuuk region in southern Greenland the GIS leaves around 100-125 km of revealed Greenland bedrock (Weidick et al., 2012) and only a small fringe of ice-free bedrock in Northern Greenland, making land-based geological records and samples in northernmost Greenland relatively sparse (Bennike, 2008; Young & Briner, 2015) which is the reason for the missing isotope background data of this region.

2.3. Analytical Procedures and Results

2.3.1. Age Chronology

The age chronologies of the sediment cores included in this study were constructed in the framework of different studies that have been previously published with the exception of the age chronology of gravity core GeoB19946-4 (Table 2.3). All age chronologies are based on accelerated mass spectrometry radiocarbon dating of marine carbonates, mainly mixed benthic foraminifera and occasionally planktonic foraminifera and mollusc shells, depending on the availability of dateable material in the corresponding cores. Ages have been calibrated to calendar years using the *Marine 13* and *IntCal13* calibration curves (Reimer et al., 2013) and the age model has been constructed based on Bayesian age modelling using the BACON (Blaauw & Christen, 2011) or CLAM 2.2 (Blaauw, 2010) software packages.

Table 2.3: Overview of age chronologies for sediment cores included into this study.

Sediment Core	Carbonate Source	Calibration Curve	Age Modelling	Reference
GeoB19905-1	mixed benthic foraminifera	*IntCal13*	BACON	Weiser et al., 2021
GeoTÜ SL170	mixed benthic & planktonic foraminifera, mollusc shells	*Marine13*	BACON	Jackson et al., 2017
GeoB19927-3	mixed benthic & planktonic foraminifera, mollusc shells	*Marine13*	BACON	Saini et al., 2020
GeoB19946-4	mixed benthic & planktonic foraminifera	*Marine13*	BACON	J. Weiser, pers. comm..
AMD14-Kane2B	mixed benthic foraminifera, mollusc shells	*Marine 13*	CLAM 2.2	Georgiadis et al., 2018

2.3.2. Isotope analysis

In preparation for radiogenic isotope analysis between 1 and 2 g of bulk sediments have been homogenised with a mortar, washed with ultrapure water (18.2 MΩ; Millipore), decarbonised with a 40% acetic acid solution (buffered to pH ~4 with 1M Na-acetate), and leached with hydroxylamine hydrochloride and 15% acetic acid (buffered to pH ~4 with NaOH) to remove possible iron-manganese (FeMn) sediment grain coatings following the procedure by Gutjahr et al. (2007) (Figure 2.3). Between each step the samples have been dried in the oven at 110°C, homogenised again and a sample fraction of around 100 mg was separated for isotopic analysis. These sample fractions of washes, decarbonised and leached sediments will in the following be labelled 'bulk', 'dc' and 'dt', respectively. The leach solution of the FeMn leaching step has been saved for analysis by centrifuging, removing the supernatant with a pipette and evaporating the residue in the oven at 110°C.

All 100 mg sediment sample fractions were transferred into 30 ml - Savillex™ beakers for stepwise hot-acid digestion to obtain the siliciclastic detrital fraction and remove organic matter. As most rock-forming minerals dissolve in hot concentrated hydrofluoric acid (HF) under atmospheric pressure (e.g. Dickin, 2005), the following acids have been added to each sample for dissolution on the hotplate: concentrated hydrofluoric acid (5:1, HF:HNO_3, 3 ml),

Aqua Regia (3:1, 6M HCl:concentrated HNO_3, 3 ml), nitric acid (concentrated HNO_3, 1 ml), hydrochloric acid (6M HCl, 3 ml) and hydrogen peroxide (H_2O_2, 100µl multiple times). Between each dissolution step, the samples have been evaporated on the hotplate at 70°C to remove acid remains. The FeMn leachates have only been treated with 2 ml of concentrated HNO_3 and 2 ml of 6M HCl, three times each. The duration and temperature these samples were left on the hotplate to evaporate between each step are the same as for the sediment fractions.

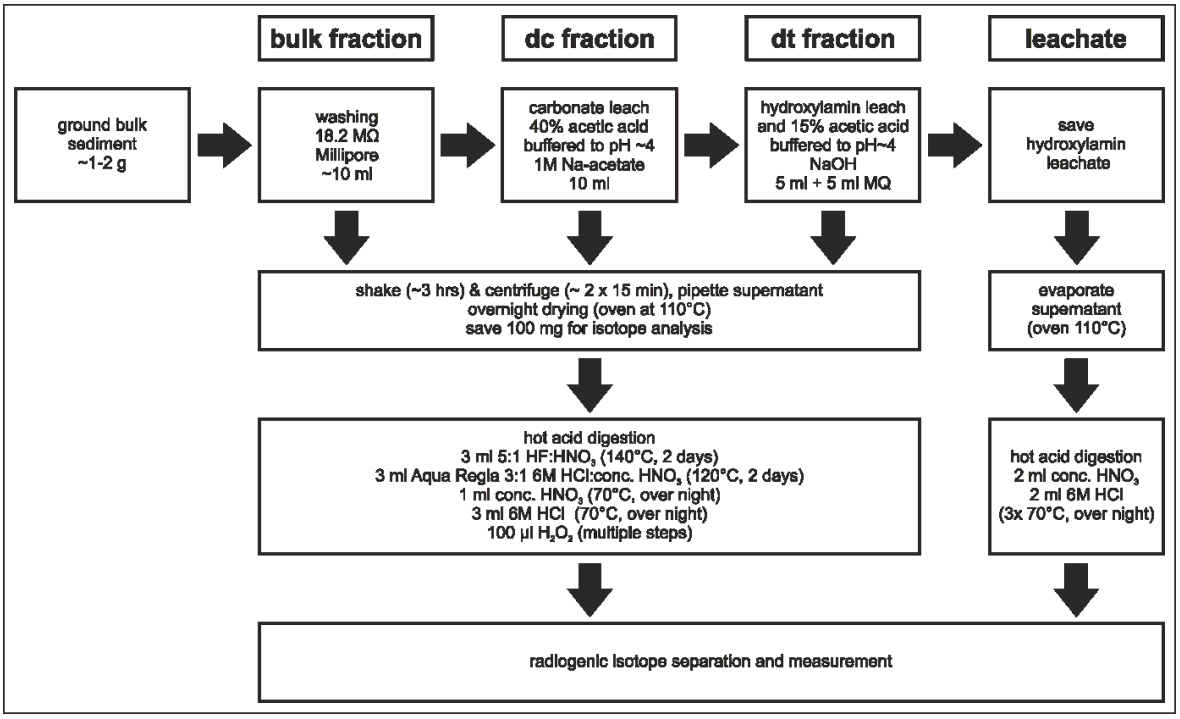

Figure 2.3: Flow chart of leaching procedure for decarbonisation, FeMn leaching and hot-acid digestion to receive the siliciclastic detrital sediment fraction. Between each leaching step a washing step with ultrapure water (18.2 MΩ; Millipore) has been applied to remove leach solution remains. Method based on Gutjahr et al. (2007).

The final sample fraction was re-dissolved in 500 µl 2M HNO_3 and analysed through column separation to collect Sr, Pd and Nd. Sr and Pb were separate from the sample matrix through TrisKem Sr.spec™ cation exchange resin eluted with 0.05M HNO_3 and 6M HCl, respectively (method modified after Deniel & Pin, 2001). The rare earth elements were saved and transferred onto columns loaded with TRU.spec™ resin to further separate the light rare earth elements. Those were directly transferred onto Nd columns for its final separation using LN.spec™ eluted with 0.25M HCl (Pin et al., 1994). After separating Sr, Pb and Nd isotopes, a drop of phosphoric acid was added to accumulate the sample while evaporating all other remaining acids and ensure easier sample transfer for subsequent measurement. H_2O_2 was additionally added and evaporated again to remove possible resin remains.

Measurements of radiogenic isotope ratios were performed on a Thermo Fisher Scientific Triton™ Plus multicollector thermal ionization mass spectrometer (TIMS). All samples were transferred onto rhenium-filaments within a drop of phosphoric acid. Sr and Pb were transferred onto single filaments with an additional emitter of tantalum and silicon, respectively, to support the ionisation process. Samples for Nd isotope ratio measurements were transferred onto double filaments without an additional emitter as the ionisation process is induced by higher temperatures. Therefore the instrument's vacuum is support with addition of liquid nitrogen filled into the cryopump of the instrument. Through heating the filaments samples have been ionized, accelerated through a magnetic field via high voltage,

where the different masses are separated and detected by Faraday cups downstream the magnetic field at different times. Each measurement series was accompanied by international standardised reference material (NIST987, NIST981, JNdi-1 for Sr, Pb, Nd, respectively) to monitor analytical accuracy. Isotopic ratios for reference material are in a range of 0.710255 ±0.000056 ($^{87}Sr/^{86}Sr$ $\pm 2SD_{mean}$; n=29), 0.512067 ±0.000423 ($^{144}Nd/^{143}Nd$ $\pm 2SD_{mean}$; n=24) and 16.8999 ±0.0172 ($^{206}Pb/^{204}Pb$ $\pm 2SD_{mean}$; n=20) throughout the measurement period of 2.5 years. These values agree with the range of published reference values (GeoReM data base; query June 2020; http://georem.mpch-mainz.gwdg.de): 0.710249 ±0.000034 ($^{87}Sr/^{86}Sr$ $\pm 2SD_{mean}$; n=1528), 0.512107 ±0.000026 ($^{144}Nd/^{143}Nd$ $\pm 2SD_{mean}$; n=339) and 16.9211 ±0.0413 ($^{206}Pb/^{204}Pb$ $\pm 2SD_{mean}$; n=254). Isotopic ratios have been measured in either multidynamic (Sr) or static (Pb, Nd) multicollection mode, the final value is the automatic calculated mean of around 100, 60, 120 (Sr, Pb, Nd) measured values, with possible outliers automatically discarded. Internal correction for isotopic fractionation during measurements has been applied by the instrumental software, using the natural occurring ratio of Sr of $^{86}Sr/^{88}Sr$ and $^{146}Nd/^{144}Nd$ of 0.1194 and 0.7219, respectively. For Pb isotopic ratios a bulk uncertainty of 0.1% per atomic mass unit was assumed to account for isotopic fractionation during the measuring process, which exclusively exceeds the measured uncertainty.

All isotopic analysis and measurements have been conducted in the Isotope Geochemistry Lab at MARUM—Center for Marine Environmental Sciences, University of Bremen.

2.3.2.1. Suitability of Sediment Leachates from Eastern Baffin Bay

Sediment leachates for FeMn sediment grain coatings have the potential to carry seawater signatures and therefore information on past water mass development (e.g. Gutjahr et al., 2007). However, in order to reliably interpret the obtained data of gravity cores GeoB19905-1, GeoB19927-3 and GeoB19946-4 (Figure 2.4), the occurrence of these FeMn sediment grain coatings should be tested via elemental composition of the corresponding leachate.

The elemental composition has been measured for six samples of gravity core GeoB19927-3 to test for possible FeMn sediment grain coatings. Analysis of Fe and Mn concentrations has been done through inductively coupled plasma mass spectrometry (ICP-MS, Plasma Quant MS Elite, Analytik Jena) and analysis of Ca and Mg concentrations through inductively coupled plasma optical emissions spectroscopy (ICP-OES, SPECTRO CIROS VISION) at Leibniz Centre for Tropical Marine Research (ZMT), Bremen, Germany. All samples were dissolved in 2M HNO_3 and further diluted with a dilution factor of 1:100 for analysis.

Concentrations of Fe and Mn in the leachates of GeoB19927-3 range from 4300-25000 µg/g and 380-1200 µg/g, respectively (Figure 2.5). The ratios between these concentrations vary from 8.4 to 23.6 which is pointing to overall low Mn concentrations and exceed the common ratio of Fe/Mn in sediment grain coatings of 2.2 (Toth, 1980) suggesting the absence of FeMn coatings. The absence of FeMn sediment grain coatings in Baffin Bay has been noted before (Blanckenburg & Nägler, 2001; Kirillova, 2017). Additionally, the molar ratio between Ca and Mg is close to one, which resembles the stoichiometric ratio of Ca/Mg in dolomite indicating that dolomite might have been leached from the sample instead of FeMn (cf. Kirillova, 2017).

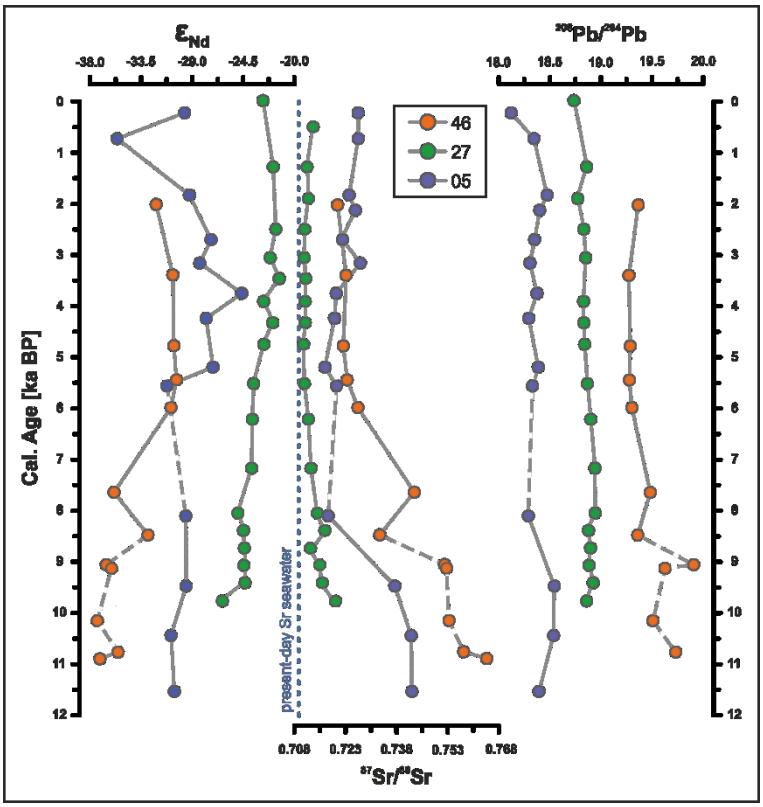

Figure 2.4: Isotopic composition of FeMn leachates of gravity cores GeoB19905-1, GeoB19927-3 and GeoB19946-4. Dashed line represents the present-day Sr isotopic composition of marine carbonates of 0.70917 (Henderson et al., 1994). Age models are based on radiocarbon dating of mixed foraminifera and shell fragments (Saini et al., 2020; Weiser et al., 2021; J. Weiser, pers. comm.) Analytical errors are smaller than data points. Data can be found in Table 8.1,Table **8.2**,Table **8.4**.

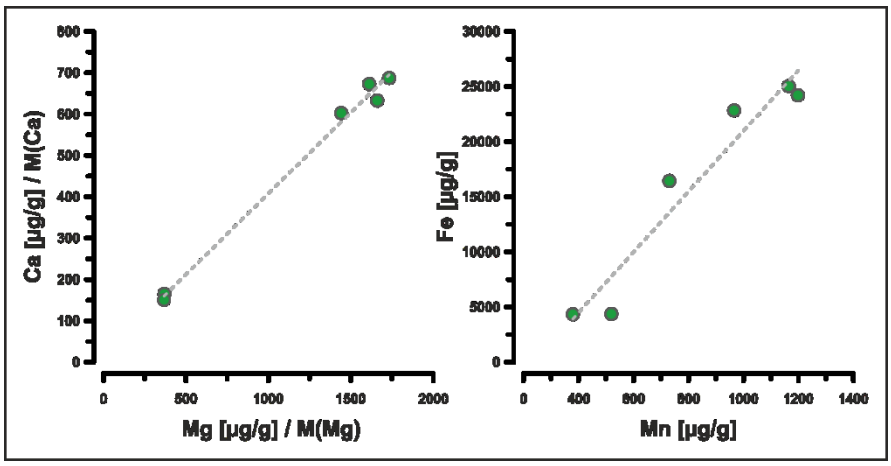

Figure 2.5: Elemental composition of leachates of gravity core GeoB19927-3. Ca and Mg concentrations are normalised by their molar mass of 40 and 24, respectively. Data can be found in Table 8.9.

Due to the presumable absence of FeMn sediment grain coatings in the samples of this study and therefore the possibly obtained isotopic seawater signal the leachate data is not included in further interpretation in order to solve the overall research question of this study and only displayed here for completeness and possible comparison.

2.3.2.2. Sediment Fractions

The three different fractions of bulk, decarbonised (dc) and detrital (dt) sediment of gravity cores GeoB19905-1, GeoB19927-3, GeoB19946-4, AMD14-Kane2B and box core GeoB19965-2A have been analysed for their radiogenic isotope composition and are below displayed together for comparison (Figure 2.6, Figure 2.7, Figure 2.8, Figure 2.9, Figure 2.10). In all records the dc and dt fraction plot close together, often overlapping, while the bulk fraction records an offset in isotopic composition towards less radiogenic Sr and more radiogenic Pb, with the exception of GeoB19946-4, where only the Pb isotopic composition records an offset. This offset in Sr isotopic composition is most likely connected to the carbonate content of the samples as it coincides with high calcite composition in core GeoB19905-1 (Figure 2.12) and cannot be detected in core Geob19946-4 which does not record any carbonate content (Figure 2.14).

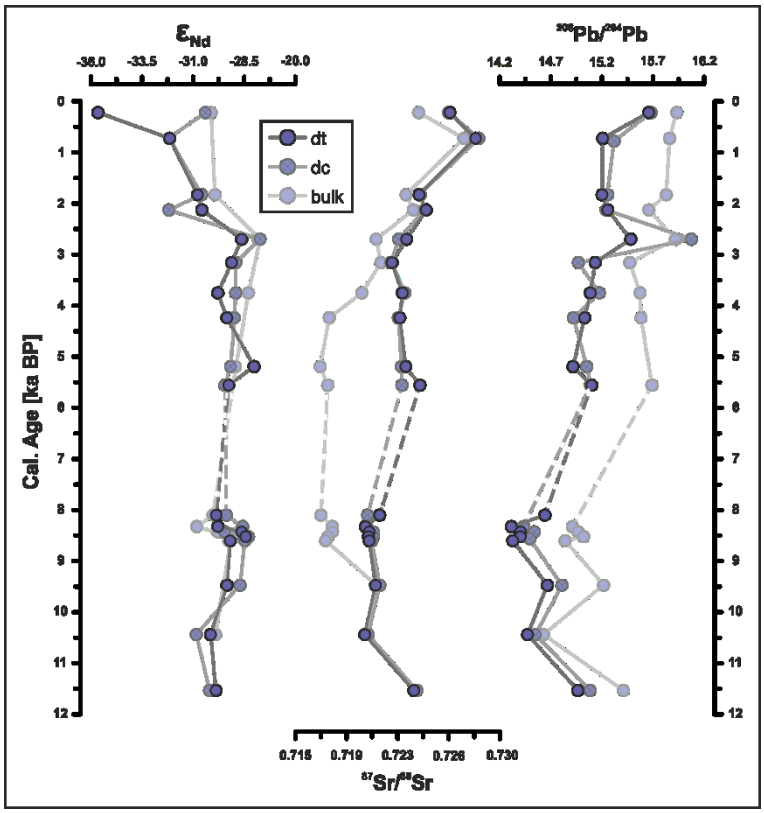

Figure 2.6: Isotopic composition of gravity core GeoB19905-1 of all three sediment fractions: bulk, decarbonised (dc), detrital (dt). The age model is based on radiocarbon dating of mixed benthic foraminifera (Weiser et al., 2021). Dashed lines represent a hiatus in the sedimentary record. Analytical errors are smaller than data points. Data can be found in Table 8.1.

The overlapping dc and dt signatures support the result of the elemental composition indicating an absence of FeMn sediment grain coatings in all included samples. They further suggest that no significant other fraction has been leached out of the sample fraction, qualifying both sediment fractions dc and dt for interpretation towards the aims of this study.

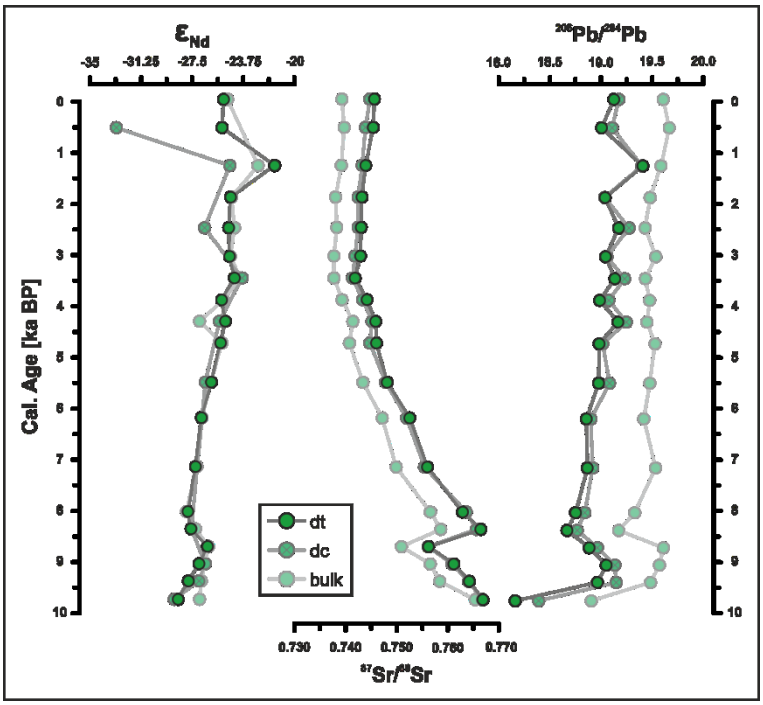

Figure 2.7: Isotopic composition of gravity core GeoB19927-3 of all three sediment fractions: bulk, decarbonised (dc), detrital (dt). The age model is based on radiocarbon dating of mixed benthic and planktonic foraminifera and mollusc shells (Saini et al., 2020). Analytical errors are smaller than data points. Data can be found in Table 8.2.

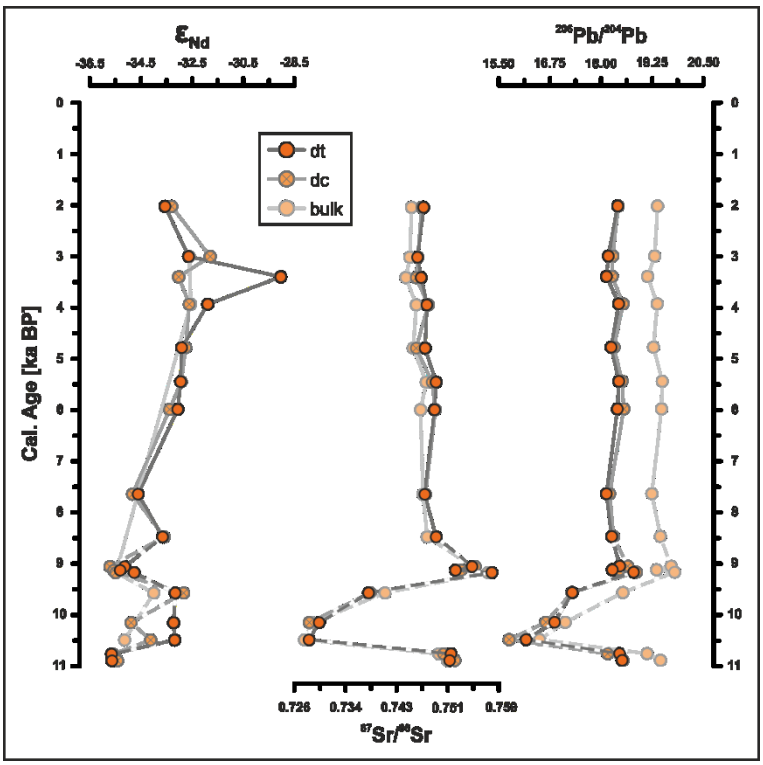

Figure 2.8: Isotopic composition of gravity core GeoB19946-4 of all three sediment fractions: bulk, decarbonised (dc), detrital (dt). The age model is based on radiocarbon dating of mixed benthic and planktonic foraminifera (J. Weiser, pers. comm.). Dashed lines mark a possible mass wasting event (see chapter 4). Analytical errors are smaller than data points. Data can be found in Table 8.4.

In the following interpretation of the data (chapters 3-5) the dt fraction will be used to rule out any possibility of remaining FeMn sediment coatings as their absence has only been tested for gravity core GeoB19927-3. It could, however, be suggested for future research to use the dc fraction for interpretation of radiogenic isotope signatures in order to trace sediment provenances in areas where FeMn sediment coatings are known to be absent (cf. Höppner et al., 2018). The isotopic variations recorded in each of the sedimentary archives are discussed in chapter three to five.

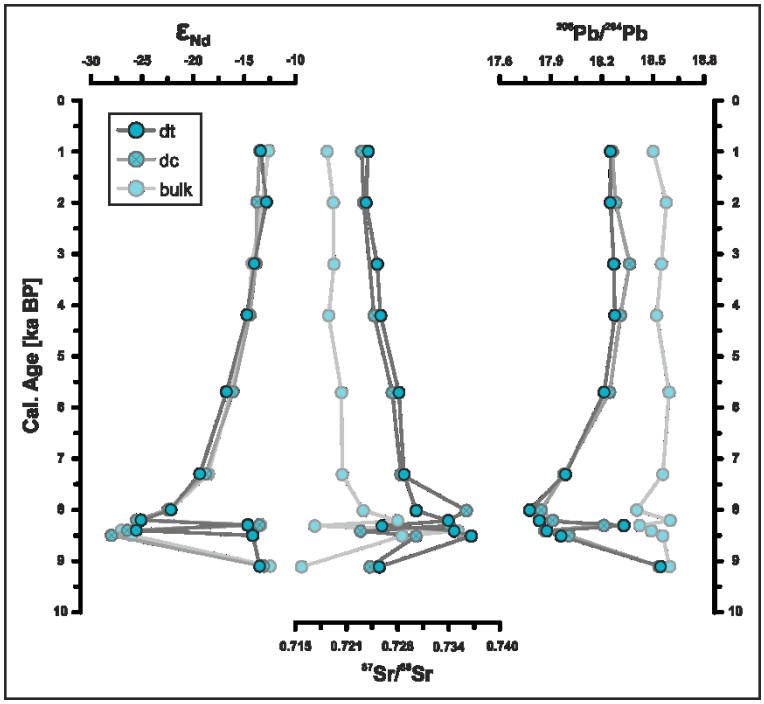

Figure 2.9: Isotopic composition of gravity core AMD14-Kane2B of all three sediment fractions: bulk, decarbonised (dc), detrital (dt). The age model is based on radiocarbon dating of mixed benthic foraminifera and mollusc shells (Georgiadis et al., 2018). Analytical errors are smaller than data points. Data can be found in Table 8.5.

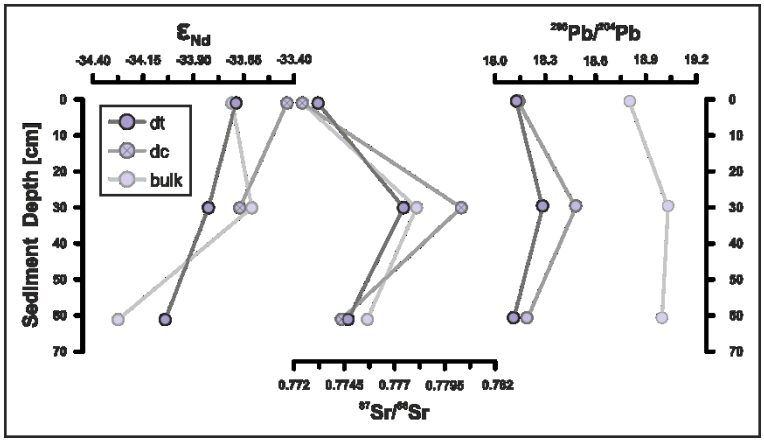

Figure 2.10: Isotopic composition of box core GeoB19965-2A of all three sediment fractions: bulk, decarbonised (dc), detrital (dt). Note this data is plotted against sediment depths as it has been used as surface sediment reference data. Analytical errors are smaller than data points. Data can be found in Table 8.3.

2.3.2. X-Ray Diffraction

The mineralogy of each sample has been obtained to compare the composition to the isotopic results and rule out possible mineralogical control of the isotopic signatures. An additional

approach was to draw conclusions from the use of both methods alongside and their particular advantages in comparison to each other. For most comparable results the mineralogical composition was measured on the same samples as used for radiogenic isotope analysis (if enough material was available), as well as the same grain-size distribution. X-ray diffraction (XRD) analysis was conducted on the non-decarbonised sediment fraction in order to also measure the carbonate content.

Between 100 and 500 mg of ground bulk sample material were prepared for XRD analysis using the 'back-side method' (Moore & Reynolds, 1997). The samples have been filled into sample trays and compressed by manually added pressure. After the first run of measurements each sample has been weighed, washed, dried and weighed again to estimate the amount of halite and to prevent any possible masking of clay minerals. Washing has been conducted by adding water and a magnetic stir bar to the samples and leaving them on the magnetic plate for a few minutes to dissolve the water-soluble fraction. After washing, residual sediment and water-soluble fraction have been separated by filtering the sample through applied vacuum. The residual sediment has been dried on the hot plate. Subsequent estimating the water-soluble fraction and passing the sample again through the diffractometer, the carbonate fraction has been removed by adding approximately 100 ml of 0.1M HCl to the sample and slowly let it pass through a filter, vacuum-supported for the first seconds to assure total calcite dissolution. The sample was dried and weighed again to estimate the calcite content. Following, the sample has been analysed again for mineral composition.

The second part of sample treatment is crucial for identification of clay minerals within the mineral matrix. Water has been added to orient the clay minerals as random orientation compared to oriented clay minerals can have a significant influence on the peak intensities and therefore peak intensity ratios between different minerals (e.g. Moore & Reynolds, 1997). After passing the oriented sample again through X-ray diffraction, it has been saturated with ethylene glycol inside a vacuum desiccator for 24 hours, measured again and heated up to 300°C for four hours before final measurement. Ethylene glycol-solvated samples show a distinct peak for smectite at 16.9 Å that is not visible in non-treated samples (e.g. Moore & Reynolds, 1997). If this peak disappears again after heating the sample, smectite can be clearly identified. In the end all samples were analysed several times, before and after the following steps of sample treatment: (1) untreated sample, (2) washed sample to calculate halite content, (3) decarbonised sample (0.1 M HCl) to calculate calcite content, (4) addition of water to orient and identify clay minerals, (5) ethylene glycol saturated sample to identify smectites and (5) heated sample (300°C) to verify smectites (cf. Moore & Reynolds, 1997).

Measurements were done in a Siemens X-ray Diffraktometer D5000 in a range between 5° and 85° 2θ. Results were based on peak intensity and contain an analytical uncertainty of ~2%. Quartz was used as a standard for horizontal peak position correction. Halite and calcite were used as a standard for peak intensity. Results have been evaluated using the DIFFRAC.EVA evaluation software by Bruker. All mineralogical measurements have been conducted at GEOTOP – Centre de recherche en géochimie et géodynamique, Université du Québec á Montréal, Canada.

2.3.2.1. Mineralogical Composition of Core Samples

Following the results of the XRD analysis for sediment cores GeoB19905-1, GeoB19927-3 and GeoB19946-4 are summarised. The mineralogical composition of core AMD14-Kane2B has

been obtained in the framework of another study (Caron et al., 2020) and is therefore not included in this section.

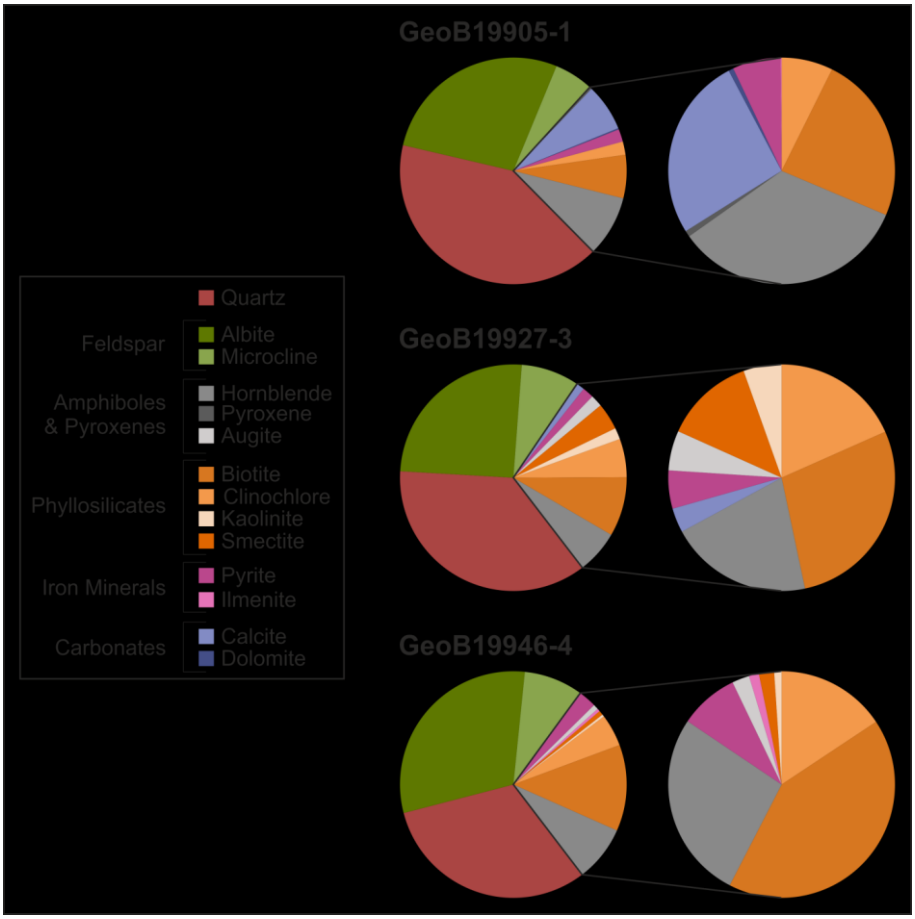

Figure 2.11: Detailed overall mineralogical composition of gravity cores GeoB19905-1, GeoB19927-3 and GeoB19946-4. The percentages represent the average mineralogical composition over the entire sedimentary records. Data for each core and sediment depth can be found in Table 8.6Table 8.7Table 8.8.

Figure 2.11 summarises the overall mineralogical composition of gravity cores GeoB19905-1, GeoB19927-3 and GeoB19946-4 averaged over the entire record. All three cores are dominated by quartz and feldspar mirroring the gneiss and granite dominated Greenland bedrock. Minor components are biotite, clinochlore, hornblende, and further phyllosilicates and iron minerals which clearly vary in their contribution in the three different cores and locations. The most obvious difference between the core locations is the decrease in carbonates from south to north; while calcite is a major component in GeoB19905-1, it is only a minor component in GeoB19927-3 and entirely absent in core GeoB19946-4.

Slight variations over time can be identified in each mineral group and core (Figure 2.12, Figure 2.13, Figure 2.14). GeoB19905-1 shows the most obvious changes in carbonate content, which is significantly higher during the mid Holocene (Figure 2.12). Generally, the mineralogical composition varies slightly more in the mid and late Holocene and exhibits an occasional increase in phyllosilicates during the late Holocene. The results are discussed in chapter three.

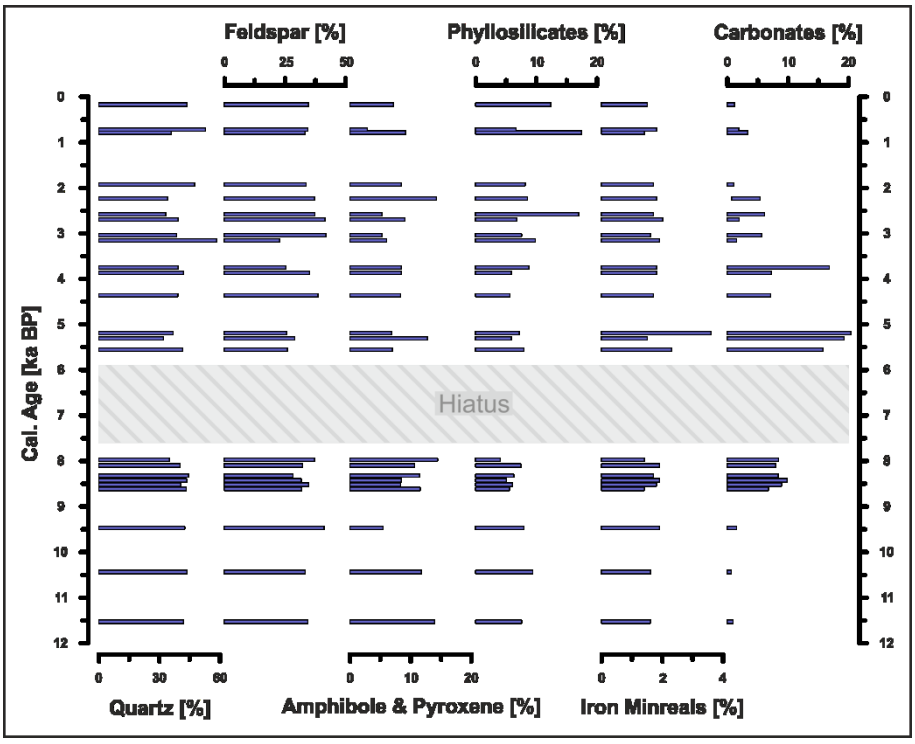

Figure 2.12: Mineralogical composition of the bulk sediment fraction of gravity core GeoB19905-1. The age model is based on radiocarbon dating of mixed benthic foraminifera (Weiser et al., 2021). Shaded interval represents a hiatus in the sedimentary record. Data can be found in Table 8.6.

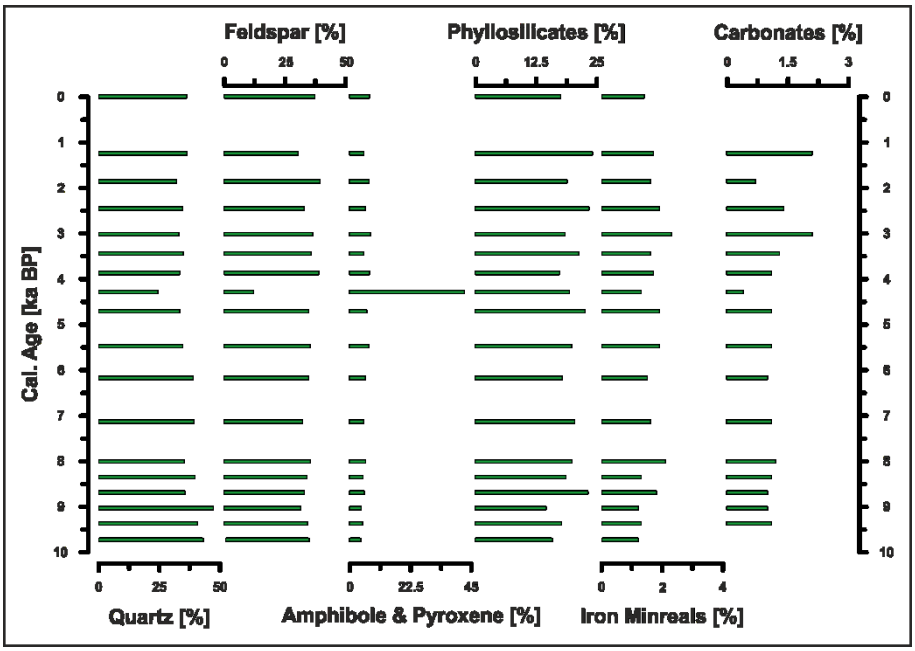

Figure 2.13: Mineralogical composition of the bulk sediment fraction of gravity core GeoB19927-3. The age model is based on radiocarbon dating of mixed benthic and planktonic foraminifera and mollusc shells (Saini et al., 2020). Data can be found in Table 8.7.

The mineralogical composition in gravity core GeoB19927-3 appears to be comparably stable throughout the Holocene with a slight increase in carbonates during the late Holocene (Figure 2.13). A striking peak is recorded around 4.3 ka BP within the amphibole and pyroxene

composition coinciding with a drop in quartz and feldspar. For interpretation of the results see chapter four.

GeoB19946-4 records low variations in quartz, feldspar and phyllosilicates and a slight decrease in amphibole and pyroxene content and a simultaneous increase in iron minerals (Figure 2.14). The lower part of the record is characterised by a mass wasting event and records some more variations within the amphibole and pyroxene, phyllosilicate and iron mineral composition. For interpretation of the results see chapter four.

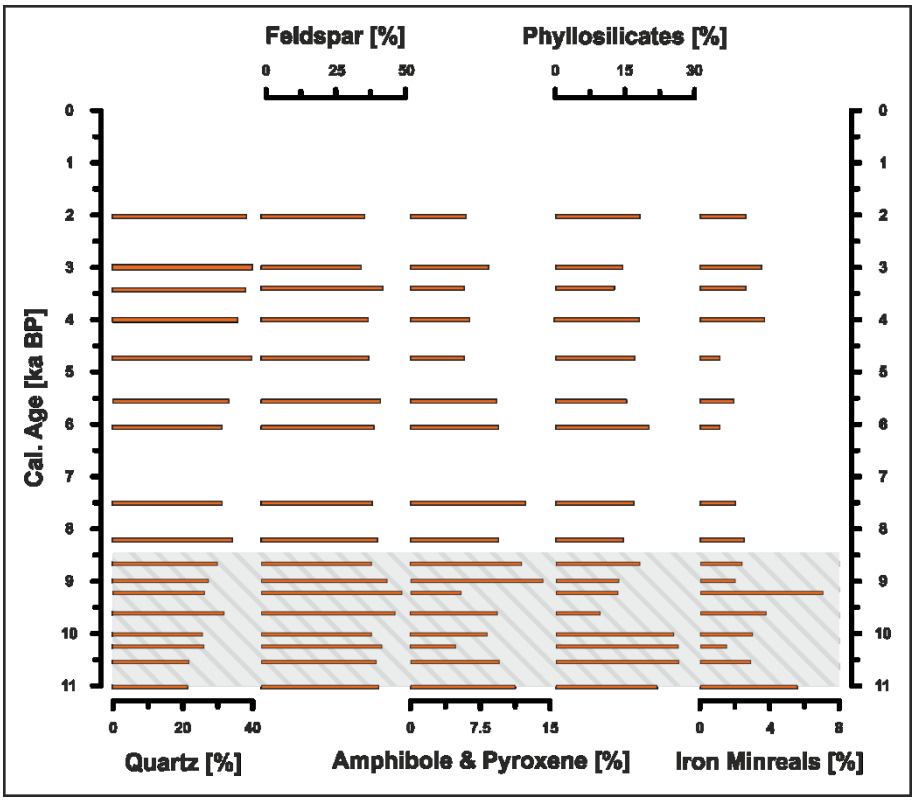

Figure 2.14: Mineralogical composition of the bulk sediment fraction of gravity core GeoB19946-4. The age model is based radiocarbon dating of mixed benthic and planktonic foraminifera (J. Weiser, pers. comm.). Shaded interval marks a possible mass wasting event. Data can be found in Table 8.8.

2.4. References

Andresen, C. S., Straneo, F., Ribergaard, M. H., Bjørk, A. A., Andersen, T. J., Kuijpers, A., … Ahlstrøm, A. P. (2012). Rapid response of Helheim Glacier in Greenland to climate variability over the past century. Nature Geoscience, 5(1), 37–41. https://doi.org/10.1038/ngeo1349

Banner, J. L. (2004). Radiogenic isotopes: Systematics and applications to earth surface processes and chemical stratigraphy. Earth-Science Reviews, 65(3–4), 141–194. https://doi.org/10.1016/S0012-8252(03)00086-2

Bennike, O. (2008). An early Holocene Greenland whale from Melville Bugt, Greenland. Quaternary Research, 69(1), 72–76. https://doi.org/10.1016/j.yqres.2007.10.004

Blaauw, M. (2010). Methods and code for "classical" age-modelling of radiocarbon sequences. Quaternary Geochronology, 5(5), 512–518. https://doi.org/10.1016/j.quageo.2010.01.002

Blaauw, M., & Christen, J. A. (2011). Flexible paleoclimate age-depth models using an autoregressive gamma process. Bayesian Analysis, 6(3), 457–474.

https://doi.org/10.1214/11-BA618
Blanckenburg, F., & Nägler, T. F. (2001). Weathering versus circulation controlled changes in radiogenic isotope tracer composition of the Labrador Sea and North Atlantic Deep Water. Paleoceanography, 16(4), 424–434.
Blaser, P., Lippold, J., Gutjahr, M., Frank, N., Link, J. M., & Frank, M. (2016). Extracting foraminiferal seawater Nd isotope signatures from bulk deep sea sediment by chemical leaching. Chemical Geology, 439, 189–204. https://doi.org/10.1016/j.chemgeo.2016.06.024
Broecker, W.S., Peng, T.S., 1982. Tracers in the Sea Eldigio Press, Palisades, NY.
Buch, E. (2002). Present oceanographic conditions in Greenland Waters. Danish Meteorological Institute, Scientific report.
Burke, W. H., Denison, R. E., Hetherington, E. A., Koepnick, R. B., Nelson, H. F., & Otto, J. B. (1982). Variation of seawater 87Sr / 86Sr throughout Phanerozoic time. Geology, 10(October), 516–519.
Caron, M., Montero-Serrano, J. C., St-Onge, G., & Rochon, A. (2020). Quantifying Provenance and Transport Pathways of Holocene Sediments From the Northwestern Greenland Margin. Paleoceanography and Paleoclimatology, 35(5), 1–23. https://doi.org/10.1029/2019PA003809
Caron, M., St-Onge, G., Montero-Serrano, J. C., Rochon, A., Georgiadis, E., Giraudeau, J., & Massé, G. (2019). Holocene chronostratigraphy of northeastern Baffin Bay based on radiocarbon and palaeomagnetic data. Boreas, 48(1), 147–165. https://doi.org/10.1111/bor.12346
Colville, E. J., Carlson, A. E., Beard, B. L., Hatfield, R. G., Stoner, J. S., Reyes, A. V, & Ullman, D. J. (2011). Sr-Nd-Pb isotope evidence for ice-sheet presence on southern Greenland during the Last Interglacial. Science, 333(6042), 620–623. https://doi.org/10.1126/science.1204673
Connelly, J. N., Thrane, K., Krawiec, A. W., & Garde, A. A. (2006). Linking the Palaeoproterozoic Nagssugtoqidian and Rinkian orogens through the Disko Bugt region of West Greenland. Journal of the Geological Society, 163(2), 319–335. https://doi.org/10.1144/0016-764904-115
Dahl-Jensen, T., Larsen, T. B., Woelbern, I., Bach, T., Hanka, W., Kind, R., … Gudmundsson, O. (2003). Depth to Moho in Greeland: Receiver-function analysis suggests two proterozoic blocks in Greenland. Earth and Planetary Science Letters, 205(3–4), 379–393. https://doi.org/10.1016/S0012-821X(02)01080-4
Dawes, P R. (2009). The bedrock geology under the Inland Ice: the next major challenge for Greenland mapping. Geological Survey of Denmark and Greenland Bulletin, 17, 57–60.
Dawes, Peter R. (2006). Explanatory notes to the Geological map of Greenland , 1 : 500 000 , Thule , Sheet 5. Geological Survey of Denmark and Greenland Map Series 2, 97 pp.
Deniel, C., & Pin, C. (2001). Single-stage method for the simultaneous isolation of lead and strontium from silicate samples for isotopic measurements. Analytica Chimica Acta, 426(1), 95–103. https://doi.org/10.1016/S0003-2670(00)01185-5
Dickin, A. P. (2005). Radiogenic Isotope Geology (second edition). Cambridge University Press. New York.
Dorschel, B., Afanasyeva, V., Bender, M., Dreutter, S., Eisermann, H., Gebhardt, A. C., … Wangner, D. J. (2015). Past Greenland Ice Sheet dynamics, Palaeoceanography and Plankton Ecology in the Northeast Baffin Bay Cruise No. MSM44 30. MARIA S. MERIAN-Berichte, 148.
Fagel, N., Hillaire-Marcel, C., Humblet, M., Brasseur, R., Weis, D., & Stevenson, R. (2004). Nd and Pb isotope signatures of the clay-size fraction of Labrador Sea sediments during the Holocene: Implications for the inception of the modern deep circulation pattern. Paleoceanography, 19(3). https://doi.org/10.1029/2003PA000993
Fagel, N., Innocent, C., Gariepy, C., & Hillaire-Marcel, C. (2002). Sources of Labrador Sea sediments since the last glacial maximum inferred from Nd-Pb isotopes. Geochemistry, Geophysics, Geosystems, 66(14), 2569–2581.

Fagel, N., Not, C., Gueibe, J., Mattielli, N., & Bazhenova, E. (2014). Late Quaternary evolution of sediment provenances in the Central Arctic Ocean: Mineral assemblage, trace element composition and Nd and Pb isotope fingerprints of detrital fraction from the Northern Mendeleev Ridge. Quaternary Science Reviews, 92, 140–154. https://doi.org/10.1016/j.quascirev.2013.12.011

Filippova, A., Frank, M., Kienast, M., Rickli, J., Hathorne, E., Yashayaev, I. M., & Pahnke, K. (2017). Water mass circulation and weathering inputs in the Labrador Sea based on coupled Hf–Nd isotope compositions and rare earth element distributions. Geochimica et Cosmochimica Acta, 199, 164–184. https://doi.org/10.1016/j.gca.2016.11.024

Frank, M. (2002). Radiogenic isotopes: Tracers of past ocean circulation and erosional input. Reviews of Geophysics, 40(1), 1001. https://doi.org/10.1029/2000RG000094

Georgiadis, E., Giraudeau, J., Martinez, P., Lajeunesse, P., St-Onge, G., Schmidt, S., & Massé, G. (2018). Deglacial to postglacial history of Nares Strait, Northwest Greenland: A marine perspective from Kane Basin. Climate of the Past, 14(12), 1991–2010. https://doi.org/10.5194/cp-14-1991-2018

Grocott, J., & McCaffrey, K. J. W. (2017). Basin evolution and destruction in an Early Proterozoic continental margin: the Rinkian fold–thrust belt of central West Greenland. Journal of the Geological Society, 174(3), 453–467. https://doi.org/10.1144/jgs2016-109

Gutjahr, M., Frank, M., Stirling, C. H., Klemm, V., van de Flierdt, T., & Halliday, A. N. (2007). Reliable extraction of a deepwater trace metal isotope signal from Fe-Mn oxyhydroxide coatings of marine sediments. Chemical Geology, (242), 351–370. https://doi.org/10.1016/j.chemgeo.2007.03.021

Haley, B. A., Frank, M., Spielhagen, R. F., & Fietzke, J. (2008). Radiogenic isotope record of Arctic Ocean circulation and weathering inputs of the past 15 million years. Paleoceanography. https://doi.org/10.1029/2007PA001486

Henderson, G. M., Martel, D. J., O'Nions, R. K., & Shackleton, N. J. (1994). Evolution of seawater 87Sr/86Sr over the last 400 ka: the absence of glacial/interglacial cycles. Earth and Planetary Science Letters, 128, 643–651.

Höppner, N., Lucassen, F., Chiessi, C. M., Sawakuchi, A. O., & Kasemann, S. A. (2018). Holocene provenance shift of suspended particulate matter in the Amazon River basin. Quaternary Science Reviews, 190, 66–80. https://doi.org/10.1016/j.quascirev.2018.04.021

Jackson, G. D., & Berman, R. G. (2000). Precambrian metamorphic and tectonic evolution of northern Baffin Island, Nunavut, Canada. Canadian Mineralogist, 38(2), 399–421. https://doi.org/10.2113/gscanmin.38.2.399

Jackson, R., Carlson, A. E., Hillaire-Marcel, C., Wacker, L., Vogt, C., & Kucera, M. (2017). Asynchronous instability of the North American-Arctic and Greenland ice sheets during the last deglaciation. Quaternary Science Reviews, 164, 140–153. https://doi.org/10.1016/j.quascirev.2017.03.020

Jacobsen, S. B., & Wasserburg, G. J. (1980). Sm-Nd Isotopic Evolution of Chondrites. Earth and Planetary Science Letters, 50, 139–155.

Kalsbeek, F., Pulvertaft, T. C. R., & Nutman, A. P. (1998). Geochemistry, age and origin of metagreywackes from the Palaeoproterozoic Karrat Group, Rinkian Belt, West Greenland. Precambrian Research, 91(3–4), 383–399. https://doi.org/10.1016/S0301-9268(98)00059-X

Kirillova, V. (2017). Radiogenic isotopes on the marine sediments from the Baffin Bay: implications for the sediment supply during the last deglaciation. Dissertation, University of Bremen, Germany.

Larsen, L. M., & Pedersen, A. K. (2009). Petrology of the paleocene picrites and flood basalts on disko and nuussuaq, West Greenland. Journal of Petrology, 50(9), 1667–1711. https://doi.org/10.1093/petrology/egp048

Laukert, G., Frank, M., Bauch, D., Hathorne, E. C., Gutjahr, M., Janout, M., & Hölemann, J. (2017). Transport and transformation of riverine neodymium isotope and rare earth element signatures in high latitude estuaries: A case study from the Laptev Sea. Earth and

Planetary Science Letters, 477, 205–217. https://doi.org/10.1016/j.epsl.2017.08.010
Laukert, G., Frank, M., Bauch, D., Hathorne, E. C., Rabe, B., von Appen, W. J., … Kassens, H. (2017). Ocean circulation and freshwater pathways in the Arctic Mediterranean based on a combined Nd isotope, REE and oxygen isotope section across Fram Strait. Geochimica et Cosmochimica Acta, 202, 285–309. https://doi.org/10.1016/j.gca.2016.12.028
Le Pichon, X., Sibuet, J.-C., & Francheteau, J. (1977). The fit of the continents around the North Atlantic Ocean. Tectonophysics, 38(3–4), 169–209. https://doi.org/10.1016/0040-1951(77)90210-4
Maccali, J., Hillaire-Marcel, C., & Not, C. (2018). Radiogenic isotope (Nd, Pb, Sr) signatures of surface and sea ice-transported sediments from the Arctic Ocean under the present interglacial conditions. Polar Research, 37(1), 1–13. https://doi.org/10.1080/17518369.2018.1442982
Martin, E. E., & Haley, B. A. (2000). Fossil fish teeth as proxies for seawater Sr and Nd isotopes. Geochimica et Cosmochimica Acta, 64(5), 835–847. https://doi.org/10.1016/S0016-7037(99)00376-2
Moore, D. M., Reynolds, R. C. Jr. (1997). X-Ray Diffraction and the Identification and Analysis of Clay Minerals (2nd edition), Oxford University Press, New York
Myers, P. G., Donnelly, C., & Ribergaard, M. H. (2009). Structure and variability of the West Greenland Current in Summer derived from 6 repeat standard sections. Progress in Oceanography, 80(1–2), 93–112. https://doi.org/10.1016/j.pocean.2008.12.003
Pin, C., Briot, D., Bassin, C., & Poitrasson, F. (1994). Concomitant separation of strontium and samarium-neodymium for isotopic analysis in silicate samples, based on specific extraction chromatography. Analytica Chimica Acta, 298(2), 209–217. https://doi.org/10.1016/0003-2670(94)00274-6
Reimer, P. J., Edouard Bard, B., Alex Bayliss, B., Warren Beck, B. J., Paul Blackwell, B. G., & Christopher Bronk Ramsey, B. (2013). Intcal13 and Marine13 Radiocarbon Age Calibration Curves 0–50,000 Years Cal Bp. Radiocarbon, 55(4), 1869–1887. https://doi.org/10.1017/S0033822200048864
Reyes, A. V, Carlson, A. E., Beard, B. L., Hatfield, R. G., Stoner, J. S., Winsor, K., … Ullman, D. J. (2014). South Greenland ice-sheet collapse during Marine Isotope Stage 11. Nature, 510(7506), 525–528. https://doi.org/10.1038/nature13456
Rhein, M., Kucera, M., Gohl, K. et al. (2013). DAVIS GATE - Geodynamic evolution of Davis Strait and Baffin Bay and their role as a paleoceanographic gateway. No. MSM09. MARIA S. MERIAN-Berichte, 137.
Rignot, E., & Kanagaratnam, P. (2006). Changes in the Velocity Structure of the Greenland Ice Sheet. Science, 311, 986–990.
Saini, J., Stein, R., Fahl, K., Weiser, J., Hebbeln, D., & Hillaire, C. (2020). Holocene variability in sea ice and primary productivity in the northeastern Baffin Bay. Arktos. https://doi.org/10.1007/s41063-020-00075-y
Schlitzer, R. (2020). Ocean Data View, odv.awi.de, 2020.
Simon, Q., Hillaire-Marcel, C., St-Onge, G., & Andrews, J. T. (2014). North-eastern Laurentide, western Greenland and southern Innuitian ice stream dynamics during the last glacial cycle. Journal of Quaternary Science, 29(1), 14–26. https://doi.org/10.1002/jqs.2648
Stordal, M. C., & Wasserburg, G. J. (1986). Neodymium isotopic study of Baffin Bay water : sources of REE from very old terranes. Earth and Planetary Science Letters, 77, 259–272.
Tang, C. C. L., Ross, C. K., Yao, T., Petrie, B., DeTracey, B. M., & Dunlap, E. (2004). The circulation, water masses and sea-ice of Baffin Bay. Progress in Oceanography, 63(4), 183–228. https://doi.org/10.1016/j.pocean.2004.09.005
Toth, J. R. (1980). Deposition of submarine crusts rich in manganese and iron. Geological Society of America Bulletin, 91(1 pt.I), 44–54. https://doi.org/10.1130/0016-7606(1980)91<44:DOSCRI>2.0.CO
Tremblay, J.-E. et al. (2014). ArcticNet Expedition Report Leg 1b – Baffin Bay and the

Canadian Arctic Archipelago. Chalut K. & Merzouk A. (editors), ArcticNet – Amundsen Science Program, Université Laval, Canada.
Tütken, T., Eisenhauer, A., Wiegand, B., & Hansen, B. T. (2002). Glacial - interglacial cycles in Sr and Nd isotopic composition of Arctic marine sediments triggered by the Svalbard / Barents Sea ice sheet. Marine Geology, 182, 351–372.
van de Flierdt, T., & Frank, M. (2010). Neodymium isotopes in paleoceanography. Quaternary Science Reviews, 29(19–20), 2439–2441. https://doi.org/10.1016/j.quascirev.2010.07.001
Weidick, A., Bennike, O., Citterio, M., & Nørgaard-pedersen, N. (2012). Neoglacial and historical glacier changes around Kangersuneq fjord in southern West Greenland. Geological Survey of Denmark and Greenland Bulletin, 27, 1–68.
Weiser, J., Titschack, J., McCave, I. N., Lochte, A. A., Saini, J., Stein, R., & Hebbeln, D. (2021). Atlantic water inflow to Labrador Sea and its interaction with ice sheet dynamics during the Holocene. Quaternary Science Reviews, 4545(4545), 4545–1. https://doi.org/10.1016/j.quascirev.2021.106833
Weiser, J. (personal communication 2021): J. Weiser constructed the age model for GeoB19946-4 which is currently in preparation for submission in the framework of his PhD thesis as well as in preparation for submission to a scientific journal: Weiser, J., Hebbeln, D., Titschack, J., Caron, M., St-Onge G. (in prep.). Widespread mass wasting in Melville Bay coincident with Nares Strait opening.
Werner, K., Frank, M., Teschner, C., Müller, J., & Spielhagen, R. F. (2014). Neoglacial change in deep water exchange and increase of sea-ice transport through eastern Fram Strait: Evidence from radiogenic isotopes. Quaternary Science Reviews, 92, 190–207. https://doi.org/10.1016/j.quascirev.2013.06.015
Young, N. E., & Briner, J. P. (2015). Holocene evolution of the western Greenland Ice Sheet: Assessing geophysical ice-sheet models with geological reconstructions of ice-margin change. Quaternary Science Reviews, 114, 1–17. https://doi.org/10.1016/j.quascirev.2015.01.018

CHAPTER THREE

Manuscript one

Radiogenic Isotopes Reveal Neoglacial Provenance Shift and Ice Advance in Southwest Greenland

Lina Madaj[1], Claude Hillaire-Marcel[2], Friedrich Lucassen[1] and Simone A. Kasemann[1]

[1] MARUM—Center for Marine Environmental Sciences & Faculty of Geosciences, University of Bremen, Germany
[2] GEOTOP—Centre de recherche en géochimie et géodynamique, Université du Québec à Montréal, Canada

This manuscript is in preparation for submission to Quaternary Science Reviews

3. Radiogenic Isotopes Reveal Neoglacial Provenance Shift and Ice Advance in Southwest Greenland

Abstract

The development of the Greenland Ice Sheet has been studied in a wide range of scientific scopes and scales. Variations in ice-sheet dynamics and meltwater discharge control the input of detrital material into the ocean and further influence oceanic circulation. Records of these variations in the past are indispensable to improve climate and ice sheet models and predict future developments as for now discrepancies between the geological record and modelled ice-sheet extents are still being reported on regional scales.

Radiogenic isotopes represent reliable tracers of detrital provenance changes induced by ice-sheet dynamics and changes in surface current activity. Here we present a Holocene record of radiogenic isotopes Sr, Nd and Pb in the siliciclastic detrital sediment fraction from the southwestern Greenland shelf. The record, spanning the past twelve thousand years, reveals insights into the Holocene history of the southwestern Greenland Ice Sheet.

A general continuous shift towards a higher contribution of local sources, mirroring the isotopic signatures of the adjacent Greenland bedrock, can be observed throughout the late and mid Holocene. This shift is most likely connected to a reduction in West Greenland Current speed, transporting less distal material to the core location. A more pronounced shift is recorded during the late Holocene, which can be connected to Neoglacial glacier and ice-sheet advance. The shift in detrital provenances after 3 ka BP is most obvious in the Nd isotopic composition and even more pronounced after 2 ka BP. We interpret this shift to be caused by interplay of increased erosion of the local bedrock through Neoglacial ice advance and a decreased quantity of material transported via the West Greenland Current.

3.1. Introduction

In the past years the development of the Greenland Ice Sheet (GIS) has gained increasing attention as it is losing mass on an accelerating rate (e.g. Castro de la Guardia et al., 2015; Harig & Simons, 2012, 2016; Rignot et al., 2011) and provides the largest uncertainty in predictions of future sea level rise (Harig & Simons, 2012; Jacob et al., 2012; McFarlin et al., 2018; Rignot et al., 2011). To improve predictions of future GIS development and its response to climatic changes, information on past developments are crucially important (e.g. Weidick et al., 2012). They further form the base in the ongoing debates about reactions of ice sheets and ice caps to a warming climate and their contribution to sea-level rise.

The GIS is the largest storage of freshwater in the Northern Hemisphere and its meltwater contribution influences the composition and physical properties of the surrounding coastal currents and the deep-water formation in the Labrador Sea (cf. Tang et al., 2004). Ice-sheet dynamics, such as retreats or advances, result in the exposure or sealing of surface rocks prone to erosion. In combination with variations in the volume of meltwater discharge, this controls the amount of siliciclastic detrital sediments transported to the Greenland shelf but may also induce compositional changes of these sediments if the exposed lithologies vary. Therefore, changes in the detrital record on the shelf may directly relate to the climate that controls GIS dynamics.

During the Holocene, climate variations triggered a variety of retreats and advances of the GIS, especially during the Holocene Thermal Maximum (HTM) warming and the following Neoglacial cooling (e.g. Kaufman et al., 2004; Solomina et al., 2015). It is known from reconstructions of past ice-sheet spatial distribution, that Arctic glaciers were smaller than today for most of the Holocene (e.g. Solomina et al., 2015). However, temporal climatic responses might differ on a regional scale, as the Arctic realm cannot be categorized as a single climatological unit (McKay et al., 2018).

The (south)western Greenland ice margin has been found to be particularly sensitive to long-term climate change (Larsen et al., 2014). Its broad shelf represents high resolution marine sedimentary records of Holocene climatic changes due to high rates of meltwater discharge and sedimentary input during GIS retreat after the Last Glacial Maximum (LGM). Variations in detrital sediment input through meltwater discharge, erosion and oceanic (surface) currents can be linked to changes in detrital sediment provenance and allow the identification of sediment source regions and transport pathways. These possible changes in detrital sediment provenances can be indirectly linked to glacier activity and ice-sheet dynamics.

Within this study we combine radiogenic isotope records (Sr, Nd, Pb) with the mineralogical composition of the sediment to trace past ice-sheet dynamics along the southwester Greenland margin. The aim of this study is to investigate variations in siliciclastic detrital sediment input onto the adjacent shelf and Labrador Sea in order to unravel potential changes in sediment provenance in response to GIS dynamics and shelf surface current intensities and hence ice sheet and ocean current-induced sediment transport patterns.

3.1.1. Holocene History of the southwestern Greenland Ice Sheet

The GIS has undergone several retreats and advances throughout the Holocene. The general retreat pattern following the LGM has been investigated and described in a number of studies along the southwestern Greenland coast (e.g Knutz et al., 2011; Larsen et al., 2014; Levy et al., 2017). The area around Godthåbsfjord (Figure 3.1) was covered by warm-based ice during the LGM, which retreated rapidly from the outer coast to the present ice margin between ~11.4 and 10.4 cal. ka BP (Larsen et al., 2014). The ice margin further retreated behind its present-day extent between ~7 and 4 cal. ka BP as documented by Larsen et al. (2015). The authors complemented existing geological data from the region with new records from threshold lakes south of 70°N and attributed this ice-sheet retreat to a response to atmospheric and oceanic warming. The described time interval coincides with the HTM (Kaufman et al., 2004)as identified for Southern Greenland between around 6 ka BP and 3 ka BP (Kelly, 1980; Fredskild, 1973; Kaplan et al., 2002; Kaufman et al., 2004). Submarine melting of marine terminating glaciers can be induced by warm ocean currents as it has already been documented for Southwest Greenland glaciers during the deglaciation (Knutz et al., 2011). Larsen et al. (2014) suggest this process to be the trigger of the early Holocene ice retreat in Godthåbsfjord, supporting evidence of the GIS being very sensitive to changes in climate, especially with regards to atmospheric and oceanic temperatures (cf. Andresen et al., 2012; Bjørk et al., 2012; Hanna et al., 2008).

Following the HTM, initiated by Neoglacial cooling, the ice margin re-advanced around 3.8 cal. ka BP and reached the present ice extent around 2.2 cal. ka BP (Kaplan et al., 2002; Larsen et al., 2011). This ice advance has not been a steady process but retreated and advanced another time from 1.5 and 1 cal. ka BP (Larsen et al., 2015, 2011; Levy et al., 2018) until it exceeded the present-day ice margin during the Little Ice Age (LIA) around 0.4 cal. ka BP

(Kaplan et al., 2002). The initiation and progression of the Neoglacial ice advance was indicated by the deposition of ice rafted debris (IRD) into glacial lakes at ~4.6, 3.6, 2.2, 1.0, 0.7, and 0.5 cal. ka BP in southernmost Greenland (Larsen et al., 2015). In southwestern Greenland the onset of the Neoglaciation was suggested to happen around 3.2 cal. ka BP based on a multi-proxy study from a marine sediment core collected in Ameralik Fjord, Godthåbsfjord system (M. S. Seidenkrantz et al., 2007). The Neoglacial has, in general, been described as a time period of decreased meltwater discharge, increased sea-ice cover in the local fjords and a significant drop in atmospheric temperatures (e.g. Møller et al., 2006; Seidenkrantz et al., 2007). Although the investigation of fluctuations in the ice-sheet margin is getting more attention in recent years (e.g. Larsen et al., 2017; Levy et al., 2017), the dynamics remain poorly documented and understood (cf. Weidick et al., 2012).

In addition to reconstructions based on lacustrine and marine sedimentary records the general development of the GIS has been analysed in a few modelling studies (e.g. Lecavalier et al., 2014; Tarasov & Peltier, 2003). Comparing these models with the geological records, Larsen et al. (2015) found that the Neoglacial ice marginal fluctuations are not detectable in these models. The *Huy3* model (Lecavalier et al., 2014), which generally agrees best with the geological records, overestimates the HTM ice margin retreat in the Isua region by around 60 km, according to Levy et al. (2017). In addition to these model discrepancies, the geomorphic evidence of Neoglacial ice advances is comparably rare as most previous evidence has been overprinted by the widest ice advance during the LIA (Long et al., 2009; Weidick et al., 2012). Mass balance calculations are, however, not easily estimated on a regional scale as the ice sheets margin is often merging with local glaciers and ice caps that have their own mass budget (Weidick et al., 2012).

3.1.2. Provenance Studies

Marine sediments commonly comprise abundant terrigenous siliciclastic detritus that is mobilized by different erosion processes and deposited on the sea floor. If the continental sources of this detrital material show sufficient compositional variability it is possible to trace the material back to its potential origin. The isotopic signatures of radiogenic Sr, Nd, and Pb of the siliciclastic component in marine sediments are directly related to their continental source area (Frank, 2002; Gutjahr et al., 2007; Werner et al., 2014). Based on the isotopic fingerprint of the sediment provenance and the activation and deactivation of various bedrock sources the isotopic record of marine sediments further allow for an indirect reconstruction of past ice-sheet movements, sea-ice transport or paleocurrents (e.g. Fagel et al., 2014; Haley et al., 2008; Maccali et al., 2018; Reyes et al., 2014).

Radiogenic isotopes have been used as provenance tracers in a variety of studies conducted on (deep sea) sediments in the Labrador Sea. Many of these studies were applied to specific grain-size fractions, in order to differentiate between different transport mechanisms (Fagel et al., 2004, 2002; Fagel & Hillaire-Marcel, 2006; Innocent et al., 2000). However, the majority of radiogenic isotope based provenance studies, including most of the aforementioned, focuses on pre-Holocene times and larger spatial scopes, such as sediment provenances during Heinrich events (Benson et al., 2003) or within glaciomarine sediments tracing their origin of the Laurentide, Greenland, Iceland and Fennoscandian ice sheets (Farmer et al., 2003). Few radiogenic isotope based provenance studies actually trace ice-sheet dynamics in southwest Greenland (Colville et al., 2011; Reyes et al., 2014), and usually not based on Holocene sedimentary records. As shown by Colville et al. (2011) and Reyes et al. (2014) the different

geological terrains of southern Greenland have unique radiogenic isotopic signatures due to their differing geological history and ages and hence present a suitable tracer of siliciclastic detrital material.

3.2. Regional Setting and Research Area

Potential source areas of detrital sediments encompass the entire Southwest of Greenland, its bedrock geology and the adjacent shelf with a focus on the area around Greenland's capital Nuuk (64°10' N 51°44' W) and the Godthåbsfjord system (Figure 3.1).

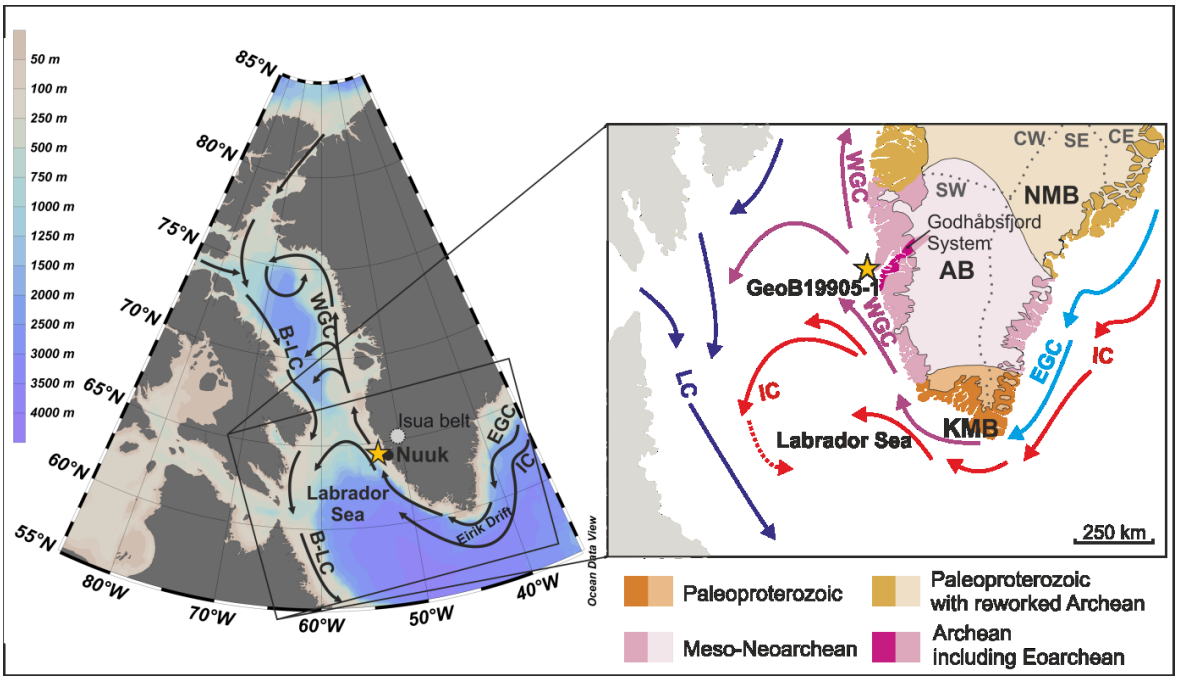

Figure 3.1: Map of the research area with simplified ocean current system and close-up on southern Greenland geological terrains. Geological map has been adapted from (P R Dawes, 2009): lighter shaded areas indicate the current extent of the Greenland Ice Sheet; dashed grey lines mark the present-day GIS drainage domains: SW = southwest, CW = central west, CE = central east, SE = southeast (White et al., 2016); Labrador Sea circulation pattern has been adapted from Fratantoni & Pickart (2007) and Myers et al. (2009). Yellow star marks the location of gravity core GeoB19905-1. Abbreviations: KMB = Ketilidian Mobile Belt, AB = Archean Block, NMB = Nagssugtoqidian Mobile Belt, EGC = East Greenland Current, WGC = West Greenland Current, B-LC = Baffin – Labrador Current, LC = Labrador Current, IC = Irminger Current. Overview map created with Ocean Data View (Schlitzer, 2020).

3.2.1. Southern Greenland Geology

Greenland holds some of the oldest rocks on Earth with Paleoproterozoic rocks in southernmost Greenland and Archean rocks in southwest (and east) Greenland (Figure 3.1) (e.g. Dawes, 2009). The main geological units covered within this study are, from south to north; the Ketilidian Mobile Belt (KMB), the Archean Block (AB) and the Nagssugtoqidian Mobile Belt (NMB), all of which mainly consist of granites and gneisses, as well as supracrustal belts and intrusions (cf. Colville et al., 2011, supplement and references therein). The major part of these bedrock terrains is presently covered by the massive GIS. The exposed surface is characterised by a variety of fjord systems and differs in its topography along the coast of western Greenland. The GIS is drained by a number of outlet glaciers, mostly land-based, but also by a few marine-terminating glaciers (Mortensen et al., 2011; Weidick et al., 2012), discharging meltwater into the local fjords. The ice-free area around Godthåbsfjord with rocks exposed to erosion and weathering is around 100 to 125 km wide (Weidick et al., 2012). The Godthåbsfjord system (Nuup Kangerlua) is the largest fjord system in southwest Greenland reaching from the coast to the GIS where some outlet glaciers reach sea level (Weidick et al.,

2012). The up to 600 m deep fjords are surrounded by an alpine mountainous terrain up to 1800 m of elevation (Mortensen et al., 2011). The fjords exchange water with the adjacent Labrador Sea off southwest Greenland. The local oceanography is characterised by the northwards flowing West Greenland Current (WGC), which originates from the East Greenland Current (EGC) transporting cold and fresh waters from the Arctic Ocean and mixing with the warm and saline waters from the Irminger Current (IC) in the subpolar North Atlantic (Figure 3.1). The WGC is warmer and more saline than the EGC but freshens on its way north due to meltwater discharge along the West Greenland coast (Buch, 2002; Myers et al., 2009).

3.2.2. Labrador Sea

The research area is adjacent to the Labrador Sea which functions as a gateway for Arctic Ocean freshwater through Baffin Bay into the North Atlantic (Myers et al., 2009). The Labrador Sea is a key site for investigations of the formation of North Atlantic Deep Water (NADW), which is overlain by the distinct Labrador Sea Water (LSW). The Labrador Sea surface circulation is characterised by a westwards flowing branch of the WGC merging with the polar Labrador Current, both transporting and eroding glacial deposits (Mao et al., 2014). Water transported by the WGC represents a mix of Arctic Ocean water transported along the east Greenland coast via the EGC, and warm and salty waters from the IC (Figure 3.1). For these Atlantic sourced waters the Labrador Sea forms the final destination (Yashayaev, 2007), as well as for material transported alongside these currents. The eastern Labrador Sea coastal waters are further influenced by seasonal variation of meltwater input from the GIS (Castelao et al., 2019). The majority of GIS meltwater reaching the interior of the Labrador Sea influencing its salinity and stratification patterns originates from southeast Greenland, whereas the southwest Greenland meltwater gets mainly transported northwards into Baffin Bay (Castelao et al., 2019; Luo et al., 2016). The current circulation pattern and the full appearance of LSW established around 3 ka BP (e.g. de Vernal & Hillaire-Marcel, 2000; Fagel et al., 2004).

3.3. Material and Methods

3.3.1. Core Description and Age Chronology

The 1036 cm long gravity core GeoB19905-1 was collected from Nuuk Trough (64°21.68'N 52°57.70'W), ~60 km northwest of Nuuk, at a water depth of 483 m during *RV Maria S. Merian* cruise *MSM44* in 2015 (Dorschel et al., 2015). The core mainly consists of uniformly olive-greyish hemipelagic muds with four alternating layers of sandy mud and muddy sand at the bottom of the core (Dorschel et al., 2015). Grain size granulometry detected no material >250 µm and on overall fining-upwards trend throughout the record (Weiser et al., 2021). Based on grain-size distributions, the core can be divided into three intervals of early, mid and late Holocene with sortable silt fractions of >28 µm, ~26 µm, ~24 µm, respectively (Weiser et al., 2021). The entire record covers the past 12 ka BP.

The previously published age model of sedimentary record GeoB19905-1 is based on Accelerator Mass Spectrometry ^{14}C-dating of ten mixed benthic foraminifera samples (Weiser et al., 2021). The resulting ages were calibrated against *IntCal13* (Reimer et al., 2013) using the *PaleoDataView* program (Langner & Mulitza, 2019) to compensate for possible reservoir age changes throughout the Holocene. The reservoir ages were used to construct the age model with the Bayesian age modelling approach using the software package *BACON* (Blaauw & Christen, 2011). The age model reveals a hiatus of around two thousand years at 640 cm, excluding the time period between 7.6 and 5.9 ka BP from the sedimentary record. This hiatus

is supported by an abrupt change in grain size and a significant and unrealistic drop in sediment accumulation rate (Weiser et al., 2021).

3.3.2. Radiogenic Isotope Analysis

Sample preparation and measurements of radiogenic isotope ratios were performed in the Isotope Geochemistry Laboratory at MARUM—Centre for Marine Environmental Sciences, University of Bremen, Germany. The first batch of 14 samples was chosen based on the age model to cover roughly every one thousand years. Additional four samples were chosen for further investigation based on existing isotopic trends. All samples were washed, decarbonised and separated from possible iron-manganese coatings following a procedure by Gutjahr et al. (2007). To obtain an overall signal not emphasizing certain transport mechanisms, the bulk grain-size fraction was chosen for analysis rather than a specific fine fraction, which is known to mirror current induced transport (e.g. Eisenhauer et al., 1999; Fagel et al., 2002; Maccali et al., 2013). Between 1 and 2 g of bulk ground sample were washed with ultrapure water (18.2 MΩ; Millipore) to remove pore water, decarbonised with a 40 % acetic acid solution (buffered to pH ~4 with 1M Na-acetate), and leached with hydroxylamine hydrochloride and 15 % acetic acid (buffered to pH ~4 with NaOH) to remove any possible sediment grain coatings (cf. Gutjahr et al., 2007). Stepwise hot-acid digestions with concentrated hydrofluoric acid (5:1, HF:HNO_3), Aqua Regia (3:1, 6M HCl:concentrated HNO_3), nitric acid (concentrated), hydrochloric acid (6M) and hydrogen peroxide were applied to around 100 mg of the decarbonised and leached sample to receive the siliciclastic detrital fraction and remove organic matter. The final sample was dissolved in nitric acid (2M) for radiogenic isotope separation. Sr and Pb were separated from the sample solution through column separation using TrisKem Sr.spec™ resin (method modified after Deniel & Pin, 2001). From the remaining solution, light rare earth elements were separated as a group using TRU.spec™ resin. Nd was isolated from Sm by LN.spec™ following the method by Pin et al. (1994). Isotopic ratios were analysed with a Thermo Fisher Scientific Triton™ Plus multicollector thermal ionization mass spectrometer (TIMS) in either multidynamic (Sr) or static (Nd, Pb) multicollection mode. The international reference materials NIST SRM 987 (Sr), JNdi-1 (Nd) and NIST SRM 981 (Pb) were measured along with the samples to monitor analytical accuracy and long-term reproducibility. The measured reference material values are in the range of 0.710253 ±0.000023 ($^{87}Sr/^{86}Sr$ ±2SD_{mean}; n=6), 0.512105 ±0.000043 ($^{144}Nd/^{143}Nd$ ±2SD_{mean}; n=6) and 16.8972 ±0.0059 ($^{206}Pb/^{204}Pb$ ±2SD_{mean}; n=4) during the measuring period of 15 months. Those values fall in the range of published reference values measured on TIMS (GeoReM data base; query June 2020; http://georem.mpch-mainz.gwdg.de): 0.710249 ±0.000034 ($^{87}Sr/^{86}Sr$ ±2SD_{mean}; n=1528), 0.512107 ±0.000026 ($^{144}Nd/^{143}Nd$ ±2SD_{mean}; n=339) and 16.9211 ±0.0413 ($^{206}Pb/^{204}Pb$ ±2SD_{mean}; n=254). A bulk uncertainty of 0.1% per atomic mass unit was assumed for Pb values to account for isotopic fractionation during the measuring process, which exclusively exceeds the measured uncertainty. Nd isotope ratios are converted to the εNd notation normalized to ancient Chondritic Uniform Reservoir (CHUR) value of 0.512638 as defined by Jacobsen & Wasserburg (1980):

$$\left(\varepsilon_{Nd} = \left\{\left[\left(^{143}Nd/^{144}Nd\right)_{Sample}/\left(^{143}Nd/^{144}Nd\right)_{CHUR}\right] - 1\right\} * 10^4\right)$$

3.3.3. Mineralogical x-ray Diffraction

The mineralogical composition was obtained through X-ray diffraction (XRD) of the bulk sediment fraction. XRD analysis was carried out at GEOTOP, Université du Québec à Montréal, Canada. Between 100 and 500 mg of ground bulk sample material were prepared for analysis

using the 'back-side method' (Moore & Reynolds, 1997) and measured in a Siemens X-ray Diffractometer D5000 in a range between 5° and 85° 2θ. Quantification is based on the respective peak intensity and comprises an estimated uncertainty of ~2%. Quartz was used as a standard for horizontal peak position correction. Halite and calcite were used as a standard for peak intensity.

3.4. Results and Interpretation

3.4.1. Radiogenic Isotope Records

The sedimentary record from Nuuk Trough can be divided into three intervals based on the radiogenic isotope record: early (before ~8 cal. ka BP), mid (~6 to 3 cal. ka BP), and late (~3 cal. ka BP to present) Holocene (Figure 3.2), note that the interval between ~7.6 and 5.9 ka BP represents a hiatus within the sedimentary archive.

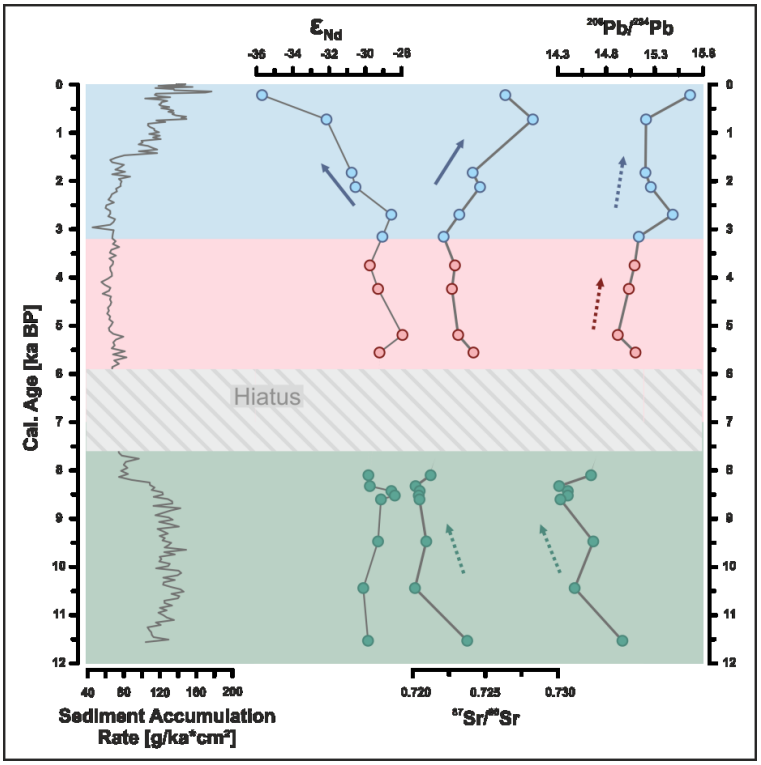

Figure 3.2: Radiogenic isotope records of the siliciclastic detrital sediment fraction of gravity core GeoB19905-1. Analytical uncertainties are smaller than data points. Highlighted time intervals represent the early (green), mid (red) and late (blue) Holocene, which coincide with the Deglacial period, Holocene Thermal Maximum and Neoglacial, respectively. Arrows indicate trends mentioned in the text. Age model and sediment accumulation rate are taken from Weiser et al. (2021).

The radiogenic isotope records commence with comparably uniform ε_{Nd} values (average ~-29.4) and a slight trend towards less radiogenic values in Sr and Pb ratios (average ~0.721 ($^{87}Sr/^{86}Sr$), ~14.5 ($^{206}Pb/^{204}Pb$)) between ~11 and 8 cal. ka BP. A small kink towards more radiogenic ε_{Nd} and $^{206}Pb/^{204}Pb$ values can be identified around 8.5 cal. ka BP. After ~6 cal. ka BP $^{87}Sr/^{86}Sr$ and $^{206}Pb/^{204}Pb$ values slightly shift towards more radiogenic values (~0.7232 ($^{87}Sr/^{86}Sr$), ~15.0 ($^{206}Pb/^{204}Pb$)) while ε_{Nd} values become slightly less radiogenic (~-29.1 (ε_{Nd})), compared to early Holocene values. Starting around 3.2 cal. ka BP, ε_{Nd} values show a pronounced shift towards even more unradiogenic values, with -29.1 at ~3.2 ka BP, -30.6 at ~2.1 ka BP and finally reaching -35.7 at the top of the record (~0.2 ka BP). A similar development is visible in the Sr and Pb isotope record. Sr values shift from 0.7221 (~3.2 ka BP)

to 0.7246 (~2.1 ka BP) and 0.7263 (~0.2 ka BP), and Pb values from 15.13 (~3.2 ka BP) to 15.25 (~2.1 ka BP) and 15.66 (~0.2 ka BP). It should be noted that the most pronounced shift in isotopic ratios coincides with the most pronounced changes in sediment accumulation rate (Figure 3.2).

3.4.2. Mineralogy

The mineralogical composition of gravity core GeoB19905-1 reveals small variations throughout the entire record (Figure 3.3). The most frequently occurring minerals are quartz, feldspar (albite, microcline), hornblende, biotite and calcite. The quartz and feldspar content is relatively stable throughout the record without any significant peaks. The amphibole and pyroxene concentration appears generally higher in the early Holocene and decreases towards the late Holocene, with only one exception around 2.2 cal. ka BP. Within the phyllosilicates record (biotite, clinochlore), three peaks where the concentration exceeds the 10% mark can be identified at ~2.6, 0.8 and 0.2 cal. ka BP. The iron mineral content (primarily pyrite) is rather stable around 2% with two higher peaks at ~5.5 and 5.2 cal. ka BP. The most significant changes are visible within the carbonate content, which drastically increases between ~8.6 and 3.8 cal ka BP.

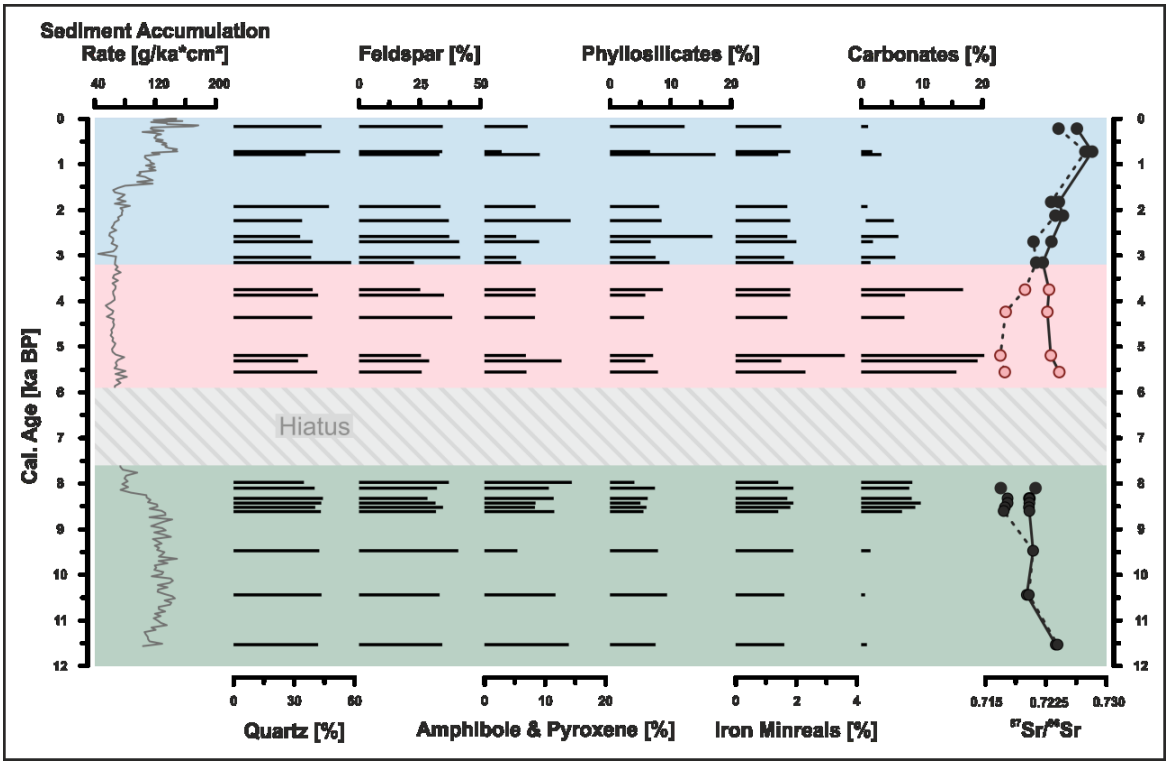

Figure 3.3: Mineralogical composition of the bulk sediment fraction of gravity core GeoB19905-1. Age model is based on radiocarbon dating of benthic and planktonic foraminifera (Weiser et al., 2021). Highlighted time intervals represent the early (green), mid (red) and late (blue) Holocene, which coincide with the Deglacial period, Holocene Thermal Maximum and Neoglacial, respectively. $^{87}Sr/^{86}Sr$ rations for bulk (dashed line) and carbonate-free detrital (solid line) sediment fraction are plotted alongside to demonstrate the biogenic origin of carbonates (Sr with seawater signature) during the mid Holocene (see 3.5.1).

Apart from the carbonate content that correlates with the bulk sediment Sr isotopic composition, the recorded changes in carbonate-free detrital isotopic composition are not aligned or show any correlation to the changes in mineralogical composition. There is no significant evidence of mineralogical control on the isotopic values.

3.4.3. Detrital Sediment Provenance

Plotting the isotopic composition of potential source areas in Greenland and of time resolved samples of gravity core GeoB19905-1 enables the identification of possible provenance shifts over time (Figure 3.4). The isotopic composition of southern Greenland bedrock are represented by stream sediments taken along the west Greenland coast (Figure 3.6; Colville et al., 2011; Reyes et al., 2014). The stream sediments represent fine-grained glaciofluvial sediments from meltwater streams and are supplemented by few glaciolacustrine sediments from ice-marginal lakes and debris entrained in icebergs near calving glacier margins (Reyes et al., 2014). All stream sediments were deposited in low energy environments along streams draining the local geology and therefore represent the isotopic composition actually delivered to the ocean rather than bedrock samples that might contain a bias towards certain rock types (Colville et al., 2011 supplement). All reference samples will hereinafter be summarised as stream sediments.

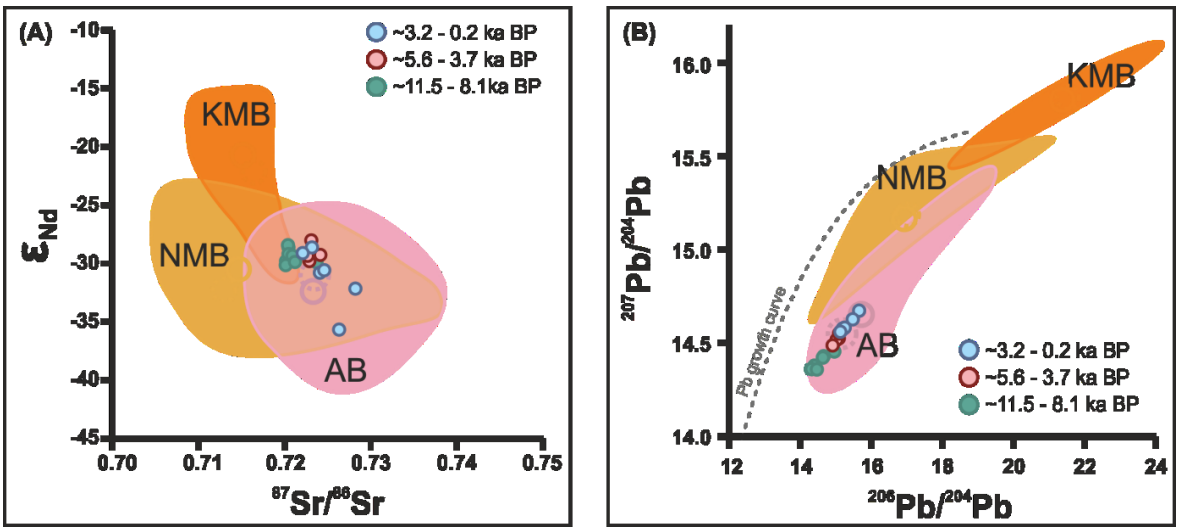

Figure 3.4: Radiogenic isotope composition of the siliciclastic detrital sediment fraction of gravity core GeoB19905-1 and isotopic ranges of the main southern Greenland geological terrains for $^{87}Sr/^{86}Sr$ versus ε_{Nd} (A) and $^{206}Pb/^{204}Pb$ versus $^{207}Pb/^{204}Pb$ (B). Colours represent the terrains included in Figure 3.1 : KMB = Ketilidian Mobile Belt, AB= Archean Block, NMB = Nagssugtoqidian Mobile Belt. Background data for isotopic ranges originates from stream sediments (Colville et al., 2011; Reyes et al., 2014). Circles represent the mean (solid) and median (dashed) of reference values for the corresponding terrain. Dashed grey line represents the Pb growth curve of continental crust (Stacey & Kramers, 1975).

The $^{87}Sr/^{86}Sr$ and ε_{Nd} provenance diagram suggests mixed detrital sediment sources of the local AB and the distant NMB as well as some contribution of the KMB for gravity core GeoB19905-1 (map: Figure 3.1). The siliciclastic detrital sediment composition displays changing proportions of the different sources over time, most pronounced in the late Holocene. While the $^{87}Sr/^{86}Sr$ ratios become gradually more radiogenic over time, the ε_{Nd} values are comparably uniform, but become pronouncedly less radiogenic in the late Holocene. The least radiogenic Nd values coincided with the most radiogenic Sr values.

The Pb isotopic composition exclusively plots into the field of AB sources. A gradual trend towards more radiogenic $^{206}Pb/^{204}Pb$ composition is recorded over time. The least radiogenic values can be found in the late Holocene and the most radiogenic values in the late Holocene. The $^{206}Pb/^{204}Pb$ versus $^{207}Pb/^{204}Pb$ provenance diagram does not reveal any indication of neither KMB nor NMB as a detrital sediment source to the GeoB19905-1 core location throughout the Holocene.

3.5. Discussion

General climate variability is usually visible in a variety of oceanic and detrital tracers. Often oceanographic changes are consistent with overall Holocene climate patterns (e.g. Fagel & Mattielli, 2011). Based on changes in isotopic composition the sedimentary record from Nuuk Trough can be divided into the three time intervals of early (before ~8 cal. ka BP), mid (~8 to 3 cal. ka BP) and late (~3 cal. ka BP to present) Holocene. Theses intervals coincide with major climatic intervals known for the Holocene time period, the Deglacial period, the HTM and the Neoglacial.

3.5.1. Early to Mid Holocene Ice-Sheet Retreat

During the early and mid Holocene, a time interval of major ice-sheet retreat (Knutz et al., 2011; Larsen et al., 2014, 2015; Levy et al., 2017), the detrital sediment input onto the west Greenland shelf appears to be dominated by local AB-sourced material with varying secondary distal input from KMB and possible NMB sources (Figure 3.4). The main sediment transport pathways are local erosion and meltwater discharge, delivering AB material, as well as distal transport via the WGC, transporting KMB material along the coast. The possible contribution of NMB-sourced material can most likely be excluded due to its geographical position north of the core location and the general transport pattern of the WGC flowing northwards (Figure 3.1). Additionally, the present-day GIS drainage domains part into a southwestern domain and a central western domain approximately at the boundary between the AB and NMB geological terrains (Figure 3.1; White et al., 2016). An identification of distal NMB sediment from east Greenland transported along the currents is also rather unlikely as the majority of this water mass is deflected westwards into the Labrador Sea (Castelao et al., 2019) and the remaining proportion would most likely be insignificantly low when mixed with other sources along the way. Sea-ice cover, which is usually an important transport pathway within the Arctic realm and could yield the potential to transport detrital sediments (NMB) southwards can most likely also be neglected. Even though sea ice formed in Baffin Bay enters the Labrador Sea through Davis Strait (e.g. Tang et al., 2004), the general present-day sea-ice border lies north of the core location (e.g Kolling et al., 2018; https://meereisportal.de: Grosfeld et al., 2016), and predominantly ice-free conditions were recorded at the core location throughout the past 11.5 ka BP of the record (Saini et al., submitted). Even though increased sea-ice cover has been recorded in the local Ameralik Fjord, Godthåbsfjord system (Figure 3.1) (Møller et al., 2006; M. S. Seidenkrantz et al., 2007), it has also been found that neither sea ice nor glacial ice leaves the fjords as it all melts prior to exiting (Mortensen et al., 2011).

The Pb isotope data clearly identify the AB as the main source region of siliciclastic detrital sediments without any indication of substantial KMB and NMB contribution (Figure 3.4). Thus the Pb data solidify the assumption drawn from the Sr and Nd data, about AB being the dominant source area as well as excluding NMB as a relevant source. However, ruling out any contribution of KMB based on the Pb isotopic composition would contradict with the general transport pattern of the WGC current, no northwards transport of detrital material along the west Greenland coast would be unlikely. Here, the Pb data simply do not lead to any indication of KMB input.

Significant changes in siliciclastic detrital sediment provenances cannot be identified throughout the early and mid Holocene. A slight shift towards a more radiogenic Sr isotope composition from the Deglacial into the HTM can be identified pointing to a relative increase in AB contribution (Figure 3.5). As one possibility this could be the result of increased

meltwater discharge driven by higher atmospheric temperatures during the HTM (e.g. Axford et al., 2013; Moros et al., 2006). This interval of more radiogenic $^{87}Sr/^{86}Sr$ between ~6 and 3.5 ka BP coincides with the timing when the ice sheet margin retreated behind its present extent (Larsen et al., 2015), which enabled the erosion of freshly exposed (AB) bedrock. Another possibility would be a decrease in WGC speed resulting in a reduction of far-travelled material (KMB). This possibility has recently been discussed by Weiser et al. (2021) who defined the preceding interval (10.6-6 ka BP) as the Holocene Speed Maximum (cf. McCave & Andrews, 2019a, 2019b) after which the WGC speed continuously decreased. Weiser et al. (2021) came to their conclusion based on endmember modelling of two grain size domains (coarse vs. fine) of the same record as used in this study (GeoB19905-1) showing reduced contribution of the far-travelled endmember during the mid Holocene. Hence, the probability of the shift in isotopic composition being a result of reduced KMB input rather than increased AB input might be more likely. Considering, that the mid Holocene sedimentary record between 7.6 and 5.9 ka BP is missing from the GeoB19905-1 record, it remains unclear if the isotopic shift from the Deglacial into the HTM was gradually or abrupt.

The general mineralogical composition during the early Holocene is stable. The most pronounced changes can be identified in the carbonate content starting around 8.6 ka BP and continuing throughout the mid Holocene. The drastic increase in carbonate content is accompanied by a slight decrease in quartz, feldspar and phyllosilicates, which is most likely a mass balance effect. This time period of high carbonate content (mainly calcium carbonate) coincides with the timing of the HTM (Kaufman et al., 2004 and references therein), which has been characterized with comparably high atmospheric and surface water temperatures. The higher temperatures lead to a significant increase in primary productivity in the upper water column, as it has been documented in several studies in the Labrador Sea, Baffin Bay and in southern Greenland lake sediments (e.g. Kaplan et al., 2002; Lochte et al., 2019; Ouellet-Bernier et al., 2014). The high calcium carbonate content can be considered as a tracer of this high surface productivity period. While the excursion cannot be seen in the Sr isotope record of the detrital (carbonate-free) fraction, it is clearly documented in the Sr isotope record of the bulk (not decarbonised) fraction (Figure 3.3), mirroring the present-day seawater signature of Sr in marine carbonates ($^{87}Sr/^{86}Sr = 0.70917$; Henderson et al., 1994). This supports the assumption of the carbonate being biogenic carbonate most likely produced by primary producers in the upper water column.

3.5.2. Ice-sheet advance – late Holocene

The onsets and timings of the Neoglaciation vary across the Arctic and generally began after 5 ka BP and proceeded through a number of ice-advance pulses with its culmination during the LIA (e.g. Solomina et al., 2015). Throughout the Arctic the main pulses of Neoglacial cooling have been identified between 4.5 and 3 ka BP, around 2 ka BP (McKay et al., 2018; Solomina et al., 2015) and between 1.5 and 0.5 ka BP, coinciding with general cooling periods (Solomina et al., 2015). A distinct cooling around 3 ka BP has been identified from different archives and proxies around southern Greenland. Especially the time between 3 and 2 ka BP is a crucial interval of Neoglacial cooling and occurred over large parts around Labrador Sea and Greenland, suggesting a teleconnection of decreased ocean heat transport through the entire East Greenland-West Greenland-Baffin current system (Kaplan et al., 2002).

The onset of the Neoglacial has been defined at 3.2 ka BP in southern Greenland (e.g. Larsen et al., 2015; Seidenkrantz et al., 2007 & references therein), which coincides with the onset of the

most pronounced shift in isotopic composition and hence in provenance in the GeoB19905-1 record (Figure 3.2). Around 2 ka BP, when the shift in Nd and Sr isotopic composition is becoming even more pronounced, atmospheric cooling accelerates and the second major pulse of Neoglacial ice-sheet advance has been documented (McKay et al., 2018). This shift in isotopic composition coincides with the ice-advance pulse and the general increase of local glaciers during the late Holocene, initiating increased erosion of the local bedrock and transport and deposition of the corresponding detrital material, as supported by the increase in sediment accumulation rate (Figure 3.2; Weiser et al., 2021).

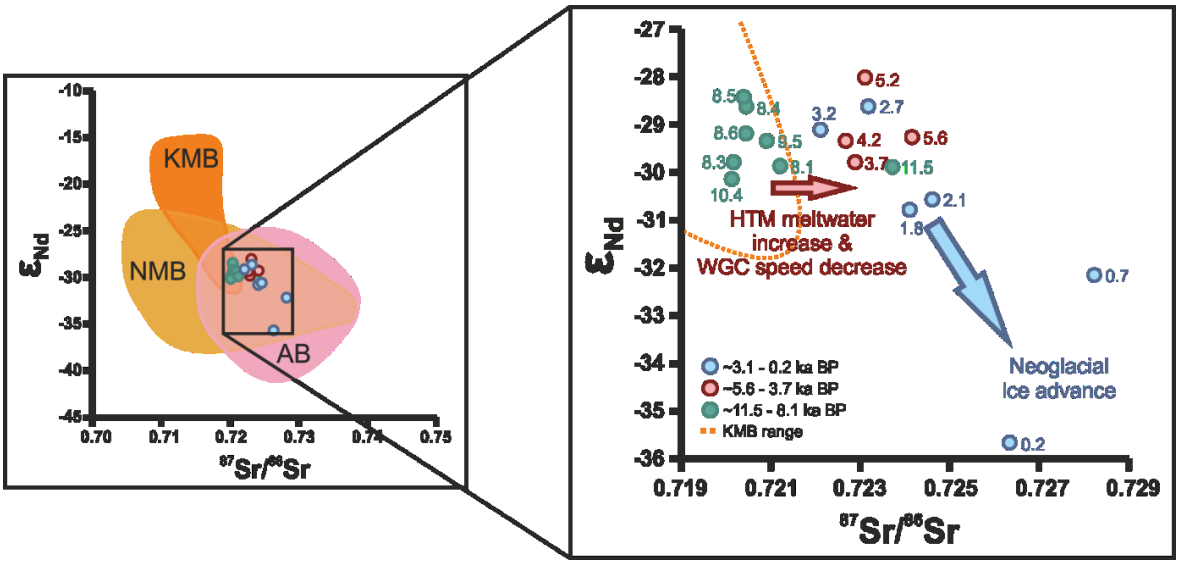

Figure 3.5: Close-up of Sr and Nd data of gravity core GeoB19905-1. Reference data for provenance plot (left) as in Figure 3.4.

For a better visualisation of the spatial distribution of isotopic signatures transported with detrital sediments onto the southwest Greenland shelf, the stream sediment data serving as reference (Colville et al., 2011; Reyes et al., 2014) have been interpolated (weighted average gridding; Schlitzer, 2020) onto the local shelf (Figure 3.6). Comparing our isotope patterns to the spatial distribution of the stream sediment data (Colville et al., 2011; Reyes et al., 2014) identifies a distinct shift away from KMB signatures and towards the local AB detrital sediment sources. The isotopic values of stream sediments closest to the core location match the Neoglacial values of GeoB19905-1 in all three isotope systems. The most radiogenic Sr values and least radiogenic Nd and Pb values can be found for AB. The dominant input of local AB to the core location is supported by the concept of basal glacial erosion, stating that detrital material is usually delivered within a radius of 50 to 100 km (cf. Farmer et al., 2003). Farmer et al. (2003) further suggests that ice-proximal sediments deposited in the northern North Atlantic originate from erosion of immediately adjacent rocks rather than erosion at the base of interior portions of the ice sheet. Furthermore, unradiogenic Nd values usually indicate older crustal terrains such as the local Archean rocks of the AB (e.g. Farmer et al., 2003). The gneisses in the ~3800 – 3700 Ma year old Isua supracrustal belt (Nutman et al., 2016), one of the geological units within AB in close vicinity to the core location (Figure 3.1), have been identified before as the source of highly unradiogenic Nd by Fagel et al. (2002).

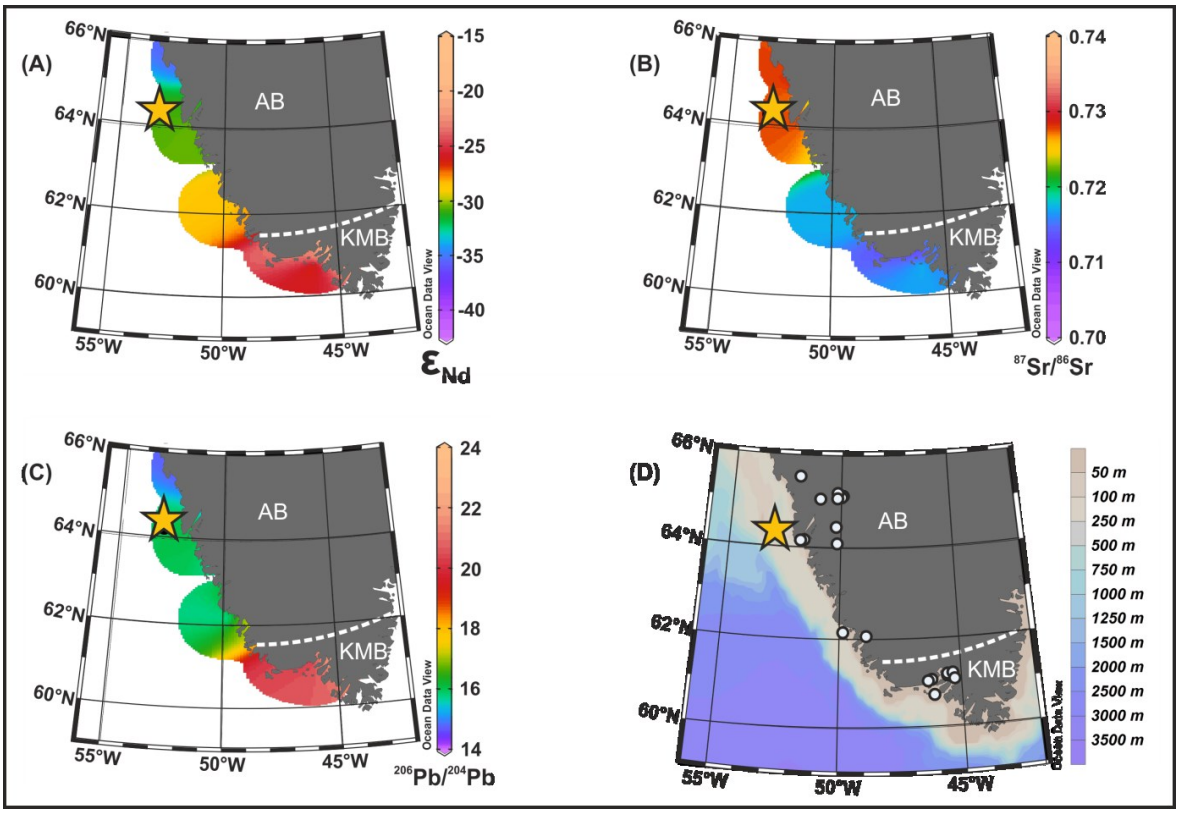

Figure 3.6: Distribution of KMB and AB stream sediment data (Colville et al., 2011; Reyes et al., 2014) for each isotope system: (A) ε_{Nd} (B) $^{87}Sr/^{86}Sr$ and(C) $^{206}Pb/^{204}Pb$. Values are interpolated (weighted average gridding) to represent the isotopic signature transported onto the shelf. (D) displays the sample locations. Yellow star marks the location of gravity core GeoB19905-1. Maps created with Ocean Data View (Schlitzer, 2020).

Despite the well matching Pb data with the local bedrock signatures, supporting our theory on increased local erosion, the data does not include any possible influence of KMB originating material as already noted for the early to mid Holocene. The Pb isotopic composition follows a continuous trend towards more radiogenic values throughout the entire record until recent values, in line with the development of the Sr isotopic composition (Figure 3.2Figure 3.4). While a possible contribution of KMB sources seems to decrease over time as indicated by the Sr-Nd system, the Pb isotopic composition rather points to an increase of this particular source.

A continuous Holocene trend towards more radiogenic Pb has been noted in other studies (Colville et al., 2011) and might as well be an effect of increased weathering or the result of younger sourced Pb caused by basaltic intrusions in the Isua supracrustal belt (Nutman et al., 2016 and references therein). The local geology of the Godthåbsfjord region is, however, quite divers with different forms of orthogneisses (Pedersen et al., 2013), whose different contributions might have caused the increasing development in Pb signatures. However, it has to be kept in mind that the stream sediment background data display the recent erosion signal and not necessarily the mean Holocene erosion signal. Despite the uncertainties in the cause of the radiogenic development of the Pb data, it yields the essential information of identifying the Archean Block as the main contributor of detrital sediments to Nuuk Trough throughout the entire Holocene. This identification could not have been made based on Sr and Nd data only. The apparent absence of KMB sources within the Pb isotopic composition can be a cause of mixing. The two sources do not yield overlapping isotopic signatures; hence the secondary source will most likely be masked by the dominant source. A possible signal of material transported via the WGC is already a mix of AB and KMB, when mixing the WGC endmember

with the local AB endmember, the KMB contribution becomes comparably small and values converge towards AB values.

The past 3000 years do not only represent the time period with the most significant changes in radiogenic isotope composition but also record some of the highest concentrations of quartz and K-feldspar, and the highest concentrations of biotite (phyllosilicates) (Figure 3.3). These mineralogical changes support the proposed provenance shift towards the dominant local AB geology (Nutman et al., 2016). While quartz and feldspar merely slightly increase overall but do not identify pronounced peaks, the phyllosilicate record shows three significant peaks in the Neoglacial period. Those peaks solely correspond to a significant increase in biotite, which has been identified as a rock-building mineral in AB, especially the Isua supracrustal belt (Nutman et al., 2016). Those peaks and general fluctuations in mineralogical composition could be caused by the observed Neoglacial ice-sheet fluctuations (Larsen et al., 2015, 2011; Levy et al., 2017), but are not recorded in the isotopic record. This could be due to the lower resolution of the isotopic record.

Generally, decreased meltwater discharge, as documented for the Neoglacial time period (Møller et al., 2006; M. S. Seidenkrantz et al., 2007) along the west Greenland margin leads to less detrital material discharged onto the Greenland shelf and fed into the WGC. Hence, less material can be transported further north to the core location. Additionally, decreased intensities of the WGC after 3.7 ka BP (Schweinsberg et al., 2017) would further decrease the fraction size of detrital material originating from southern Greenland (KMB) transported northwards. For the same record (GeoB19905-1) Weiser et al. (2021) report a decrease of their far-travelled endmember and an increase of their local endmember, in combination with a significant fining trend in sortable silt and mean grain size after 3.3 ka BP. They suggest a further decrease in WGC speed following the ongoing decrease after the Holocene Speed Maximum (10.6-6 ka BP), and notice a speed minimum during the past ~2 ka. This WGC speed minimum (Weiser et al., 2021) in combination with the Neoglacial ice advance culminating during the LIA around 0.4 ka BP (e.g. Kaplan et al., 2002) can be identified in the intensification of the late Holocene provenance shift in Sr and Nd and to some extent also in the Pb isotopic composition (Figure 3.2), emphasising erosion of the adjacent bedrock as the main source of siliciclastic detrital sediments into Nuuk Trough.

Furthermore, the Nd isotopic composition of water masses is known to represent the geological signatures of the geological surrounding of their source areas (cf. Frank, 2002). Filippova et al. (2017) find the least radiogenic surface water Nd composition (-25 to -23) in the (western) Labrador Sea closest to the coast of Labrador, documenting input from the Precambrian terrains of the Canadian Shield, the geological equivalent of AB in Greenland (cf. Dawes, 2009). With increasing distance from the shore, the values become more radiogenic. Certainly, seawater and sediment signatures differ from each other, but the trend of local input coinciding with unradiogenic Nd signatures, further supports our assumption of increased local erosion.

Based on the above mentioned assumptions, we suggest that the main transport pathway of detrital sediments into Nuuk Trough during the late Holocene is a mix of increased local erosion and meltwater discharge, while distal transport via the WGC can be noted as the secondary transport pathway. This interplay of transport pathway divergence can be concluded as the reason for the Neoglacial provenance shift. This conclusion is supported by

the recent study of Weiser et al. (2021), who also suggest decreased distal sediment transport at the core location of GeoB19905-1.

However, actual fluctuations in the ice-sheet margin as mentioned in recent studies (Larsen et al., 2017; Levy et al., 2017) are not resolved in the isotopic records of Sr, Nd and Pb radiogenic isotopes. This might be mainly due to the data resolution but also connected to the mixed sediment composition and the decreasing but still existing influence of far-travelled material from southernmost Greenland. The fluctuations in mineralogical composition, however, do hint to the observed fluctuations in ice-sheet extent. Further investigations of higher resolution radiogenic isotope (and mineralogical) records might shed new light onto this topic of still poorly documented and understood Neoglacial GIS fluctuations (cf. Weidick et al., 2012).

Finally, significant changes and paleoenvironmental variability after 3 ka BP have been found in a variety of studies in and around southern Greenland or other places in the Arctic. These changes encompass reorganisation of fjords, cooler atmospheric temperatures, increased sea-ice cover and decreased meltwater discharge, as well as variations in deep current compositions and intensities (Fagel et al., 2004; Kaplan et al., 2002; Seidenkrantz et al., 2007; Werner et al., 2014). The establishment of the modern Labrador Sea circulation pattern around 3 ka BP was aligned with the full appearance of LSW (cf. Fagel et al., 2004). Fagel et al. (2004) further identified a sudden increase in North American Shield components (old cratons of western Greenland and Labrador) delivered into Labrador Sea after 3 ka BP and suggest increased supply from Labrador Sea margins driven by enhanced LSW formation. The distinguishing climatic and oceanographic changes in the northern north Atlantic region coincide and are to some extent connected to the pronounced shift in radiogenic isotope composition during the Neoglacial. The interplay of atmospheric cooling and oceanographic reorganisation increased the input of local southern Greenland detrital sediments onto the adjacent shelf, most likely influencing the entire Labrador Sea realm (cf. Fagel et al., 2004). Our radiogenic isotope data highlight that these overall climatologically and oceanographic shifts not only influence local sedimentation patterns but can be identified on a small and local scale.

3.6. Conclusions

The combined record of radiogenic Sr, Nd and Pb isotope composition of gravity core GeoB19905-1 retrieved from Nuuk Trough identifies systematic changes in siliciclastic detrital sediment provenance discharged onto the west Greenland shelf throughout the Holocene. The overall siliciclastic detrital sediment composition is dominated by input from the local Archean Block (AB), with additional but minor contribution from the distal Ketilidian Mobile Belt (KMB). Shifts in isotopic composition follow continuous trends and coincide with the transitions between early, mid and late Holocene and are hence connected to major climatological changes. A slight decrease in distal KMB sources, transported from southernmost Greenland via the West Greenland Current (WGC) can be noted at the beginning of the mid Holocene. We attribute this shift to an increase of meltwater discharge during the prevailing Holocene Thermal Maximum and a decrease in speed of the WGC as recently observed by Weiser et al. (2021). With the transition into the late Holocene and Neoglacial the detrital sediment composition shifts towards increased local input and further decreased distal input. This shift is more pronounced and abrupt than the aforementioned. It is recorded by a distinct shift towards unradiogenic Nd isotopic composition and supported by the Sr and Pb isotopic composition becoming more radiogenic. The most likely cause of this late Holocene detrital provenance shift is the widely recorded Neoglacial ice advance and the concomitant

enhanced local erosion. Additionally, a continuous decrease in WGC speed and a speed minimum after 2 ka BP (Weiser et al., 2021), further reduced the amount of distal transported detrital sediment sources (KMB).

We hereby identify local erosion and meltwater discharge as the main transport pathway for detrital sediments onto the west Greenland shelf during the Holocene, especially during the late Holocene. Material transported from distal sources via coastal currents seems to play a subordinate role.

Slight changes in sediment mineralogical composition, mirroring the local geology, can be detected with the transition into the Neoglacial and support the conclusion of enhanced local detrital sediment sources. Furthermore, the sediment mineralogy data corroborate the provenance implications drawn from radiogenic isotope records by ruling out major influences through mineralogical control.

This study documents the potential of radiogenic isotopes as tracers for detrital provenance changes linked to ice-sheet dynamics along the southwestern Greenland shelf. The combination of multiple isotope systems (Sr, Nd, Pb) enabled the clear identification of the Archean Block as the main source of siliciclastic detrital sediments into Nuuk Trough.

3.7. Acknowledgements

We would like to thank the captain, crew members and science party on board RV Maria S. Merian during expedition MSM44 for retrieving the sample material included in this study.

We would further like to thank Michel Preda from Geotop-UQÁM. We are especially grateful to him for performing the X-ray diffraction analysis as well as his support, time and discussion regarding the corresponding data and theory.

This project was supported by the Deutsche Forschungsgemeinschaft (DFG) through the International Research Training Group "Processes and impacts of climate change in the North Atlantic Ocean and the Canadian Arctic" (IRTG 1904 ArcTrain).

3.8. References

Andresen, C. S., Straneo, F., Ribergaard, M. H., Bjørk, A. A., Andersen, T. J., Kuijpers, A., … Ahlstrøm, A. P. (2012). Rapid response of Helheim Glacier in Greenland to climate variability over the past century. Nature Geoscience, 5(1), 37–41. https://doi.org/10.1038/ngeo1349

Axford, Y., Losee, S., Briner, J. P., Francis, D. R., Langdon, P. G., & Walker, I. R. (2013). Holocene temperature history at the western Greenland Ice Sheet margin reconstructed from lake sediments. Quaternary Science Reviews, 59, 87–100. https://doi.org/10.1016/j.quascirev.2012.10.024

Benson, L., Barber, D., Andrews, J. T., Taylor, H., & Lamothe, P. (2003). Rare-earth elements and Nd and Pb isotopes as source indicators for Labrador Sea clay-size sediments during Heinrich event 2. Quaternary Science Reviews, 22(8–9), 881–889. https://doi.org/10.1016/S0277-3791(03)00011-8

Bjørk, A. A., Kjær, K. H., Korsgaard, N. J., Khan, S. A., Kjeldsen, K. K., Andresen, C. S., … Funder, S. (2012). An aerial view of 80 years of climate-related glacier fluctuations in southeast Greenland. Nature Geoscience, 5(6), 427–432. https://doi.org/10.1038/ngeo1481

Blaauw, M., & Christen, J. A. (2011). Flexible paleoclimate age-depth models using an autoregressive gamma process. Bayesian Analysis, 6(3), 457–474. https://doi.org/10.1214/11-BA618

Buch, E. (2002). Present oceanographic conditions in Greenland Waters. Danish Meteorological Institute, Scientific report.

Castelao, R. M., Luo, H., Oliver, H., Rennermalm, A. K., Tedesco, M., Bracco, A., … Medeiros, P. M. (2019). Controls on the Transport of Meltwater From the Southern Greenland Ice Sheet in the Labrador Sea. Journal of Geophysical Research: Oceans, 124(6), 3551–3560. https://doi.org/10.1029/2019JC015159

Castro de la Guardia, L., Hu, X., & Myers, P. G. (2015). Greenland Ice Sheet melt increases Baffin Bay heat content on the west Greenland shelf. Geophysical Research Letters, https://doi.org/10.1038/nature05320

Colville, E. J., Carlson, A. E., Beard, B. L., Hatfield, R. G., Stoner, J. S., Reyes, A. V, & Ullman, D. J. (2011). Sr-Nd-Pb isotope evidence for ice-sheet presence on southern Greenland during the Last Interglacial. Science, 333(6042), 620–623. https://doi.org/10.1126/science.1204673

Dawes, P. R. (2009). The bedrock geology under the Inland Ice: the next major challenge for Greenland mapping. Geological Survey of Denmark and Greenland Bulletin, 17, 57–60.

De Vernal, A., & Hillaire-Marcel, C. (2000). Sea-ice cover, sea-surface salinity and halo-/thermocline structure of the northwest North Atlantic: Modern versus full glacial conditions. Quaternary Science Reviews, 19(1–5), 65–85. https://doi.org/10.1016/S0277-3791(99)00055-4

Deniel, C., & Pin, C. (2001). Single-stage method for the simultaneous isolation of lead and strontium from silicate samples for isotopic measurements. Analytica Chimica Acta, 426(1), 95–103. https://doi.org/10.1016/S0003-2670(00)01185-5

Dorschel, B., Afanasyeva, V., Bender, M., Dreutter, S., Eisermann, H., Gebhardt, A. C., … Wangner, D. J. (2015). Past Greenland Ice Sheet dynamics, Palaeoceanography and Plankton Ecology in the Northeast Baffin Bay Cruise No. MSM44 30. MARIA S. MERIAN-Berichte, 148.

Eisenhauer, A., Meyer, H., Rachold, V., Tütken, T., Wiegand, B., Hansen, B. T., … Kassens, H. (1999). Grain size separation and sediment mixing in Arctic Ocean sediments: Evidence from the strontium isotope systematic. Chemical Geology, 158(3–4), 173–188. https://doi.org/10.1016/S0009-2541(99)00026-1

Fagel, N., Hillaire-Marcel, C., Humblet, M., Brasseur, R., Weis, D., & Stevenson, R. (2004). Nd and Pb isotope signatures of the clay-size fraction of Labrador Sea sediments during the Holocene: Implications for the inception of the modern deep circulation pattern. Paleoceanography, 19(3). https://doi.org/10.1029/2003PA000993

Fagel, N., & Mattielli, N. (2011). Holocene evolution of deep circulation in the northern North Atlantic traced by Sm, Nd and Pb isotopes and bulk sediment mineralogy. Paleoceanography, 26(4), 1–15. https://doi.org/10.1029/2011PA002168

Fagel, N., Not, C., Gueibe, J., Mattielli, N., & Bazhenova, E. (2014). Late Quaternary evolution of sediment provenances in the Central Arctic Ocean: Mineral assemblage, trace element composition and Nd and Pb isotope fingerprints of detrital fraction from the Northern Mendeleev Ridge. Quaternary Science Reviews, 92, 140–154. https://doi.org/10.1016/j.quascirev.2013.12.011

Fagel, N, Innocent, C., Gariepy, C., & Hillaire-Marcel, C. (2002). Sources of Labrador Sea sediments since the last glacial maximum inferred from Nd-Pb isotopes. Geochemistry, Geophysics, Geosystems, 66(14), 2569–2581.

Fagel, Nathalie, & Hillaire-marcel, C. (2006). Glacial / interglacial instabilities of the Western Boundary Under Current during the last 365 kyr from Sm / Nd ratios of the sedimentary clay-size fractions at ODP site 646 (Labrador Sea). Marine Geology, 232, 87–99. https://doi.org/10.1016/j.margeo.2006.08.006

Farmer, G. L., Barber, D., & Andrews, J. (2003). Provenance of Late Quaternary ice-proximal sediments in the North Atlantic : Nd , Sr and Pb isotopic evidence. Earth and Planetary

Science Letters, 209, 227–243. https://doi.org/10.1016/S0012-821X(03)00068-2
Filippova, A., Frank, M., Kienast, M., Rickli, J., Hathorne, E., Yashayaev, I. M., & Pahnke, K. (2017). Water mass circulation and weathering inputs in the Labrador Sea based on coupled Hf–Nd isotope compositions and rare earth element distributions. Geochimica et Cosmochimica Acta, 199, 164–184. https://doi.org/10.1016/j.gca.2016.11.024
Frank, M. (2002). Radiogenic isotopes: Tracers of past ocean circulation and erosional input. Reviews of Geophysics, 40(1), 1001. https://doi.org/10.1029/2000RG000094
Fratantoni, P. S., & Pickart, R. S. (2007). The western North Atlantic shelfbreak current system in summer. Journal of Physical Oceanography, 37(10), 2509–2533. https://doi.org/10.1175/JPO3123.1
Fredskild, B., 1973. Studies in the vegetational history of Greenland. Meddelelser om Grönland 198, 1–245
Grosfeld, K.; Treffeisen, R.; Asseng, J.; Bartsch, A.; Bräuer, B.; Fritzsch, B.; Gerdes, R.; Hendricks, S.; Hiller, W.; Heygster, G.; Krumpen, T.; Lemke, P.; Melsheimer, C.; Nicolaus, M.; Ricker, R. and Weigelt, M. (2016), Online sea-ice knowledge and data platform <www.meereisportal.de>, Polarforschung, Bremerhaven, Alfred Wegener Institute for Polar and Marine Research & German Society of Polar Research, 85 (2), 143-155, doi:10.2312/polfor.2016.011.
Gutjahr, M., Frank, M., Stirling, C. H., Klemm, V., van de Flierdt, T., & Halliday, A. N. (2007). Reliable extraction of a deepwater trace metal isotope signal from Fe-Mn oxyhydroxide coatings of marine sediments. Chemical Geology, (242), 351–370. https://doi.org/10.1016/j.chemgeo.2007.03.021
Haley, B. A., Frank, M., Spielhagen, R. F., & Fietzke, J. (2008). Radiogenic isotope record of Arctic Ocean circulation and weathering inputs of the past 15 million years. Paleoceanography. https://doi.org/10.1029/2007PA001486
Hanna, E., Huybrechts, P., Steffen, K., Cappelen, J., Huff, R., Shuman, C., … Griffiths, M. (2008). Increased runoff from melt from the Greenland Ice Sheet: A response to global warming. Journal of Climate, 21(2), 331–341. https://doi.org/10.1175/2007JCLI1964.1
Harig, C., & Simons, F. J. (2012). Mapping Greenland's mass loss in space and time. Proceedings of the National Academy of Sciences of the United States of America, 109(49), 19934–19937. https://doi.org/10.1073/pnas.1206785109
Harig, C., & Simons, F. J. (2016). Ice mass loss in Greenland, the Gulf of Alaska, and the Canadian Archipelago: Seasonal cycles and decadal trends. Geophysical Research Letters, 43(7), 3150–3159. https://doi.org/10.1002/2016GL067759
Henderson, G. M., Martel, D. J., O'Nions, R. K., & Shackleton, N. J. (1994). Evolution of seawater 87Sr/86Sr over the last 400 ka: the absence of glacial/interglacial cycles. Earth and Planetary Science Letters, 128, 643–651.
Innocent, C., Fagel, N., & Hillaire-Marcel, C. (2000). Sm-Nd isotope systematics in deep-sea sediments: Clay-size versus coarser fractions. Marine Geology, 168(1–4), 79–87. https://doi.org/10.1016/S0025-3227(00)00052-9
Jacob, T., Wahr, J., Pfeffer, W. T., & Swenson, S. (2012). Recent contributions of glaciers and ice caps to sea level rise. Nature, 482(7386), 514–518. https://doi.org/10.1038/nature10847
Jacobsen, S. B., & Wasserburg, G. J. (1980). Sm-Nd Isotopic Evolution of Chondrites. Earth and Planetary Science Letters, 50, 139–155.
Kaplan, M. R., Wolfe, A. P., & Miller, G. H. (2002). Holocene Environmental Variability in Southern Greenland Inferred from Lake Sediments. Quaternary Research, 58(2), 149–159. https://doi.org/10.1006/qres.2002.2352
Kaufman, D. S., Ager, T. A., Anderson, N. J., Anderson, P. M., Andrews, J. T., Bartlein, P. J., … Wolfe, B. B. (2004). Holocene thermal maximum in the western Arctic (0-180°W). Quaternary Science Reviews, 23(5–6), 529–560. https://doi.org/10.1016/j.quascirev.2003.09.007
Kelly, M., 1980. The status of the neoglacial in western Greenland. Rapport Grönlands Geologiske Unders^gelse 64, 1–26.

Knutz, P. C., Sicre, M. A., Ebbesen, H., Christiansen, S., & Kuijpers, A. (2011). Multiple-stage deglacial retreat of the southern Greenland Ice Sheet linked with Irminger Current warm water transport. Paleoceanography, 26(3), 1–18. https://doi.org/10.1029/2010PA002053

Kolling, H. M., Stein, R., Fahl, K., Perner, K., & Moros, M. (2018). New insights into sea ice changes over the past 2 . 2 kyr in Disko Bugt , West Greenland. Arktos, 4(11). https://doi.org/10.1007/s41063-018-0045-z

Lang Farmer, G., Barber, D., & Andrews, J. (2003). Provenance of Late Quaternary ice-proximal sediments in the North Atlantic: Nd, Sr and Pb isotopic evidence. Earth and Planetary Science Letters, 209(1–2), 227–243. https://doi.org/10.1016/S0012-821X(03)00068-2

Langner, M., & Mulitza, S. (2019). Technical note: PaleoDataView - A software toolbox for the collection, homogenization and visualization of marine proxy data. Climate of the Past, 15(6), 2067–2072. https://doi.org/10.5194/cp-15-2067-2019

Larsen, N. K., Funder, S., Kjær, K. H., Kjeldsen, K. K., Knudsen, M. F., & Linge, H. (2014). Rapid early Holocene ice retreat in West Greenland. Quaternary Science Reviews, 92, 310–323. https://doi.org/10.1016/j.quascirev.2013.05.027

Larsen, N. K., Kjær, K. H., Lecavalier, B., Bjørk, A. A., Colding, S., Huybrechts, P., … Olsen, J. (2015). The response of the southern Greenland ice sheet to the Holocene thermal maximum. Geology, 43(4), 291–294. https://doi.org/10.1130/G36476.1

Larsen, N. K., Kjær, K. H., Olsen, J., Funder, S., Kjeldsen, K. K., & Nørgaard-Pedersen, N. (2011). Restricted impact of Holocene climate variations on the southern Greenland Ice Sheet. Quaternary Science Reviews, 30(21–22), 3171–3180. https://doi.org/10.1016/j.quascirev.2011.07.022

Larsen, N. K., Strunk, A., Levy, L. B., Olsen, J., Bjørk, A., Lauridsen, T. L., … Davidson, T. A. (2017). Strong altitudinal control on the response of local glaciers to Holocene climate change in southwest Greenland. Quaternary Science Reviews, 168, 69–78. https://doi.org/10.1016/j.quascirev.2017.05.008

Lecavalier, B. S., Milne, G. A., Simpson, M. J. R., Wake, L., Huybrechts, P., Tarasov, L., … Larsen, N. K. (2014). A model of Greenland ice sheet deglaciation constrained by observations of relative sea level and ice extent. Quaternary Science Reviews, 102, 54–84. https://doi.org/10.1016/j.quascirev.2014.07.018

Levy, L. B., Larsen, N. K., Davidson, T. A., Strunk, A., Olsen, J., & Jeppesen, E. (2017). Contrasting evidence of Holocene ice margin retreat, south-western Greenland. Journal of Quaternary Science, 32(5), 604–616. https://doi.org/10.1002/jqs.2957

Levy, B, Kelly, M. A., Applegate, P. A., Howley, J. A., Virginia, R. A., Levy, L. B., … Howley, J. A. (2018). Middle to late Holocene chronology of the western margin of the Greenland Ice Sheet : A comparison with Holocene temperature and precipitation records. Arctic, Antarctic, and Alpine Research, 50(1), 1–12. https://doi.org/10.1080/15230430.2017.1414477

Lochte, A. A., Repschläger, J., Seidenkrantz, M. S., Kienast, M., Blanz, T., & Schneider, R. R. (2019). Holocene water mass changes in the Labrador Current. Holocene, 29(4), 676–690. https://doi.org/10.1177/0959683618824752

Long, A. J., Woodroffe, S. A., Dawson, S., Roberts, D. H., & Bryant, C. L. (2009). Late Holocene relative sea level rise and the Neoglacial history of the Greenland ice sheet. Journal of Quaternary Science, 24(4), 345–359. https://doi.org/10.1002/jqs

Luo, H., Castelao, R. M., Rennermalm, A. K., Tedesco, M., Bracco, A., Yager, P. L., & Mote, T. L. (2016). Oceanic transport of surface meltwater from the southern Greenland ice sheet. Nature Geoscience, 9(7), 528–532. https://doi.org/10.1038/ngeo2708

Maccali, J., Hillaire-Marcel, C., Carignan, J., & Reisberg, L. C. (2013). Geochemical signatures of sediments documenting Arctic sea-ice and water mass export through Fram Strait since the Last Glacial Maximum. Quaternary Science Reviews, 64, 136–151. https://doi.org/10.1016/j.quascirev.2012.10.029

Maccali, J., Hillaire-Marcel, C., & Not, C. (2018). Radiogenic isotope (Nd, Pb, Sr) signatures of

surface and sea ice-transported sediments from the Arctic Ocean under the present interglacial conditions. Polar Research, 37(1), 1–13. https://doi.org/10.1080/17518369.2018.1442982
Mao, L., Piper, D. J. W., Saint-Ange, F., Andrews, J. T., & Kienast, M. (2014). Provenance of sediment in the Labrador Current: A record of hinterland glaciation over the past 125 ka. Journal of Quaternary Science, 29(7), 650–660. https://doi.org/10.1002/jqs.2736
McCave, I. N., & Andrews, J. T. (2019a). Distinguishing current effects in sediments delivered to the ocean by ice. I. Principles, methods and examples. Quaternary Science Reviews, 212, 92–107. https://doi.org/10.1016/j.quascirev.2019.03.031
McCave, I. N., & Andrews, J. T. (2019b). Distinguishing current effects in sediments delivered to the ocean by ice. II. Glacial to Holocene changes in high latitude North Atlantic upper ocean flows. Quaternary Science Reviews, 223, 105902. https://doi.org/10.1016/j.quascirev.2019.105902
McFarlin, J. M., Axford, Y., Osburn, M. R., Kelly, M. A., Osterberg, E. C., & Farnsworth, L. B. (2018). Pronounced summer warming in northwest Greenland during the Holocene and Last Interglacial. Proceedings of the National Academy of Sciences of the United States of America, 115(25), 6357–6362. https://doi.org/10.1073/pnas.1720420115
McKay, N. P., Kaufman, D. S., Routson, C. C., Erb, M. P., & Zander, P. D. (2018). The Onset and Rate of Holocene Neoglacial Cooling in the Arctic. Geophysical Research Letters, 45(22), 12,487-12,496. https://doi.org/10.1029/2018GL079773
Møller, H. S., Jensen, K. G., Kuijpers, A., Aagaard-Sørensen, S., Seidenkrantz, M., Prins, M., … Mikkelsen, N. (2006). Late-Holocene environment and climatic changes in Ameralik Fjord , southwest Greenland : evidence from the sedimentary record. The Holocene, 16(5), 685–695. https://doi.org/10.1191/0959683606hl963rp
Moore, D. M., Reynolds, R. C. Jr. (1997). X-Ray Diffraction and the Identification and Analysis of Clay Minerals (2nd edition), Oxford University Press, New York
Moros, M., Jensen, K. G., & Kuijpers, A. (2006). Mid- to late-Holocene hydrological and climatic variability in Disko Bugt, central West Greenland. The Holocene, 16(3), 357–367.
Mortensen, J., Lennert, K., Bendtsen, J., & Rysgaard, S. (2011). Heat sources for glacial melt in a sub-Arctic fjord (Godthåbsfjord) in contact with the Greenland Ice Sheet. Journal of Geophysical Research: Oceans, 116(1), 1–13. https://doi.org/10.1029/2010JC006528
Myers, P. G., Donnelly, C., & Ribergaard, M. H. (2009). Structure and variability of the West Greenland Current in Summer derived from 6 repeat standard sections. Progress in Oceanography, 80(1–2), 93–112. https://doi.org/10.1016/j.pocean.2008.12.003
Nutman, A. P., Bennett, V. C., Friend, C. R. L., & Chivas, A. R. (2016). The isua supracrustal belt of the North Atlantic Craton (Greenland): Spotlight on sedimentary systems with the oldest preserved sedimentary structures (w3.7, w3.75, and w3.8 Ga). Sediment Provenance: Influences on Compositional Change from Source to Sink, 563–591. https://doi.org/10.1016/B978-0-12-803386-9.00020-4
Ouellet-Bernier, M.-M., de Vernal, A., Hillaire-Marcel, C., & Moros, M. (2014). Paleoceanographic changes in the Disko Bugt area, West Greenland, during the Holocene. The Holocene, 24(11), 1573–1583. https://doi.org/10.1177/0959683614544060
Pedersen, M., Weng, W. L., Keulen, N., & Kokfelt, T. F. (2013). A new seamless digital 1:500 000 scale geological map of Greenland. Geological Survey of Denmark and Greenland Bulletin, (28), 65–68. https://doi.org/10.34194/geusb.v28.4727
Pin, C., Briot, D., Bassin, C., & Poitrasson, F. (1994). Concomitant separation of strontium and samarium-neodymium for isotopic analysis in silicate samples, based on specific extraction chromatography. Analytica Chimica Acta, 298(2), 209–217. https://doi.org/10.1016/0003-2670(94)00274-6
Reimer, P. J., Edouard Bard, B., Alex Bayliss, B., Warren Beck, B. J., Paul Blackwell, B. G., & Christopher Bronk Ramsey, B. (2013). Intcal13 and Marine13 Radiocarbon Age Calibration Curves 0–50,000 Years Cal Bp. Radiocarbon, 55(4), 1869–1887. https://doi.org/10.1017/S0033822200048864

Reyes, A. V, Carlson, A. E., Beard, B. L., Hatfield, R. G., Stoner, J. S., Winsor, K., … Ullman, D. J. (2014). South Greenland ice-sheet collapse during Marine Isotope Stage 11. Nature, 510(7506), 525–528. https://doi.org/10.1038/nature13456

Rignot, E., Velicogna, I., Van Den Broeke, M. R., Monaghan, A., & Lenaerts, J. (2011). Acceleration of the contribution of the Greenland and Antarctic ice sheets to sea level rise. Geophysical Research Letters, 38(5), 1–5. https://doi.org/10.1029/2011GL046583

Saini, J., Stein R., Fahl K., Weiser J., Hebbeln D., Madaj L. (submitted). Holocene variability in sea ice and primary productivity in the eastern Baffin Bay - Labrador Sea - A North-South transect study. Boreas.

Schweinsberg, A. D., Briner, J. P., Miller, G. H., Bennike, O., & Thomas, E. K. (2017). Local glaciation in West Greenland linked to North Atlantic ocean circulation during the Holocene. Geology, 45(3), 195–198. https://doi.org/10.1130/G38114.1

Seidenkrantz, M. S., Aagaard-Sørensen, S., Sulsbrück, H., Kuijpers, A., Jensen, K. G., & Kunzendorf, H. (2007). Hydrography and climate of the last 4400 years in a SW Greenland fjord: Implications for Labrador Sea palaeoceanography. The Holocene, 17(3), 387–401. https://doi.org/10.1177/0959683607075840

Solomina, O. N., Bradley, R. S., Hodgson, D. A., Ivy-Ochs, S., Jomelli, V., Mackintosh, A. N., … Young, N. E. (2015). Holocene glacier fluctuations. Quaternary Science Reviews, 111, 9–34. https://doi.org/10.1016/j.quascirev.2014.11.018

Stacey, J. S., & Kramers, J. D. (1975). APPROXIMATION OF TERRESTRIAL LEAD ISOTOPE EVOLUTION BY A TWO-STAGE MODEL. Earth and Planetary Science Letters, 26, 207–221.

Schlitzer, R. (2020). Ocean Data View, odv.awi.de, 2020.

Tang, C. C. L., Ross, C. K., Yao, T., Petrie, B., DeTracey, B. M., & Dunlap, E. (2004). The circulation, water masses and sea-ice of Baffin Bay. Progress in Oceanography, 63(4), 183–228. https://doi.org/10.1016/j.pocean.2004.09.005

Tarasov, L., & Peltier, W. R. (2003). Greenland glacial history, borehole constraints, and Eemian extent. Journal of Geophysical Research: Solid Earth, 108(B3), 1–20. https://doi.org/10.1029/2001jb001731

Weidick, A., Bennike, O., Citterio, M., & Nørgaard-pedersen, N. (2012). Neoglacial and historical glacier changes around Kangersuneq fjord in southern West Greenland. Geological Survey of Denmark and Greenland Bulletin, 27, 1–68.

Weiser, J., Titschack, J., McCave, I. N., Lochte, A. A., Saini, J., Stein, R., & Hebbeln, D. (2021). Atlantic water inflow to Labrador Sea and its interaction with ice sheet dynamics during the Holocene. Quaternary Science Reviews, 4545(4545), 4545–1. https://doi.org/10.1016/j.quascirev.2021.106833

Werner, K., Frank, M., Teschner, C., Müller, J., & Spielhagen, R. F. (2014). Neoglacial change in deep water exchange and increase of sea-ice transport through eastern Fram Strait: Evidence from radiogenic isotopes. Quaternary Science Reviews, 92, 190–207. https://doi.org/10.1016/j.quascirev.2013.06.015

White, L. F., Bailey, I., Foster, G. L., Allen, G., Kelley, S. P., Andrews, J. T., … Storey, C. D. (2016). Tracking the provenance of Greenland-sourced, Holocene aged, individual sand-sized ice-rafted debris using the Pb-isotope compositions of feldspars and 40Ar/39Ar ages of hornblendes. Earth and Planetary Science Letters, 433, 192–203. https://doi.org/10.1016/j.epsl.2015.10.054

Yashayaev, I. (2007). Hydrographic changes in the Labrador Sea, 1960–2005 [Prog. Oceanogr. 73 (2007) 242–276]. Progress in Oceanography, 75(4), 857–859. https://doi.org/10.1016/j.pocean.2007.09.001

CHAPTER FOUR

Manuscript two

Northwestern Greenland Ice Sheet Dynamics traced by radiogenic isotopes

Lina Madaj[1], Valeriia Kirillova[1], Friedrich Lucassen[1], Claude Hillaire-Marcel[2] and Simone A. Kasemann[1]

[1] MARUM—Center for Marine Environmental Sciences & Faculty of Geosciences, University of Bremen, Germany

[2] GEOTOP—Centre de recherche en géochimie et géodynamique, Université du Québec à Montréal, Canada

This manuscript is in preparation for submission to Climate of the Past

4. Northwestern Greenland Ice Sheet Dynamics traced by radiogenic isotopes

Abstract

The ongoing atmospheric warming and its impact on the planet's environment and climate system are gaining increasing attention throughout the past years. Glaciers and icecaps are especially sensible to these warming processes and reduction of land ice masses is favouring meltwater discharge into surrounding oceans. Meltwater contributions from the west Greenland Ice Sheet are adding to the freshwater budget of Baffin Bay and Labrador Sea, where deepwater formation takes place and can hence influence global ocean circulation and climate patterns. Predicting future changes and impacts of ice-sheet mass balance and meltwater discharge variations is not only essential for assessment of global ocean circulation and climate developments but also to predict future sea-level rise. Sedimentary records of past environmental changes are a key component when predicting future changes and contribute to improving climate models.

The west Greenland shelf hosts several meters of sediments archiving Holocene climate history, representing a sufficient analogue for future predictions based on the Holocene climate developments with atmospheric temperatures warmer than present-day temperatures. Here we present records of radiogenic isotopes (Sr, Nd, Pb) of the siliciclastic detrital sediment fraction along a transect of three sedimentary archives along the mid-west to northwest Greenland shelf. Based on their ability to fingerprint the isotopic signature of their corresponding source regions, radiogenic isotopes serve as tracers for detrital provenance changes and past ice-sheet dynamics.

The radiogenic isotope and mineralogical data indicate distinct regional differences between Upernavik Trough (midwest Greenland) and northern Melville Bay (northernmost Greenland) in detrital sediment composition as well as temporal variations. In both locations input of the local bedrock through erosion and meltwater discharge appear to be the main sources of detrital sediments delivered to the west Greenland shelf. While additional sources of detrital sediment delivery to the comparably sheltered region of northern Melville Bay play a secondary role throughout the Holocene, detrital sediment provenances in the Upernavik region indicate temporal differences caused by ice-sheet dynamics and oceanic surface current variations. A shift in radiogenic isotope composition is marking an increased contribution of detrital sediments delivered via a strengthened West Greenland Current during the transition from early to mid Holocene. This shift is followed by a clear signal of continuous basalt input from the Disko Bay region after the opening of Vaigat Strait around 6 ka BP, establishing the current coastal circulation pattern and sediment delivery regime.

4.1. Introduction

Baffin Bay is an important pathways of Arctic Ocean freshwater entering through Nares Strait and the Canadian Arctic Archipelago (CAA) and leaving through Davis Strait into the Labrador Sea and hence into the subpolar North Atlantic where deep water formation takes place. The Greenland Ice Sheet (GIS) is contributing an additional but not insignificant part of freshwater through meltwater discharge into Baffin Bay (Castro de la Guardia et al., 2015; Harig & Simons, 2016; McMillan et al., 2016). Variations in freshwater input into Baffin Bay and the Labrador Sea may have a significant influence on deep water formation and hence global ocean

circulation and climate patterns. The GIS has been retreating and discharging meltwater into Baffin Bay on varying rates throughout the entire Holocene in the progress of the deglaciation after the Last Glacial Maxium (LGM). With increasing rates of GIS melt in the past decades and an increasing long-term trend caused by anthropogenic global warming (Church et al., 2013; Harig & Simons, 2012, 2016; Jacob et al., 2012; Rignot et al., 2011), the improvement of climate models predicting these trends and their impacts on global climate and sea-level rise becomes essentially important. The GIS holds a potential of 7.42 ± 0.05 m to global sea-level rise (Morlighem et al., 2017). Modelling studies assessing past and future GIS development (Lecavalier et al., 2014; Tarasov & Peltier, 2003) have been found to yield discrepancies despite main similarities to geological records (Young & Briner, 2015) and may overestimate ice-sheet extents on a more local scale (L. B. Levy et al., 2017). A wide spatial range of actual data of past climatic changes is therefore an indispensable tool for improving those climate models. The Holocene represents the closest analogue to future climate scenarios as it covers a time period with atmospheric temperatures warmer than at present by an average of 1.6±0.8 (Kaufman et al., 2004; Young & Briner, 2015) and contains still intact geological records while earlier records are mainly overprinted by ice-sheet advances (Long et al., 2009; Weidick et al., 2012). The west Greenland shelf hosts several thick marine sediments of environmental archives deposited during the past twelve thousand years providing high-resolution environmental archives of past ice-sheet dynamics and meltwater discharge variations.

While a variety of studies has been conducted on past oceanographic and ice-sheet development in southern west Greenland (e.g. Kaplan et al., 2002; Larsen et al., 2015, 2017; Levy et al., 2017; Weiser et al., 2021) and the Disko Bay (e.g. Allan et al., 2018; Ouellet-Bernier et al., 2014; Perner et al., 2012; Seidenkrantz et al., 2013) and Uummannaq area (e.g. Philipps et al., 2018; Rignot et al., 2016; Sheldon et al., 2016), northern Baffin Bay, with exception of the North Water polynya (e.g. Levac et al, 2001), is still underrepresented in palaeoclimatologial research and only recently became more often subject to scientific studies. High-resolution swath-bathymetry based studies interpreting glacial landforms across the northwest Greenland shelf shed light on the deglaciation pattern of the northwestern GIS after the LGM and palaeo ice-stream and GIS drainage development prior to Holocene records (Freire et al., 2015; Slabon et al., 2018a, 2018b; Slabon et al., 2016). Recent studies based on Holocene sedimentary archives from the northwest Greenland shelf focus on past sea surface conditions and variations, especially within transition from the Deglacial to Postglacial, period based on microfossils and sea-ice biomarkers (Caron et al., 2019b; Hansen et al., 2020; Limoges et al., 2020; Saini et al., 2020), highlighting a clear impact of meltwater discharge from the GIS and ocean current variability on those sea-surface conditions (Caron et al., 2019b).

Detailed studies on the development of the northwestern GIS during the Holocene are comparably rare despite the fact that it has been identified as one of the most sensitive sectors (Freire et al., 2015) and currently drains around 27% into Melville Bay, northernmost Baffin Bay (Rignot & Kanagaratnam, 2006). Especially in Melville Bay reconstructions on marine sedimentary records might be of essential advantage, as the region only consists of a small fraction of ice-free land, which is limiting geological and land-based records (e.g. Young & Briner, 2015), additional to possible overprint of land-based records after ice-sheet re-advance. One of the most recent studies from the northwest Greenland shelf is indeed a provenance study identifying source regions of glacier and ice-stream dynamics based on elemental composition through X-ray fluorescence (XRF) (Giraudeau et al., 2020). High counts in source region specific minerals combined with principal component analysis were used to

distinguish the different detrital sources of material discharged by meltwater and erosion throughout the past 9,100 years delivered to Upernavik Trough. Furthermore, Caron et al. (2020) provided XRF data and X-ray diffraction data (XRD) in combination with the SedUnMixMC programme (Andrews & Eberl, 2012; Andrews et al., 2015) to reconstruct past provenance and transport pathways also in the Upernavik area as well as in northernmost Melville Bay. This study has been supported by previously conducted grains-size analysis on the same records (Caron et al., 2019a). However, these studies only form a first base in order to establish more detailed data availability and record past changes of the northwestern GIS margin. Our study is adding to this existing data by introducing reconstructions of Holocene provenance shifts based on radiogenic isotopes along a transect of three sedimentary archives from midwest to northernmost Greenland.

The radiogenic isotope composition within the siliciclastic detrital sediment fraction of marine deposits reflects the isotopic composition and age range of their corresponding source regions and hence radiogenic isotopes serve as reliable provenance tracers (e.g. Frank, 2002; Gutjahr et al., 2007). The discriminative geology of Greenland (Dawes, 2009a) provides the foundation of these provenance studies through visible temporal and spatial differences on this rather local scale (Colville et al., 2011; Reyes et al., 2014). In combination with the sediment mineralogical composition we aim to apply our radiogenic isotope records to investigate provenance shifts and associated variation in meltwater discharge and ice-sheet extent of the northwestern GIS as well as further transport pathways of detrital sediments such as oceanic currents and sea ice. This will provide additional and essential information on this sparsely investigated but highly sensible area of the western Greenland Ice Sheet and provide insights into its future development.

4.2. Regional Setting and Research Area

Baffin Bay is a mediterranean sea bordered by west Greenland, Baffin Island and the Canadian Arctic Archipelago encompassing roughly 690,000 km^2 (e.g. Simon, et al., 2014; Tang et al., 2004). At present Baffin Bay is characterised by a counter-clockwise surface current gyre consisting of the comparably warm and saline West Greenland Current (WGC) travelling along the West Greenland coast and merging at the northern tip of the bay with polar waters from the Arctic Ocean entering through Nares Strait and the Jones and Lancaster Sound of the CAA, forming the cold and fresh Baffin Island and Labrador Currents (Figure 4.1). The WGC originates from the East Greenland Current (EGC) transporting Arctic Ocean sourced waters along the east Greenland coast and a westwards flowing branch of the Irminger Current transporting Atlantic waters. Both currents merge at the southern tip of Greenland and enter Baffin Bay through Davis Strait (Fratantoni & Pickart, 2007; Myers et al., 2009). A large component of the WGC is turning westwards into Labrador Sea at 61°N, resulting in a notably slower current speed of the remaining portion (Cuny et al., 2002; Fratantoni & Pickart, 2007; Myers et al., 2009) that flows northwards, freshening on its way to northern Baffin Bay due to freshwater input through meltwater discharge along the west Greenland coast (Buch, 2002; Myers et al., 2009). The Arctic Ocean waters forming the Baffin Island Current mostly travel south and via Davis Strait into the Labrador Sea and the subpolar North Atlantic Ocean, making Baffin Bay an important pathway for these Arctic Ocean waters. A certain amount of these polar sourced waters have been noted to penetrate onto the northwest Greenland shelf (e.g. Hansen et al., 2020; Sheldon et al., 2016). Baffin Bay is seasonally ice-covered with sea ice forming from October onwards and growing continuously from northwest to southeast and becomes ice-free from August to September (Tang et al., 2004).

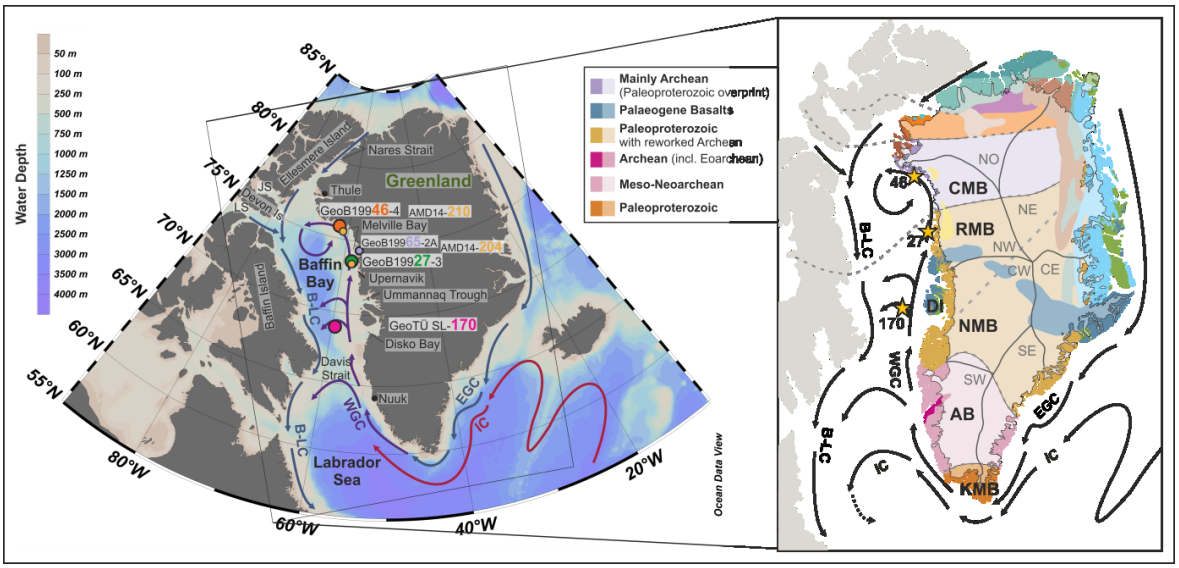

Figure 4.1: Overview map of research area, main ocean surface currents and core locations of this study and cores mentioned in the text (small yellow dots), EGC = East Greenland Current, WGC = West Greenland Current, B-LC = Baffin – Labrador Current, IC = Irminger Current, JS = Jones Sound, LS = Lancaster Sound, VS = Vaigat Strait. Map on the right summarises the main geological terrains of Greenland; lighter shaded areas indicate the current extent of the Greenland Ice Sheet; dashed grey line represents the border between NMB and RMB (Dahl-Jensen et al., 2003): KMB = Ketilidian Mobile Belt, AB = Archean Block, NMB = Nagssugtoqidian Mobile Belt, DI = Disko Island, RMB = Rinkian Mobile Belt, CMB = Committee-Melville Belt (map adapted from Dawes, 2009a); solid grey lines mark the present-day GIS drainage domains: SW = southwest, CW = central west, CE = central east, SE = southeast (White et al., 2016); yellow stars mark the location of the cores included in this study. Overview map created with Ocean Data View (Schlitzer, 2020).

The research area of this study is spanning from north of Disko Bay to northernmost Melville Bay, with the main focus being the wider Melville Bay area. Melville Bay is a heavily glaciated area with only a narrow fringe of ice-free island, peninsulas and nunataks between the open Baffin Bay and the GIS (Bennike, 2008; Briner et al., 2013). The wider Melville Bay is characterised by three main cross-shelf troughs which were occupied and eroded by marine-terminating ice streams during at least the last glacial period (Batchelor & Dowdeswell, 2014). The Melville Bay cross-shelf troughs can be divided into a southern, central and northern one and comprise an average width and length of 45-120 km and 170-320 km, respectively (Slabon et al., 2018b, 2018a, 2016; Søndergaard et al., 2020). Around 70 km south of Melville Bay Upernavik Trough, the aforementioned southern cross-shelf trough, forms the southern end of the main research area. The trough was shaped by the Upernavik Isstrøm, one of northwest Greenland's major outlet glaciers (Briner et al., 2013), currently draining around 2% of the GIS (Rignot & Kanagaratnam, 2006).

Greenland holds some of the oldest rocks on earth, with Archean rocks in southern and northern Greenland and Palaeoproterozoic rocks in midwest Greenland (e.g. Dawes, 2009a) (Figure 4.1). In west Greenland comparably young rocks can only be found in the Disko Bay area, which contains Paleaogene basalts and intrusions (e.g. Dawes, 2009a). The research area of this study, is characterised by the Paleaoproterozoic Rinkian Mobile Belt (RMB) containing mainly orthogneisses and metagreywackes of the Karrat Group between the Uummannaq area and southern Melville Bay (e.g. Connelly et al., 2006; Grocott & McCaffrey, 2017; Kalsbeek et al., 1998; and references therein) and the orthogneisses of the Neoarchean Committee-Melville Belt (Dawes, 2006). Due to its origin from an extension of the North Atlantic-Labrador Shelf Sea rift system (MacLean et al., 1990; Simon et al., 2014) the main geological units in Greenland

and Baffin Island mirror each other (Dawes, 2009b; Jackson & Berman, 2000; Le Pichon et al., 1977) and have been found to be chemically comparable (cf. Jackson & Berman, 2000).

4.2.1. Northern Greenland Ice Sheet History

Due to the close position of the GIS to the northwestern Greenland coastline with only a small fraction of ice-free land, land-based geological records such as radiocarbon and ^{10}Be exposure dates marking the complete deglaciation of Melville Bay are relatively sparse (Bennike, 2008; Young & Briner, 2015). During the LGM the entire shelf has been covered by the GIS which retreated towards the mid shelf until around the Younger Dryas and fully retreated to its current position before 8.4 BP in southern (Slabon et al., 2016) and before 9.5 ka BP in northern Melville Bay (Bennike, 2008; Caron et al., 2019a; Young & Briner, 2015). Despite its early retreat towards the current outline, high-resolution swath-bathymetry based studies revealed a slow retreat of the northern west Greenland ice-streams after the LGM (Slabon et al., 2016).

Based on radiocarbon ages and ^{10}Be exposure ages the GIS must have retreated from the shelf between 11.3±0.5 ka BP (Corbett et al., 2013), 9.9±0.1 ka BP (Briner et al., 2013) and 9.5 ka BP (Bennike, 2000) in the Upernavik region. This temporal evolution was confirmed by amino acid ratios (Briner et al., 2014) and ice-sheet modelling (Lecavalier et al., 2014). These modelling studies also show that after 9 ka BP the northwestern GIS margin mainly remained at its current position and did not experience larger-scale fluctuations as modelled and observed for the southern GIS margin (e.g. Larsen et al., 2015; Lecavalier et al., 2014). The WGC flowing along the west Greenland coast was established prior to 14 ka BP and most likely favoured the GIS retreat after the LGM by warm Atlantic water intrusion (Sheldon et al., 2016b).

4.3. Material and Methods

This study is based on three sedimentary archives collected along the west Greenland coast. Gravity cores GeoB19927-3 (73°35.26'N 58°05.66'W) and GeoB19946-4 (75°49.99'N 62°30.98'W) were collected during research cruise *MSM44* in 2015 (Dorschel et al., 2015c) and were raised from Upernavik Trough (water depth 932 m) and northern Melville Bay Trough (water depth 718 m), respectively. Gravity core GeoTÜ SL170 (68°58.15'N 59°23.58'W) was raised from the west Greenland slope (water depth 1078 m) slightly north of Disko Bay during research cruise *MSM09/2* in 2008 (Rhein et al., 2013). Additionally, surface sediment data from box core GeoB19965-2A (74°23.51'N 56°35.70'W, *MSM44*) was included as reference material for northwest Greenland sediment sources.

4.3.1. Core Description and Age Chronology

The age models of these cores are based on radiocarbon dating and have been described in detail in the corresponding publications. All have been constructed using the *Marine13*-calibration curve (Reimer et al., 2013) to convert the ages into calendar years followed by Bayesian age modelling using the BACON software package (Blaauw & Christen, 2011).

The age model of core GeoTÜ SL170 (recovery 683 cm) is based on Accelerator Mass Spectrometry radiocarbon dating of mixed planktonic and benthic foraminifera and mollusc fragments (Jackson et al., 2017). The complete record spans the past 18 ka and is based on 21 radiocarbon ages, here however, only the past 12 ka will be considered for comparison with the other two records included into this study. This upper part of the core consists of sandy mud with occasional dropstones. It has to be noted that due to carbonate shell availability within the record the youngest radiocarbon age dates to 10.2 ka BP and the remaining age

chronology had to be extended by interpolation assuming constant sedimentation rates (Jackson et al., 2017).

Core GeoB19927-3 (recovery 1147 cm) mainly consists of grey to olive hemipelagic clayey mud (Dorschel et al., 2015c) and covers the past 10 ka years (Saini et al., 2020). The age model is based on a combination of 12 radiocarbon dates and ^{210}Pb dating. Sedimentation rates range between 32 and 172 cm/ka with a mean sedimentation rate between 100-150 cm/ka, a decrease can be observed between 8 and 6 ka BP and around 3.1 ka BP as well as an overall decreasing trend towards the core top (Saini et al., 2020).

Core GeoB19946-4 (recovery 1372 cm) consists of olive grey silty clay with occasional fine sandy mud lenses and a thicker sandy mud layer towards the bottom of the core (Dorschel et al., 2015c). The age model covers the past 11 ka and was based on seven radiocarbon ages (J. Weiser, pers. comm.). The record displays decreasing sedimentation rates from around 100 cm/ka to 20 cm/ka towards the top of the core which was dated to ~1.8 ka BP, missing the youngest roughly 2 ka of the record. The sandy mud layer (679-1080 cm) representing the period between around 9 and 10.5 ka BP and the finer layer underneath were identified as a turbidite layer and mass wasting event due to significantly higher sedimentation rates around 380 cm/ka and will therefore be excluded from palaeoclimatological reconstruction. It has to be noted that this age model is preliminary and part of the PhD thesis by J. Weiser to be submitted within 2021.

4.3.2. Radiogenic Isotope Analysis

Sample preparation and measurements of radiogenic isotope ratios were performed in the Isotope Geochemistry Laboratory at MARUM—Centre for Marine Environmental Sciences, University of Bremen, Germany. The bulk sample has been used for analysis without separation for any specific grain-size to receive a general sediment transport signal, not biased by specific transport pathways, such as finer fraction generally used to reconstruct current induced sediment transport (e.g. Eisenhauer et al., 1999; Fagel et al., 2002; Maccali et al., 2013). Between 1 and 2 g of bulk sample were homogenised using a mortar, washed with ultrapure water (18.2 MΩ; Millipore) to remove pore water, decarbonised with a 40 % acetic acid solution (buffered to pH ~4 with 1M Na-acetate) and leached with hydroxylamine hydrochloride and 15 % acetic acid (buffered to pH ~4 with NaOH) to remove any possible sediment grain coatings (cf. Gutjahr et al., 2007). Following, stepwise hot-acid digestion with hydrofluoric acid (5:1, HF:HNO_3), Aqua Regia (3:1, 6M HCl:concentrated HNO_3), nitric acid (concentrated), hydrochloric acid (6M) and hydrogen peroxide was applied to 100 mg of the sample to receive the siliciclastic detrital sediment fraction and remove organic matter. The final sample was dissolved in nitric acid (2M) for radiogenic isotope separation. Radiogenic isotopes were received through column separation using TrisKem Sr.spec™ resin (method modified after Deniel & Pin, 2001), TRU.spec™ resin and LN.spec™ resin (method from Pin et al., 1994) for Sr and Pb isotopes, light rare earth elements and Nd isotope separation, respectively. Isotopic ratios were analysed on a Thermo Fisher Scientific Triton™ Plus multicollector thermal ionization mass spectrometer (TIMS) in either multidynamic (Sr) or static (Pb, Nd) multicollection mode. The following international reference materials were measured along with the samples in order to monitor measurement consistency: NIST SRM 987 (Sr), NIST SRM 981 (Pb) and JNdi-1 (Nd). Throughout the measurement period of 2.5 years, standard values varied within the range of published reference values measured on TIMS (GeoReM data base; query June 2020; http://georem.mpch-mainz.gwdg.de): ^{87}Sr/^{86}Sr:

0.710251 ±0.000013 ($2SD_{mean}$; n=8), 0.710249 ±0.000034 (GeoReM; $\pm 2SD_{mean}$; n=1528); $^{206}Pb/^{204}Pb$: 16.8981 ±0.0157 ($2SD_{mean}$; n=8), 16.9211 ±0.0413 (GeoReM; $\pm 2SD_{mean}$; n=254); $^{143}Nd/^{144}Nd$: 0.512100 ±0.000048 ($2SD_{mean}$; n=11), 0.512107 ±0.000026 (GeoReM; $\pm 2SD_{mean}$; n=339). A bulk uncertainty of 0.1% per atomic mass unit was assumed for Pb values to account for isotopic fractionation during the measuring process, which exclusively exceeds the measured uncertainty. Nd isotope ratios are displayed in εNd notation normalized to the ancient Chondritic Uniform Reservoir (CHUR) value of 0.512638 as defined by Jacobsen & Wasserburg (1980):

$$(\varepsilon_{Nd} = \left\{\left[\left(^{143}Nd/^{144}Nd\right)_{Sample}/\left(^{143}Nd/^{144}Nd\right)_{CHUR}\right] - 1\right\} * 10^4)$$

4.3.3 Mineralogical x-ray diffraction

Additional to radiogenic isotope measurements, XRD measurements were performed on 100 to 500 mg of the bulk sample of cores GeoB19927-3 and GeoB19946-4 at GEOTOP, Université du Québec à Montréal, Canada. All samples have been homogenised using a mortar and prepared for analysis using the 'back-side method' (Moore & Reynolds, 1997). Analysis has been conducted on a Siemens X-ray Diffraktometer D5000 in a range between 5° and 85° 2θ. Horizontal peak correction was done using the quartz peak. Peak intensity was corrected using halite and calcite peaks. After the first measurement samples have been washed to estimate the halite content, then decarbonised (0.1 M HCl) for calcite content estimation and as a final step clay minerals were oriented by adding water. Ethylene glycol saturation was used to identify smectites and heating the sample to 300°C was used to verify these smectites (cf. Moore & Reynolds, 1997).

4.4. Results and Interpretation

For better comparison and easier assessment of isotopic shifts connected to climatological changes the isotopic and mineralogical records were shaded by the extension of the three main Holocene climatological units, the Deglacial period, the Holocene Thermal Maximum (HTM) and the Neoglacial period. The timing of these units was defined by the regional varying extension of the HTM as summarised for the western Arctic by Kaufman et al. (2004).

4.4.1. GeoTÜ SL170 – Midwest Greenland Slope

The sedimentary record GeoTÜ SL170 collected from the midwest Greenland slope display some minor variations in isotopic composition throughout the Holocene (Figure 4.2). From ~12 ka BP to ~4.5 ka BP the $^{87}Sr/^{86}Sr$ isotopic composition follows a trend towards less radiogenic values ranging from 0.7245 to 0.7201, with two set-backs around 11.1 and 6.8 ka BP. After ~4.5 ka BP $^{87}Sr/^{86}Sr$ follow a more pronounced trend towards more radiogenic values, reaching 0.7270 at the top of the record (~0.9 ka BP). The ε_{Nd} isotopic composition shows comparably stable values around -28.5 in the lower part of the record, some distinct fluctuations from -24.8 to -28.0 between 9.6 and 5.0 ka BP and a continuous trend towards initial values around -27.9 towards the core top. The $^{206}Pb/^{204}Pb$ isotopic composition mainly records a continuous trend towards more radiogenic Pb, starting with 17.2 (~12.1 ka BP) and reaching 17.7 at the core tope with one small excursion around 6.8 ka BP ($^{206}Pb/^{204}Pb$: 17.3).

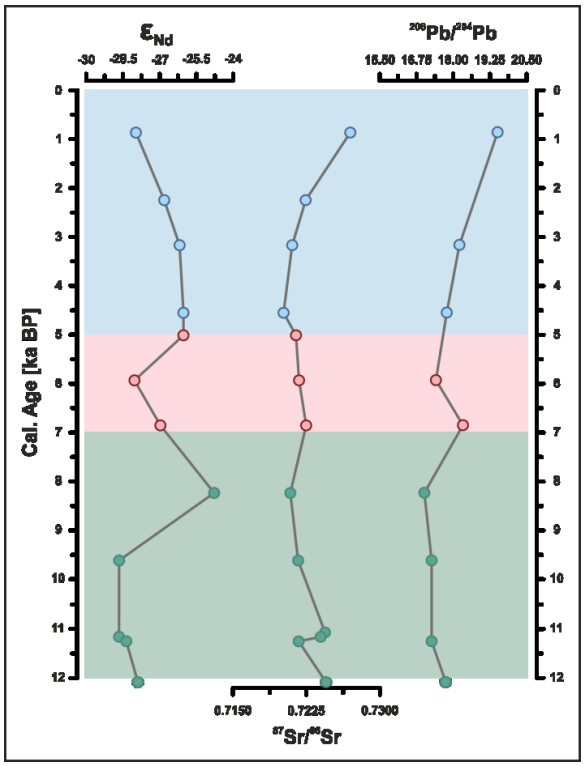

Figure 4.2: Radiogenic isotope records of siliciclastic detrital sediment fraction of gravity core GeoTÜ SL170. Analytical uncertainties are smaller than data points. Highlighted time intervals represent the main Holocene climate periods: Deglacial period (green), Holocene Thermal Maximum (red; as summarised by Kaufman et al., 2004) and the Neoglacial period (blue). The age model has been constructed by Jackson et al. (2017).

4.4.2. GeoB19927-3 - Upernavik Trough

The general trends of the isotopic record of gravity core GeoB19927-3 go towards less radiogenic $^{87}Sr/^{86}Sr$ and more radiogenic ε_{Nd} and $^{206}Pb/^{204}Pb$ values over time (Figure 4.3). Sr and Nd records start off with values of ~0.7667 ($^{87}Sr/^{86}Sr$) and ~-28.5 (ε_{Nd}), following a steep trend towards less radiogenic $^{87}Sr/^{86}Sr$ and more radiogenic ε_{Nd} values until ~8.4 ka BP, when the record displays a kink towards the initial values of the record. From there onwards the trend continues towards less radiogenic $^{87}Sr/^{86}Sr$ and more radiogenic ε_{Nd} until ~3 ka BP when both records seem to stabilise around values of 0.7439 and -24.35, respectively. Sr isotope ratios actually reveal a very slight trend towards more radiogenic values, Nd towards more unradiogenic values within this part of the record. Around 1.2 ka BP a peak towards more radiogenic ε_{Nd} can be identified; however, this peak is only based on one data point. $^{206}Pb/^{204}Pb$ signatures follow a slight trend towards more radiogenic values from the bottom ($^{206}Pb/^{204}Pb$: 18.2) to the top ($^{206}Pb/^{204}Pb$: 19.1) of the record. In the lower part of the record a small excursion towards more radiogenic values ($^{206}Pb/^{204}Pb$: 19.1) can be identified between 9.7 and 8.4 ka BP. The peak visible in the Nd isotopic record around 1.2 ka BP can also be identified in the Pb isotopic record, pointing towards more radiogenic values ($^{206}Pb/^{204}Pb$: 19.4).

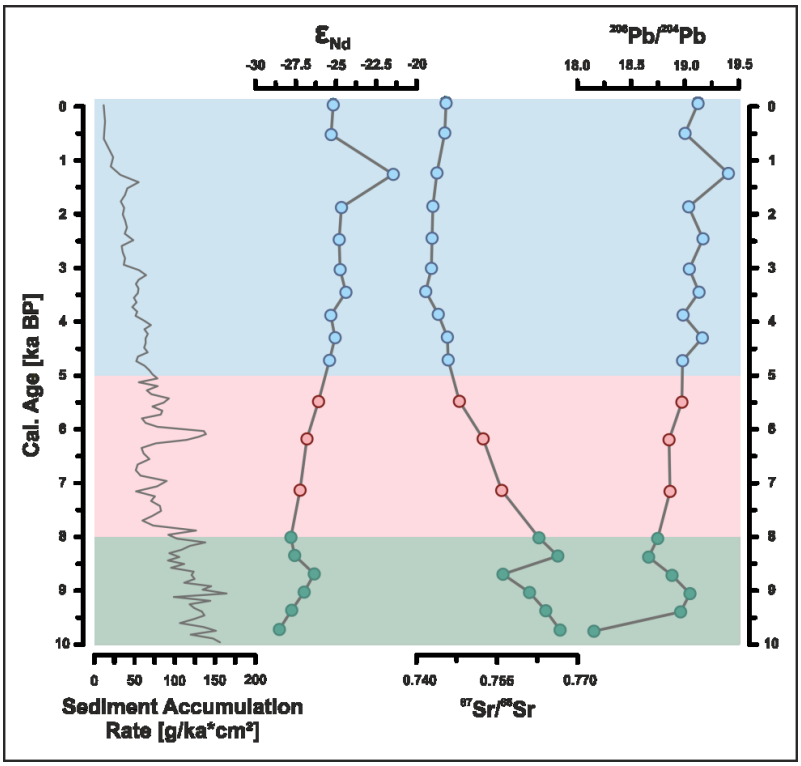

Figure 4.3: Radiogenic isotope records of siliciclastic detrital sediment fraction of gravity core GeoB19927-3. Analytical uncertainties are smaller than data points. Highlighted time intervals represent the main Holocene climate periods: Deglacial period (green), Holocene Thermal Maximum (red; as summarised by Kaufman et al., 2004) and the Neoglacial period (blue). Age model and sediment accumulation rate have been previously published by Saini et al. (2020).

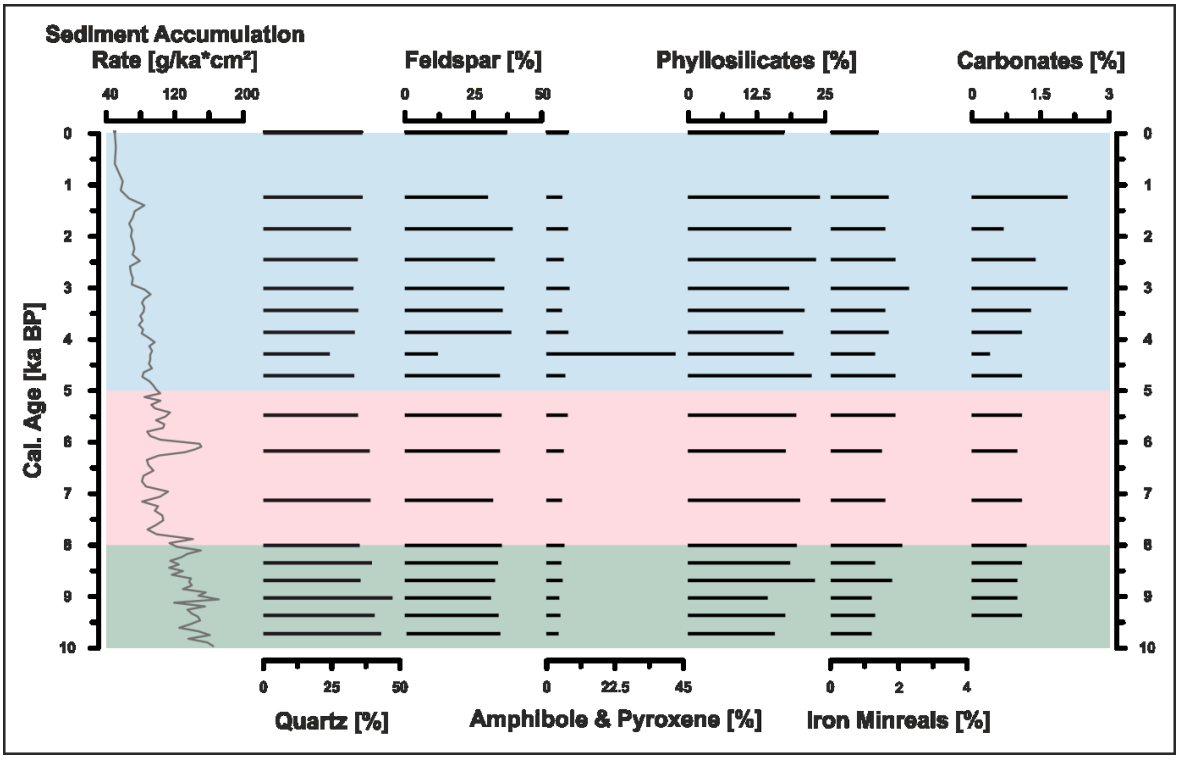

Figure 4.4: Mineralogical composition of gravity core GeoB19927-3. Highlighted time intervals represent the main Holocene climate periods: Deglacial period (green), Holocene Thermal Maximum (red; as summarised by Kaufman et al., 2004) and the Neoglacial period (blue). Age model and sediment accumulation rate have been previously published by Saini et al. (2020).

The mineralogical record of GeoB19927-3 shows little variability (Figure 4.4). The main components are quartz, feldspar (albite, microcline), phyllosilicates (clinochlore, biotite) and hornblende. Minor components are pyrite, augite, smectite, kaolinite and calicite (for details see chapter 2 and Table 8.7). The most pronounced difference can be identified around 4.2 ka BP where a significant peak in hornblende of 42% is visible differing from the average 4%. This time interval also shows the highest concentration in kaolinite and the lowest concentrations in quartz, albite and microcline. Any slight coinciding differences in other components might be simply caused by a mass balance effect. Carbonate content seems to be slightly higher during the late Holocene from around 3 ka BP onwards.

4.4.3. GeoB19946-4 – Northern Melville Bay

The northern Melville Bay record GeoB19946-4 (Figure 4.5) is disturbed by a mass wasting event in the lower part (~10.9 – 9.1 ka BP), which is characterised by an isotopic excursion of the least radiogenic $^{87}Sr/^{86}Sr$ (0.7284) and $^{206}Pb/^{204}Pb$ (16.2) values and some more radiogenic ε_{Nd} values (-33.2). The beginning and the end of this event are marked by similar isotopic values within all three isotopic systems. These values stay comparatively stable throughout the entire $^{87}Sr/^{86}Sr$ and $^{206}Pb/^{204}Pb$ record of around 0.7475 and 18.3, respectively.

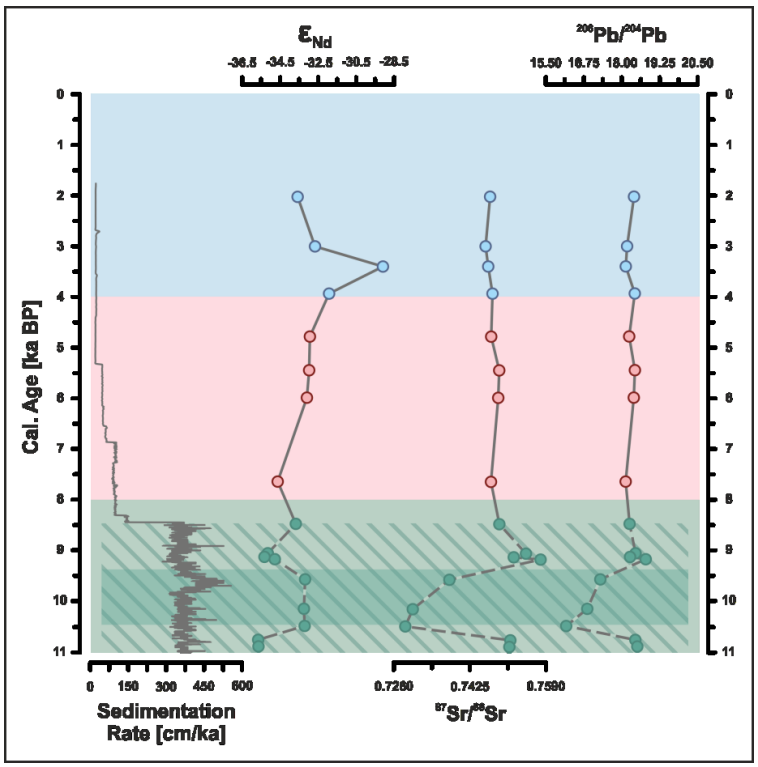

Figure 4.5: Radiogenic isotope records of siliciclastic detrital sediment fraction of gravity core GeoB19946-4. Analytical uncertainties are smaller than data points. Highlighted time intervals represent the main Holocene climate periods: Deglacial period (green), Holocene Thermal Maximum (red; as summarised by Kaufman et al., 2004) and the Neoglacial period (blue). Green shaded interval marks the mass wasting event in the bottom of the record. Age model and sedimentation rate were constructed by J. Weiser (pers. comm.).

The ε_{Nd} isotopic composition records a slight trend towards more radiogenic values, similar to those in the mass wasting interval, culminating in a pronounced peak around 3.4 ka BP (-29.1). Following, the ε_{Nd} isotopic composition develops towards less radiogenic values until the upper end of the record (-33.6, ~2.0 ka BP). The pronounced peak in ε_{Nd} values is exclusively visible within this record but not within the $^{87}Sr/^{86}Sr$ and $^{206}Pb/^{204}Pb$ isotopic record and only based upon one data point and therefore has to be considered with caution.

The main occurring minerals in the GeoB19946-4 record are the same as for GeoB19927-3: quartz, feldspar (albite, microcline), phyllosilicates (clinochlore, biotite) and hornblende. Minor components are augite, smectite, kaolinite, pyrite and ilmenite (for details see chapter 2 and Table 8.8). No carbonate occurrence was detected throughout the entire record. The quartz content seems to follow an increasing trend towards the late Holocene while the amphibole and pyroxene record seems to follow a decreasing trend. The phyllosilicate and iron mineral content display the highest concentrations during the early Holocene. However, these time intervals fall into the inception and termination of the mass wasting event and have to be interpreted with caution.

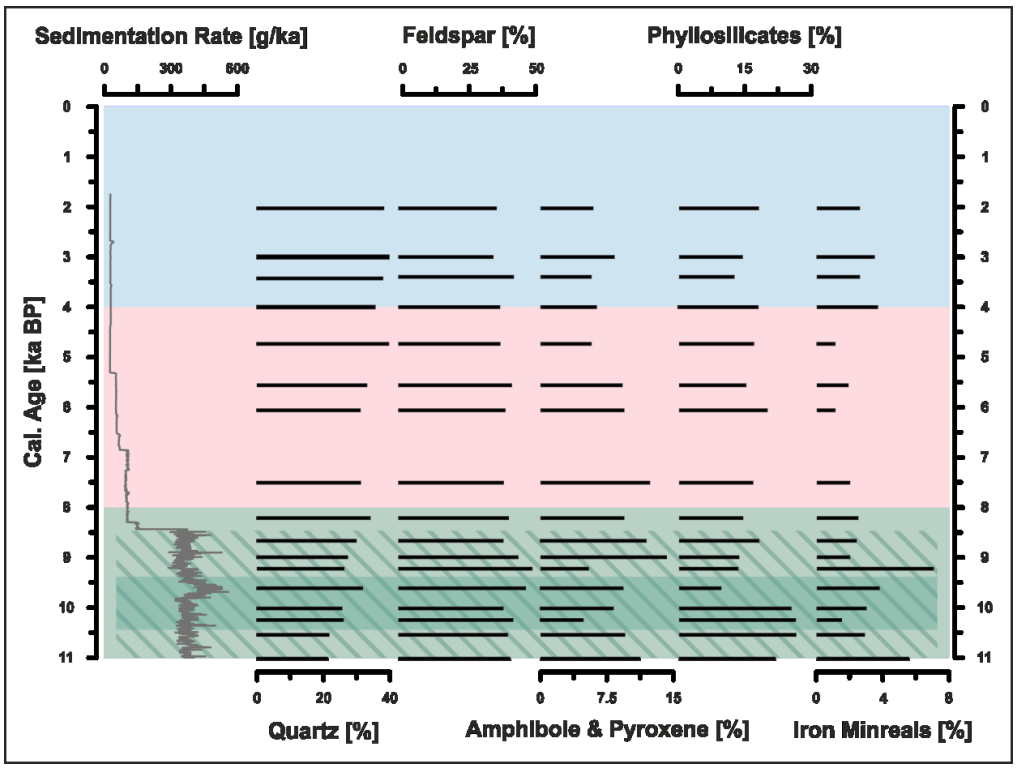

Figure 4.6: Mineralogical composition of gravity core GeoB19946-4. Highlighted time intervals represent the main Holocene climate periods: Deglacial period (green), Holocene Thermal Maximum (red; as summarised by Kaufman et al., 2004) and the Neoglacial period (blue). Green shaded interval marks the mass wasting event in the bottom of the record. Age model and sedimentation rate were constructed by J. Weiser (pers. comm.).

4.4.4. Detrital Sediment Provenance

To unravel detrital sediment composition and identify contributing sources, the isotopic records have to be put in context with background data of the possible source regions. Isotopic background data has been taken from literature and consist of rock, stream sediment and surface sediment data, depending on data availability (see Figure 4.1). While radiogenic isotope data availability for southern Greenland is sufficient due to similar provenance studies that included stream sediments for the purpose of establishing background data (Colville et al., 2011; Reyes et al., 2014), data availability in northern Greenland is sparse. To compensate for missing background data from the Melville Bay region, we additionally analysed surface sediment data from a northwest Greenland fjord to represent detrital sediment input from the Committee-Melville Belt (GeoB19965-2A, Figure 4.1), following the approach of Colville et al. (2011) who chose stream sediment data over rock data as those reflect the actual isotopic signatures discharged into Baffin Bay, while rock data tends to over-represent certain rock or mineral types. So-called provenance plots, cross plots of $^{87}Sr/^{86}Sr$ against ε_{Nd} as well as

$^{206}Pb/^{204}Pb$ against $^{207}Pb/^{204}Pb$, combining the isotopic records with reference data, reveal detrital sediment sources and their possible development over time (Figure 4.7). All three cores represent detrital sediments of mixed sources. GeoTÜ SL170 appears to be a mix of the southern Greenland Archean Block (AB) and the Nagssugtoqidian Mobile Belt (NMB). The detrital sediment composition of GeoB19927-3 reflects a mix of these AB and NMB sources as a southern endmember and the Rinkian Mobile Belt (RMB) as a local endmember. Over time the sediment provenance focus shifts towards a different proportion of these two endmembers. GeoB19946-4 appears to be a stable mix of the southern endmembers AB and NMB and the local Committee-Melville Belt (CMB). A slight temporal shift to a slightly higher contribution of the southern endmembers AB and NMB can be identified during the mid and late Holocene.

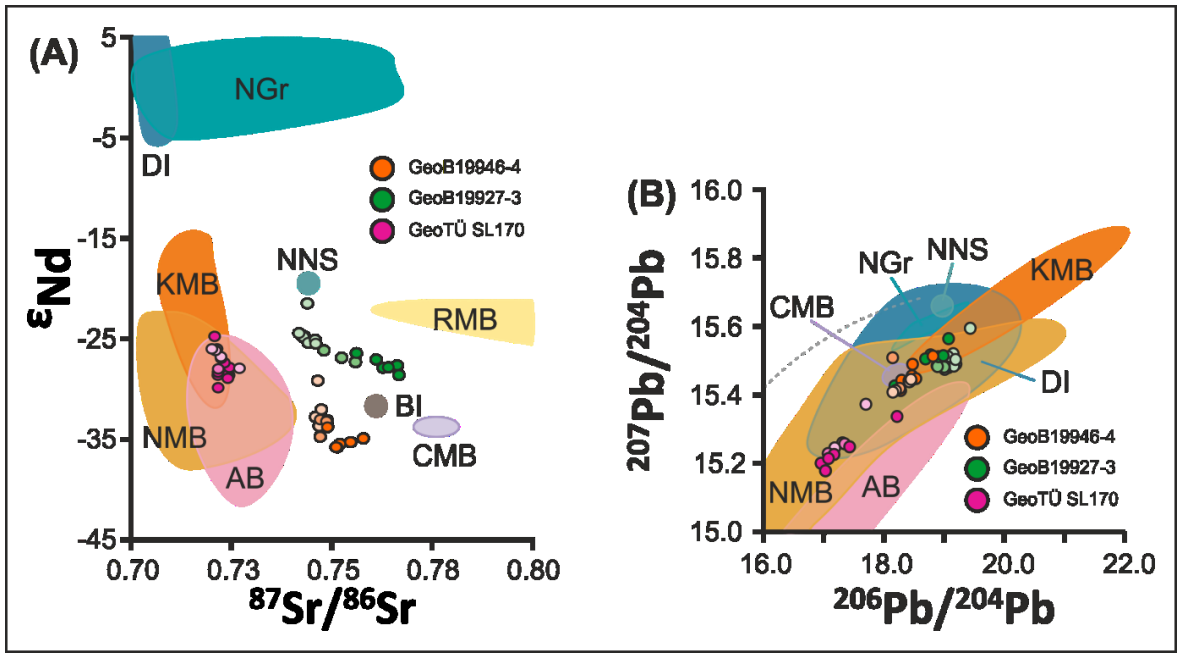

Figure 4.7: Radiogenic isotope composition of the siliciclastic detrital sediment fraction of gravity cores GeoTÜ SL170, GeoB19927-3 and GeoB19946-4 and isotopic ranges of the main Greenland geological terrains for $^{87}Sr/^{86}Sr$ versus ε_{Nd} (A) and $^{206}Pb/^{204}Pb$ versus $^{207}Pb/^{204}Pb$ (B). The colour shading within the core data represents the temporal evolution of Deglacial (dark), Holocene Thermal Maximum (medium) and Neoglacial period (light) as defined in Figure 4.2, Figure **4.3** and Figure **4.5**. Abbreviations and colours representing the main geological terrains of Greenland are the same as in Figure 4.1 with addition of: BI = Baffin Island, NNS = Northern Nares Strait, NGr = Northern Greenland. Background data for isotopic ranges originates from stream sediments (KMB, AB, NMB: Colville et al., 2011; Reyes et al., 2014), surface sediments (NNS: Maccali et al., 2018; CMB: this study) and rock data (DI: Larsen & Pedersen, 2009; BI: McCulloch & Wasserburg, 1978; RMB: Kalsbeek et al., 1998; NGr: Thorarinsson et al., 2012, 2011). Dashed grey line in Pb provenance plot (B) represents the Pb growth curve of continental crust (Stacey & Kramers, 1975). The most extreme isotopic values of GeoB19946-4 during the mast wasting event (Figure 4.5, dark green shaded) have been excluded from this figure.

4.5. Discussion

The main discussion will focus on the isotopic records of GeoB19927-3 and GeoB19946-4 (thereafter referred to as 27-3 and 46-4, respectively) raised from the Greenland shelf as they cover the northwestern GIS drainage sector. GeoTÜ SL170 (thereafter referred to as SL170) was raised from the west Greenland slope, therefore underlying a slightly different sediment transport regime and the age model contains higher uncertainties as it was interpolated based on the lower record. Therefore SL170 will mainly serve as a southern endmember and support for interpretation of the two other records from Upernavik Trough (27-3) and northern Melville Bay (46-4). The radiogenic isotope data will be interpreted and compared to sediment

geochemistry (and micropalaeontological) data from other studies on sediment cores AMD14-204 (thereafter referred to as 204) (Caron et al., 2020, 2019a, 2019b; Giraudeau et al., 2020; Hansen et al., 2020) and AMD14-210 (thereafter referred to as 210) (Caron et al., 2020, 2019a, 2019b), taken from locations close to our core locations of GeoB19927-3 and GeoB19946-4 (Figure 4.1).

The discussion will be divided into the three main Holocene climatic intervals following the LGM: the Deglacial period, the HTM and the Neoglacial period. These three intervals were determined based on the timing of the HTM, which represents warmer-than-present temperatures and varied on a spatio-temporal scale in the western Arctic due to lingering ice sheets (Kaufman et al., 2004). The transition between each of these periods has been characterised with pronounced changes in sea surface conditions in northeastern Baffin Bay (Caron et al., 2019b; Hansen et al., 2020).

Generally, the detrital sediment composition in northeastern Baffin Bay sedimentary archives is composed of mixed sources of mainly local input with differing contribution of distal sources. The highest temporal variability can be observed in core 27-3 from Upernavik Trough. While core 46-6 from northern Melville Bay appears to be characterised by mainly local sources without significant provenance shifts over time, the detrital sediment composition of core 27-3 is generally influence by Holocene climatological and oceanographical changes. Based on surface sediment data Andrews et al. (2018) defined West Greenland Mineral Clusters (WGMC), for Melville Bay and Upernavik sources, which clearly state specific mineralogical compositions of Melville Bay surface sediments, mainly influenced by input of the local bedrock through meltwater discharge and erosion. Based on these mineral clusters Caron et al. (2020) conducted Principal Component Analysis which identified their record 210 from Melville Bay as characterised by local sourced detrital sediment input, while their core 204 from Upernavik is composed of mixed sources. Ternary plots differentiating these provenances defined based on the WGMC identify mixed sources in the quartz-kalifeldspar-plagioclase ternary plot for both cores 204 and 201, while the carbonate-amphibole-pyroxene ternary plot differentiates between increased local northern Greenland sources for 210 and a mix of northern Greenland and Disko Bay sources for 204 (Caron et al., 2020).

4.5.1. Deglacial Period

The Deglacial period in the wider Melville Bay and Upernavik region has formerly been described as a period of harsh conditions with extended sea-ice cover and wide spread meltwater input from the retreating GIS after the LGM (Caron et al., 2019b; Hansen et al., 2020; Seidenkrantz et al., 2013). The isotopic records within this time interval reveal continuous trends with a slight kink in Sr isotopic composition around 11 and 8.4 ka BP for SL170 and 27-3, respectively. A shift in Nd isotopic composition can be identified around 8.2 ka BP in core SL170. The sediment composition seems to be a mix of material transported via the WGC as it reflects southern Greenland sources and the local RMB, with a stronger influence of local sources which would be supported by high meltwater discharge rates, transporting local material onto the shelf (Marit Solveig Seidenkrantz et al., 2013). SL170 clearly reflects the isotopic composition of the local NMB terrain. The Pb provenance plot supports the input of NMB sources at the SL170 location as well as at the 27-3 location, which would be the closest southern component to the core location. For the RMB unfortunately no Pb data is available within literature. Giraudeau et al. (2020) propose a high contribution of Melville Bay glaciers to Upernavik Trough in the early Holocene which is agreeing with the isotopic data plotting in

between CMB and RMB sources, as well as the Baffin Island component. Although Baffin Island is located on the western coast of Baffin Bay and most likely does not contribute any detrital sediment material to the eastern part of the bay, the geological terrains continue through Baffin Bay from northern Greenland to Baffin Island (Jackson & Berman, 2000; Le Pichon et al., 1977) and isotopic signatures have been reported to be chemically comparable (cf. Jackson & Berman, 2000). Therefore the Baffin Island component can be seen as another hint for local detrital sediment input, as it should be representing the wider RMB signatures, while the possible influence of CMB transporting material from northern Melville Bay agrees with the suggestion by Giraudeau et al. (2020) of glacial input from that area.

The most obvious changes in isotopic composition are recorded within the 46-4 record with pronounced shifts towards less radiogenic Sr and Pb and more radiogenic Nd. However, this shift falls into the aforementioned mass wasting event with significantly higher sedimentation rates possibly related to the GIS retreat. Similar findings have been observed in the 210 record by Caron et al. (2019a), who also found higher sedimentation rates in the lower part of the record as well as coarser grain sizes, unsorted sediments and the highest IRD counts. They interpret this period as unstable with occasional turbidity current activity related to the destabilization of the GIS inducing sediment remobilisation throughout the deglaciation process. Caron et al. (2019a) further suggest that the period prior to 9.4 was characterised by ice-proximal glaciomarine sedimentation regimes following the retreat of grounding ice in Melville Bay. The general sediment composition seems to reflect a mix of the local CMB and the AB from southern Greenland. However, the CMB signal originates from surface sediments from a fjord south of the core location and therefore represents a very local signal and may not reflect the exact same isotopic signatures discharged directly at the core location. Additionally, CMB is mainly of Archean age as is the AB (Figure 4.1) and therefore the contribution of this core might more likely reflect the similarity of the isotopic composition of the actual CMB signature in northern most Greenland than the surface sediment does. The major CMB contribution is however clearly supported by the Pb isotope provenance plot, that differs from AB contribution. However, Pb is generally known to become more radiogenic in younger sources and as CMB contains some Palaeoproterozoic overprints, it should overall not reflect the exact same age range as the Archean Block.

The mineralogical composition of both records does not indicated significant changes within this time period. While 27-3 does not show a lot of variability, the mineralogical composition of 46-4 differs slightly from the rest of the record, with reduced quartz content compared to the following part and some fluctuations in accessory minerals as amphibole and pyroxene, phyllosilicates and iron minerals (Figure 4.6). These changes coincide with the changes in isotopic composition indicating the differing sediment composition during the mass wasting event.

The kink in Sr isotopic composition around 8.4 ka BP within the 27-3 record (Figure 4.3) is neither visible in any of the other Sr records nor in the mineralogical composition. A first assumption of this kink being related to the 8.2 cold event (Thomas et al., 2007) coinciding with atmospheric cooling and local glacier increase as observed within XRF data in a southern Greenland record (Weiser et al., 2021) is equivocal. While the western GIS melting pattern did not seem to be affected by the 8.2 cooling event and no visible changes and signs of cooling within different records have been observed (Marit Solveig Seidenkrantz et al., 2013), moraines in the Disko Bay area suggest a short, regionally differing GIS advance or stillstand

between 8.5 and 8.0 ka BP (Young et al., 2013). The set-back in Sr isotopic composition towards initial values would suggest a short ice-sheet advance around 8.4 ka BP based on the obvious isotopic shift, identifying continental erosion as the dominating sediment pathway, over meltwater discharge (cf. Seidenkrantz et al., 2013). SL170 records records a pronounced peak around in Nd isotopic composition around 8.2 ka BP (Figure 4.2), favouring the possible recording of 8.2 event related GIS impacts (Young et al., 2013) within the radiogenic isotope composition. However, the different timings of the recorded isotopic signatures and different reported reactions of the GIS with regards to extent and meltwater discharge patterns leave some uncertainties in the overall interpretation and require further investigation.

With regards to basal ages of the sedimentary records Caron, et al. (2019a) concluded that the GIS retreated from the shelf before 10.3 ka BP in the Upernavik region, which can be supported by the age model of the 27-3 record. The 46-4 record points to an earlier retreat than the proposed one around 9.5 ka BP (Caron et al., 2019a). However, the age model has to be treated with care prior to ~9 ka BP due to the observed mass wasting event and therefore does support this assumption to some extent and confirms and asynchronous retreat of the GIS between Melville Bay and Upernavik as stated by Caron et al. (2019a) as well as earlier studies, that reporting this development on a larger scale (Jackson et al., 2017; Young & Briner, 2015).

4.5.2. Holocene Thermal Maximum

The beginning of the HTM has still been characterised with the ongoing pronounced meltwater discharge reported from southern Greenland and the Disko Bay area and most likely continued along the west Greenland coast until around 7.5 ka BP (Marit Solveig Seidenkrantz et al., 2013). With the transition into the HTM the amounts of warmer Atlantic-sourced waters transported northwards along the coast via the WGC increased and induced pronounced shifts in sea-surface conditions (Caron et al., 2019b; Hansen et al., 2020), with a coinciding reduction in sea-ice cover (Caron et al., 2019a; Saini et al., 2020).

The most obvious shift in Sr and Nd isotopic composition of 27-3 was recorded during the HTM, with trends towards less radiogenic Sr (0.763 to 0.746) and more radiogenic Nd (-27.8 to -25.4) indicating a continuous shift towards changing detrital sediment composition and source distribution (Figure 4.3). This period was not only marked by reduced sea-ice cover and warmer surface waters (Caron et al., 2019b; Saini et al., 2020) but also by a stronger WGC from 7.9 to 6.7 ka BP (Hansen et al., 2020), changing sediment delivery regimes towards increased input from southern sources as indicated by Sr-Nd provenance plot through an increasing contribution from NMB (Figure 4.7). The continuous shift in detrital sediment provenance beyond the proposed interval of increased WGC strength could be caused by input of additional sources. Around 6 ka BP the modern circulation pattern of the WGC within Disko Bay was established by the opening of Vaigat Strait, which was blocked by glacial ice up to this point (Perner et al., 2013). Disko Island and the Nuussuaq Peninsula are comprised of Palaeogene basalts which are characterised by entirely different isotopic signatures compared to other west Greenland bedrock terrains, with $^{87}Sr/^{86}Sr$ signatures between 0.703 and 0.709 and ε_{Nd} signatures ranging from -4.4 to 10 (Larsen & Pedersen, 2009). The exposed bedrock and open channel between the Disko and Nuussuaq islands lead to northwards transport of basaltic material which before remained in Disko Bay (Perner et al., 2013). The distinct isotopic signatures of the Palaeogene basalts from Disko Bay might have induced the continuous shift in isotopic signatures. This shift cannot be identified from Pb isotopic data, as the isotopic signatures for the corresponding sources are overlapping, which might also explain the stable

Pb record within this time interval. However, the proportion of basaltic material within the overall detrital sediment composition still seems to be small compared to the local detrital sediment input, as the mineralogical composition does not indicate any major contribution of additional material. This basaltic influence is most likely only visible due to the rather large differences in isotopic composition of the different sources. The input of basaltic sources has recently been observed by Giraudeau et al. (2020) based on an increase in Fe counts within measured XRF data from core 204 as well as by mineralogical based Principal Component Analysis by Caron et al. (2020). Caron et al. (2020) observe a progressive change in mineralogical composition and input of the local RMB Karrat Group (Kalsbeek et al., 1998) and basalts after ~7.7 ka BP, which is the same interval when the continuous shift in isotopic composition is recorded. They additionally find that the signal of basaltic component delivery to Upernavik Trough becomes even more distinct after 4.9 ka BP and suggest a fast flowing Upernavik ice stream until ~7.7 cal ka BP, associated with strong meltwater discharge from the GIS, which transported fine detrital sediment material to the core site, which is supported by their earlier studies on the same record (Caron et al., 2020, 2019a, 2019b).

The isotopic composition of the 46-4 record does not show any variability apart from a slight shift towards more radiogenic Nd, which might also be related to the aforementioned Vaigat Strait opening. The Sr isotopic composition does not show any indication of basalt input from the Disko Bay area which could be an effect of dilution as the WGC transporting these signatures is continuously fed by meltwater discharge (Buch, 2002) and therefore detrital material from the surrounding landmasses that will add to the original isotopic signature. However, a study conducted by Andrews et al. (2018) showed that the mineralogical distribution of Melville Bay surface sediments varies from that of other areas in Baffin Bay and is not significantly influenced by material from other than local sources and does not show any basalt input. Comparing the mineralogical composition of the 46-4 record to the 27-3 record suggests a rather insignificant input of northwards transported material as the carbonate visible in core 27-3 is not visible in 46-4, which should have been the case if a significant fraction was transported to the core location of 46-4. Furthermore, the slight trend in more radiogenic Nd values continues into the late Holocene and culminates into a peak around 3.4 ka BP, where it also is not visible in any of the other two isotopic records, which might indicate that the cause of the shift is caused by other effects than basalt input from the Disko Bay area.

Core SL170 records a pronounced shift in Nd isotopic composition around 6 ka BP towards more unradiogenic values similar to the Deglacial values, which could also be related to Vaigat Strait opening as the Deglacial values represent erosion conditions during ice-sheet retreat. Generally, this event impacted the circulation pattern in Disko Bay (Perner et al., 2013) and hence should influence the sediment delivery pathways to the adjacent slope.

4.5.3 Neoglacial Period

The Neoglacial period is generally characterised by atmospheric cooling and glacier advance that has been recorded in different locations around Greenland (e.g. Kaplan et al., 2002; Larsen et al., 2011, 2017; Solomina et al., 2015). The warmer HTM sea-surface conditions in northeastern Baffin Bay lasted until around 3.4 to 2.9 ka BP (Caron et al., 2019b; Hansen et al., 2020). Following sea-surface condition changes with some visibility of Neoglacial cooling around 2.9 ka BP where marked by an abrupt transition in benthic foraminiferal assemblages (Hansen et al., 2020) and to some extent by dinocyst data around 2 ka BP (Caron et al., 2019b),

while the sea ice biomarker IP_{25} does not record any evidence any evidence of Neoglacial cooling (Saini et al., 2020). The decrease in WGC strength observed after 6 ka BP further decreased after ~3.5 ka BP (Hansen et al., 2020; Perner et al., 2012; Weiser et al., 2021).

The isotopic composition after the HTM appears to be comparably stable with low variability within the cores from northeastern Baffin Bay, 27-3 and 46-4. The trends within the Sr and Nd composition of core 27-3 continue slightly towards less radiogenic Sr and more radiogenic Nd between ~5 and ~3 ka BP. After ~3 ka BP Nd values become stable while Sr displays an even minor trend towards more radiogenic values until the top of the core. Pb values stay comparable stable throughout this entire interval with one exception of a small peak around 1.2 ka BP towards more radiogenic Pb, which can also be seen in a more pronounced way in the Nd isotopic composition, also becoming more radiogenic. In northern most Melville Bay the isotopic Sr and Pb composition of core 46-4 stays stable while Nd isotopic composition continues the trend initiated during the HTM towards more radiogenic values. The trend culminates in a pronounced peak of more radiogenic Nd (-29.1) around 3.4 ka BP and from then onwards moving towards less radiogenic values until the top of the record. Core SL170 displays continuous trends towards more radiogenic Sr and Pb and less radiogenic Nd. The provenance plots (Figure 4.7) indicate some shifts in detrital sediment provenance in 27-3 and SL170 during the late Holocene, both shift towards an increase in Disko Bay contribution. Within core 204 from Upernavik Trough Caron et al. (2020) also observed a continuous increase in basalt contribution with the highest contribution between 2.0 and 2.4 ka BP. Additionally, Giraudeau et al. (2020) report reduced contributions of northern Melville Bay as well as local Upernavik sourced material at the 204 core location and suggest this being caused by a rapid response of the GIS towards Neoglacial cooling and a possible connected stagnancy or re-advance of the GIS margin. Both observations coincide with the isotopic development moving towards Disko Island sources and away from CMB sources. From the provenance plot it might appear as SL170 also received increasing contribution from Disko Island basalts, but the general trend towards less radiogenic Nd contradicts with this assumption. It might be more likely that the change in detrital sediment composition delivered to the west Greenland slope was influenced by the observed decrease in WGC strength (Perner et al., 2012; Weiser et al., 2021) transporting reduced amounts of distal material.

The peak in Nd isotopic composition around 3.4 ka BP recorded in core 46-4 is not that obvious to explain. It does coincide with a peak in smectite/amphibole ratio in core 210 which was, however, not further explained (Caron et al., 2020). A similar peak was recorded in core 27-3 around 1.2 ka BP, which can also be observed in the Pb isotopic composition. Those timings roughly coincided with pulses of Neoglacial ice advance documented on the Nuussuaq Peninsula and in southern Greenland around 3.7 to 3.6 ka BP and 1.4 to 1.0 ka BP (Larsen et al., 2015; Schweinsberg et al., 2019; Schweinsberg et al., 2017). Changes in Nd isotopic composition have been noted before to record Neoglacial ice advance through erosion of Archean bedrock in southern Greenland (see chapter 3). However, in southern Greenland Nd values indicating Neoglacial ice-advance became less radiogenic, while the values in 27-3 and 46-4 became more radiogenic, which might either be due to the different isotopic composition of the corresponding source rock or point towards a different cause of isotopic shift.

4.6. Conclusions

This study presents radiogenic isotope and sediment mineralogy data from the west Greenland margin identifying regional and temporal variations in detrital sediment provenances

throughout the Holocene. The northwestern Greenland Ice Sheet margin seemed to be comparably stable after its deglaciation during the early Holocene. Main sources for detrital sediment delivery to northernmost Melville Bay are local glaciers and ice streams reflected by the radiogenic isotope composition of the local geology without any distinct variation during the mid and late Holocene.

Farther south in the Upernavik region local glaciers and ice streams also define the main source for detrital sediment delivered onto the shelf. However, in contrast to northernmost Melville Bay, here a clear influence of distal detrital sediment transported via the West Greenland Current can be identified. With an increase in West Greenland Current strength between ~7.9 and 6.7 ka BP (Hansen et al., 2020) radiogenic isotope signatures indicate a shift towards a higher proportion of southern Greenland detrital sediment sources, most pronounced in the $^{87}Sr/^{86}Sr$ composition. This shift towards less radiogenic Sr values in combination with an increased shift towards more radiogenic ε_{Nd} identifies the Vaigat Strait opening and increased input of basalts from ~6 ka BP onwards (Perner et al., 2013).

We conclude that our radiogenic isotope based provenance study records rather unstable conditions during the Deglacial period caused by ice-sheet retreat and more stable conditions during the mid to late Holocene. Shifts in detrital provenance are mainly caused by oceanic current strength variations and ice-sheet retreat rather than ice-sheet fluctuations. Generally, sediment transport pathways of detrital sediment to the west Greenland shelf are locally influenced by ice-sheet dynamics and meltwater discharge with the West Greenland Current playing a minor role but a clear visible one with regards to current strength and circulation changes (cf. Andrews et al., 2018; Giraudeau et al., 2020).

This study further points out the advantage and reliability in the application of radiogenic isotope based provenance studies. Shifts in isotopic composition identify major climatological changes in line with previously published data and reveal additional information that has not been identified from changes in mineralogical data, such as the influence of the Vaigat Strait opening. However, this study also points out the need for further studies including more radiogenic isotope background data in the form of stream and surface sediments as already existing for southern Greenland (Colville et al., 2011; Reyes et al., 2014).

4.7. Acknowledgements

This project was supported by the Deutsche Forschungsgemeinschaft (DFG) through the International Research Training Group "Processes and impacts of climate change in the North Atlantic Ocean and the Canadian Arctic" (IRTG 1904 ArcTrain).

We would like to thank the captain, crew members and science party during expeditions MSM44 and MSM09/2, *RV Maria S. Merian*, for their support with retrieving the sample material included in this study.

Special thanks go to Michel Preda, Geotop—UQÁM, for performing the XRD analysis as well as his support, time and discussion regarding the data and theory.

4.8. References

Allan, E., Vernal, A., Knudsen, M. F., Hillaire-Marcel, C., Moros, M., Ribeiro, S., … Seidenkrantz, M. (2018). Late Holocene sea-surface instabilities in the Disko Bugt area, west Greenland, in phase with δ18O-oscillations at Camp Century. Paleoceanography and Paleoclimatology. https://doi.org/10.1002/2017PA003289

Andrews, J. T., & Eberl, D. D. (2012). Determination of sediment provenance by unmixing the mineralogy of source-area sediments: The "SedUnMix" program. Marine Geology, 291–294, 24–33. https://doi.org/10.1016/j.margeo.2011.10.007

Andrews, J. T., Bjork, A. A., Eberl, D. D., Jennings, A. E., & Verplanck, E. P. (2015). Significant differences in late Quaternary bedrock erosion and transport: East versus West Greenland ~70°N - evidence from the mineralogy of offshore glacial marine sediments. Journal of Quaternary Science, 30(5), 452–463. https://doi.org/10.1002/jqs.2787

Andrews, J. T., Klein, A. J., Jenner, K. A., Jennings, A. E., & Campbell, C. (2018). The variability of Baffin Bay seafloor sediment mineralogy: The identification of discrete glacial sediment sources and application to Late Quaternary downcore analysis. Canadian Journal of Earth Sciences, 55(6), 620–639. https://doi.org/10.1139/cjes-2017-0223

Batchelor, C. L., & Dowdeswell, J. A. (2014). The physiography of High Arctic cross-shelf troughs. Quaternary Science Reviews, 92, 68–96. https://doi.org/10.1016/j.quascirev.2013.05.025

Bennike, O. (2000). Palaeoecological studies of Holocene lake sediments from west Greenland. Palaeogeography, Palaeoclimatology, Palaeoecology, 155(3–4), 285–304. https://doi.org/10.1016/S0031-0182(99)00121-2

Bennike, O. (2008). An early Holocene Greenland whale from Melville Bugt, Greenland. Quaternary Research, 69(1), 72–76. https://doi.org/10.1016/j.yqres.2007.10.004

Blaauw, M., & Christen, J. A. (2011). Flexible paleoclimate age-depth models using an autoregressive gamma process. Bayesian Analysis, 6(3), 457–474. https://doi.org/10.1214/11-BA618

Briner, J. P., Håkansson, L., & Bennike, O. (2013). The deglaciation and neoglaciation of upernavik isstrøm, greenland. Quaternary Research (United States), 80(3), 459–467. https://doi.org/10.1016/j.yqres.2013.09.008

Briner, J. P., Kaufman, D. S., Bennike, O., & Kosnik, M. A. (2014). Amino acid ratios in reworked marine bivalve shells constrain Greenland Ice Sheet history during the holocene. Geology, 42(1), 75–78. https://doi.org/10.1130/G34843.1

Buch, E. (2002). Present oceanographic conditions in Greenland Waters. Danish Meteorological Institute, Scientific report.

Caron, M., Montero-Serrano, J. C., St-Onge, G., & Rochon, A. (2020). Quantifying Provenance and Transport Pathways of Holocene Sediments From the Northwestern Greenland Margin. Paleoceanography and Paleoclimatology, 35(5), 1–23. https://doi.org/10.1029/2019PA003809

Caron, M., Rochon, A., Montero-Serrano, J. C., & St-Onge, G. (2019b). Evolution of sea-surface conditions on the northwestern Greenland margin during the Holocene. Journal of Quaternary Science, 34(7), 569–580. https://doi.org/10.1002/jqs.3146

Caron, M., St-Onge, G., Montero-Serrano, J. C., Rochon, A., Georgiadis, E., Giraudeau, J., & Massé, G. (2019a). Holocene chronostratigraphy of northeastern Baffin Bay based on radiocarbon and palaeomagnetic data. Boreas, 48(1), 147–165. https://doi.org/10.1111/bor.12346

Castro de la Guardia, L., Hu, X., & Myers, P. G. (2015). Greenland Ice Sheet melt increases Baffin Bay heat content on the west Greenland shelf. Geophysical Research Letters, n/a-n/a. https://doi.org/10.1038/nature05320

Church, J. A., Clark, P. U., Cazenave, A., Gregory, J. M., Jevrejeva, S., Levermann, A., … Unnikrishnan, A. S. (2013). Sea Level Change. In: Climate Change 2013: The Physical Science Basis. Contribution of Working Group I to the Fifth Assessment Report of the Intergovernmental Panel on Climate Change [Stocker, T.F., D. Qin, G.-K. Plattner, M. Tignor, S.K. Allen, J. Boschung, A. Nauels, Y. Xia, V. Bex and P.M. Midgley (eds.)].

Cambridge University Press, Cambridge, United Kingdom and New York, NY, USA.
Colville, E. J., Carlson, A. E., Beard, B. L., Hatfield, R. G., Stoner, J. S., Reyes, A. V, & Ullman, D. J. (2011). Sr-Nd-Pb isotope evidence for ice-sheet presence on southern Greenland during the Last Interglacial. Science, 333(6042), 620–623. https://doi.org/10.1126/science.1204673
Connelly, J. N., Thrane, K., Krawiec, A. W., & Garde, A. A. (2006). Linking the Palaeoproterozoic Nagssugtoqidian and Rinkian orogens through the Disko Bugt region of West Greenland. Journal of the Geological Society, 163(2), 319–335. https://doi.org/10.1144/0016-764904-115
Corbett, L. B., Bierman, P. R., Graly, J. A., Neumann, T. A., & Rood, D. H. (2013). Constraining landscape history and glacial erosivity using paired cosmogenic nuclides in upernavik, northwest greenland. Bulletin of the Geological Society of America, 125(9–10), 1539–1553. https://doi.org/10.1130/B30813.1
Cuny, J., Rhines, P. B., Niiler, P. P., & Bacon, S. (2002). Labrador Sea boundary currents and the fate of the Irminger Sea Water. Journal of Physical Oceanography, 32(2), 627–647. https://doi.org/10.1175/1520-0485(2002)032<0627:LSBCAT>2.0.CO;2
Dahl-Jensen, T., Larsen, T. B., Woelbern, I., Bach, T., Hanka, W., Kind, R., … Gudmundsson, O. (2003). Depth to Moho in Greeland: Receiver-function analysis suggests two proterozoic blocks in Greenland. Earth and Planetary Science Letters, 205(3–4), 379–393. https://doi.org/10.1016/S0012-821X(02)01080-4
Dawes, P R. (2009). The bedrock geology under the Inland Ice: the next major challenge for Greenland mapping. Geological Survey of Denmark and Greenland Bulletin, 17, 57–60.
Dawes, Peter R. (2009). Precambrian - Palaeozoic geology of Smith Sound, Canada and Greenland: Key constraint to palaeogeographic reconstructions of northern Laurentia and the North Atlantic region. Terra Nova, 21(1), 1–13. https://doi.org/10.1111/j.1365-3121.2008.00845.x
Dawes, Peter R. (2006). Explanatory notes to the Geological map of Greenland , 1 : 500 000 , Thule , Sheet 5. Geological Survey of Denmark and Greenland Map Series 2, 97pp.
Deniel, C., & Pin, C. (2001). Single-stage method for the simultaneous isolation of lead and strontium from silicate samples for isotopic measurements. Analytica Chimica Acta, 426(1), 95–103. https://doi.org/10.1016/S0003-2670(00)01185-5
Dorschel, B., Afanasyeva, V., Bender, M., Dreutter, S., Eisermann, H., Gebhardt, A. C., … Wangner, D. J. (2015). Past Greenland Ice Sheet dynamics, Palaeoceanography and Plankton Ecology in the Northeast Baffin Bay Cruise No. MSM44 30. MARIA S. MERIAN-Berichte, 148.
Eisenhauer, A., Meyer, H., Rachold, V., Tütken, T., Wiegand, B., Hansen, B. T., … Kassens, H. (1999). Grain size separation and sediment mixing in Arctic Ocean sediments: Evidence from the strontium isotope systematic. Chemical Geology, 158(3–4), 173–188. https://doi.org/10.1016/S0009-2541(99)00026-1
Fagel, N., Innocent, C., Gariepy, C., & Hillaire-Marcel, C. (2002). Sources of Labrador Sea sediments since the last glacial maximum inferred from Nd-Pb isotopes. Geochemistry, Geophysics, Geosystems, 66(14), 2569–2581.
Frank, M. (2002). Radiogenic isotopes: Tracers of past ocean circulation and erosional input. Reviews of Geophysics, 40(1), 1001. https://doi.org/10.1029/2000RG000094
Fratantoni, P. S., & Pickart, R. S. (2007). The western North Atlantic shelfbreak current system in summer. Journal of Physical Oceanography, 37(10), 2509–2533. https://doi.org/10.1175/JPO3123.1
Freire, F., Gyllencreutz, R., Greenwood, S. L., Mayer, L., Egilsson, A., Thorsteinsson, T., & Jakobsson, M. (2015). High resolution mapping of offshore and onshore glaciogenic features in metamorphic bedrock terrain, Melville Bay, northwestern Greenland. Geomorphology, 250, 29–40. https://doi.org/10.1016/j.geomorph.2015.08.011
Giraudeau, J., Georgiadis, E., Caron, M., Martinez, P., Saint-Onge, G., Billy, I., … Massé, G. (2020). A high-resolution elemental record of post-glacial lithic sedimentation in Upernavik Trough, western Greenland: history of ice-sheet dynamics and ocean circulation changes

over the last 9 100 years. Paleoceanography and Paleoclimatology, 1–37.
Grocott, J., & McCaffrey, K. J. W. (2017). Basin evolution and destruction in an Early Proterozoic continental margin: the Rinkian fold–thrust belt of central West Greenland. Journal of the Geological Society, 174(3), 453–467. https://doi.org/10.1144/jgs2016-109
Gutjahr, M., Frank, M., Stirling, C. H., Klemm, V., van de Flierdt, T., & Halliday, A. N. (2007). Reliable extraction of a deepwater trace metal isotope signal from Fe-Mn oxyhydroxide coatings of marine sediments. Chemical Geology, (242), 351–370. https://doi.org/10.1016/j.chemgeo.2007.03.021
Hansen, K. E., Giraudeau, J., Wacker, L., Pearce, C., & Seidenkrantz, M. S. (2020). Reconstruction of Holocene oceanographic conditions in eastern Baffin Bay. Climate of the Past, 16(3), 1075–1095. https://doi.org/10.5194/cp-16-1075-2020
Harig, C., & Simons, F. J. (2012). Mapping Greenland's mass loss in space and time. Proceedings of the National Academy of Sciences of the United States of America, 109(49), 19934–19937. https://doi.org/10.1073/pnas.1206785109
Harig, C., & Simons, F. J. (2016). Ice mass loss in Greenland, the Gulf of Alaska, and the Canadian Archipelago: Seasonal cycles and decadal trends. Geophysical Research Letters, 43(7), 3150–3159. https://doi.org/10.1002/2016GL067759
Jackson, G. D., & Berman, R. G. (2000). Precambrian metamorphic and tectonic evolution of northern Baffin Island, Nunavut, Canada. Canadian Mineralogist, 38(2), 399–421. https://doi.org/10.2113/gscanmin.38.2.399
Jackson, R., Carlson, A. E., Hillaire-Marcel, C., Wacker, L., Vogt, C., & Kucera, M. (2017). Asynchronous instability of the North American-Arctic and Greenland ice sheets during the last deglaciation. Quaternary Science Reviews, 164, 140–153. https://doi.org/10.1016/j.quascirev.2017.03.020
Jacob, T., Wahr, J., Pfeffer, W. T., & Swenson, S. (2012). Recent contributions of glaciers and ice caps to sea level rise. Nature, 482(7386), 514–518. https://doi.org/10.1038/nature10847
Jacobsen, S. B., & Wasserburg, G. J. (1980). Sm-Nd Isotopic Evolution of Chondrites. Earth and Planetary Science Letters, 50, 139–155.
Kalsbeek, F., Pulvertaft, T. C. R., & Nutman, A. P. (1998). Geochemistry, age and origin of metagreywackes from the Palaeoproterozoic Karrat Group, Rinkian Belt, West Greenland. Precambrian Research, 91(3–4), 383–399. https://doi.org/10.1016/S0301-9268(98)00059-X
Kaplan, M. R., Wolfe, A. P., & Miller, G. H. (2002). Holocene Environmental Variability in Southern Greenland Inferred from Lake Sediments. Quaternary Research, 58(2), 149–159. https://doi.org/10.1006/qres.2002.2352
Kaufman, D. S., Ager, T. A., Anderson, N. J., Anderson, P. M., Andrews, J. T., Bartlein, P. J., … Wolfe, B. B. (2004). Holocene thermal maximum in the western Arctic (0-180°W). Quaternary Science Reviews, 23(5–6), 529–560. https://doi.org/10.1016/j.quascirev.2003.09.007
Larsen, L. M., & Pedersen, A. K. (2009). Petrology of the paleocene picrites and flood basalts on disko and nuussuaq, West Greenland. Journal of Petrology, 50(9), 1667–1711. https://doi.org/10.1093/petrology/egp048
Larsen, N. K., Kjær, K. H., Lecavalier, B., Bjørk, A. A., Colding, S., Huybrechts, P., … Olsen, J. (2015). The response of the southern Greenland ice sheet to the Holocene thermal maximum. Geology, 43(4), 291–294. https://doi.org/10.1130/G36476.1
Larsen, N. K., Kjær, K. H., Olsen, J., Funder, S., Kjeldsen, K. K., & Nørgaard-Pedersen, N. (2011). Restricted impact of Holocene climate variations on the southern Greenland Ice Sheet. Quaternary Science Reviews, 30(21–22), 3171–3180. https://doi.org/10.1016/j.quascirev.2011.07.022
Larsen, N. K., Strunk, A., Levy, L. B., Olsen, J., Bjørk, A., Lauridsen, T. L., … Davidson, T. A. (2017). Strong altitudinal control on the response of local glaciers to Holocene climate change in southwest Greenland. Quaternary Science Reviews, 168, 69–78.

https://doi.org/10.1016/j.quascirev.2017.05.008
Le Pichon, X., Sibuet, J.-C., & Francheteau, J. (1977). The fit of the continents around the North Atlantic Ocean. Tectonophysics, 38(3–4), 169–209. https://doi.org/10.1016/0040-1951(77)90210-4
Lecavalier, B. S., Milne, G. A., Simpson, M. J. R., Wake, L., Huybrechts, P., Tarasov, L., … Larsen, N. K. (2014). A model of Greenland ice sheet deglaciation constrained by observations of relative sea level and ice extent. Quaternary Science Reviews, 102, 54–84. https://doi.org/10.1016/j.quascirev.2014.07.018
Levac, E., De Vernal, A., & Blake, W. (2001). Sea-surface conditions in northernmost Baffin Bay during the Holocene: Palynological evidence. Journal of Quaternary Science, 16(4), 353–363. https://doi.org/10.1002/jqs.614
Levy, L. B., Larsen, N. K., Davidson, T. A., Strunk, A., Olsen, J., & Jeppesen, E. (2017). Contrasting evidence of Holocene ice margin retreat, south-western Greenland. Journal of Quaternary Science, 32(5), 604–616. https://doi.org/10.1002/jqs.2957
Limoges, A., Weckström, K., Ribeiro, S., Georgiadis, E., Elnegaard Hansen, K., Martinez, P., … Massé, G. (2020). Learning from the past: impact of the Arctic Oscillation on sea ice and marine productivity off northwest Greenland over the last 9000 years, in press. https://doi.org/10.1111/gcb.15334
Long, A. J., Woodroffe, S. A., Dawson, S., Roberts, D. H., & Bryant, C. L. (2009). Late Holocene relative sea level rise and the Neoglacial history of the Greenland ice sheet. Journal of Quaternary Science, 24(4), 345–359. https://doi.org/10.1002/jqs
Maccali, J., Hillaire-Marcel, C., Carignan, J., & Reisberg, L. C. (2013). Geochemical signatures of sediments documenting Arctic sea-ice and water mass export through Fram Strait since the Last Glacial Maximum. Quaternary Science Reviews, 64, 136–151. https://doi.org/10.1016/j.quascirev.2012.10.029
Maccali, J., Hillaire-Marcel, C., & Not, C. (2018). Radiogenic isotope (Nd, Pb, Sr) signatures of surface and sea ice-transported sediments from the Arctic Ocean under the present interglacial conditions. Polar Research, 37(1), 1–13. https://doi.org/10.1080/17518369.2018.1442982
Maclean B, Williams GL, Srivastava SP. 1990. Geology of Baffin Bay and Davis Strait. In Geology of Canada No.2: Geology of the continental margin of eastern Canada, Keen MJ, Williams GL (eds). Geological Survey of Canada: 293–348.
McCulloch, M. T., & Wasserburg, G. J. (1978). Sm-Nd and Rb-Sr Chronology of Continental Crust Formation. Science, 200(June), 1003–1011.
McMillan, M., Leeson, A., Shepherd, A., Briggs, K., Armitage, T. W., Hogg, A., … Gilbert, L. (2016). A high-resolution record of Greenland mass balance. Geophysical Research Letters, 43, 7002–7010. https://doi.org/10.1007/978-3-642-41714-6_130721
Moore, D. M., Reynolds, R. C. Jr. (1997). X-Ray Diffraction and the Identification and Analysis of Clay Minerals (2nd edition), Oxford University Press, New York
Morlighem, M., Williams, C. N., Rignot, E., An, L., Arndt, J. E., Bamber, J. L., … Zinglersen, K. B. (2017). BedMachine v3: Complete Bed Topography and Ocean Bathymetry Mapping of Greenland From Multibeam Echo Sounding Combined With Mass Conservation. Geophysical Research Letters, 44(21), 11,051-11,061. https://doi.org/10.1002/2017GL074954
Myers, P. G., Donnelly, C., & Ribergaard, M. H. (2009). Structure and variability of the West Greenland Current in Summer derived from 6 repeat standard sections. Progress in Oceanography, 80(1–2), 93–112. https://doi.org/10.1016/j.pocean.2008.12.003
Ouellet-Bernier, M.-M., de Vernal, A., Hillaire-Marcel, C., & Moros, M. (2014). Paleoceanographic changes in the Disko Bugt area, West Greenland, during the Holocene. The Holocene, 24(11), 1573–1583. https://doi.org/10.1177/0959683614544060
Perner, K., Moros, M., Jennings, A. E., Lloyd, J. M., & Knudsen, K. L. (2012). Holocene palaeoceanographic evolution off West Greenland. The Holocene, 23(3), 374–387. https://doi.org/10.1177/0959683612460785

Perner, Kerstin, Moros, M., Snowball, I., Lloyd, J. M., Kuijpers, A., & Richter, T. (2013). Establishment of modern circulation pattern at c. 6000 cal a BP in Disko Bugt, central West Greenland: Opening of the Vaigat Strait. Journal of Quaternary Science, 28(5), 480–489. https://doi.org/10.1002/jqs.2638

Philipps, W., Briner, J. P., Bennike, O., Schweinsberg, A., Beel, C., & Lifton, N. (2018). Earliest Holocene deglaciation of the central Uummannaq Fjord system, West Greenland. Boreas, 47, 311–325. https://doi.org/10.1111/bor.12270

Pin, C., Briot, D., Bassin, C., & Poitrasson, F. (1994). Concomitant separation of strontium and samarium-neodymium for isotopic analysis in silicate samples, based on specific extraction chromatography. Analytica Chimica Acta, 298(2), 209–217. https://doi.org/10.1016/0003-2670(94)00274-6

Reimer, P. J., Edouard Bard, B., Alex Bayliss, B., Warren Beck, B. J., Paul Blackwell, B. G., & Christopher Bronk Ramsey, B. (2013). Intcal13 and Marine13 Radiocarbon Age Calibration Curves 0–50,000 Years Cal Bp. Radiocarbon, 55(4), 1869–1887. https://doi.org/10.1017/S0033822200048864

Reyes, A. V, Carlson, A. E., Beard, B. L., Hatfield, R. G., Stoner, J. S., Winsor, K., … Ullman, D. J. (2014). South Greenland ice-sheet collapse during Marine Isotope Stage 11. Nature, 510(7506), 525–528. https://doi.org/10.1038/nature13456

Rhein, M., Kucera, M., Gohl, K. et al. (2013). DAVIS GATE - Geodynamic evolution of Davis Strait and Baffin Bay and their role as a paleoceanographic gateway. No. MSM09. MARIA S. MERIAN-Berichte, 137.

Rignot, E., Fenty, I., Xu, Y., Cai, C., Velicogna, I., Cofaigh, C., … Duncan, D. (2016). Bathymetry data reveal glaciers vulnerable to ice-ocean interaction in Uummannaq and Vaigat glacial fjords, west Greenland. Geophysical Research Letters, 43(6), 2667–2674. https://doi.org/10.1002/2016GL067832

Rignot, E., Velicogna, I., Van Den Broeke, M. R., Monaghan, A., & Lenaerts, J. (2011). Acceleration of the contribution of the Greenland and Antarctic ice sheets to sea level rise. Geophysical Research Letters, 38(5), 1–5. https://doi.org/10.1029/2011GL046583

Rignot, Eric, & Kanagaratnam, P. (2006). Changes in the Velocity Structure of the Greenland Ice Sheet. Science, 311, 986–990.

Saini, J., Stein, R., Fahl, K., Weiser, J., Hebbeln, D., & Hillaire, C. (2020). Holocene variability in sea ice and primary productivity in the northeastern Baffin Bay. Arktos. https://doi.org/10.1007/s41063-020-00075-y

Schlitzer, R. (2020). Ocean Data View, odv.awi.de, 2020.

Schweinsberg, A. D., Briner, J. P., Licciardi, J. M., Bennike, O., Lifton, N. A., Graham, B. L., … Zimmerman, S. H. (2019). Multiple independent records of local glacier variability on Nuussuaq, West Greenland, during the Holocene. Quaternary Science Reviews, 215, 253–271. https://doi.org/10.1016/j.quascirev.2019.05.007

Schweinsberg, A. D., Briner, J. P., Miller, G. H., Bennike, O., & Thomas, E. K. (2017). Local glaciation in West Greenland linked to North Atlantic ocean circulation during the Holocene. Geology, 45(3), 195–198. https://doi.org/10.1130/G38114.1

Seidenkrantz, M. S., Ebbesen, H., Aagaard-Sørensen, S., Moros, M., Lloyd, J. M., Olsen, J., … Kuijpers, A. (2013). Early Holocene large-scale meltwater discharge from Greenland documented by foraminifera and sediment parameters. Palaeogeography, Palaeoclimatology, Palaeoecology, 391, 71–81. https://doi.org/10.1016/j.palaeo.2012.04.006

Sheldon, C., Jennings, A., Andrews, J. T., Ó Cofaigh, C., Hogan, K., Dowdeswell, J. A., & Seidenkrantz, M. S. (2016). Ice stream retreat following the LGM and onset of the west Greenland current in Uummannaq Trough, west Greenland. Quaternary Science Reviews, 147, 27–46. https://doi.org/10.1016/j.quascirev.2016.01.019

Simon, Q., Hillaire-Marcel, C., St-Onge, G., & Andrews, J. T. (2014). North-eastern Laurentide, western Greenland and southern Innuitian ice stream dynamics during the last glacial cycle. Journal of Quaternary Science, 29(1), 14–26. https://doi.org/10.1002/jqs.2648

Slabon, P., Dorschel, B., Jokat, W., & Freire, F. (2018a). Bedrock morphology reveals drainage

network in northeast Baffin Bay. Geomorphology, 303, 133–145. https://doi.org/10.1016/j.geomorph.2017.11.024
Slabon, P., Dorschel, B., Jokat, W., & Freire, F. (2018b). Submarine geomorphology of northeast Baf fi n Bay and its implications for local paleo-ice sheet dynamics. Geomorphology, 318, 88–100. https://doi.org/10.1016/j.geomorph.2018.06.007
Slabon, P., Dorschel, B., Jokat, W., Myklebust, R., Hebbeln, D., & Gebhardt, C. (2016). Greenland ice sheet retreat history in the northeast Baffin Bay based on high-resolution bathymetry. Quaternary Science Reviews, 154, 182–198. https://doi.org/10.1016/j.quascirev.2016.10.022
Solomina, O. N., Bradley, R. S., Hodgson, D. A., Ivy-Ochs, S., Jomelli, V., Mackintosh, A. N., … Young, N. E. (2015). Holocene glacier fluctuations. Quaternary Science Reviews, 111, 9–34. https://doi.org/10.1016/j.quascirev.2014.11.018
Søndergaard, A. S., Larsen, N. K., Lecavalier, B. S., Olsen, J., Fitzpatrick, N. P., Kjær, K. H., & Khan, S. A. (2020). Early Holocene collapse of marine-based ice in northwest Greenland triggered by atmospheric warming. Quaternary Science Reviews, 239. https://doi.org/10.1016/j.quascirev.2020.106360
Stacey, J. S., & Kramers, J. D. (1975). APPROXIMATION OF TERRESTRIAL LEAD ISOTOPE EVOLUTION BY A TWO-STAGE MODEL. Earth and Planetary Science Letters, 26, 207–221.
Tang, C. C. L., Ross, C. K., Yao, T., Petrie, B., DeTracey, B. M., & Dunlap, E. (2004). The circulation, water masses and sea-ice of Baffin Bay. Progress in Oceanography, 63(4), 183–228. https://doi.org/10.1016/j.pocean.2004.09.005
Tarasov, L., & Peltier, W. R. (2003). Greenland glacial history, borehole constraints, and Eemian extent. Journal of Geophysical Research: Solid Earth, 108(B3), 1–20. https://doi.org/10.1029/2001jb001731
Thomas, E. R., Wolff, E. W., Mulvaney, R., Steffensen, J. P., Johnsen, S. J., Arrowsmith, C., … Popp, T. (2007). The 8.2 ka event from Greenland ice cores. Quaternary Science Reviews, 26(1–2), 70–81. https://doi.org/10.1016/j.quascirev.2006.07.017
Thorarinsson, S. B., Holm, P. M., Duprat, H. I., & Tegner, C. (2012). Petrology and Sr-Nd-Pb isotope geochemistry of Late Cretaceous continental rift ignimbrites, Kap Washington peninsula, North Greenland. Journal of Volcanology and Geothermal Research, 219–220, 63–86. https://doi.org/10.1016/j.jvolgeores.2012.01.011
Thorarinsson, S. B., Holm, P. M., Duprat, H., & Tegner, C. (2011). Silicic magmatism associated with Late Cretaceous rifting in the Arctic Basin-petrogenesis of the Kap Kane sequence, the Kap Washington Group volcanics, North Greenland. Lithos, 125(1–2), 65–85. https://doi.org/10.1016/j.lithos.2011.01.013
Weidick, A., Bennike, O., Citterio, M., & Nørgaard-pedersen, N. (2012). Neoglacial and historical glacier changes around Kangersuneq fjord in southern West Greenland. Geological Survey of Denmark and Greenland Bulletin, 27, 1–68.
Weiser, J., Titschack, J., McCave, I. N., Lochte, A. A., Saini, J., Stein, R., & Hebbeln, D. (2021). Atlantic water inflow to Labrador Sea and its interaction with ice sheet dynamics during the Holocene. Quaternary Science Reviews, 4545(4545), 4545–1. https://doi.org/10.1016/j.quascirev.2021.106833
Weiser, J. (personal communication 2021): J. Weiser constructed the age model for GeoB19946-4 which is currently in preparation for submission in the framework of his PhD thesis as well as in preparation for submission to a scientific journal: Weiser, J., Hebbeln, D., Titschack, J., Caron, M., St-Onge G. (in prep.). Widespread mass wasting in Melville Bay coincident with Nares Strait opening.
White, L. F., Bailey, I., Foster, G. L., Allen, G., Kelley, S. P., Andrews, J. T., … Storey, C. D. (2016). Tracking the provenance of Greenland-sourced, Holocene aged, individual sand-sized ice-rafted debris using the Pb-isotope compositions of feldspars and 40Ar/39Ar ages of hornblendes. Earth and Planetary Science Letters, 433, 192–203. https://doi.org/10.1016/j.epsl.2015.10.054
Young, N. E., & Briner, J. P. (2015). Holocene evolution of the western Greenland Ice Sheet:

Assessing geophysical ice-sheet models with geological reconstructions of ice-margin change. Quaternary Science Reviews, 114, 1–17. https://doi.org/10.1016/j.quascirev.2015.01.018

Young, N. E., Briner, J. P., Rood, D. H., Finkel, R. C., Corbett, L. B., & Bierman, P. R. (2013). Age of the Fjord Stade moraines in the Disko Bugt region , western Greenland , and the 9 . 3 and 8 . 2 ka cooling events. Quaternary Science Reviews, 60, 76–90. https://doi.org/10.1016/j.quascirev.2012.09.028

CHAPTER FIVE

Manuscript three

Radiogenic Isotope Signatures of Holocene Sediments from Kane Basin: Linkage with the Re-opening and Evolution of Nares Strait

Lina Madaj[1], Friedrich Lucassen[1], Claude Hillaire-Marcel[2] and Simone A. Kasemann[1]

[1] MARUM—Center for Marine Environmental Sciences & Faculty of Geosciences, University of Bremen, Germany
[2] GEOTOP—Centre de recherche en géochimie et géodynamique, Université du Québec à Montréal, Canada

This manuscript is in preparation for submission to Journal of Quaternary Sciences

5. Radiogenic Isotope Signatures of Holocene Sediments from Kane Basin: Linkage with the Re-opening and Evolution of Nares Strait

Abstract

The re-opening of the Arctic Ocean-Baffin Bay gateway through Nares Strait, following the Last Glacial Maximum, has been partly documented, discussed and revised in the past decades. The Nares Strait opening has led to the inception of the modern fast circulation pattern carrying low salinity Arctic water towards Baffin Bay and further towards the Labrador Sea. This low-salinity water impacts thermohaline conditions in the North Atlantic, thus the Atlantic Meridional Overturning Circulation. Available land-based and marine records set the complete opening between 9 and 7.5 ka BP, although the precise timing and intensification of the southward flowing currents is still open to debate. A recent study of a marine deglacial sedimentary record from Kane Basin, central Nares Strait, adds information about subsequent paleoceanographic conditions in this widened sector of the strait and proposed the complete opening at ~8.3 ka BP.

We present complementary radiogenic Sr, Nd and Pb isotope data of the siliciclastic detrital sediment fraction of this very record further documenting the timing and pattern of Nares Strait opening from a sediment provenance approach. The data permit to distinguish detrital material from northern Greenland and Ellesmere Island, transported to the core location from both sides of Nares Strait. Throughout the Holocene, the evolution of contributions of these two sources hint to the timing of the collapse of the ice saddle in Kennedy Channel, north of Kane Basin, which led to the complete opening of Nares Strait. The newly established gateway of material transported to the core location from the north via Kennedy Channel is recorded by increased contribution of northern Ellesmere Island detrital sediment input. This shift from a Greenland (Inglefield Land) dominated sediment input to a northern Ellesmere Island dominated sediment input supports the hypothesis of the newly proposed timing of the complete opening of Nares Strait at 8.3 ka BP and highlights a progressive trend towards modern-like conditions, reached around 4 ka BP.

5.1. Introduction

The Nares Strait is an important gateway of Arctic Ocean freshwater continuing through Baffin Bay into the Labrador Sea and the subpolar North Atlantic. Nares Strait connects the Lincoln Sea in the Arctic Ocean and Baffin Bay, a mediterranean sea between Greenland and Baffin Island, Canada. During the Last Glacial Maximum (LGM) the strait has been blocked by the prevailing ice sheets, the Greenland Ice Sheet (GIS) and the Innuitian Ice Sheet (IIS). The freshwater pathway between the Arctic Ocean and the subpolar North Atlantic via Baffin Bay and the Labrador Sea has therefore been disabled during these times and only fully re-established around 8.3 ka BP (Georgiadis et al., 2018). The complete opening of Nares Strait for Arctic Ocean freshwater into Baffin Bay initiated the current ocean circulation pattern of Baffin Bay, a counter-clockwise surface current gyre merging Atlantic sourced waters with Arctic Ocean freshwater (Jennings et al., 2011; Tang et al., 2004). The re-connection of Baffin Bay and the Arctic Ocean via Nares Strait plays an important role in freshwater and sea-ice contribution into the Labrador Sea (Goosse et al., 1997; Kwok, 2005; Tang et al., 2004) where deep convection occurs and the formation of North Atlantic Deep Water represents the initiation of the Atlantic Meridional Overturning Circulation.

The Holocene deglacial development of Nares Strait and its complete re-opening have been studied in a number of studies but still remain subject to uncertainty (Georgiadis et al., 2018; Jennings et al., 2019; Mudie et al., 2004). Until recently the most accurate timeline has been established and summarised by England (1999) who reconstructed the GIS and IIS extent and deglaciation based on radio carbon dates collected along Nares Strait. England (1999) concluded that the northern part of the strait was deglaciated by 10.1 ka BP and the southern end by 9.0 ka BP, certain parts were still blocked by ice around 8 ka BP and not entirely ice-free until 7.5 ka BP. Additionally, Zreda et al. (1999) measured cosmogenic ^{36}Cl on glacially polished bedrock from two island in Nares Strait, where the ice retreated around 10 ka BP. These land-based records were later supplemented by marine records from Hall Basin, northern Nares Strait, which revealed new insights into its deglacial history (Jennings et al., 2011; Mudie et al., 2004) and reclassified the complete opening of Nares Strait to around 9.0 ka BP (Jennings et al., 2011).

More recently a well-preserved record from Kane Basin, central Nares Strait, covering the past 9,000 years served as the basis to re-date the complete opening of Nares Strait to around 8.3 ka BP (Georgiadis et al., 2018). The record further contains indications for the earlier suggested opening around 9 ka BP (Jennings et al., 2011) but Georgiadis et al. (2018) argued substantiated for the later opening around 8.3 ka BP. Their hypothesis has been complemented and corroborated through subsequent studies on the same record (Caron et al., 2020, 2019a). This record represents the first well-preserved marine sedimentary archive documenting ice-free condition in Kane Basin during the Holocene (Georgiadis et al., 2018). Later Jennings et al. (2019) pointed out that due to uncertainties in radio carbon ages and correction values (ΔR) it is still hard to define an exact age for the opening of Nares Strait and proposed a time frame between 9.0 and 8.3 ka BP. This time interval agrees with the most recent date for the Nares Strait opening of 9.0 ± 1.1 ka BP (Ceperley et al., 2020).

The prevailing uncertainties concerning the deglaciation history of Nares Strait and differing timings proposed for its complete opening yield potential for further investigations, especially with regards to the Arctic Ocean freshwater gateway and its influence on the Baffin Bay and Labrador Sea circulation patterns (Jennings et al., 2011; Jennings et al., 2019). Here we present radiogenic isotope records of the sedimentary archive from Kane Basin to further corroborate the hypothesis of the complete Nares Strait opening around 8.3 ka BP as proposed by Georgiadis et al. (2018). Radiogenic isotopes serve as reliable provenance tracers for detrital sediment input and indirect reconstruction of past ice-sheet and glacier movements. Newly established detrital sediment sources caused by unblocking of ice in Nares Strait can be detected by changes in radiogenic isotope composition.

5.2. Regional Setting and Research Area

5.2.1. Current Setting

Nares Strait is a 530 km long channel between northern Greenland and Ellesmere Island (Figure 5.1). It consists of two basins, a larger but shallower one (Kane Basin, 220 m water depth) and a smaller but deeper one (Hall Basin, 800 m water depth), both are connected via Kennedy Channel. Robeson Channel and Smith Sound form the northern and southern end of Nares Strait, respectively. Nares Strait is the main gateway of Arctic Ocean freshwater into Baffin Bay and Labrador Sea and therefore into the North Atlantic. Further gateways are through straits in the Canadian Arctic Archipelago (CAA) which, together with Nares Strait,

make up around 30% of the Arctic Ocean fresh water export (e.g. Jennings et al., 2011; Zreda et al., 1999). The water is spilling over a sill in Kane Basin (Tang et al., 2004) and is merging with water from the West Greenland Current (WGC) in Northern Baffin Bay and forming the Baffin Island Current travelling southwards along the Canadian coast to leave Baffin Bay through Davis Strait and contribute to deep water formation in the Labrador Sea and the subpolar North Atlantic. Nares Strait is seasonally ice-covered, at least 80% for 11 months (Jennings et al., 2011). A seasonal ice bridge at the southern end of the strait (Smith Sound) is functioning as an important block of sea ice sustaining the North Water polynya (NOW), one of the most productive and the largest polynyas in the western Arctic (Barber et al., 2001; Melling et al., 2001; Dunbar, 1981; Dunbar & Dunbar, 1972). When the polynya is ice-free by May or June it spans over wide parts of northernmost Baffin Bay with its northern boundary in southern Kane Basin and has been active throughout most of the past 9,000 years (Levac et al., 2001).

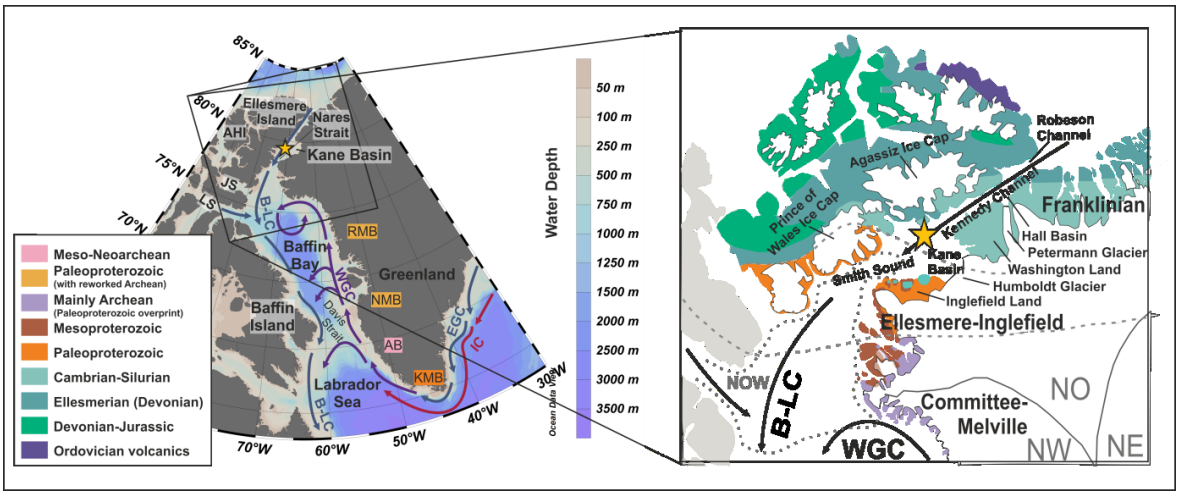

Figure 5.1: Area map of Baffin Bay and Nares Strait and their present-day surface current patterns. Core location of gravity core AMD14-Kane2B is marked by the yellow star. Colours in the right map (legend left) indicate the different geological terrains of northern Greenland and Ellesmere and Axel Heiberg Islands (AHI). White areas represent the Greenland Ice Sheet and the Ellesmere and Axel Heiberg Islands ice caps. Grey lines represent the present day drainage areas of the Greenland Ice Sheet, NO = North, NW = North West, NE = North East (White et al., 2016). Greenland geology and boundary extensions (dashed grey lines) are taken from Dawes (2009a), Ellesmere and Axel Heiberg Islands geology is taken from Harrison et al. (2011) and Estrada (2015, and references therein). The dotted outline sketches the average June extent of the North Water polynya (NOW) (Dunbar, 1969). JS = Jones Sound, LS = Lancaster Sound, B-LC = Baffin-Labrador Current, WGC = West Greenland Current, EGC = East Greenland Current, IC = Irminger Current. KMB = Ketilidian Mobile Belt, AB = Archean Block, NMB = Nagssugtoqidian Mobile Belt and RMB = Rinkian Mobile Belt (left figure) represent the locations of further Greenland geological units used for reference. Overview map created with Ocean Data View (Schlitzer, 2020).

Nares Strait receives meltwater and detrital material input from the surrounding Greenland Ice Sheet and glaciers, especially Humboldt and Peterman Glaciers and the remaining ice caps of Ellesmere Island, including the Agassiz and Prince of Wales ice caps. The ice-free coast of Nares Strait is characterised by dissected plateaus on the Greenland side and northern Ellesmere Island, while southern Ellesmere Island is characterised by narrow valleys and fjords (England, 1999). The surrounding geology comprises of the Paleoproterozoic gneisses and granites of the Ellesmere-Inglefield Mobile Belt around southern Kane Basin and Nares Strait and Palaeozoic carbonate rocks of the Ellesmerian-Franklinian Basin north of Kane Basin (Dawes, 2009a; Dawes, 2009b; England, 1999) (Figure 5.1).

5.2.2. Past Setting

During the LGM Nares Strait has been entirely covered by extensions of the GIS and the IIS whose retreat enabled the inflow of Arctic Ocean water into Baffin Bay and the initiation of its current circulation pattern. GIS and IIS merged offshore, in the middle of Nares Strait (England, 1999) and their deglaciation was recorded by meltwater channels and moraines that mark the progressive thinning and separation of those ice sheets (England et al., 2006). The deglaciation began around 10.1 ka BP at the northern end and around 9.0 ka BP at the southern end of the strait (England, 1999); however, total deglaciation and resulting reconnection of the Arctic Ocean and Baffin Bay did not complete until 8.3 ka BP (Georgiadis et al., 2018). The IIS covering Ellesmere Island retreated from west to east after 11 ka BP, leaving only island-based ice caps by 9 ka BP and the sea penetrating the eastern CAA by 8.5 ka (England et al., 2006). On the Greenland side, Washington Land, adjacent to Humboldt Glacier, was one of the last major land masses that became deglaciated after the LGM (Bennike, 2002; Bennike & Björck, 2002). Across all elevations the GIS retreated from Washington Land by 8.6 ±1.1 ka BP (Ceperley et al., 2020).

Within Nares Strait, Kane Basin and Hall Basin were not connected until ~8.3 ky BP as a result of the break-up of the ice saddle connecting the GIS and IIS in Kennedy Channel (Georgiadis et al., 2018). Hall Basin became deglaciated soon before 10.3 ka BP (Jennings et al., 2011) while the GIS retreated in eastern Kane Basin around 8.1 ka BP (Georgiadis et al., 2018). The seasonal sea-ice cover of Nares Strait, especially in Kane Basin, has been prevailing at least throughout the past 9,000 years, with periods of highly variable sea-ice extent due to climate and oceanographic changes (Georgiadis et al., 2020).

5.3. Material and Methods

A 425 cm sediment core (AMD14-Kane2B) has been collected in Kane Basin, central Nares Strait (79°30.91'N; 70°49.74'W) at a water depth of 220 m onboard *CCGS Amundsen* during ArcticNet expedition (Leg 1b) in 2014 (Tremblay et al., 2014). The core was taken with a square section gravity corer (Calypso Square) and immediately subsampled onboard. The core has previously been object to different studies, including grain size and X-ray fluorescence (XRF) (Georgiadis et al., 2018), mineralogical composition trough X-ray diffraction (XRD) (Caron et al., 2020), sediment magnetic properties (Caron et al., 2019a), sea-ice biomarker (Georgiadis et al., 2020) as well as dinoflagellate cyst assemblages and organic linings of (benthic) foraminifera (Caron et al., 2019b).

5.3.1. Core Description and Age Chronology

The sediment lithology of gravity core AMD14-Kane2B has been described in detailed by Georgiadis et al. (2018) and Caron et al. (2019a). The core consists of varying sand and silt contents integrated in a clay-dominating greyish brown sediment matrix. In the bottom of the core alternating layers of coarser and finer material with occasional occurrence of clasts can be observed. Two intervals of increased sedimentation rates, ~130cm/ka and ~190cm/ka, can be found from 370 to 320 cm and from 300 to 280 cm, respectively (Georgiadis et al., 2018). Between 280 and 250 cm a significant increase in sand content and decrease in clay content can be noted. From 250 cm onwards the silt content gradually increases and the sediments become comparably homogenous with nearly even proportions of silt and clay. Generally, some appearance of ice rafted debris (IRD) is recorded throughout the entire record, with the only significant increase between 298 and 320 cm (Caron et al., 2020, 2019a).

The age model has been constructed by Georgiadis et al. (2018) and is based on 18 radiocarbon dates of mixed benthic foraminifera and unidentified mollusc shells. The core top has been dated to -5 years BP (1955 CE) by ^{210}Pb chronology, which is in accordance with the ^{210}Pb record of a boxcore from the same location (Georgiadis et al., 2018). The ages were calibrated according to the *Marine 13* curve (Reimer et al., 2013) using the CALIB 7.1 software (Stuiver et al., 2017) with a marine reservoir correction of 640 years (ΔR = 240±51), based on three pre-bomb collected mollusc shells from Nares Strait (Georgiadis et al., 2018). The final age model has been constructed using the CLAM 2.2 software (Blaauw, 2010) and covers the past 9,000 years. The interval between 320 and 298 cm has been excluded from the age model as the very high sedimentation rates suggest a rapidly deposited layer (Georgiadis et al., 2018).

Based on CT scans and grain size data (Georgiadis et al., 2018) divided the core into five lithological units (their figure 6 & table 2), which will be further used to support the radiogenic isotope data obtained in this study and mainly agree with the intervals defined by Caron et al. (2019a) for the AMD14-Kane2B record.

5.3.2. Isotope Ratio Measurements

Sample preparation and measurements of radiogenic isotope ratios were performed in the Isotope Geochemistry Laboratory at MARUM—Centre for Marine Environmental Sciences, University of Bremen, Germany. The bulk samples have been used for analysis, no grain-size separation has been conducted to receive a combined transport signal, not biased by any specific transport pathway. Between 1 – 2 g of bulk sample were homogenised using a mortar, washed with ultrapure water (18.2 MΩ; Millipore) to remove pore water, decarbonised with a 40 % acetic acid solution (buffered to pH ~4 with 1M Na-acetate) and leached with hydroxylamine hydrochloride and 15 % acetic acid (buffered to pH ~4 with NaOH) to remove any possible sediment grain coatings (cf. Gutjahr et al., 2007). Following, stepwise hot-acid digestion with hydrofluoric acid (5:1, HF:HNO_3), Aqua Regia (3:1, 6M HCl:concentrated HNO_3), nitric acid (concentrated), hydrochloric acid (6M) and hydrogen peroxide was applied to 100 mg of the sample to receive the siliciclastic detrital sediment fraction and remove organic matter. The final sample was dissolved in nitric acid (2M) for radiogenic isotope separation. Radiogenic isotopes were received through column separation using TrisKem Sr.spec™ resin (method modified after Deniel & Pin, 2001), TRU.spec™ resin and LN.spec™ resin (method from Pin et al., 1994) for Sr and Pb, light rare earth elements and Nd separation, respectively. Isotopic ratios were analysed on a Thermo Fisher Scientific Triton™ Plus multicollector thermal ionization mass spectrometer (TIMS) in either multidynamic (Sr) or static (Nd, Pb) multicollection mode. The following international reference materials were measured along with the samples for measurement consistency: NIST SRM 987 (Sr), JNdi-1 (Nd) and NIST SRM 981 (Pb). Throughout the measurement period of ten days, standard values varied within the range of 0.710246 ±0.000009 (^{87}Sr/^{86}Sr ±2SD$_{mean}$; n=3), 0.512136 ±0.000016 (^{143}Nd/^{144}Nd ±2SD$_{mean}$; n=3) and 16.8928 ±0.0069 (^{206}Pb/^{204}Pb ±2SD$_{mean}$; n=2), which are within the range of published reference values measured on TIMS (GeoReM data base; query June 2020; http://georem.mpch-mainz.gwdg.de): 0.710249 ±0.000034 (^{87}Sr/^{86}Sr ±2SD$_{mean}$; n=1528), 0.512107 ±0.000026 (^{143}Nd/^{144}Nd ±2SD$_{mean}$; n=339) and 16.9211 ±0.0413 (^{206}Pb/^{204}Pb ±2SD$_{mean}$; n=254). A bulk uncertainty of 0.1% per atomic mass unit was assumed for Pb values to account for isotopic fractionation during the measuring process, which exclusively exceeds the measured uncertainty. Nd isotope ratios are displayed in εNd notation normalized to ancient Chondritic Uniform Reservoir (CHUR) value of 0.512638 as defined by Jacobsen & Wasserburg (1980):

$$(\varepsilon_{Nd} = \left\{\left[\left(^{143}Nd/^{144}Nd\right)_{Sample}/\left(^{143}Nd/^{144}Nd\right)_{CHUR}\right] - 1\right\} * 10^4)$$

5.4. Results

5.4.1. Radiogenic Isotope Records

The siliciclastic detrital radiogenic isotope record of AMD14-Kane2B (Figure 5.2) can be subdivided into the temporal intervals proposed by Georgiadis et al. (2018) and Caron et al. (2019a): the Deglacial (~8.9-7.5 ka BP) and Postglacial (~7.5 ka BP onwards) periods. The lower part of the core (~8.9-7.5 ka BP) is characterised by pronounced variations in isotopic composition throughout all three isotopic systems, ranging between 0.725 and 0.736 ($^{87}Sr/^{86}Sr$), -25.5 and -13.4 (εNd) and 17.78 and 18.54 ($^{206}Pb/^{204}Pb$). While the $^{87}Sr/^{86}Sr$ and εNd records display actual fluctuations the variations within the $^{206}Pb/^{204}Pb$ isotopic composition is rather composted of a steep trend towards initial values with one peak around 8.3 ka BP. Around 7.5 ka BP values follow a trend towards more radiogenic εNd and $^{206}Pb/^{204}Pb$ values and less radiogenic $^{87}Sr/^{86}Sr$ values. This trend is diminished after ~4.5 ka BP when only a slight trend continuous towards the core top. Within this interval values range from 0.728 to 0.724 ($^{87}Sr/^{86}Sr$), -16.7 to -13.3 (εNd), and 18.21 to 18.28 ($^{206}Pb/^{204}Pb$).

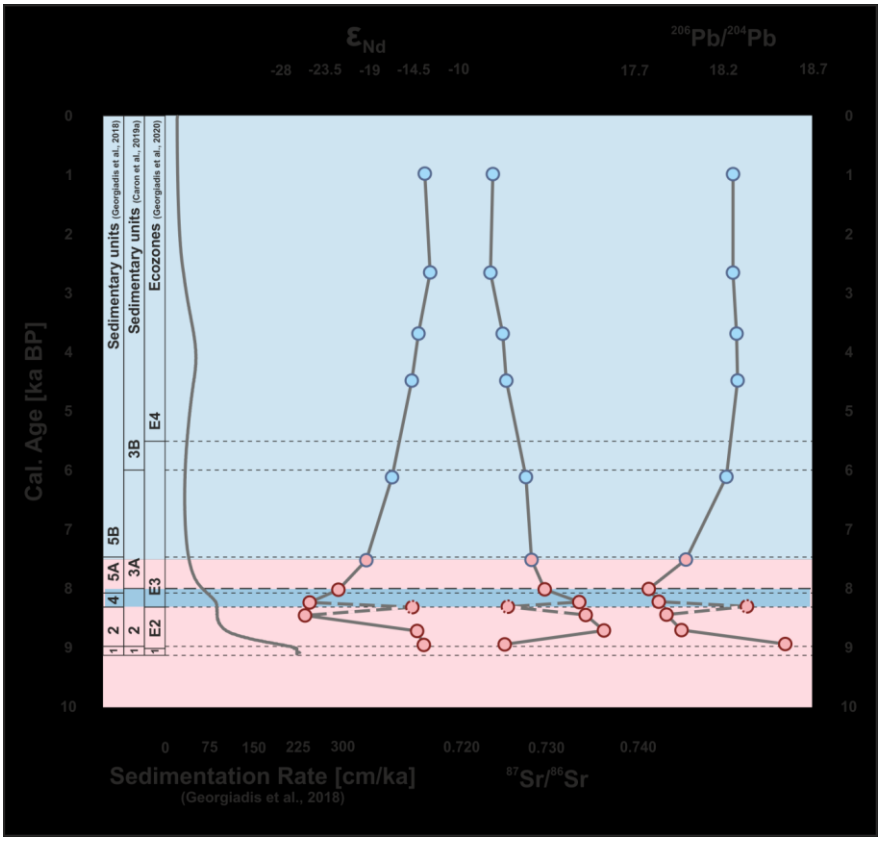

Figure 5.2: Radiogenic isotope records of the siliciclastic detrital sediment fraction of gravity core AMD14-Kane2B. Analytical uncertainties are smaller than data points. Highlighted time intervals represent the Holocene Thermal Maximum (red), the thicker dashed line marks the end of the Deglacial period, and Neoglacial (blue) Holocene. Dashed lines and corresponding boxes on the left mark the sedimentary units and ecozones of previous publications (Caron, et al., 2019a; Georgiadis et al., 2020, 2018). Age model and sedimentation rate were previously published by Georgiadis et al. (2018).

Changes in isotopic composition go along with the changes in lithology previously described by Georgiadis et al. (2018) and Caron et al. (2019a). Their sedimentary units five and three

(~8.1-0 ka BP, Figure 5.2), respectively, cover the interval of less isotopic variability, while all other intervals cover higher variability in the lower part of the core.

5.4.2. Detrital Sediment Provenance

To identify possible provenance shifts, data of $^{87}Sr/^{86}Sr$ versus εNd (Figure 5.3 A) and $^{206}Pb/^{204}Pb$ versus $^{207}Pb/^{204}Pb$ (Figure 5.3 B) of gravity core AMD14-Kane2B are plotted alongside ranges of isotopic background data of possible source regions taken from literature. While the Sr-Nd data plot in between of several sources from northern and western Greenland as well as Ellesmere Island, the Pb data plot directly into the range of these mainly overlapping sources. Both plots identify a clear shift of source region within the detrital sediment composition over time with an obvious difference between the Deglacial and Postglacial Holocene.

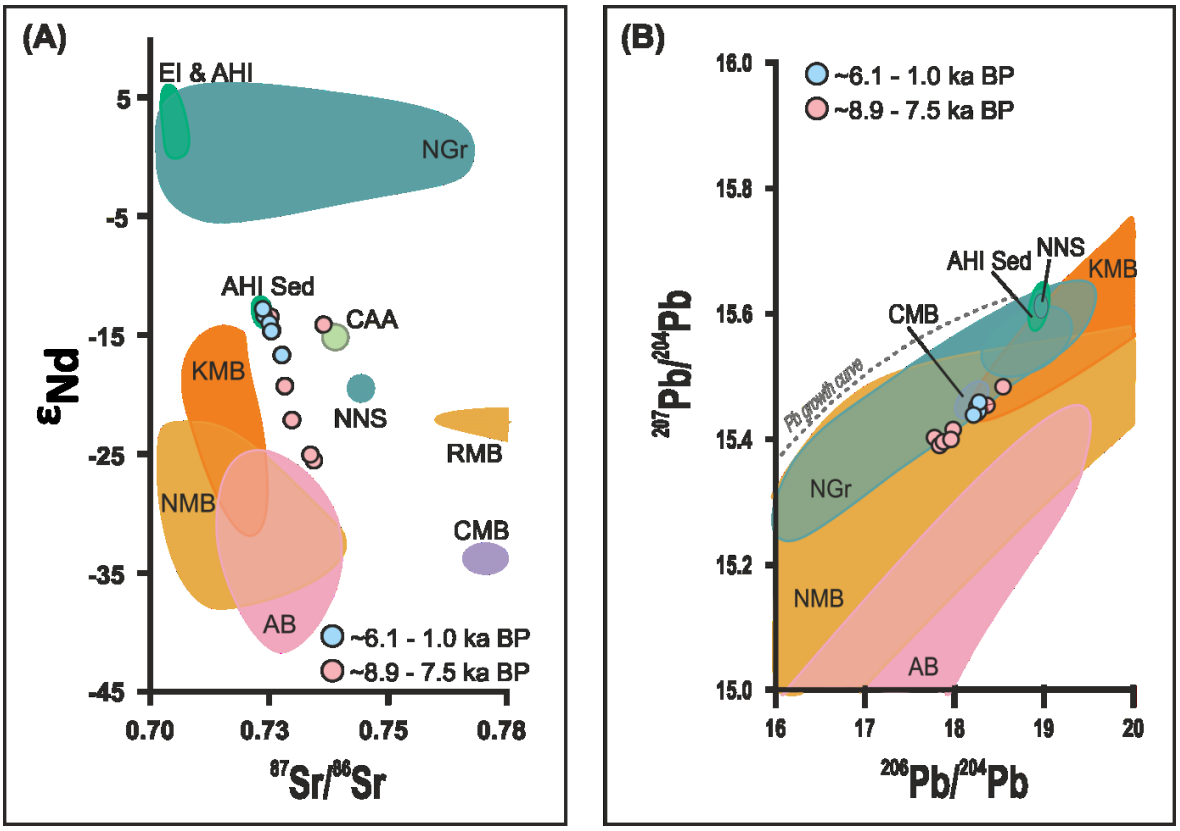

Figure 5.3: Radiogenic isotope composition of the siliciclastic detrital sediment fraction from gravity core AMD14-Kane2B and isotopic ranges of the main Greenland and Ellesmere Island geological terrains for $^{87}Sr/^{86}Sr$ versus ε_{Nd} (A) and $^{206}Pb/^{204}Pb$ versus $^{207}Pb/^{204}Pb$ (B). Colours represent the geological terrains included in Figure 5.1**Figure 3.1** : KMB = Ketilidian Mobile Belt, AB= Archean Block, NMB = Nagssugtoqidian Mobile Belt, RMB = Rinkian Mobile Belt, CMB = Committee Melville Belt, NGr = Northern Greenland, EI & AHI = Ellesmere & Axel Heiberg Islands, CAA = Canadian Arctic Archipelago, NNS = Northern Nares Strait. Background data for isotopic ranges originates from stream sediments (Colville et al., 2011; Reyes et al., 2014), surface sediments (Maccali et al., 2018; this thesis study (see chapter 4)) and rock data (Dostal & Macrae, 2018; Estrada, 2015; Estrada et al., 2010; Kalsbeek et al., 1998; Thorarinsson et al., 2012, 2011). Dashed grey line in figure (B) represents the Pb growth curve of continental crust (Stacey & Kramers, 1975).

5.5. Discussion

In the framework of the previous studies by Georgiadis et al. (2018) and Caron et al. (2019a) gravity core AMD14-Kane2B has been divided into different time intervals and sedimentary units based on lithology and micropaleontological species abundances. These intervals will serve in this study as a structure of discussion and support of the radiogenic record as changes

in isotopic composition coincide with changes in other lithological, geochemical and micropaleontological parameters and tracers.

5.5.1. Deglacial Period and Holocene Thermal Maximum (~9.0 – 7.5 ka BP)

5.5.1.1. Time Interval 9 – 8.3 ka BP

The period between ~9 and 8.3 ka BP has been described by Georgiadis et al. (2020, 2018) as the deglaciation of Kane Basin. This time interval was characterised by a short-lived transition from an ice-proximal deposition environment to a secluded and narrow bay while the adjacent ice sheets IIS and GIS retreaded. An abrupt change was recorded around 8.3 ka BP with the collapse of the ice saddle in Kennedy Channel that was the last connection between the IIS and GIS and marked the complete opening of Nares Strait as an Arctic Ocean water gateway (Georgiadis et al., 2018). Caron, et al. (2019a) defined this deglacial period until ~8 ka BP which is in better agreement with the isotopic record and will be further used for interpretation. The isotopic composition of radiogenic isotopes Sr, Nd and Pb displays the highest ranges of the entire record within this time interval. εNd shifts from nearly most radiogenic to the most unradiogenic values, while $^{87}Sr/^{86}Sr$ follows the exact opposite trend, nearly most unradiogenic to most radiogenic. $^{206}Pb/^{204}Pb$ displays the most pronounced trend from most radiogenic values to least radiogenic values between ~8.9 and 8 ka BP.

The lowest value of the isotopic record (~8.9 ka BP) represents entirely different $^{87}Sr/^{86}Sr$ and $^{206}Pb/^{204}Pb$ values than the values of the following millennium (Figure 5.2). With the exception of the second lowest value (~8.7 ka BP) this is also the case for the εNd values. These differences in isotopic composition around 8.9 ka BP and between 8.7 and the following time interval, represent distinct differences in detrital sediment composition (Figure 5.4). While the ~8.9 ka BP values plot into the range of surface sediments around Ellesmere Island and Axel Heiberg Island the following data points plot into the vicinity of southern Greenland sources. The Pb isotopic composition at ~8.9 ka BP supports the higher Ellesmere Island and Axel Heiberg Island influence. Here the possible Archean to Palaeoproterozoic sources of gneisses and granites that is represented by the southern Greenland signatures is not as certain. However, it has to be noted that the closest isotopic background signatures are those of the southern and midwest Greenland terrains (Colville et al., 2011; Reyes et al., 2014). The Ketilidian Mobile Belt (KMB) of southernmost Greenland is geologically similar to the Ellesmere-Inglefield Mobile Belt of northern Greenland and southern Ellesmere Island (Dawes, 2009a) and will therefore be used as the closes analogue due to limited background data availability.

In comparison with the geochemical and mineralogical record of AMD14-Kane2B provided by Caron et al. (2020) the detrital sediment provenance shift after 8.9 ka BP can be confirmed. Caron et al. (2020) defined provenances based on the SedUnMixMC programm (Andrews & Eberl, 2012; Andrews et al., 2015) which suggest an interplay of Ellesmere Island and Inglefield Land provenances, with a dominant contribution of Ellesmere Island sources before 8.8 ka BP and a dominating contribution of Inglefield Land sources afterwards. The lowest part of the isotopic record covers the time interval interpreted by Caron et al. (2020) and Georgiadis et al. (2018) as an interval of major retreat of the ice sheets on both Ellesmere Island and Inglefield Land and the corresponding discharge of detrital sediments into Kane Basin. They ascribe the shift around 8.8 ka BP towards a dominance of Inglefield Land sources in response to faster retreat of the GIS and discharge from the adjacent Humboldt Glacier (cf. Reusche et al., 2018).

The most abrupt changes in isotopic composition are recorded between 8.9 and 8.3 ka BP during intervals of high sedimentation rates (~130 cm/ka mean sedimentation rate (Georgiadis et al., 2018)). This interval is also the time period for which Georgiadis et al. (2018) interpreted the location of the GIS to be yet relatively close to the core location, suggesting high local input through meltwater discharge. Generally, this time interval has been described as an interval of unstable conditions with input of different sedimentary sources, supported by the numerous changes in lithology (Caron et al., 2019a; Georgiadis et al., 2018) (Figure 5.2). This interplay of different sources further supports the interpretation of the isotopic record and might explain the Nd isotopic composition at ~8.7 ka BP that does not follow the same trend as the Sr and Pb isotopic compositions.

This time period also coincides with the Holocene Thermal Maximum (HTM) between 9 and 5 ka as summarised by Kaufman et al., (2004) and further defined by Lecavalier et al., (2017) to last until 7.5. Increased atmospheric temperatures during the HTM support the assumption of high melting rates discharging large amount of local material from both coasts (Georgiadis et al., 2018; Lecavalier et al., 2017).

5.5.1.2. Time Interval 8.3 ka BP – Opening of Kennedy Channel

An IRD-rich layer within the AMD14-Kane2B record with extremely high sedimentation rates between 320 and 298 cm core depth has been dated to 8.3 ka BP as a rapidly deposited layer (Georgiadis et al., 2018). This layer has been interpreted to mark the opening of Kennedy Channel, which might have led to intense calving of GIS sourced glaciers, including intensified calving of the local Humboldt Glacier (Georgiadis et al., 2018; Reusche et al., 2018). The isotopic composition of this layer clearly differs from that of the prior (and following) interval within all three isotopic systems, it display similar Sr and Nd values as the ~8.9 ka BP sample and points to a larger contribution of Ellesmere Island sources. The isotopic signatures together with an increased carbonate signal in the sediment geochemistry (Georgiadis et al., 2018) point to northern Ellesmere Island as the origin of the increased amounts of IRD recorded around 8.3 ka BP, transported southwards through the newly opened gateway into Kane Basin. This assumption is further supported by the simultaneously established general circulation pattern (cf. Georgiadis et al., 2018). However, Georgiadis et al. (2018) as well as Jennings et al. (2019) discussed the plausibility of this layer marking the opening of the strait, with respect to the earlier IRD-rich layer deposited around 8.9 ka BP. Georgiadis et al. (2018) argue for 8.3 ka BP based on elemental composition and source region determination, rather than input from Humboldt Glacier through intensified calving as suggested by Reusche et al. (2018). Later, Jennings et al. (2019) found no evidence for intensified Humboldt Glacier calving around 8.3 ka BP within their record south of Smith Sound, but point out that the exact timing of Nares Strait opening is still difficult to determine. Due to the close temporal spacing of both IRD-rich layers and the given uncertainties of the corresponding age models based on ΔR uncertainties Jennings et al. (2019) suggest to define the opening of Nares Strait within the time interval of 9.0 and 8.3 ka BP rather than an exact timing. The isotopic composition of both these layers is comparably similar in Sr und Nd composition. The Pb isotopic composition, however, differs with the older layer being more radiogenic. At 8.3 ka BP the Pb isotopic composition is similar to the composition of those samples clearly deposited after the strait was completely open, representing northern Ellesmere Island sources, while the composition at 8.9 ka BP differs from all other signatures recorded throughout the core (Figure 5.4 B).

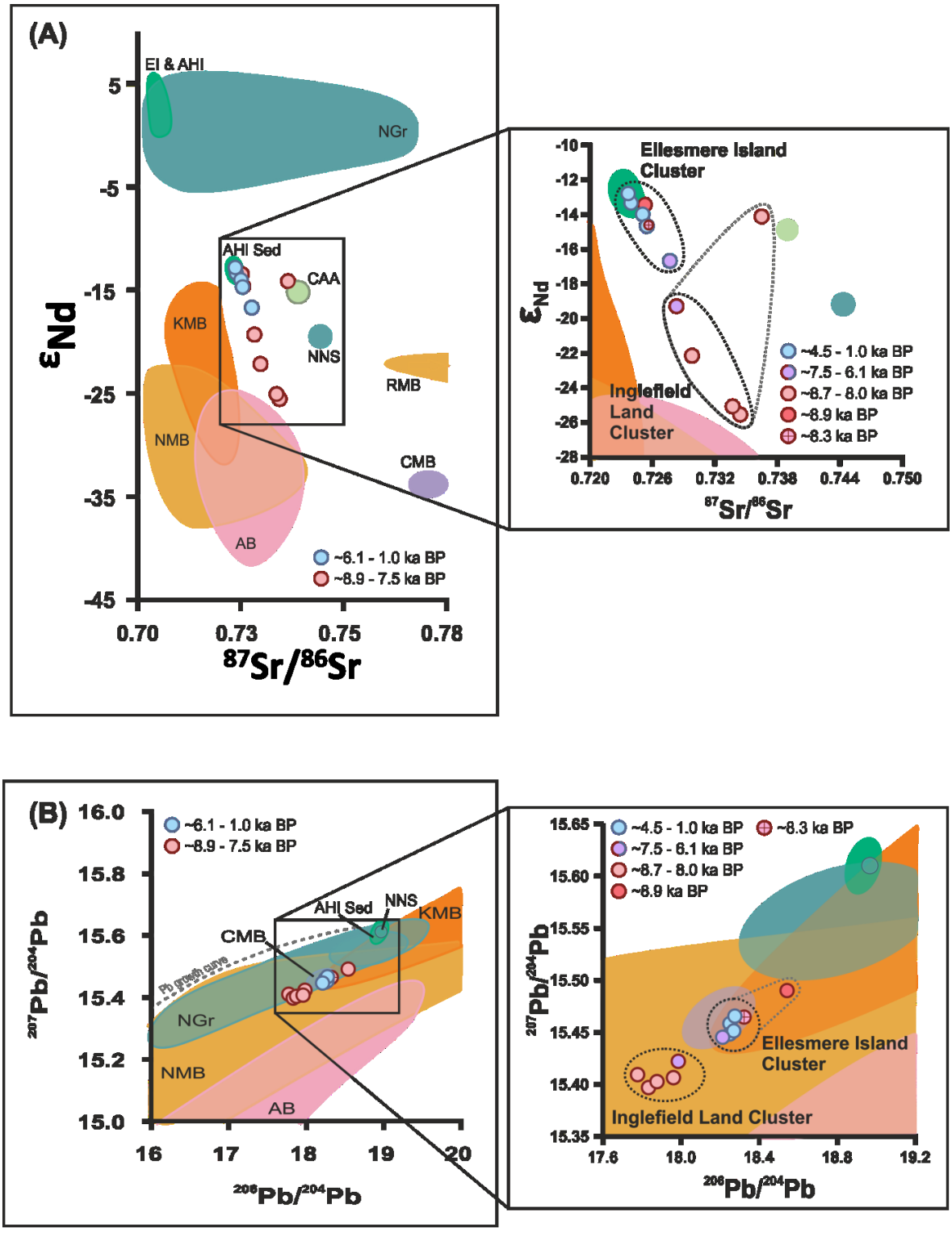

Figure 5.4: Close-up of Sr – Nd (A) and Pb (B) provenance plot for gravity core AMD14-Kane2B data. KMB = Ketilidian Mobile Belt, AB= Archean Block, NMB = Nagssugtoqidian Mobile Belt, RMB = Rinkian Mobile Belt, CMB = Committee Melville Belt, NGr = Northern Greenland, EI & AHI = Ellesmere & Axel Heiberg Islands, CAA = Canadian Arctic Archipelago, NNS = Northern Nares Strait. Reference data for provenance plots as in Figure 5.3.

The unique 8.9 ka BP signature also pointing to Ellesmere Island sources is most likely connected to the retreat of glaciers and ice caps on both sides of Kane Basin, marking the deglaciation of the basin (cf. Caron et al., 2020; Georgiadis et al., 2020, 2018). Therefore, we suggest that the proposed timing of 8.3 ka BP (Georgiadis et al., 2018) is more likely to represent the complete opening of Nares Strait.

5.5.1.3. Time Interval 8.3-7.5

From 8.3 ka BP onwards the radiogenic isotope composition is starting to follow a trend towards more radiogenic εNd and $^{206}Pb/^{204}Pb$ and less radiogenic $^{87}Sr/^{86}Sr$ values, indicating a shift in sediment provenances. A decrease in clay content and sedimentation rates suggesting decreased meltwater discharge as well as a drop in Fe/Ca ratios from 8.1 ka BP onwards lead Georgiadis et al. (2018) to the assumption that the GIS rapidly retreated in eastern Kane Basin. This rapidly retreating GIS on Inglefield Land in addition to the newly opened gateway for northern Ellesmere Island and Greenland sources can be interpreted as the cause of the continuous shift in radiogenic isotope composition, as it points to a change in primary sources of detrital sediments into Kane Basin. This continuous shift towards initial values proceeds throughout the following millennia and points towards a higher contribution of northern Nares Strait sources.

From 7.9 ka BP (until 7.2 ka BP) enhanced Atlantic water inflow has been recorded at the core location (Caron et al., 2019b). This comparably short interval of larger Atlantic sourced waters, in this case the WGC transporting material from the west Greenland margin, might explain the slow transition towards a dominated Ellesmere Island input as it brings material isotopically more similar to Inglefield Land and inhibits the complete shift towards the newly enabled sources in the sedimentary signature.

5.5.2. Post- and Neoglacial Period (~7.5 – 0 ka BP)

From 7.5 ka BP onwards the radiogenic isotope composition continuous the trend towards more radiogenic εNd and $^{206}Pb/^{204}Pb$ and less radiogenic $^{87}Sr/^{86}Sr$ values at a steeper slope than directly following the opening of Kennedy Channel around ~8.3 ka BP (Georgiadis et al., 2018). This shift seems to stabilise after ~5 ka BP in Pb isotopic composition and after ~3 ka BP in Nd and Sr compositions. The detrital sediment provenances seem to clearly shift towards an Ellesmere Island dominated sediment input regime with similar values as at the start of the record.

5.5.2.1. Time Interval 7.5-5.5 ka BP

The transition to stable values coincides with a decrease in the coarse grain size fraction and sedimentation rates within the AMD14-Kane2B record (Georgiadis et al., 2018) and is accompanied by a decrease in atmospheric temperatures around 7.5 ka BP (Lecavalier et al., 2017). Georgiadis et al. (2018) suggest that this transition might be related to a reduced input of marine-terminating glaciers of the GIS when most of the north Greenland coast deglaciated (cf. Bennike, 2002; Ceperley et al., 2020; Reusche et al., 2018).

The radiogenic isotope composition (Sr, Nd, Pb) points to a shift in detrital sediment provenance towards increased input of northern Ellesmere Island sources after 7.5 ka BP and hence a decreased input from Inglefield Land (Figure 5.4). The increasing input of detrital carbonates from Ellesmere Island as well as northernmost Greenland is possibly connected to the established inflow of Arctic Ocean water from the north and sediment transport from sources north of Kane Basin after the complete opening of Nares Strait (Caron et al., 2020; Georgiadis et al., 2018). Geochemical and mineralogical data by Caron et al. (2020) also indicate a shift towards northern Ellesmere Island and Greenland sources. This shift appears to be continuous, initiated around 8.2 ka BP and intensified around 7.5 ka BP, until ~5.8 ka BP according to Caron et al. (2020) data, displaying increased detrital carbonate input. The isotopic data encompass only two data points within this interval but indicate the same continuous shift (Figure 5.2 &Figure 5.4). Extended sea-ice cover in Kane Basin between ~7.5

and 5.5 ka BP (Georgiadis et al., 2020) might have supported and enhanced this transition to dominating northern Ellesmere Island sources by transporting the corresponding detrital material from the north into Kane Basin (cf. Caron et al., 2020). This time period appears to be a transitional period for the provenance shift from Inglefield Land dominated detrital sediment sources to Ellesmere Island dominated sources. At the end of this transitional period the data indicate more stable conditions.

5.5.2.2. Time Interval 5.5-0 ka BP

The detrital sediment sources appear to be more stable during the late Holocene and the Neoglacial (~5 ka BP, Kaufman et al., 2004), when main input most likely was dominated by glacial erosion. Along with the isotopic composition the geochemical and mineralogical composition of the AMD14-Kane2B record (Caron et al., 2020) stabilises. Based on the SedUnMixMC analysis (Andrews & Eberl, 2012; Andrews et al., 2015) 70-80 wt% of detrital sediments originate from Ellesmere Island sources, which are the highest recorded proportions, and 20-30 wt% from Inglefield Land (Caron et al., 2020). The isotopic composition shifts towards these higher proportions of Ellesmere Island sources concordant in all three isotopic systems. The comparably stable values after 5 ka BP coincide with the onset of recurrent and seasonal formation of ice arches in Kane Basin, favoured by a negative phased Arctic Oscillation and ongoing Neoglacial cooling, (Funder et al., 2011; Georgiadis et al., 2020). The stabilisation in radiogenic isotope composition and hence detrital sediment input indicates the establishment of modern oceanographic conditions and sediment delivery regimes in Kane Basin and Nares Strait, as suggested before by other studies (Caron et al., 2020; Jennings et al., 2019). The increased influence of northern Nares Strait sources clearly indicates the influence of detrital material transported from further north and deposited in Kane Basin.

5.5.3. Detrital Sediment Clusters

Generally, the radiogenic isotope data can be divided into two clusters, an Inglefield Land sourced (~8.7-7.5 ka BP) and an Ellesmere Island sourced (~8.9 ka BP & ~6.1-1.0 ka BP) cluster. While the Pb isotopic composition may not identify the two source regions as clearly as the Sr-Nd data, it separates the two clusters more explicitly and indicates the difference in detrital sediment composition prior and after the opening of Kennedy Channel. The $^{206}Pb/^{204}Pb$ composition at ~8.9 ka BP could even be separated into a third cluster, as it clearly distinguishes from the composition including newly enabled Ellesmere Island sources (~6.1-1.0 ka BP) and certainly proves the contribution of distal transported sediment sources from northern Ellesmere Island and Greenland after the opening of Kennedy Channel. However, it has to be kept in mind that the background data originates from the southern Greenland KMB and only serves as the closest fit, due to age agreement. Furthermore, ternary plots of geochemical tracers by Caron et al. (2020) point to a generally higher contribution of carbonate-bearing rocks, this also accounts for most of the IRD samples, which are continuously recorded throughout the core indicating iceberg calving throughout the entire Holocene (cf. Caron et al., 2019a). Some of these IRD samples indicate gneissic and basaltic origin, supporting the assumption of input from both Nares Straits coasts, as well as northern Greenland, where basaltic rocks occur (e.g. Kalsbeek & Frei, 2006; Thorarinsson et al., 2011).

The three different clusters of isotopic change do not only coincide with lithological changes (Caron, et al., 2019a; Georgiadis et al., 2018), but coincide with changes in foraminifera assemblages (Georgiadis et al., 2020) that indicate different oceanographic and climatic conditions. A glacimarine environment with limited Atlantic water inflow but increased

meltwater discharge prevailed from ~9-8.3 ka BP (Georgiadis et al., 2020) supporting the local Inglefield Land input indicated through isotopic composition as the main detrital sediment source. As glaciers mainly discharge detrital material within 50 to 100 km of their location (Farmer et al., 2003), the dominant Inglefield Land provenance underlines the assumption that the gateway for far-travelled detrital sediments via ocean currents through Kennedy Channel must have still been blocked at that time. After 5.5 ka BP when this connection is clearly open and modern-like conditions start to gradually establish, Arctic water inflow is recorded by foraminiferal assemblages (Georgiadis et al., 2020) and enables the detrital sediment transport from northern sources towards the core location.

5.6. Conclusions

This study supplements the already existing data on gravity core AMD14-Kane2B, a marine sedimentary archive from Kane Basin, central Nares Strait, recording the deglaciation of the Greenland and Innuitian Ice Sheets (Caron et al., 2020, 2019a, 2019b; Georgiadis et al., 2020, 2018). The newly produced radiogenic isotope data corroborate the hypothesis of the timing of the complete re-opening of Nares Strait around 8.3 ka BP (Georgiadis et al., 2018). The combination of the three radiogenic isotope systems Sr, Nd and Pb enabled the classification of sediment samples into two main detrital sediment source clusters, an Inglefield Land source (~8.7-7.5 ka BP) and an Ellesmere Island source (~6.1-1.0 ka BP). A continuous shift towards increased Ellesmere Island sources can be identified after the complete opening of Nares Strait. Around 5 ka BP the isotopic composition becomes stable, supporting the establishment of modern-like sedimentation and oceanic conditions. A possible assumption of the opening of Nares Strait already having occurred around 9 ka BP seems less likely based on distinct $^{206}Pb/^{204}Pb$ composition around this time. The isotopic composition around 8.3 ka BP represents the same isotopic composition as the material deposited during times when the strait was clearly open. The collapse of the ice saddle in Kennedy Channel at ~8.3 ka BP enabled material from northern Ellesmere Island to be transported to the core location, as it is the case for times after the re-opening and during the establishment of the current oceanic circulation pattern.

The agreement of the isotopic data with independently compiled mineralogical and geochemical data (Caron et al., 2020) highlights the potential and reliability of radiogenic isotopes in provenance studies related to ice-sheet dynamics. The study further supports the conclusion by Caron et al. (2020) regarding the importance of multiproxy studies based on their potential of comparison with different data types to better understand data and resulting indications as well as to make better predictions for the future.

5.7. Acknowledgements

This project was supported by the Deutsche Forschungsgemeinschaft (DFG) through the International Research Training Group "Processes and impacts of climate change in the North Atlantic Ocean and the Canadian Arctic" (IRTG 1904 ArcTrain).

We are grateful to the captain, crew members and science party on board the *CCGS Amundsen* during the 2014 ArcticNet (Leg 1b) expedition for recovering the sample material included in this study.

We would like to thank Myriam Caron, Université du Québec à Rimouski, for kindly providing the samples for radiogenic isotopic analysis of AMD14-Kane2B and all her additional help regarding data access and discussion.

5.8. References

Andrews, J. T., & Eberl, D. D. (2012). Determination of sediment provenance by unmixing the mineralogy of source-area sediments: The "SedUnMix" program. Marine Geology, 291–294, 24–33. https://doi.org/10.1016/j.margeo.2011.10.007

Andrews, J. T, Bjork, A. A., Eberl, D. D., Jennings, A. E., & Verplanck, E. P. (2015). Significant differences in late Quaternary bedrock erosion and transport : East versus West Greenland ~ 70 ° N – evidence from the mineralogy of offshore glacial marine sediments. Journal of Quaternary Science, 30(5), 452–463. https://doi.org/10.1002/jqs.2787

Barber, D. G., Hanesiak, J. M., Chan, W., & Piwowar, J. (2001). Sea-ice and meteorological conditions in Northern Baffin Bay and the North Water polynya between 1979 and 1996. Atmosphere - Ocean, 39(3), 343–359. https://doi.org/10.1080/07055900.2001.9649685

Bennike, O. (2002). Late Quaternary history of Washington Land, North Greenland. Boreas, 31(3), 260–272. https://doi.org/10.1111/j.1502-3885.2002.tb01072.x

Bennike, O., & Björck, S. (2002). Chronology of the last recession of the Greenland Ice Sheet. Journal of Quaternary Science, 17(3), 211–219. https://doi.org/10.1002/jqs.670

Blaauw, M. (2010). Methods and code for "classical" age-modelling of radiocarbon sequences. Quaternary Geochronology, 5(5), 512–518. https://doi.org/10.1016/j.quageo.2010.01.002

Caron, M., Montero-Serrano, J. C., St-Onge, G., & Rochon, A. (2020). Quantifying Provenance and Transport Pathways of Holocene Sediments From the Northwestern Greenland Margin. Paleoceanography and Paleoclimatology, 35(5), 1–23. https://doi.org/10.1029/2019PA003809

Caron, M., Rochon, A., Montero-Serrano, J. C., & St-Onge, G. (2019b). Evolution of sea-surface conditions on the northwestern Greenland margin during the Holocene. Journal of Quaternary Science, 34(7), 569–580. https://doi.org/10.1002/jqs.3146

Caron, M., St-Onge, G., Montero-Serrano, J. C., Rochon, A., Georgiadis, E., Giraudeau, J., & Massé, G. (2019a). Holocene chronostratigraphy of northeastern Baffin Bay based on radiocarbon and palaeomagnetic data. Boreas, 48(1), 147–165. https://doi.org/10.1111/bor.12346

Ceperley, E. G., Marcott, S. A., Reusche, M. M., Barth, A. M., Mix, A. C., Brook, E. J., & Caffee, M. (2020). Widespread early Holocene deglaciation, Washington Land, northwest Greenland. Quaternary Science Reviews, 231, 106181. https://doi.org/10.1016/j.quascirev.2020.106181

Colville, E. J., Carlson, A. E., Beard, B. L., Hatfield, R. G., Stoner, J. S., Reyes, A. V, & Ullman, D. J. (2011). Sr-Nd-Pb isotope evidence for ice-sheet presence on southern Greenland during the Last Interglacial. Science, 333(6042), 620–623. https://doi.org/10.1126/science.1204673

Dawes, P R. (2009a). The bedrock geology under the Inland Ice: the next major challenge for Greenland mapping. Geological Survey of Denmark and Greenland Bulletin, 17, 57–60.

Dawes, Peter R. (2009b). Precambrian - Palaeozoic geology of Smith Sound, Canada and Greenland: Key constraint to palaeogeographic reconstructions of northern Laurentia and the North Atlantic region. Terra Nova, 21(1), 1–13. https://doi.org/10.1111/j.1365-3121.2008.00845.x

Deniel, C., & Pin, C. (2001). Single-stage method for the simultaneous isolation of lead and strontium from silicate samples for isotopic measurements. Analytica Chimica Acta, 426(1), 95–103. https://doi.org/10.1016/S0003-2670(00)01185-5

Dostal, J., & Macrae, A. (2018). Cretaceous basalts of the High Arctic large igneous province at

Axel Heiberg Island (Canada): Volcanic stratigraphy, geodynamic setting, and origin. Geological Journal, (August 2017), 1–17. https://doi.org/10.1002/gj.3132
Dunbar, M.J. (1981). Physical causes and biological significance of polynyas and other open water in sea ice. In: Polynyas in the Canadian Arctic, I. Stirling and H. Cleator (Eds) Canadian Wildlife Service, Occasional Paper 45, pp. 29–43.
Dunbar, M. and M.J. Dunbar. (1972). The history of the North Water. Proc. R. Soc. Edingburgh, B72: 231–241.
Dunbar,M. 1969: The geophysical position of the NorthWater. Arctic 22, 438–441.
England, J., Atkinson, N., Bednarski, J., Dyke, A. S., Hodgson, D. A., & Ó Cofaigh, C. (2006). The Innuitian Ice Sheet: configuration, dynamics and chronology. Quaternary Science Reviews, 25(7–8), 689–703. https://doi.org/10.1016/j.quascirev.2005.08.007
England, John. (1999). Coalescent Greenland and Innuitian ice during the Last Glacial Maximum: Revising the Quaternary of the Canadian High Arctic. Quaternary Science Reviews, 18(3), 421–456. https://doi.org/10.1016/S0277-3791(98)00070-5
Estrada, S. (2015). Geochemical and Sr–Nd isotope variations within Cretaceous continental flood-basalt suites of the Canadian High Arctic, with a focus on the Hassel Formation basalts of northeast Ellesmere Island. International Journal of Earth Sciences, 104(8), 1981–2005. https://doi.org/10.1007/s00531-014-1066-x
Estrada, S., Henjes-Kunst, F., Melcher, F., & Tessensohn, F. (2010). Paleocene alkaline volcanism in the Nares Strait region: Evidence from volcanic pebbles. International Journal of Earth Sciences, 99(4), 863–890. https://doi.org/10.1007/s00531-009-0432-6
Farmer, G. L., Barber, D., & Andrews, J. (2003). Provenance of Late Quaternary ice-proximal sediments in the North Atlantic : Nd , Sr and Pb isotopic evidence. Earth and Planetary Science Letters, 209, 227–243. https://doi.org/10.1016/S0012-821X(03)00068-2
Funder, S., Goosse, H., Jepsen, H., Kaas, E., Kjær, K. H., Korsgaard, N. J., … Willerslev, E. (2011). A 10,000-Year Record of Arctic Ocean Sea-Ice Variability—View from the Beach. Science, 333(August), 747–750. https://doi.org/10.7551/mitpress/8876.003.0036
Georgiadis, E., Giraudeau, J., Jennings, A., Limoges, A., Jackson, R., Ribeiro, S., & Massé, G. (2020). Local and regional controls on Holocene sea ice dynamics and oceanography in Nares Strait, Northwest Greenland. Marine Geology, 422(October 2019). https://doi.org/10.1016/j.margeo.2020.106115
Georgiadis, E., Giraudeau, J., Martinez, P., Lajeunesse, P., St-Onge, G., Schmidt, S., & Massé, G. (2018). Deglacial to postglacial history of Nares Strait, Northwest Greenland: A marine perspective from Kane Basin. Climate of the Past, 14(12), 1991–2010. https://doi.org/10.5194/cp-14-1991-2018
Goosse, H., Fichefet, T., & Campin, J. M. (1997). The effects of the water flow through the Canadian Archipelago in a global ice-ocean model. Geophysical Research Letters, 24(12), 1507–1510. https://doi.org/10.1029/97GL01352
Gutjahr, M., Frank, M., Stirling, C. H., Klemm, V., van de Flierdt, T., & Halliday, A. N. (2007). Reliable extraction of a deepwater trace metal isotope signal from Fe-Mn oxyhydroxide coatings of marine sediments. Chemical Geology, (242), 351–370. https://doi.org/10.1016/j.chemgeo.2007.03.021
Harrison, J. C., St-Onge, M. R., Petrov, O. V., Strelnikov, S. I., Lopatin, B. G., Wilson, F. H., Tella, S., Paul, D., Lynds, T., Shokalsky, S. P., Hults, C. K., Bergman, S., Jepsen, H. F., and Solli, A. (2011). Geological map of the Arctic. Geological Survey of Canada, Map 2159A, scale 1:5 000 000
Jacobsen, S. B., & Wasserburg, G. J. (1980). Sm-Nd Isotopic Evolution of Chondrites. Earth and Planetary Science Letters, 50, 139–155.
Jennings, A E, Sheldon, C., Cronin, T., Francus, P., Stoner, J. S., & Andrews, J. (2011). The Holocene History of Nares Strait. Oceanography, 24(3), 26–41. https://doi.org/10.5670/oceanog.2011.52
Jennings, Anne E., Andrews, J. T., Oliver, B., Walczak, M., & Mix, A. (2019). Retreat of the Smith Sound Ice Stream in the Early Holocene. Boreas, 48(4), 825–840. https://doi.org/10.1111/bor.12391

Kalsbeek, F., Pulvertaft, T. C. R., & Nutman, A. P. (1998). Geochemistry, age and origin of metagreywackes from the Palaeoproterozoic Karrat Group, Rinkian Belt, West Greenland. Precambrian Research, 91(3–4), 383–399. https://doi.org/10.1016/S0301-9268(98)00059-X

Kalsbeek, Feiko, & Frei, R. (2006). The Mesoproterozoic Midsommersø, dolerites and associated high-silica intrusions, North Greenland: Crustal melting, contamination and hydrothermal alteration. Contributions to Mineralogy and Petrology, 152(1), 89–110. https://doi.org/10.1007/s00410-006-0096-1

Kaufman, D. S., Ager, T. A., Anderson, N. J., Anderson, P. M., Andrews, J. T., Bartlein, P. J., … Wolfe, B. B. (2004). Holocene thermal maximum in the western Arctic (0-180°W). Quaternary Science Reviews, 23(5–6), 529–560. https://doi.org/10.1016/j.quascirev.2003.09.007

Kwok, R. (2005). Variability of Nares Strait ice flux. Geophysical Research Letters, 32(24), 1–4. https://doi.org/10.1029/2005GL024768

Lecavalier, B. S., Fisher, D. A., Milne, G. A., Vinther, B. M., Tarasov, L., Huybrechts, P., … Dyke, A. S. (2017). High Arctic Holocene temperature record from the Agassiz ice cap and Greenland ice sheet evolution. Proceedings of the National Academy of Sciences, 114(23), 5952–5957. https://doi.org/10.1073/pnas.1616287114

Levac, E., De Vernal, A., & Blake, W. (2001). Sea-surface conditions in northernmost Baffin Bay during the Holocene: Palynological evidence. Journal of Quaternary Science, 16(4), 353–363. https://doi.org/10.1002/jqs.614

Maccali, J., Hillaire-Marcel, C., & Not, C. (2018). Radiogenic isotope (Nd, Pb, Sr) signatures of surface and sea ice-transported sediments from the Arctic Ocean under the present interglacial conditions. Polar Research, 37(1), 1–13. https://doi.org/10.1080/17518369.2018.1442982

Melling, H., Gratton, Y., & Ingram, G. (2001). Ocean circulation within the North Water polynya of Baffin Bay. Atmosphere - Ocean, 39(3), 301–325. https://doi.org/10.1080/07055900.2001.9649683

Mudie, P. J., Rochon, A., Prins, M. A., Soenarjo, D., Troelstra, S. R., Levac, E., … Kuijpers, A. (2004). Late Pleistocene-Holocene marine geology of Nares Strait region: Palaeoceanography from foraminifera and dinoflagellate cysts, sedimentology and stable isotopes. Polarforschung, 74(1–3), 169–183.

Pin, C., Briot, D., Bassin, C., & Poitrasson, F. (1994). Concomitant separation of strontium and samarium-neodymium for isotopic analysis in silicate samples, based on specific extraction chromatography. Analytica Chimica Acta, 298(2), 209–217. https://doi.org/10.1016/0003-2670(94)00274-6

Reimer, P. J., Edouard Bard, B., Alex Bayliss, B., Warren Beck, B. J., Paul Blackwell, B. G., & Christopher Bronk Ramsey, B. (2013). Intcal13 and Marine13 Radiocarbon Age Calibration Curves 0–50,000 Years Cal Bp. Radiocarbon, 55(4), 1869–1887. https://doi.org/10.1017/S0033822200048864

Reusche, M. M., Marcott, S. A., Ceperley, E. G., Barth, A. M., Brook, E. J., Mix, A. C., & Caffee, M. W. (2018). Early to Late Holocene Surface Exposure Ages From Two Marine-Terminating Outlet Glaciers in Northwest Greenland. Geophysical Research Letters, 45(14), 7028–7039. https://doi.org/10.1029/2018GL078266

Reyes, A. V, Carlson, A. E., Beard, B. L., Hatfield, R. G., Stoner, J. S., Winsor, K., … Ullman, D. J. (2014). South Greenland ice-sheet collapse during Marine Isotope Stage 11. Nature, 510(7506), 525–528. https://doi.org/10.1038/nature13456

Schlitzer, R. (2020). Ocean Data View, odv.awi.de, 2020.

Stacey, J. S., & Kramers, J. D. (1975). APPROXIMATION OF TERRESTRIAL LEAD ISOTOPE EVOLUTION BY A TWO-STAGE MODEL. Earth and Planetary Science Letters, 26, 207–221.

Stuiver, M., Reimer, P. J., and Reimer, R. W.: CALIB 7.1 [WWW program], available at: http://calib.org, last access: 6 June 2018.

Tang, C. C. L., Ross, C. K., Yao, T., Petrie, B., DeTracey, B. M., & Dunlap, E. (2004). The

circulation, water masses and sea-ice of Baffin Bay. Progress in Oceanography, 63(4), 183–228. https://doi.org/10.1016/j.pocean.2004.09.005
Thorarinsson, S. B., Holm, P. M., Duprat, H. I., & Tegner, C. (2012). Petrology and Sr-Nd-Pb isotope geochemistry of Late Cretaceous continental rift ignimbrites, Kap Washington peninsula, North Greenland. Journal of Volcanology and Geothermal Research, 219–220, 63–86. https://doi.org/10.1016/j.jvolgeores.2012.01.011
Thorarinsson, S. B., Holm, P. M., Duprat, H., & Tegner, C. (2011). Silicic magmatism associated with Late Cretaceous rifting in the Arctic Basin-petrogenesis of the Kap Kane sequence, the Kap Washington Group volcanics, North Greenland. Lithos, 125(1–2), 65–85. https://doi.org/10.1016/j.lithos.2011.01.013
Tremblay, J.-E. et al. (2014). ArcticNet Expedition Report Leg 1b – Baffin Bay and the Canadian Arctic Archipelago. Chalut K. & Merzouk A. (editors), ArcticNet – Amundsen Science Program, Université Laval, Canada.
White, L. F., Bailey, I., Foster, G. L., Allen, G., Kelley, S. P., Andrews, J. T., … Storey, C. D. (2016). Tracking the provenance of Greenland-sourced, Holocene aged, individual sand-sized ice-rafted debris using the Pb-isotope compositions of feldspars and 40Ar/39Ar ages of hornblendes. Earth and Planetary Science Letters, 433, 192–203. https://doi.org/10.1016/j.epsl.2015.10.054
Zreda, M., England, J., Phillips, F., Elmore, D., & Sharma, P. (1999). Unblockingof the Nares Strait by Greenland and Ellesmere ice-sheet retreat 10,000 years ago. Letter to Nature, 398, 139–142. https://doi.org/10.1038/246170a0

CHAPTER SIX

Conclusions and Outlook

6. Conclusions and Outlook

The aim of this thesis work was to reconstruct changes in detrital sediment provenances along the west Greenland shelf to gain new insights into Holocene Greenland Ice Sheet dynamics and ocean current-induced sediment transport. The three manuscripts included in this study (chapters 3-5) focus on three different research areas: the Labrador Sea and the southwest Greenland coast, the Upernavik and Melville Bay area along the northwest Greenland coast and Kane Basin in central Nares Strait, northernmost coast of west Greenland. All five sedimentary records collected within those three research areas reveal systematic changes in their radiogenic isotope composition pointing to shifts in detrital sediment provenance connected to past ice-sheet dynamics. The most obvious shifts were identified to be caused by the Neoglacial ice-sheet advance in southwestern Greenland (chapter 3), the Vaigat Strait opening in midwest Greenland (chapter 4) and the Nares Strait re-opening (chapter 5). By combining records along the entire west Greenland coast overall similarities as well as differences in detrital sediment delivery onto the west Greenland shelf could be detected.

The main transport pathway of detrital sediments onto the west Greenland shelf are invariably characterised by local glaciers and ice streams through meltwater discharge and erosion, identified by the specific isotopic signatures of the corresponding local Greenland bedrock. Minor contributions but clearly visible variations in distal transported material via the West Greenland Current can be identified in southern and midwest Greenland while the comparable sheltered region of northern Melville Bay appears to be exclusively dominated by local erosion and meltwater discharge. In Kane Basin the proportion of local and distal input changes with the proposed timing of the re-opening of Nares Strait (Georgiadis et al., 2018), enabling a southwards flow of Arctic Ocean waters through the strait and transporting material from former blocked detrital sediment sources.

This study demonstrates the reliability of the application of radiogenic isotopes in provenance studies with respect to ice-sheet dynamics through their agreement with data from other studies based on different provenance approaches (Caron et al., 2020; Georgiadis et al., 2018; Giraudeau et al., 2020). In comparison to the mineralogical composition measured for three of the five included records, certain conclusions could only been drawn from the radiogenic isotope composition, but not from the mineralogical composition. The Neoglacial ice advance in southern Greenland for example cannot be verified by the mineralogical composition, but only in combination with the radiogenic isotope records. The basalt input marking the opening of Vaigat Strait and the establishment of the present-day circulation pattern of the West Greenland Current in the Disko Bay area can also not be identified by the mineralogical composition alone.

By combining the three isotopic systems Sr, Nd and Pb uncertainties in source region determination resulting from similar isotopic compositions could be diminished. The identification of the Archean Block as the main source for detrital sediments onto the southwestern Greenland shelf was confirmed by the Pb isotopic composition, clearly differentiating Archean Block-sourced material from material originating from the Nagssugtoqidian Mobile Belt. This distinction was not obvious from the Sr and Nd isotopic composition due to overlapping signatures of both source regions. Within the sedimentary record from Kane Basin a clear distribution of the different sources into sediment clusters as

well as differentiating the two IRD-rich layers related to the Nares Strait opening was possible by combining the Sr and Nd data with Pb data.

This thesis work also points out the 'gaps' in the application. To identify source regions a solid knowledge of their isotopic signatures is required, which is the current limiting factor. Stream sediment data as used in chapter three (Colville et al., 2011; Reyes et al., 2014) sufficiently function as background values as they have been taken for the purpose of serving as reference values and represent the signatures and composition of material that is actually eroded and delivered onto the shelf (cf. Colville et al., 2011, supplement). These kind of data are comparably sparse and the reason why the available fjord surface sediment data from northwest Greenland was additionally analysed to compensate for the missing background data for the Committee-Mobile Belt (chapter 4 - 5). All other data comprise of rock data from different studies available in literature (Table 8.11). However, these data have been collected for an entirely different purpose, mainly for specific geological developments (e.g. Kalsbeek et al., 1998; Kalsbeek & Frei, 2006; Larsen & Pedersen, 2009) and therefore have to be interpreted with caution as they do not necessarily represent the isotopic signatures actually eroded and delivered onto the shelf, but the closest analogue. In comparison, the isotopic data of sedimentary record AMD14-Kane2B (chapter 5) plot closer to the surface sediment data than the rock data included in the corresponding provenance diagram (Figure 5.3), confirming the conclusion already drawn by Colville et al. (2011, supplement) that surface and stream sediments are the closer estimated endmember for isotopic signatures of detrital sediments delivered into the ocean. However, here it also has to be considered that surface and stream sediments represent the current erosion pattern and signature and do not compensate for sources not being available in the past due to variable extents of land-ice cover.

In summary, this study demonstrates the potential of combined Sr, Nd and Pb radiogenic isotopes in provenances studies and the clear distinction between southern, midwestern and northern Greenland detrital sediment sources which holds potential for small scale high-resolution studies. The consistency with other proxy data supports their reliability but also highlights the advantages of multiproxy studies for more solid interpretation.

However, to improve the application of radiogenic isotopes in provenance studies with regards to tracing ice-sheet dynamics, it requires a more detailed database of background data of mid to northwestern Greenland isotopic ranges.

Based on the conclusions of this study the following ideas and advice for future research are being proposed:

(1) Extending the data base of available background data with stream and surface sediments and whole rock samples analysed for the purpose of provenance studies. Especially, stream and surface sediment data are highly recommended to ensure a complete and unbiased signal of the local erosion pattern.
(2) Regional high-resolution studies to define whether the observed ice-sheet fluctuations (Larsen et al., 2015, 2011; Levy et al., 2017) can also be traced by radiogenic isotope records in order to compensate for geological overprints limiting land-based data.
(3) Generally increase the number of high-resolution provenance studies on a local scale further documenting possible provenance shifts through ice-sheet dynamics pointing out regional differences and increasing data on asynchronous development of the Greenland Ice Sheet.

With the (south)western Greenland Ice Sheet margin observed to be particularly sensitive to long-term climate change (Larsen et al., 2014) and its mass loss expected to continue into the future (e.g. McFarlin et al., 2018) as well as the effect of Arctic Amplification if greenhouse gas emissions continue to rise (Miller et al., 2010), studies of Holocene climatic changes become more and more important. The Holocene Thermal Maximum recorded warmer-than-present temperatures with glaciers and ice-sheet extent smaller than today (Kaufman et al., 2004; Young & Briner, 2015) and therefore represents the closest analogue to the development of the Greenland Ice Sheet in a warmer climate. As the current atmospheric warming will not be counter-balanced by the lingering ice sheets on the north American continent as it was the case for the Holocene Thermal Maximum (Kaufman et al., 2004), data and insights on past Greenland Ice Sheet dynamics are extremely crucial for its future development and related impacts on global climate and ocean circulation patterns and the fate of the Arctic realm overall.

6.1. References

Caron, M., Montero-Serrano, J. C., St-Onge, G., & Rochon, A. (2020). Quantifying Provenance and Transport Pathways of Holocene Sediments From the Northwestern Greenland Margin. Paleoceanography and Paleoclimatology, 35(5), 1–23. https://doi.org/10.1029/2019PA003809

Colville, E. J., Carlson, A. E., Beard, B. L., Hatfield, R. G., Stoner, J. S., Reyes, A. V, & Ullman, D. J. (2011). Sr-Nd-Pb isotope evidence for ice-sheet presence on southern Greenland during the Last Interglacial. Science, 333(6042), 620–623. https://doi.org/10.1126/science.1204673

Georgiadis, E., Giraudeau, J., Martinez, P., Lajeunesse, P., St-Onge, G., Schmidt, S., & Massé, G. (2018). Deglacial to postglacial history of Nares Strait, Northwest Greenland: a marine perspective. Climate of the Past Discussions, (July), 1–29. https://doi.org/10.5194/cp-2018-78

Giraudeau, J., Georgiadis, E., Caron, M., Martinez, P., Saint-Onge, G., Billy, I., … Massé, G. (2020). A high-resolution elemental record of post-glacial lithic sedimentation in Upernavik Trough, western Greenland: history of ice-sheet dynamics and ocean circulation changes over the last 9 100 years. Paleoceanography and Paleoclimatology, 1–37.

Kalsbeek, F., Pulvertaft, T. C. R., & Nutman, A. P. (1998). Geochemistry, age and origin of metagreywackes from the Palaeoproterozoic Karrat Group, Rinkian Belt, West Greenland. Precambrian Research, 91(3–4), 383–399. https://doi.org/10.1016/S0301-9268(98)00059-X

Kalsbeek, Feiko, & Frei, R. (2006). The Mesoproterozoic Midsommersø, dolerites and associated high-silica intrusions, North Greenland: Crustal melting, contamination and hydrothermal alteration. Contributions to Mineralogy and Petrology, 152(1), 89–110. https://doi.org/10.1007/s00410-006-0096-1

Kaufman, D. S., Ager, T. A., Anderson, N. J., Anderson, P. M., Andrews, J. T., Bartlein, P. J., … Wolfe, B. B. (2004). Holocene thermal maximum in the western Arctic (0-180°W). Quaternary Science Reviews, 23(5–6), 529–560. https://doi.org/10.1016/j.quascirev.2003.09.007

Larsen, L. M., & Pedersen, A. K. (2009). Petrology of the paleocene picrites and flood basalts on disko and nuussuaq, West Greenland. Journal of Petrology, 50(9), 1667–1711. https://doi.org/10.1093/petrology/egp048

Larsen, N. K., Funder, S., Kjær, K. H., Kjeldsen, K. K., Knudsen, M. F., & Linge, H. (2014). Rapid early Holocene ice retreat in West Greenland. Quaternary Science Reviews, 92, 310–323. https://doi.org/10.1016/j.quascirev.2013.05.027

Larsen, N. K., Kjær, K. H., Lecavalier, B., Bjørk, A. A., Colding, S., Huybrechts, P., … Olsen, J.

(2015). The response of the southern Greenland ice sheet to the Holocene thermal maximum. Geology, 43(4), 291–294. https://doi.org/10.1130/G36476.1
Larsen, N. K., Kjær, K. H., Olsen, J., Funder, S., Kjeldsen, K. K., & Nørgaard-Pedersen, N. (2011). Restricted impact of Holocene climate variations on the southern Greenland Ice Sheet. Quaternary Science Reviews, 30(21–22), 3171–3180. https://doi.org/10.1016/j.quascirev.2011.07.022
Levy, L. B., Larsen, N. K., Davidson, T. A., Strunk, A., Olsen, J., & Jeppesen, E. (2017). Contrasting evidence of Holocene ice margin retreat, south-western Greenland. Journal of Quaternary Science, 32(5), 604–616. https://doi.org/10.1002/jqs.2957
McFarlin, J. M., Axford, Y., Osburn, M. R., Kelly, M. A., Osterberg, E. C., & Farnsworth, L. B. (2018). Pronounced summer warming in northwest Greenland during the Holocene and Last Interglacial. Proceedings of the National Academy of Sciences of the United States of America, 115(25), 6357–6362. https://doi.org/10.1073/pnas.1720420115
Miller, G. H., Alley, R. B., Brigham-Grette, J., Fitzpatrick, J. J., Polyak, L., Serreze, M. C., & White, J. W. C. (2010). Arctic amplification: Can the past constrain the future? Quaternary Science Reviews, 29(15–16), 1779–1790. https://doi.org/10.1016/j.quascirev.2010.02.008
Reyes, A. V, Carlson, A. E., Beard, B. L., Hatfield, R. G., Stoner, J. S., Winsor, K., … Ullman, D. J. (2014). South Greenland ice-sheet collapse during Marine Isotope Stage 11. Nature, 510(7506), 525–528. https://doi.org/10.1038/nature13456
Young, N. E., & Briner, J. P. (2015). Holocene evolution of the western Greenland Ice Sheet: Assessing geophysical ice-sheet models with geological reconstructions of ice-margin change. Quaternary Science Reviews, 114, 1–17. https://doi.org/10.1016/j.quascirev.2015.01.018

ACKNOWLEDGEMENTS

7. Acknowledgements

First of all, I would like to thank my supervisor Simone Kasemann for giving me the opportunity to conduct this project and write this PhD thesis, for always having an open office door and time when I had questions, for giving me the freedom to shape this project to my own interests and collecting further experiences in science communication side projects, for all her input during data discussions and telling me that the 'solution' was sometimes the simple one, for her passion for isotopes and always trusting our data and ideas in discussions with non-isotope geochemists and finally for telling me over and over again to just get this thesis done.

Secondly, I would like to thank my co-supervisor and project partner from ArcTrain Canada Claude Hillaire-Marcel for sharing his impressive knowledge and experiences of Holocene Baffin Bay climate history with me, for all his input during discussions, for his quick responses and comments on (short notice) conference abstracts and contributions, for giving me the opportunity to conduct my research stay at Geotop—UQÀM in Montréal and making me a priority in getting discussion time with him while I was there. Merci beaucoup, Claude.

Thirdly, I have to thank Friedrich Lucassen for his indefinite time when I had any questions or problems with lab procedures and beyond, for always having an open door and ending some of these advices with input from other important things in life as art and history, for teaching me the methods and secrets of radiogenic isotope separation and measurements, for asking me if I was okay after the only time I spilled a sample dissolved in HF, for his input during data discussion and making so many of my text drafts for conference abstracts and manuscripts sound more professional, even after he started his well-deserved retirement.

The fourth person in this line of great scientists that shared their experiences with me and gave me advice in so many different ways is Michel Preda. I would like to thank him for all his time and patience with measuring the mineralogy of my samples during my research stay at Geotop—UQÀM. Merci Michel, for explaining the methods and results of X-ray diffraction in all its details to me and for always being happy when I passed by with just other question.

Special thanks go to Cristiano Chiessi for agreeing so quickly, happily and motivated to read and grade this thesis. Agreeing to be a second examiner is one thing, doing so with such enthusiasm is another. Thanks a lot for this inspiring discussion during my PhD defence.

I would also like to thank Dierk Hebbeln and Rüdiger Stein for being on my PhD thesis committee, for all their comments, input and advice during the thesis committee meetings every six months, with their expertise being the perfect addition to the expertise of the other members of this committee: Simone Kasemann, Claude Hillaire-Marcel and Friedrich Lucassen. Additionally, I would like to thank Rüdiger Stein for giving me the opportunity to join the research cruise *MSM44* during my master studies in 2015, which was the starting point of my Arctic research adventure leading to this PhD thesis. I would also further like to thank Dierk Hebbeln for asking me to join the second part of this scientific expedition in 2017 and entrust me with some additional responsibilities during *MSM66* that made me gain a lot of new experiences.

With that being said I automatically have to thank all the members of the *RV Maria S. Merian* crew and the scientific party during *MSM44* and *MSM66* for making both of these scientific cruises such a great, inspiring, uncomplicated and memorable experience. Special thanks go to

Boris Dorschel for being an amazing chief scientist with the perfect mix of chaos and organisation, always happy, always part of the group, always interested in everyone's work and input. I also have to thank Boris for unintentionally making sure I started this journey being one of the few people being aware of the reality that a PhD in geosciences is most likely being finished on unemployment money, which is just part of the journey and that is totally okay. I further would like to thank Henriette Kolling and Maren Wohltmann for making this very first expedition an unforgettable memory, for all the long but fun hours of sediment sampling in the hangar with good music and talks, not knowing that those samples would one day be included into my PhD thesis. Thank you both so much for all your support and advice and hours of good talks and good times during those past years and for becoming my little *MSM44* group that lasted beyond this expedition and many more years to come.

I would like to thank the entire MARUM working group of Isotope Geochemistry for welcoming me so warmly, for all their support and help, nice chats and good laughs during meetings, coffee breaks with birthday cakes, Christmas parties, input during practice talks, conference experience and just for being always around with open office doors. Thank you for this past 4.5 years together, I will be missing all of you: Simone Kasemann, Friedrich Lucassen, Anette Meixner, Barbara Muntz, Susann Henkel, Karina Zavala, Frederike Wilckens, Natalie Höppner, Valeriia Kirillova, Gustavo Macedo de Paula Santos, Johanna Hingst, Chico Teixeira Vilela and of course Tina Klein, Lucy Schlicht, Javiera González Alarcón, Carisa Sarchi and Juan Camilo Gómez Gutiérrez for sharing the office with me and keeping me company in a perfect mix of a silent, concentrated, relaxed, constructive, and sometimes goofy atmosphere.

Rieke, Lera and Natalie I especially would like to thank you for integrating me into your group right away, for taking me to every lunch and coffee break, answering all of my (stupid) questions and just having been there through this entire journey, supporting and believing in me – changing from colleagues to friends already half way through and becoming a constant part of my life. I know you have been the isotope girls long before I even met you all but to me you are all my favourite isotope girls! <3

I also would like to thank Johanna again for now asking me all these questions I asked Rieke, Lera and Natalie four years ago and giving me the opportunity to give back some of the support I received when I started by PhD. Thank you for looking up to me as the 'experienced' one and letting me somehow also be part of your project. Lots of luck for the rest of your journey.

This PhD project is part of the International Research Training Group ArcTrain, an international research network between the University of Bremen and eight Canadian Universities. I am immensely grateful for all the support through ArcTrain, for the opportunity of building my own research network during annual meetings in Bremen and Canada, gaining presentation and other soft skills during research seminars and courses, being financially supported during scientific conferences and for the opportunity to conduct a research stay at Geotop-UQÀM. Thank you Michal Kucera, Anne de Vernal, Jade Falardeau, Gabriela Wehr and Sabine Schulz for all the energy you put into ArcTrain and for all your administrative support, coordination and organisation skills. I also would like to thank Siccha for organising all our research seminars, being equally enthusiastically interested in all our projects and for discussing my results with me when almost noone else was around during my seminar presentations in the summer months.

Besides these professional aspects of support making this PhD a unique and diverse experience, the biggest added value ArcTrain could have possible given me is the community of amazing and inspiring people that turned out to be so much more than colleagues – an actual ArcTrain family. Each of the members of my ArcTrain (extended) family added an essential piece to the puzzle without this it would have not been complete: Thank you Bea, Estelle, Jeetendra, Jens, Mattia, Pierre, Quentin, and Martin for being this amazing ArcTrain team during *MSM66*; Thank you Alexandra and Mattia for this perfect trip through Iceland afterwards; Thank you Anouk, Bea and Hannah for sharing apartments with me during two amazing years of EGU General Assembly and making this such a great conference experience; Merci Cynthia and Lucille for welcoming me into your homes during my research stay in Montréal; Merci Amélie, Camille, Charles, Estelle, Jade, Mathieu, Myriam, Pascal, Alice and Adina for making this time in Montréal such a great memory with lovely lunch breaks, evenings and little excursions; thanks to all of you plus Damien, Dima, Luisa, Marilena, Nicole, Rémi and Valentin for all the ArcTrain lunches, coffee breaks, after work beers, nice summer evenings, Christmas market visits and quality hours of good talks and exchange, scientifically and other matters. I might have been able to do this without you, but it would have doubtlessly been so much harder. I could not be more grateful to have met you all.

I especially would like to thank Damien Ringeisen and Valentin Ludwig for being the amazing science communication team they were. It was an honour to manage and edit all these posts of the ArcTrain blog with you and getting excited every time the ArcTrain twitter account reached another 100 followers. We can be certainly proud of what we achieved here. I also would like to thank Franziska Tell for making me feel like I'm leaving this legacy in really good hands with her and the new team.

Another huge thanks to Anouk Vlug and Jens Weiser for being a great team of ArcTrain representatives. It was the perfect shared team work in distributing tasks, taking turns writing minutes, attending meetings while always just one of us was away. Thank you for this entirely positive experience. Here, I also would like to thank Michal Kucera, Maren Walter and Rüdiger Stein for the monthly speaker's meetings, the coffee and the insights into ArcTrain matters, the opportunity of being part of decisions, board meetings and all the valued input.

Another word of thanks clearly goes to Jens Weiser (again) for constructing the age models without those my isotopic records would have been useless. Thank you for all your work, constant adjustments, quick responses to any data related question and generally your unique way of writing emails that made my day so many times, even those that contained just another update of the age model leading to me changing my 'final' figures again. I also would like to thank Jens, as well as Jeetendra Saini, Myriam Caron and Estelle Allan for constructive data discussions and scientific input. Finally, thank you Jens, Jeetendra and Sabrina Hohmann for a fun and encouraging sampling party at the start of this PhD.

Furthermore, I would like to thank the GLOMAR graduate school for their support and numerous opportunities for exchange with fellow PhD students at MARUM through monthly seminars and gaining new soft skills through a variety of courses. I especially would like to thank Christina Klose for all her support and organisation skills and putting together the amazing collection of courses and for offering the MARUM writing space together with Sinah Teumer which helped me a lot during the final writing phase. I also would like to thank Dana Ransby and Chelsea Korpanty for all their energy and enthusiasm they put into the monthly GLOMAR research seminars.

I also would like to thank the entire team of Once Upon A Time (especially Gema, Sandy, Dharma, Hadar, Eva and Neele) for their enthusiasm and for showing me, that science is so much more than data and that the opportunities for science communication are endless and endlessly important as good sciences are only really good sciences if they have been shared with the world. On that topic, I would also like to mention the Association of Polar Early Career Scientists (APECS) and the early career EGU Cryosphere blog team for the great experience, advice and network I gained through these groups that will last beyond my PhD.

Additionally, I would like to thank Jule Mawick from Leibniz Centre for Tropical Marine Research (ZMT) for measuring the elemental composition of selected samples and the MARUM core repository for providing the sediment cores included into this work. Myriam Caron from Université du Québec à Rimouski is thanked again for providing the samples of the Kane Basin record.

As this PhD thesis has been written during a global pandemic, which first seemed like a good point of time to lock oneself away and write and later turned out to unfortunately not be entirely true, I cannot get around but also mention a few other things that kept me sane and focussed. Apart from the many digital talks and walks outside with good friends, I am also thankful for the regular yoga sessions from Yoga with Adriene, brooks for making my running shoes, the Gilmore Girls and Glee cast for keeping me company during deserved evening breaks, the producers of my favourite Arctic (Curiously Polar, The Icepod, Polar Times) and non-Arctic (The Waterwomen Podcast, 1.5 Grad) podcasts that once again made me realise why I started this PhD in the first place, the stranger who told me how to play guitar, Cold Play for writing 'the Scientist' and the person that turned it into a piano cover, this song somehow had the power to make me feel super emotional and discouraged about this entire process and situation but at the same time motivated me to finish.

Finally, I would like to thank all my friends for believing in me and supporting me throughout these past years, for unintentional stacking my tea collection, being my 'vacation' from thinking over science but also listened to the science I loved to share and generally for repeatedly telling me that I could do this. I also would like to thank all the other people I met along the way and might have forgotten here, you all contributed to this journey somehow, by (unintentional) advice, motivation and inspiration. Mostly, I am extremely thankful for Lisa Grosfeld, for sharing her home office, her time and energy with me during the last months and for my favourite ArcTrainees Anouk, Damien, Valentin and Mattia. Thank you for all the good talks, the listening, the hugs, especially over the past months. Dank je wel, Anouk and tack, Lisa for going these last kilometres of this PhD marathon so closely together with me, you clearly were my rocks and motivation.

And last but not least I would like to thank my family who always believed in me, supported me and was already proud of me before this was even nearly done. For their endless love and understanding and support with food and last needed things, for being happy about all the little things on the way. The last word of thanks goes to my mom who's simple advice of doing everything step by step that I didn't want to hear during a stressful exam period of my bachelor studies, now became the most useful advice of all - because step by step is the only way it can be done.

"We don't have a word for the opposite of loneliness, but if we did, I could say that's what I want in life. […] It's not quite love and it's not quite community; it's just this feeling that here are people, an abundance of people, who are in this together. […] That time we did, we went, we saw, we laughed, we felt. The hats." – Marina Keegan 'The opposite of loneliness'

Doing a PhD is a journey, it's a marathon, not a sprint, it's so much more than what is summarised in this thesis, it's the people you meet and the experiences you have, your personal growth, all of this together is the real achievement and value.

'It always seems impossible until it is done.' – Nelson Mandela

APPENDICES

8. Appendices

8.1. Radiogenic Isotope Data

Table 8.1: Radiogenic isotope data of gravity core GeoB19905-1 for dt, dc, bulk fraction and FeMn leaching. All values were automatically corrected for internal fractionation. Pb data was additionally corrected by a bulk uncertainty of 0.1% per atomic mass unit (Pb^{corr}). εNd values were calculated with CHUR value of 0.512638 (Jacobsen & Wasserburg, 1980).

Sample ID	Sediment Depth [cm]		cal. Age	Isotope Data dt Fraction						
	Top	Bottom	[ka BP]	$^{87}Sr/^{86}Sr$	$^{206}Pb/^{204}Pb$	$^{206}Pb/^{204}Pb^{corr}$	$^{207}Pb/^{204}Pb$	$^{207}Pb/^{204}Pb^{corr}$	$^{143}Nd/^{144}Nd$	εNd
LM #032	50	51	0.22	0.726340±4	15.6417±21	15.66	14.6593±19	14.67	0.510810±7	-35.66
LM #033	150	151	0.72	0.728231±4	15.1890±7	15.20	14.5612±7	14.58	0.510990±7	-32.15
LM #034	290	291	1.83	0.724105±5	15.1835±8	15.20	14.5634±8	14.58	0.511060±6	-30.78
LM #035	320	321	2.13	0.724610±5	15.2376±19	15.25	14.5682±22	14.58	0.511071±4	-30.57
LM #036	370	371	2.70	0.723181±5	15.4639±10	15.48	14.6131±10	14.63	0.511171±7	-28.62
LM #037	410	411	3.16	0.722109±6	15.1156±58	15.13	14.5464±60	14.56	0.511146±8	-29.10
LM #038	460	461	3.75	0.722885±5	15.0705±8	15.09	14.5114±9	14.53	0.511111±7	-29.79
LM #039	500	501	4.24	0.722676±4	15.0119±7	15.03	14.5041±7	14.52	0.511134±4	-29.34
LM #040	580	581	5.19	0.723107±6	14.8985±14	14.91	14.4734±15	14.49	0.511202±12	-28.01
LM #041	610	611	5.56	0.724156±5	15.0802±58	15.10	14.5373±54	14.55	0.511138±7	-29.26
LM #042	680	681	8.11	0.721210±6	14.6237±8	14.64	14.4088±9	14.42	0.511107±5	-29.87
LM #066	700	701	8.33	0.720167±4	14.2951±12	14.31	14.3477±12	14.36	0.511111±8	-29.79
LM #067	710	711	8.44	0.720451±9	14.3855±6	14.40	14.3648±6	14.38	0.511171±6	-28.62
LM #068	720	721	8.53	0.720394±7	14.3840±6	14.40	14.3640±6	14.38	0.511181±9	-28.42
LM #069	730	731	8.62	0.720448±6	14.3092±6	14.32	14.3472±6	14.36	0.511142±5	-29.18
LM #043	820	821	9.48	0.720909±5	14.6462±60	14.66	14.4154±54	14.43	0.511134±6	-29.34
LM #044	920	921	10.45	0.720127±5	14.4547±5	14.47	14.3452±6	14.36	0.511093±7	-30.14
LM #045	1030	1031	11.54	0.723719±5	14.946±6	14.96	14.4413±6	14.46	0.511106±8	-29.88

Sample ID	Sediment Depth [cm]		cal. Age	Isotope Data dc Fraction						
	Top	Bottom	[ka BP]	$^{87}Sr/^{86}Sr$	$^{206}Pb/^{204}Pb$	$^{206}Pb/^{204}Pb^{corr}$	$^{207}Pb/^{204}Pb$	$^{207}Pb/^{204}Pb^{corr}$	$^{143}Nd/^{144}Nd$	εNd
LM #032	50	51	0.22	0.726263±5	15.6618±37	15.68	14.7001±43	14.71	0.511080±6	-30.39
LM #033	150	151	0.72	0.728463±5	15.3004±6	15.32	14.5733±7	14.59	0.510990±8	-32.15
LM #034	290	291	1.83	0.724188±6	15.2379±23	15.25	14.5706±22	14.59	0.511070±6	-30.59
LM #035	320	321	2.13	0.724506±9	15.2252±15	15.24	14.5554±16	14.57	0.510988±16	-32.19
LM #036	370	371	2.70	0.722612±6	16.0571±7	16.07	14.6799±7	14.69	0.511217±5	-27.72
LM #037	410	411	3.16	0.722000±4	14.9505±16	14.97	14.4822±18	14.50	0.511156±11	-28.91
LM #038	460	461	3.75	0.723049±6	15.1562±28	15.17	14.5341±27	14.55	0.511156±7	-28.91
LM #039	500	501	4.24	0.722578±5	14.9028±11	14.92	14.4748±90	14.49	0.511152±6	-28.99
LM #040	580	581	5.19	0.722799±6	15.0328±45	15.05	14.5117±48	14.53	0.511143±4	-29.16
LM #041	610	611	5.56	0.722853±6	15.0723±46	15.09	14.5471±44	14.56	0.511129±5	-29.44
LM #042	680	681	8.11	0.720330±6					0.511132±4	-29.38
LM #066	700	701	8.33	0.720230±5	14.4161±13	14.43	14.3713±13	14.39	0.511173±5	-28.58
LM #067	710	711	8.44	0.720737±8	14.5206±5	14.54	14.3964±5	14.41	0.511128±8	-29.46
LM #068	720	721	8.53	0.720725±4	14.3999±10	14.41	14.3768±10	14.39	0.511188±6	-28.29
LM #069	730	731	8.62	0.720624±6	14.4752±6	14.49	14.3929±7	14.41	0.511179±14	-28.46
LM #043	820	821	9.48	0.721224±5	14.7905±9	14.81	14.4774±9	14.49	0.511167±11	-28.69
LM #044	920	921	10.45	0.720373±5	14.5307±36	14.55	14.4172±46	14.43	0.511057±6	-30.84
LM #045	1030	1031	11.54	0.723924±6	15.0659±50	15.08	14.5142±48	14.53	0.511090±6	-30.20

Sample ID	Sediment Depth [cm]		cal. Age	Isotope Data bulk Fraction						
	Top	Bottom	[ka BP]	$^{87}Sr/^{86}Sr$	$^{206}Pb/^{204}Pb$	$^{206}Pb/^{204}Pb^{corr}$	$^{207}Pb/^{204}Pb$	$^{207}Pb/^{204}Pb^{corr}$	$^{143}Nd/^{144}Nd$	εNd
LM #032	50	51	0.22	0.724063±7	15.9164±12	15.93	14.7201±11	14.73	0.511094±6	-30.12
LM #033	150	151	0.72	0.727388±16	15.8451±58	15.86	14.7557±69	14.77		
LM #034	290	291	1.83	0.723148±5	15.8129±23	15.83	14.7291±30	14.74	0.511104±6	-29.92
LM #035	320	321	2.13	0.723674±7	15.6414±6	15.66	14.6296±6	14.64		
LM #036	370	371	2.70	0.720962±5	15.9028±55	15.92	14.6636±53	14.68	0.511212±6	-27.82

Sample ID	Sediment Depth [cm]		cal. Age	Isotope Data bulk Fraction						
	Top	Bottom	[ka BP]	$^{87}Sr/^{86}Sr$	$^{206}Pb/^{204}Pb$	$^{206}Pb/^{204}Pb^{corr}$	$^{207}Pb/^{204}Pb$	$^{207}Pb/^{204}Pb^{corr}$	$^{143}Nd/^{144}Nd$	εNd
LM #037	410	411	3.16	0.721295±7	15.4554±46	15.47	14.6529±56	14.67		
LM #038	460	461	3.75	0.719905±6	15.5567±51	15.57	14.6597±55	14.67	0.511188±7	-28.29
LM #039	500	501	4.24	0.717513±5	15.5646±7	15.58	14.6073±7	14.62		
LM #040	580	581	5.19	0.716855±6	15.6730±80	15.69	14.6290±80	14.64	0.511155±6	-28.93
LM #041	610	611	5.56	0.717403±7						-10000.00
LM #042	680	681	8.11	0.716906±5					0.511099±8	-30.02
LM #066	700	701	8.33	0.717747±3	14.8928±10	14.91	14.4517±10	14.47	0.511058±30	-30.82
LM #067	710	711	8.44	0.717746±4	14.9480±16	14.96	14.4695±15	14.48	0.511111±4	-29.79
LM #068	720	721	8.53	0.717415±5	15.0014±17	15.02	14.4909±17	14.51	0.511150±5	-29.03
LM #069	730	731	8.62	0.717260±4	14.8203±13	14.84	14.4523±13	14.47	0.511139±8	-29.24
LM #043	820	821	9.48	0.720914±7	15.1978±9	15.21	14.5136±8	14.53		
LM #044	920	921	10.45	0.720378±6	14.6082±26	14.62	14.4183±34	14.43	0.511105±11	-29.90
LM #045	1030	1031	11.54	0.723939±5	15.3926±5	15.41	14.5062±6	14.52		
Sample ID	Sediment Depth [cm]		cal. Age	Isotope Data Leachate						
	Top	Bottom	[ka BP]	$^{87}Sr/^{86}Sr$	$^{206}Pb/^{204}Pb$	$^{206}Pb/^{204}Pb^{corr}$	$^{207}Pb/^{204}Pb$	$^{207}Pb/^{204}Pb^{corr}$	$^{143}Nd/^{144}Nd$	εNd
LM #032	50	51	0.22	0.726708±6	19.4243±317	19.44	15.5882±262	15.60	0.511118±14	-29.65
LM #033	150	151	0.72	0.726752±4	20.2640±130	20.28	15.5413±95	15.56	0.510813±73	-35.60
LM #034	290	291	1.83	0.724097±12	20.7440±200	20.76	15.612±153	15.63	0.511140±16	-29.22
LM #035	320	321	2.13	0.725932±5	20.4760±91	20.50	15.5381±66	15.55		
LM #036	370	371	2.70	0.722154±6	20.2885±89	20.31	15.4808±68	15.50	0.511238±16	-27.31
LM #037	410	411	3.16	0.727382±8	20.1166±614	20.14	15.5012±478	15.52	0.511187±26	-28.30
LM #038	460	461	3.75	0.720305±6	20.3745±141	20.39	15.5021±110	15.52	0.511377±40	-24.60
LM #039	500	501	4.24	0.719832±8	20.0745±209	20.09	15.4418±162	15.46	0.511216±21	-27.74
LM #040	580	581	5.19	0.717044±6	20.4233±115	20.44	15.5340±93	15.55	0.511247±12	-27.13
LM #041	610	611	5.56	0.720403±4	20.2088±89	20.23	15.4764±72	15.49	0.511038±34	-31.21

Sample ID	Sediment Depth [cm]		cal. Age	Isotope Data Leachate						
	Top	Bottom	[ka BP]	$^{87}Sr/^{86}Sr$	$^{206}Pb/^{204}Pb$	$^{206}Pb/^{204}Pb^{corr}$	$^{207}Pb/^{204}Pb$	$^{207}Pb/^{204}Pb^{corr}$	$^{143}Nd/^{144}Nd$	εNd
LM #042	680	681	8.11	0.717992±7	20.0556±234	20.08	15.4744±179	15.49	0.511124±56	-29.53
LM #043	820	821	9.48	0.737451±5	21.0136±72	21.03	15.5457±52	15.56	0.511125±26	-29.51
LM #044	920	921	10.45	0.742222±19	20.9836±50	21.00	15.4748±35	15.49	0.511057±50	-30.84
LM #045	1030	1031	11.54	0.742438±6	20.4478±193	20.47	15.3711±146	15.39	0.511072±10	-30.55

Table 8.2: Radiogenic isotope data of gravity core GeoB19927-3 for dt, dc, bulk fraction and FeMn leaching. All values were automatically corrected for internal fractionation. Pb data was additionally corrected by a bulk uncertainty of 0.1% per atomic mass unit (Pb^{corr}). εNd values were calculated with CHUR value of 0.512638 (Jacobsen & Wasserburg, 1980).

Sample ID	Sediment Depth [cm]		cal. Age	Isotope Data dt Fraction						
	Top	Bottom	[ka BP]	$^{87}Sr/^{86}Sr$	$^{206}Pb/^{204}Pb$	$^{206}Pb/^{204}Pb^{corr}$	$^{207}Pb/^{204}Pb$	$^{207}Pb/^{204}Pb^{corr}$	$^{143}Nd/^{144}Nd$	εNd
LM #001	0	1	-0.05	0.745559±3	19.1048±10	19.12	15.5013±10	15.52	0.511348±6	-25.16
LM #019	18	19	0.51	0.745312±6	18.9836±38	19.00	15.4732±31	15.49	0.511341±3	-25.30
LM #011	50	51	1.25	0.743858±5	19.3862±79	19.41	15.5756±73	15.59	0.511539±76	-21.44
LM #002	100	101	1.86	0.743121±4	19.0174±16	19.04	15.4929±18	15.51	0.511374±8	-24.66
LM #012	150	151	2.46	0.742956±6	19.1504±7	19.17	15.4714±5	15.49	0.511367±13	-24.79
LM #003	200	201	3.02	0.742853±4	19.0234±4	19.04	15.4613±2	15.48	0.511370±5	-24.73
LM #013	250	251	3.45	0.741789±5	19.1139±6	19.13	15.4656±5	15.48	0.511388±6	-24.38
LM #004	300	301	3.87	0.744111±5	18.9642±6	18.98	15.4560±6	15.47	0.511340±6	-25.32
LM #014	350	351	4.29	0.745802±8	19.1443±8	19.16	15.4847±7	15.50	0.511354±4	-25.05
LM #005	400	401	4.72	0.74596±4	18.9596±4	18.98	15.4658±4	15.48	0.511336±6	-25.40
LM #006	500	501	5.48	0.748032±5	18.9543±10	18.97	15.4626±10	15.48	0.511301±10	-26.08
LM #007	600	601	6.18	0.752440±7	18.8353±6	18.85	15.4669±5	15.48	0.511264±12	-26.80
LM #008	700	701	7.14	0.755882±2	18.8445±6	18.86	15.4641±6	15.48	0.511242±4	-27.23
LM #009	800	801	8.01	0.762797±6	18.7286±47	18.75	15.4981±40	15.51	0.511213±6	-27.80
LM #015	850	851	8.35	0.766294±5	18.6455±6	18.66	15.4864±5	15.50	0.511225±6	-27.56
LM #010	900	901	8.69	0.75613±6	18.8626±6	18.88	15.4929±6	15.51	0.511287±8	-26.35
LM #016	950	951	9.03	0.761031±7	19.0285±27	19.05	15.5451±22	15.56	0.511255±23	-26.98

Sample ID	Sediment Depth [cm]		cal. Age	Isotope Data dt Fraction						
	Top	Bottom	[ka BP]	$^{87}Sr/^{86}Sr$	$^{206}Pb/^{204}Pb$	$^{206}Pb/^{204}Pb^{corr}$	$^{207}Pb/^{204}Pb$	$^{207}Pb/^{204}Pb^{corr}$	$^{143}Nd/^{144}Nd$	εNd
LM #017	1000	1001	9.37	0.764051±5	18.9427±5	18.96	15.4959±4	15.51	0.511215±21	-27.76
LM #018	1050	1051	9.73	0.766715±5	18.1372±5	18.16	15.4075±4	15.42	0.511176±8	-28.52

Sample ID	Sediment Depth [cm]		cal. Age	Isotope Data dc Fraction						
	Top	Bottom	[ka BP]	$^{87}Sr/^{86}Sr$	$^{206}Pb/^{204}Pb$	$^{206}Pb/^{204}Pb^{corr}$	$^{207}Pb/^{204}Pb$	$^{207}Pb/^{204}Pb^{corr}$	$^{143}Nd/^{144}Nd$	εNd
LM #001	0	1	-0.05	0.744676±4	19.1518±34	19.17	15.5160±28	15.53		
LM #019	18	19	0.51	0.743851±6	19.0850±12	19.10	15.4976±11	15.51	0.510944±5	-33.04
LM #011	50	51	1.25	0.743169±5	19.3780±70	19.40	15.5141±6	15.53	0.511371±14	-24.72
LM #002	100	101	1.86	0.742377±6	19.0134±42	19.03	15.4696±34	15.49		
LM #012	150	151	2.46	0.742384±5	19.2503±6	19.27	15.4884±5	15.50	0.511276±47	-26.57
LM #003	200	201	3.02	0.741794±5	19.0348±40	19.05	15.4918±34	15.51		
LM #013	250	251	3.45	0.741291±7	19.2077±7	19.23	15.4649±6	15.48	0.511417±12	-23.82
LM #004	300	301	3.87	0.743286±4	19.0539±66	19.07	15.5247±54	15.54		
LM #014	350	351	4.29	0.745119±6	19.2251±12	*19.24*	15.4940±11	15.51	0.511332±29	-25.48
LM #005	400	401	4.72	0.744673±6	18.9934±24	19.01	15.5167±20	15.53		
LM #006	500	501	5.48	0.747764±5	19.0614±18	19.08	15.4806±16	15.50	0.511279±13	-26.51
LM #007	600	601	6.18	0.751878±4	18.8775±12	18.90	15.4582±10	15.47		
LM #008	700	701	7.14	0.755372±34	18.8956±13	18.91	15.4700±11	15.49		
LM #009	800	801	8.01	0.763492±3	18.8181±6	18.84	15.4763±6	15.49		
LM #015	850	851	8.35	0.765488±5	18.7448±6	18.76	15.4716±5	15.49	0.511226±10	-27.54
LM #010	900	901	8.69	0.756076±7	18.9427±6	18.96	15.4875±6	15.50		
LM #016	950	951	9.03	0.760701±6	19.1138±8	19.13	15.5290±8	15.54	0.511278±5	-26.53
LM #017	1000	1001	9.37	0.763954±6	19.1261±10	19.15	15.5665±9	15.58	0.511255±70	-26.98
LM #018	1050	1051	9.73	0.766584±6	18.3664±46	18.38	15.4683±51	15.48	0.511162±10	-28.79

Sample ID	Sediment Depth [cm]		cal. Age	Isotope Data bulk Fraction						
	Top	Bottom	[ka BP]	$^{87}Sr/^{86}Sr$	$^{206}Pb/^{204}Pb$	$^{206}Pb/^{204}Pb^{corr}$	$^{207}Pb/^{204}Pb$	$^{207}Pb/^{204}Pb^{corr}$	$^{143}Nd/^{144}Nd$	εNd
LM #001	0	1	-0.05	0.739209±4	19.5855±8	19.61	15.5558±7	15.52	0.511362±5	-24.89
LM #019	18	19	0.51	0.739672±5	19.6459±20	19.67	15.5681±16	15.58		
LM #011	50	51	1.25	0.739117±8	19.5649±7	19.58	15.5320±7	15.59	0.511477±39	-22.65
LM #002	100	101	1.86	0.737976±4	19.4578±11	19.48	15.5269±8	15.51	0.511377±4	-24.60
LM #012	150	151	2.46	0.738232±5	19.4080±12	19.43	15.5087±10	15.49	0.511388±8	-24.38
LM #003	200	201	3.02	0.737688±4	19.5144±10	19.53	15.5610±9	15.48	0.511373±5	-24.68
LM #013	250	251	3.45	0.737694±5	19.4118±172	19.43	15.5186±130	15.48	0.51141±21	-23.95
LM #004	300	301	3.87	0.739240±5	19.4532±15	19.47	15.5285±14	15.47	0.511347±3	-25.18
LM #014	350	351	4.29	0.741375±7	19.4263±9	19.45	15.5263±7	15.50	0.511257±27	-26.94
LM #005	400	401	4.72	0.740693±6	19.5071±11	19.53	15.5382±11	15.48	0.511341±5	-25.30
LM #006	500	501	5.48	0.743324±5	19.4547±80	19.47	15.5809±64	15.48	0.511299±6	-26.12
LM #007	600	601	6.18	0.747083±5	19.3958±9	19.42	15.5358±8	15.48	0.511266±5	-26.76
LM #008	700	701	7.14	0.749823±6	19.5112±20	19.53	15.549±16	15.48	0.511247±6	-27.13
LM #009	800	801	8.01	0.756492±6	19.3074±8	19.33	15.5358±7	15.51	0.511208±6	-27.89
LM #015	850	851	8.35	0.758493±27	19.1495±7	19.17	15.5226±6	15.50	0.511241±6	-27.25
LM #010	900	901	8.69	0.750835±6	19.5881±38	19.61	15.5639±30	15.51	0.511291±7	-26.28
LM #016	950	951	9.03	0.756465±8	19.5491±8	19.57	15.5689±6	15.56	0.511276±8	-26.57
LM #017	1000	1001	9.37	0.758329±5	19.4627±8	19.48	15.5596±6	15.51	0.511264±22	-26.80
LM #018	1050	1051	9.73	0.765220±5	18.8818±52	18.90	15.5258±41	15.42	0.511257±41	-26.94

Sample ID	Sediment Depth [cm]		cal. Age	Isotope Data Leachate						
	Top	Bottom	[ka BP]	$^{87}Sr/^{86}Sr$	$^{206}Pb/^{204}Pb$	$^{206}Pb/^{204}Pb^{corr}$	$^{207}Pb/^{204}Pb$	$^{207}Pb/^{204}Pb^{corr}$	$^{143}Nd/^{144}Nd$	εNd
LM #001	0	1	-0.05	0.712190±4	21.7255±50	21.75	15.8350±36	15.85	0.511470±7	-22.78
LM #019	18	19	0.51	0.713552±8	22.3592±14	22.38	15.8800±11	15.90	0.511840±30	-15.57
LM #011	50	51	1.25	0.711774±6	22.1998±18	22.22	15.8568±13	15.87	0.511516±6	-21.89
LM #002	100	101	1.86	0.710912±3	21.8619±77	21.88	15.8316±55	15.85		

Sample ID	Sediment Depth [cm]		cal. Age	Isotope Data Leachate						
	Top	Bottom	[ka BP]	$^{87}Sr/^{86}Sr$	$^{206}Pb/^{204}Pb$	$^{206}Pb/^{204}Pb^{corr}$	$^{207}Pb/^{204}Pb$	$^{207}Pb/^{204}Pb^{corr}$	$^{143}Nd/^{144}Nd$	εNd
LM #012	150	151	2.46	0.711104±5	22.0915±29	22.11	15.8317±21	15.85	0.511528±8	-21.65
LM #003	200	201	3.02	0.711223±6	22.1591±74	22.18	15.8477±53	15.86	0.511503±8	-22.14
LM #013	250	251	3.45	0.711339±4					0.511543±7	-21.36
LM #004	300	301	3.87	0.710729±5	22.0817±127	22.10	15.8293±95	15.85	0.511473±6	-22.73
LM #014	350	351	4.29	0.711231±9	22.0939±88	22.12	15.8728±63	15.89	0.511514±7	-21.93
LM #005	400	401	4.72	0.710987±4	22.1202±76	22.14	15.8363±54	15.85	0.511474±5	-22.71
LM #006	500	501	5.48	0.712138±5	22.2233±30	22.25	15.8618±21	15.88	0.511428±4	-23.60
LM #007	600	601	6.18	0.712915±5	22.3466±119	22.37	15.8625±85	15.88	0.511422±13	-23.72
LM #008	700	701	7.14	0.714735±6	22.5030±245	22.53	15.9017±175	15.92	0.511419±13	-23.78
LM #009	800	801	8.01	0.712745±5	22.5087±89	22.53	15.9338±62	15.95	0.511357±11	-24.99
LM #015	850	851	8.35	0.716964±5	22.2669±12	22.29	15.9188±10	15.93	0.511382±6	-24.50
LM #010	900	901	8.69	0.723719±5	22.3403±211	22.36	15.9004±152	15.92	0.511386±6	-24.42
LM #016	950	951	9.03	0.715448±5	22.2868±13	22.31	15.9177±10	15.93	0.511391±7	-24.33
LM #017	1000	1001	9.37	0.716201±4	22.4358±17	22.46	15.9366±12	15.95	0.511389±7	-24.36
LM #018	1050	1051	9.73	0.720072±6	22.1955±38	22.22	15.9239±27	15.94	0.511287±8	-26.35

Table 8.3: Radiogenic isotope data of box core GeoB199265-2A for dt, dc, and bulk fraction. All values were automatically corrected for internal fractionation. Pb data was additionally corrected by a bulk uncertainty of 0.1% per atomic mass unit (Pb^{corr}). εNd values were calculated with CHUR value of 0.512638 (Jacobsen & Wasserburg, 1980).

Sample ID	Sediment Depth [cm]		Isotope Data dt Fraction						
	Top	Bottom	$^{87}Sr/^{86}Sr$	$^{206}Pb/^{204}Pb$	$^{206}Pb/^{204}Pb^{corr}$	$^{207}Pb/^{204}Pb$	$^{207}Pb/^{204}Pb^{corr}$	$^{143}Nd/^{144}Nd$	εNd
LM #061	1	3	0.773199±4	18.1088±8	18.13	15.4356±7	15.45	0.510911±17	-33.69
LM #062	30	32	0.777440±7	18.2645±9	18.28	15.4544±8	15.47	0.510904±7	-33.83
LM #063	61	63	0.774694±5	18.0903±19	18.11	15.435±16	15.45	0.510893±7	-34.04

Sample ID	Sediment Depth [cm]		Isotope Data dc Fraction						
	Top	Bottom	$^{87}Sr/^{86}Sr$	$^{206}Pb/^{204}Pb$	$^{206}Pb/^{204}Pb^{corr}$	$^{207}Pb/^{204}Pb$	$^{207}Pb/^{204}Pb^{corr}$	$^{143}Nd/^{144}Nd$	εNd
LM #046	6	7	0.772418±6	18.1226±10	18.14	15.4378±90	15.45	0.510924±13	-33.43
LM #047	28	29	0.780308±9	18.4618±8	18.48	15.4776±6	15.49	0.510912±6	-33.67
LM #048	37	38	0.774363±6	18.1705±10	18.19	15.4415±9	15.46		
Sample ID	**Sediment Depth [cm]**		**Isotope Data bulk Fraction**						
	Top	**Bottom**	$^{87}Sr/^{86}Sr$	$^{206}Pb/^{204}Pb$	$^{206}Pb/^{204}Pb^{corr}$	$^{207}Pb/^{204}Pb$	$^{207}Pb/^{204}Pb^{corr}$	$^{143}Nd/^{144}Nd$	εNd
LM #046	6	7	0.772439±11	18.7845±10	18.80	15.5155±8	15.53	0.510910±8	-33.71
LM #047	28	29	0.778086±5	19.0131±12	19.03	15.5387±10	15.55	0.510915±3	-33.61
LM #048	37	38	0.775649±6	18.9765±10	19.00	15.5422±8	15.56	0.510881±3	-34.27

Table 8.4: Radiogenic isotope data of gravity core GeoB19946-4 for dt, dc, bulk fraction and FeMn leaching. All values were automatically corrected for internal fractionation. Pb data was additionally corrected by a bulk uncertainty of 0.1% per atomic mass unit (Pb^{corr}). εNd values were calculated with CHUR value of 0.512638 (Jacobsen & Wasserburg, 1980).

Sample ID	Sediment Depth [cm]		cal. Age	Isotope Data dt Fraction						
	Top	Bottom	[ka BP]	$^{87}Sr/^{86}Sr$	$^{206}Pb/^{204}Pb$	$^{206}Pb/^{204}Pb^{corr}$	$^{207}Pb/^{204}Pb$	$^{207}Pb/^{204}Pb^{corr}$	$^{143}Nd/^{144}Nd$	εNd
LM #020	6	7	2.02	0.746856±5	18.3853±7	18.40	15.4253±5	15.44	0.510917±4	-33.57
LM #064	28	29	3.00	0.745883±5	18.1554±8	18.17	15.3994±8	15.41	0.510964±8	-32.65
LM #021	37	38	3.40	0.746459±6	18.1134±13	18.13	15.3951±16	15.41	0.511148±5	-29.07
LM #065	49	50	3.93	0.747385±17	18.4085±8	18.43	15.4320±7	15.45	0.511002±3	-31.91
LM #022	68	69	4.78	0.747093±5	18.2248±9	18.24	15.4060±7	15.42	0.510950±8	-32.93
LM #023	92	93	5.45	0.748852±7	18.4123±9	18.43	15.4294±8	15.44	0.510948±4	-32.97
LM #024	116	117	5.99	0.748625±4	18.3760±6	18.39	15.4281±5	15.44	0.510942±4	-33.08
LM #025	223	224	7.64	0.747062±7	18.1078±110	18.13	15.4960±130	15.51	0.510863±4	-34.62
LM #026	291	292	8.48	0.748861±5	18.2405±6	18.26	15.3999±5	15.42	0.510912±4	-33.67
LM #027	400	401	9.06	0.754656±6	18.4357±19	18.45	15.4768±21	15.49	0.510836±4	-35.15
LM #028	517	518	9.12	0.751992±7	18.2552±5	18.27	15.4299±4	15.45	0.510827±4	-35.33

Sample ID	Sediment Depth [cm]		cal. Age	Isotope Data dt Fraction						
	Top	Bottom	[ka BP]	$^{87}Sr/^{86}Sr$	$^{206}Pb/^{204}Pb$	$^{206}Pb/^{204}Pb^{corr}$	$^{207}Pb/^{204}Pb$	$^{207}Pb/^{204}Pb^{corr}$	$^{143}Nd/^{144}Nd$	εNd
LM #058	600	601	9.17	0.757818±6	18.7703±10	18.79	15.5004±8	15.52	0.510855±9	-34.78
LM #059	750	751	9.57	0.738014±4	17.2738±6	17.29	15.2591±6	15.27	0.510937±13	-33.18
LM #029	909	910	10.15	0.730072±13	16.8445±27	16.86	15.1880±24	15.20	0.510934±5	-33.24
LM #060	1000	1001	10.49	0.728444±4	16.1493±8	16.17	15.0927±7	15.11	0.510936±5	-33.20
LM #030	1101	1102	10.76	0.751269±4	18.4259±7	18.44	15.4427±7	15.46	0.510810±7	-35.66
LM #031	1278	1279	10.89	0.751046±6	18.4914±9	18.51	15.4348±8	15.45	0.510811±4	-35.64
Sample ID	**Sediment Depth [cm]**		**cal. Age**	**Isotope Data dc Fraction**						
	Top	**Bottom**	**[ka BP]**	$^{87}Sr/^{86}Sr$	$^{206}Pb/^{204}Pb$	$^{206}Pb/^{204}Pb^{corr}$	$^{207}Pb/^{204}Pb$	$^{207}Pb/^{204}Pb^{corr}$	$^{143}Nd/^{144}Nd$	εNd
LM #020	6	7	2.02	0.746569±7	18.3931±31	18.41	15.4333±25	15.45	0.510930±3	-33.32
LM #064	28	29	3.00	0.745936±7	18.2623±8	18.28	15.4106±8	15.43	0.511007±24	-31.82
LM #021	37	38	3.40	0.745680±7	18.2458±45	18.26	15.4509±57	15.47	0.510944±5	-33.04
LM #065	49	50	3.93	0.747611±5	18.5121±7	18.53	15.4372±6	15.45	0.510965±6	-32.64
LM #022	68	69	4.78	0.745680±6	18.2879±7	18.31	15.4093±6	15.42	0.510958±3	-32.77
LM #023	92	93	5.45	0.748227±5	18.4884±24	18.51	15.4723±23	15.49	0.510949±4	-32.95
LM #024	116	117	5.99	0.748745±8	18.5300±69	18.55	15.4978±75	15.51	0.510926±9	-33.40
LM #025	223	224	7.64	0.747148±6	18.1844±18	18.20	15.4251±22	15.44	0.510852±3	-34.84
LM #026	291	292	8.48		18.2786±22	18.30	15.4098±22	15.43	0.510915±3	-33.61
LM #027	400	401	9.06	0.755142±6	18.6271±20	18.65	15.5212±23	15.54	0.510807±24	-35.72
LM #028	517	518	9.12	0.752899±7	18.4261±15	18.44	15.4421±15	15.46	0.510814±5	-35.58
LM #058	600	601	9.17	0.757768±5	18.8358±9	18.85	15.5118±8	15.53	0.510818±7	-35.50
LM #059	750	751	9.57	0.738303±5	17.2680±13	17.29	15.2387±11	15.25	0.510954±8	-32.85
LM #029	909	910	10.15	0.728503±5	16.6317±20	16.65	15.1628±21	15.18	0.510849±4	-34.90
LM #060	1000	1001	10.49	0.728439±4	15.7384±7	15.75	15.0022±7	15.02	0.510888±6	-34.14
LM #030	1101	1102	10.76	0.750045±8	18.1383±18	18.16	15.4242±19	15.44	0.510813±3	-35.60
LM #031	1278	1279	10.89	0.751872±6	18.5088±14	18.53	15.4485±15	15.46	0.510822±18	-35.42

Sample ID	Sediment Depth [cm]		cal. Age	Isotope Data bulk Fraction						
	Top	Bottom	[ka BP]	$^{87}Sr/^{86}Sr$	$^{206}Pb/^{204}Pb$	$^{206}Pb/^{204}Pb^{corr}$	$^{207}Pb/^{204}Pb$	$^{207}Pb/^{204}Pb^{corr}$	$^{143}Nd/^{144}Nd$	εNd
LM #020	6	7	2.02	0.744919±5	19.3533±23	19.37	15.5973±24	15.61		
LM #064	28	29	3.00	0.744633±6	19.2832±12	19.30	15.5332±10	15.55	0.510965±11	-32.64
LM #021	37	38	3.40	0.744013±7	19.1117±14	19.13	15.5411±15	15.56		
LM #065	49	50	3.93	0.745683±5	19.3444±7	19.36	15.5443±6	15.56	0.510968±9	-32.58
LM #022	68	69	4.78	0.745198±7	19.2528±44	19.27	15.6158±46	15.63		
LM #023	92	93	5.45	0.747292±11	19.4670±9	19.49	15.5592±10	15.57		
LM #024	116	117	5.99	0.746384±6	19.4493±33	19.47	15.6098±36	15.63		
LM #025	223	224	7.64	0.746776±5	19.2131±39	19.23	15.5835±33	15.60		
LM #026	291	292	8.48	0.747442±5	19.4208±10	19.44	15.5815±8	15.60		
LM #027	400	401	9.06	0.754744±8	19.6821±88	19.70	15.6713±74	15.69		
LM #028	517	518	9.12	0.752197±6	19.3317±24	19.35	15.5328±19	15.55		
LM #058	600	601	9.17	0.757252±5	19.7671±9	19.79	15.6223±9	15.64	0.510819±7	-35.48
LM #059	750	751	9.57	0.740666±5	18.5095±12	18.53	15.4231±10	15.44	0.510894±5	-34.02
LM #029	909	910	10.15	0.728887±5	17.1048±44	17.12	15.2508±39	15.27		
LM #060	1000	1001	10.49	0.727729±7	16.4804±9	16.50	15.1333±8	15.15	0.510836±6	-35.15
LM #030	1101	1102	10.76	0.749321±7	19.0980±12	19.12	15.5009±10	15.52		
LM #031	1278	1279	10.89	0.750680±5	19.4253±37	19.44	15.6235±38	15.64		

Sample ID	Sediment Depth [cm]		cal. Age	Isotope Data Leachate						
	Top	Bottom	[ka BP]	$^{87}Sr/^{86}Sr$	$^{206}Pb/^{204}Pb$	$^{206}Pb/^{204}Pb^{corr}$	$^{207}Pb/^{204}Pb$	$^{207}Pb/^{204}Pb^{corr}$	$^{143}Nd/^{144}Nd$	εNd
LM #020	6	7	2.02	0.720577±11	24.0964±22	24.12	16.1106±15	16.13	0.510987±6	-32.21
LM #021	37	38	3.40	0.723054±8	23.7554±21	23.78	16.0631±14	16.08	0.511062±10	-30.74
LM #022	68	69	4.78	0.722231±6	23.8020±16	23.83	16.0803±10	16.10	0.511067±5	-30.65
LM #023	92	93	5.45	0.723364±15	23.7744±56	23.80	16.0665±38	16.08	0.511079±5	-30.41
LM #024	116	117	5.99	0.726567±6	23.8627±15	23.89	16.0844±10	16.10	0.511054±7	-30.90
LM #025	223	224	7.64	0.743083±11	24.5383±39	24.56	16.1831±25	16.20	0.510797±7	-35.91

Sample ID	Sediment Depth [cm]		cal. Age	Isotope Data Leachate						
	Top	Bottom	[ka BP]	$^{87}Sr/^{86}Sr$	$^{206}Pb/^{204}Pb$	$^{206}Pb/^{204}Pb^{corr}$	$^{207}Pb/^{204}Pb$	$^{207}Pb/^{204}Pb^{corr}$	$^{143}Nd/^{144}Nd$	εNd
LM #026	291	292	8.48	0.73296±45	24.0762±40	24.10	16.1387±27	16.15	0.510950±5	-32.93
LM #027	400	401	9.06	0.751981±11	26.1281±23	26.15	16.2721±15	16.29	0.510762±7	-36.60
LM #028	517	518	9.12	0.752546±9	25.0788±32	25.10	16.2712±21	16.29	0.510785±8	-36.15
LM #029	909	910	10.15	0.753286±12	24.6379±185	24.66	16.1673±119	16.18	0.510721±135	-37.39
LM #030	1101	1102	10.76	0.757578±5	25.4666±227	25.49	16.2757±144	16.29	0.510815±6	-35.56
LM #031	1278	1279	10.89	0.764360±11					0.510733±13	-37.16

Table 8.5: Radiogenic isotope data of gravity core AMD14-Kane2B for dt, dc, and bulk fraction. All values were automatically corrected for internal fractionation. Pb data was additionally corrected by a bulk uncertainty of 0.1% per atomic mass unit (Pb^{corr}). εNd values were calculated with CHUR value of 0.512638 (Jacobsen & Wasserburg, 1980).

Sample ID	Sediment Depth [cm]		cal. Age	Isotope Data dt Fraction						
	Top	Bottom	[ka BP]	$^{87}Sr/^{86}Sr$	$^{206}Pb/^{204}Pb$	$^{206}Pb/^{204}Pb^{corr}$	$^{207}Pb/^{204}Pb$	$^{207}Pb/^{204}Pb^{corr}$	$^{143}Nd/^{144}Nd$	εNd
LM #046	20	21	0.99	0.723919±6	18.2321±10	18.25	15.4428±8	15.46	0.511954±5	-13.34
LM #047	60	61	2.65	0.723648±9	18.2316±7	18.25	15.4328±7	15.45	0.511982±7	-12.80
LM #048	100	101	3.68	0.725033±7	18.2518±12	18.27	15.4358±11	15.45	0.511921±7	-13.99
LM #049	140	141	4.48	0.725441±6	18.2576±8	18.28	15.4500±9	15.47	0.511886±4	-14.67
LM #050	204	205	6.11	0.727661±7	18.1949±7	18.21	15.4297±6	15.45	0.511783±6	-16.68
LM #051	252	253	7.51	0.728296±7	17.9679±9	17.99	15.4066±8	15.42	0.511649±7	-19.29
LM #052	276	277	8.00	0.729787±6	17.7593±9	17.78	15.3938±8	15.41	0.511503±7	-22.14
LM #053	292	293	8.22	0.733694±6	17.8154±8	17.83	15.3814±8	15.40	0.511353±8	-25.07
LM #054	316	317	8.30	0.725613±5	18.3102±6	18.33	15.4497±6	15.47	0.511889±7	-14.61
LM #055	332	333	8.44	0.734424±10	17.8588±11	17.88	15.3871±9	15.40	0.511329±7	-25.53
LM #056	356	357	8.70	0.736485±5	17.9431±10	17.96	15.3909±10	15.41	0.511914±8	-14.12
LM #057	388	389	8.93	0.725260±5	18.5249±8	18.54	15.4745±7	15.49	0.511949±6	-13.44

Sample ID	Sediment Depth [cm]		cal. Age	Isotope Data dc Fraction						
	Top	Bottom	[ka BP]	$^{87}Sr/^{86}Sr$	$^{206}Pb/^{204}Pb$	$^{206}Pb/^{204}Pb^{corr}$	$^{207}Pb/^{204}Pb$	$^{207}Pb/^{204}Pb^{corr}$	$^{143}Nd/^{144}Nd$	εNd
LM #046	6	7	0.99	0.723153±4	18.2416±8	18.26	15.4417±6	15.46	0.511949±20	-13.44
LM #047	28	29	2.65	0.723374±4	18.2623±10	18.28	15.4454±8	15.46	0.511937±7	-13.67
LM #048	37	38	3.68		18.3441±9	18.36	15.4500±8	15.47	0.511930±10	-13.81
LM #049	49	50	4.48	0.724667±5	18.2904±30	18.31	15.4444±25	15.46	0.511899±21	-14.42
LM #050	68	69	6.11	0.726877±6	18.2268±27	18.25	15.4388±22	15.45	0.511814±11	-16.07
LM #051	92	93	7.51	0.727927±6	17.9586±17	17.98	15.4101±14	15.43	0.511679±15	-18.71
LM #052	116	117	8.00	0.735891±5	17.8259±12	17.84	15.3888±11	15.40	0.511490±9	-22.39
LM #053	223	224	8.22	0.733655±5	17.8935±11	17.91	15.3971±10	15.41	0.511332±9	-25.48
LM #054	291	292	8.30	0.733858±5	18.1934±11	18.21	15.4342±9	15.45	0.511948±11	-13.46
LM #055	400	401	8.44	0.722999±6	17.8483±11	17.87	15.3925±11	15.41	0.511284±11	-26.41
LM #056	517	518	8.70	0.729758±4	17.9877±8	18.01	15.3990±7	15.41	0.511206±30	-27.93
LM #057	600	601	8.93	0.724163±5	18.5166±15	18.54	15.4803±12	15.50	0.511970±7	-13.03

Sample ID	Sediment Depth [cm]		cal. Age	Isotope Data bulk Fraction						
	Top	Bottom	[ka BP]	$^{87}Sr/^{86}Sr$	$^{206}Pb/^{204}Pb$	$^{206}Pb/^{204}Pb^{corr}$	$^{207}Pb/^{204}Pb$	$^{207}Pb/^{204}Pb^{corr}$	$^{143}Nd/^{144}Nd$	εNd
LM #046	6	7	0.99	0.718935±5	18.4819±12	18.50	15.4827±9	15.50	0.511994±6	-12.56
LM #047	28	29	2.65	0.719696±5	18.5580±9	18.58	15.4777±8	15.49	0.511962±8	-13.19
LM #048	37	38	3.68	0.719770±7	18.5305±12	18.55	15.4790±10	15.49	0.511911±4	-14.18
LM #049	49	50	4.48	0.719104±5	18.5017±8	18.52	15.4692±8	15.48	0.511892±22	-14.55
LM #050	68	69	6.11	0.720681±6	18.5747±12	18.59	15.4807±11	15.50	0.511806±7	-16.23
LM #051	92	93	7.51	0.720768±9	18.5377±16	18.56	15.4803±13	15.50	0.511691±13	-18.47
LM #052	116	117	8.00	0.723324±6	18.3858±9	18.40	15.4525±7	15.47	0.511502±4	-22.16
LM #053	223	224	8.22	0.727517±5	18.5815±9	18.60	15.4707±9	15.49	0.511346±51	-25.20
LM #054	291	292	8.30	0.717436±6	18.4025±13	18.42	15.4598±12	15.48	0.511954±6	-13.34
LM #055	400	401	8.44	0.734891±10	18.4710±22	18.49	15.4690±18	15.48	0.511255±9	-26.98
LM #056	517	518	8.70	0.728056±6	18.5380±14	18.56	15.4638±11	15.48	0.511307±10	-25.96

Sample ID	Sediment Depth [cm]		cal. Age	Isotope Data bulk Fraction						
	Top	Bottom	[ka BP]	$^{87}Sr/^{86}Sr$	$^{206}Pb/^{204}Pb$	$^{206}Pb/^{204}Pb^{corr}$	$^{207}Pb/^{204}Pb$	$^{207}Pb/^{204}Pb^{corr}$	$^{143}Nd/^{144}Nd$	εNd
LM #057	600	601	8.93	0.715823±7	18.5780±15	18.60	15.4930±13	15.51	0.512001±7	-12.43

8.2. Mineralogical Data (XRD)

Table 8.6: Mineralogical composition of gravity core GeoB19905-1. Data underlies an estimated uncertainty of ~2%.

Sample ID	Sediment Depth [cm]		cal. Age	Mineral Content [%]										
	Top	Bottom	[ka BP]	Quartz	Albite	Micro-cline	Horn-blende	Pyroxene	Biotite	Clino-chlore	Pyrite	Ilmenite	Calcite	Dolomite
LM #033	40	41	0.17	43.5	29.4	5.1	7.1	0.0	10.6	1.7	1.5	0.0	1.1	0.0
LM #036	150	151	0.72	52.7	29.6	4.7	2.8	0.0	4.7	1.9	1.8	0.0	1.6	0.2
LM #037	160	161	0.79	35.7	27.4	5.7	9.1	0.0	15.7	1.7	1.4	0.0	2.3	1.0
LM #038	300	301	1.93	47.2	28.8	4.8	8.4	0.0	6.5	1.6	1.7	0.0	1	0.0
LM #040	330	331	2.24	33.9	32.9	4.1	14.2	0.0	7.1	1.4	1.8	0.0	4.6	0.0
LM #041	360	361	2.58	32.9	30.1	7.1	5.2	0.0	14.8	2.1	1.7	0.0	6.1	0.0
LM #042	370	371	2.70	39.1	32.2	9.1	9	0.0	3.4	3.3	2.0	0.0	1.9	0.0
LM #043	400	401	3.04	38.4	37.3	4.4	5.2	0.0	5.5	2	1.6	0.0	5.6	0.0
LM #044	410	411	3.16	58.2	10.9	11.7	6	0.0	7.6	2.2	1.9	0.0	1.5	0.0
LM #045	460	461	3.75	39.1	14.8	10.4	8.4	0.0	5.6	3.1	1.8	0.0	16.8	0.0
LM #066	470	471	3.87	41.8	30.4	4.6	7.1	1.3	4.2	1.6	1.8	0.0	7.2	0.0
LM #067	510	511	4.36	38.9	33.9	4.5	7.2	1.1	4.1	1.5	1.7	0.0	7.1	0.0
LM #068	580	581	5.19	36.7	20.4	5.1	6.8	0.0	5	2.1	3.6	0.0	20.3	0.0
LM #069	590	591	5.31	31.9	25.5	3.4	12.7	0.0	4.1	1.7	1.5	0.0	17	2.2
LM #070	610	611	5.56	41.4	20.5	5.3	6.9	0.0	5.3	2.6	1.4	0.9	15.7	0.0
LM #071	670	671	7.97	34.8	32.2	4.8	14.4	0.0	2.6	1.4	1.4	0.0	8.4	0.0
LM #072	680	681	8.11	40.1	26.9	5.2	10.6	0.0	5.3	2.1	1.9	0.0	7.9	0.0

Sample ID	Sediment Depth [cm]		cal. Age	Mineral Content [%]										
	Top	Bottom	[ka BP]	Quartz	Albite	Micro-cline	Horn-blende	Pyroxene	Biotite	Clino-chlore	Pyrite	Ilmenite	Calcite	Dolomite
LM #073	700	701	8.33	44.2	23.6	4.6	11.4	0.0	4.9	1.3	1.7	0.0	7.3	1.0
LM #074	710	711	8.44	43.4	27.1	4.4	6.9	1.5	3.5	1.5	1.9	0.0	9.8	0.0
LM #075	720	721	8.53	40.4	29.3	5.3	8.3	0.0	4.2	1.8	1.8	0.0	8.9	0.0
LM #076	730	731	8.62	43.2	26.2	5.5	11.5	0.0	4.3	1.2	1.4	0.0	6.7	0.0
LM #077	820	821	9.48	42.4	34.3	6.6	5.4	0.0	5.8	2.1	1.9	0.0	1.5	0.0
LM #078	920	921	10.45	43.5	28.8	4.4	11.7	0.0	8.1	1.3	1.6	0.0	0.6	0.0
LM #087	1030	1031	11.54	41.8	29.2	5.1	12.5	1.4	5.4	2.1	1.6	0.0	0.9	0.0

Table 8.7: Mineralogical composition of gravity core GeoB19927-3. Data underlies an estimated uncertainty of ~2%.

Sample ID	Sediment Depth [cm]		cal. Age	Mineral Content [%]										
	Top	Bottom	[ka BP]	Quartz	Albite	Micro-cline	Horn-blende	Augite	Biotite	Clino-chlore	Kaolinite	Smectite	Pyrite	Calcite
LM #001	0	1	-0.05	36.4	26.5	11	4.4	2.8	7.1	5.7	1.1	3.6	1.4	0.0
LM #002	50	51	1.25	36.5	22.6	7.9	3.5	1.7	12.8	6.3	1.1	3.8	1.7	2.1
LM #003	100	101	1.86	32.2	29.2	10.4	5	2.1	8.7	5.4	1.2	3.5	1.6	0.7
LM #004	150	151	2.46	34.7	26.4	6.6	3.9	1.8	8.5	8.4	1.4	5	1.9	1.4
LM #005	200	201	3.02	33.1	26.3	10.2	5	2.6	7.5	5.7	1.3	3.9	2.3	2.1
LM #006	250	251	3.45	34.9	26.7	9.2	3.6	1.5	8.2	6.7	1.3	5	1.6	1.3
LM #007	300	301	3.87	33.6	29.6	9.5	5.1	2.1	7.2	5.4	1.2	3.5	1.7	1.1
LM #008	350	351	4.29	24.4	9.8	2.3	41.7	0.8	5.1	6.8	4.3	3.1	1.3	0.4
LM #009	400	401	4.72	33.4	25.4	9.5	4.2	2.0	10.4	5.1	2.7	4.3	1.9	1.1
LM #010	500	501	5.48	34.8	25.9	9.6	5.3	1.7	9.2	5.1	1	4.4	1.9	1.1
LM #011	600	601	6.18	39.1	27.2	7.7	4.3	1.4	9.2	4.2	0.9	3.5	1.5	1.0
LM #012	700	701	7.14	39.4	24.2	8.2	3.6	1.5	9.8	5.1	1.8	3.7	1.6	1.1
LM #013	800	801	8.01	35.4	26.8	8.8	3.8	2.1	9.2	4.8	2.9	2.9	2.1	1.2

Sample ID	Sediment Depth [cm]		cal. Age	Mineral Content [%]										
	Top	Bottom	[ka BP]	Quartz	Albite	Micro-cline	Horn-blende	Augite	Biotite	Clino-chlore	Kaolinite	Smectite	Pyrite	Calcite
LM #014	850	851	8.35	39.9	25.9	8.3	3.7	1.2	8.6	4.3	0.9	4.8	1.3	1.1
LM #015	900	901	8.69	35.7	24.2	8.9	3.4	1.9	10	6.2	3.2	3.7	1.8	1.0
LM #016	950	951	9.03	47.5	23.9	7.7	3.1	1.1	6.3	3.9	0.9	3.4	1.2	1.0
LM #017	1000	1001	9.37	40.9	26.1	8.3	3.4	1.2	7.7	5.2	1.1	3.7	1.3	1.1
LM #018	1050	1051	9.73	43.3	28.4	7.3	2.9	1.1	7	4.5	1	3.3	1.2	0.0

Table 8.8: Mineralogical composition of gravity core GeoB19946-4. Data underlies an estimated uncertainty of ~2%.

Sample ID	Sediment Depth [cm]		cal. Age	Mineral Content [%]										
	Top	Bottom	[ka BP]	Quartz	Albite	Micro-cline	Horn-blende	Augite	Biotite	Clino-chlore	Kaolinite	Smectite	Pyrite	Ilmenite
LM #020	6	7	2.02	38.4	26.1	8.8	5.2	0.7	4.1	6.6	5.3	2.2	2.6	0.0
LM #021	28	29	3.00	40.0	25.5	8.2	8.3	0.0	10.3	4.2	0.0	0.0	2.5	1.0
LM #022	37	38	3.40	38.1	31.3	9.7	4.6	1.1	5.7	5.3	0.0	1.6	1.6	1.0
LM #023	49	50	3.93	35.8	27.3	8.8	6.3	0.0	13.6	4.5	0.0	0.0	2.7	1.0
LM #024	68	69	4.78	39.9	26.1	10.1	4.9	0.8	10.1	5.5	0.0	1.5	1.1	0.0
LM #025	92	93	5.45	33.3	32.1	8.2	6.1	3.1	11.0	2.9	0.0	1.4	1.9	0.0
LM #026	116	117	5.99	31.3	29.3	8.7	8.3	1.1	15.4	3.5	0.0	1.3	1.1	0.0
LM #027	223	224	7.64	31.4	29.5	7.9	11.3	1.0	12.8	2.9	0.0	1.2	2.0	0.0
LM #028	291	292	8.48	34.3	33.8	5.4	8.4	1.0	10.3	4.3	0.0	0.0	2.5	0.0
LM #029	400	401	9.06	30.1	29.7	7.6	10.4	1.5	10.3	6.4	0.0	1.6	2.4	0.0
LM #030	517	518	9.12	27.5	40.0	2.6	13.2	1.0	9.7	4.0	0.0	0.0	2.0	0.0
LM #031	600	601	9.17	26.4	33.1	14.5	5.4	0.0	8.8	4.7	0.0	0.0	5.6	1.5
LM #058	750	751	9.57	32.0	37.2	8.1	9.3	0.0	7.2	2.4	0.0	0.0	2.8	1.0
LM #059	909	910	10.15	25.8	31.1	6.2	7.1	1.1	21.1	4.6	0.0	0.0	3.0	0.0

Sample ID	Sediment Depth [cm]		cal. Age	Mineral Content [%]										
	Top	Bottom	[ka BP]	Quartz	Albite	Micro-cline	Horn-blende	Augite	Biotite	Clino-chlore	Kaolinite	Smectite	Pyrite	Ilmenite
LM #060	1000	1001	10.49	26.2	29.5	11.3	4.8	0.0	20.9	5.8	0.0	0.0	1.5	0.0
LM #064	1101	1102	10.76	21.9	29.4	9.5	9.5	0.0	21.9	4.9	0.0	0.0	2.9	0.0
LM #065	1278	1279	10.89	21.5	30.4	9.3	11.2	0.0	16.2	5.8	0.0	0.0	4.0	1.6

8.3. Elemental Composition (ICP-OES, ICP-MS)

Table 8.9: Elemental composition of gravity core GeoB19927-3 FeMn leachates. Mg and Ca were measured on ICP-OES. Mn and Fe were measured on ICP-MS. Samples were diluted by 1:100 upon measurement.

						Elemental Composition Leachate								
Sample ID	Sediment Depth [cm]		Weight	Addition 2M HNO_3	Dilution Factor	Mg		Ca		Mn		Fe		Fe/Mn ratio
	Top	Bottom	[g]	[ml]		[mg/l]	[µg/g sed]	[mg/l]	[µg/g sed]	[µg/l]	[µg/g sed]	[µg/l]	[µg/g sed]	
LM #002	100	101	0.0341	1.1	32.26	10.7	34606.45	7.5	24070.97	227	733	5097	16442	22.4
LM #004	300	301	0.0302	1.1	36.42	11.4	41552.32	7.54	27463.58	266	967	6271	22841	23.6
LM #007	600	601	0.0306	1.1	35.95	11.1	39819.28	7.03	25278.43	324	1166	6966	25041	21.5
LM #015	850	851	0.0290	1.1	37.93	10.2	38670.69	7.09	26881.72	316	1200	6383	24211	20.2
LM #010	900	901	0.0868	1.1	12.67	6.98	8850.69	5.21	6597.47	412	522	3471	4398	8.4
LM #017	1000	1001	0.0860	1.1	12.79	6.89	8817.91	4.72	6030.81	298	381	3409	4360	11.4

8.4. Radiogenic Isotope Data for Standard Reference Material

Table 8.10: Radiogenic isotope data for standard reference material measured along with all samples for data accuracy control over the measuring period of 2.5 years.

NIST SRM 987		JNdi-1		NIST SRM 981		
Date	**$^{87}Sr/^{86}Sr$**	**Date**	**$^{144}Nd/^{143}Nd$**	**Date**	**$^{206}Pb/^{204}Pb$**	**$^{207}Pb/^{204}Pb$**
15.05.2017	0.710247±6	13.06.2017	0.512096±6	16.06.2017	16.9145±6	15.4624±8
23.06.2017	0.710258±8	30.06.2017	0.512091±5	29.06.2017	16.9046±7	15.4494±7
29.06.2017	0.710243±5	18.12.2017	0.512090±6	05.12.2017	16.8952±5	15.4364±6
10.11.2017	0.710251±6	17.01.2018	0.512072±5	07.12.2017	16.8982±4	15.4402±5
30.11.2017	0.710248±4	19.01.2018	0.512096±8	08.12.2017	16.9021±5	15.4453±4
08.12.2017	0.710257±5	19.03.2018	0.512126±2	18.12.2017	16.9000±6	15.4427±7
19.06.2018	0.710256±5	04.09.2018	0.512103±6	31.08.2018	16.8985±5	15.4406±6
25.06.2018	0.710246±6	04.10.2018	0.512088±5	06.09.2018	16.9247±6	15.4766±7
21.08.2018	0.710272±7	05.10.2018	0.512088±4	12.09.2018	16.9062±6	15.4519±5
14.09.2018	0.710253±6	28.01.2019	0.512081±9	14.09.2018	16.9047±6	15.4494±6
08.10.2018	0.710249±7	29.01.2019	0.512089±6	10.12.2018	16.8958±6	15.4370±6
10.10.2018	0.710370±2	12.02.2019	0.512084±7	11.01.2019	16.8951±7	15.4362±6
16.01.2019	0.710245±7	14.02.2019	0.512088±4	15.01.2019	16.8871±4	15.4249±4
17.01.2019	0.710260±5	04.03.2019	0.512106±6	01.03.2019	16.8969±9	15.4387±9
13.02.2019	0.710248±8	06.04.2019	0.512085±4	07.10.2019	16.8983±1	15.4411±1
02.04.2019	0.710250±6	18.03.2019	0.512097±9	08.10.2019	16.9001±8	15.4430±8
28.06.2019	0.710257±6	28.06.2019	0.511176±8	23.11.2019	16.8903±5	15.4297±7
29.06.2019	0.710259±6	05.07.2019	0.512143±7	24.11.2019	16.8952±8	15.4367±9
04.07.2019	0.710246±6	25.10.2019	0.512108±1	26.11.2019	16.9014±6	15.4451±5
05.07.2019	0.710241±6	29.10.2019	0.512176±8	27.11.2019	16.8889±5	15.4284±5
08.07.2019	0.710251±7	05.11.2019	0.512110±7			
09.07.2019	0.710260±6	19.11.2019	0.512144±5			
22.10.2019	0.710247±5	20.11.2019	0.512129±5			
31.10.2019	0.710248±5	22.11.2019	0.512133±6			
08.11.2019	0.710248±5					
16.11.2019	0.710241±6					
16.11.2019	0.710249±6					
19.11.2019	0.710255±4					
20.11.2019	0.710252±9					

8.5. Radiogenic Isotope Data for Geological Terrains

Table 8.11: Radiogenic isotope data of geological terrains of Greenland, Ellesmere Island, Axel Heiberg Island and Baffin Island. Data taken from previously published literature.

Ketilidian Mobile Belt (KMB)					
Colville et al., 2011 (1); Reyes et al., 2014 (2)					
Sample Type	**$^{87}Sr/^{86}Sr$**	**$^{206}Pb/^{204}Pb$**	**$^{207}Pb/^{204}Pb$**	**ε_{Nd}**	**Ref.**
stream sediment	0.718350	22.249	15.907	-22.0	(1)
stream sediment	0.717699	22.289	15.897	-22.1	(2)
stream sediment	0.716310	22.872	15.961	-21.9	(1)
stream sediment	0.716278	22.657	15.935	-22.1	(2)
stream sediment	0.716580	23.835	16.071	-21.6	(1)
stream sediment	0.717930	22.253	15.910	-22.2	(1)
stream sediment	0.708922	21.779	15.849	-17.4	(2)
stream sediment	0.712708	20.474	15.718	-18.7	(2)
stream sediment	0.717290	20.733	15.741	-15.2	(1)
stream sediment	0.712411	18.791	15.529	-23.6	(2)
stream sediment	0.712676	18.566	15.484	-23.5	(2)
stream sediment	0.713137	21.195	15.751	-23.4	(2)
stream sediment	0.711059	20.758	15.695	-22.2	(2)
stream sediment	0.720920	20.667	15.764	-31.4	(1)
Archean Block (AB)					
Colville et al., 2011 (1); Reyes et al., 2014 (2)					
Sample Type	**$^{87}Sr/^{86}Sr$**	**$^{206}Pb/^{204}Pb$**	**$^{207}Pb/^{204}Pb$**	**ε_{Nd}**	**Ref.**
stream sediment	0.738501	14.278	35.138	-32.3	(2)
stream sediment	0.71588	14.659	35.192	-31.1	(2)
stream sediment	0.716788	14.512	34.958	-31.2	(2)
stream sediment	0.720129	14.400	35.471	-32.8	(2)
stream sediment	0.726286	14.418	34.372	-25.8	(2)
stream sediment	0.733156	14.562	34.979	-32.8	(2)
stream sediment	0.71702	14.559	34.544	-29.0	(2)
stream sediment	0.715696	14.575	35.029	-31.0	(2)
stream sediment	0.727575	14.391	35.197	-35.8	(2)
stream sediment	0.7264	14.512	34.663	-27.3	(1)
stream sediment	0.72331	14.518	34.718	-28.3	(1)
stream sediment	0.72669	15.072	37.463	-40.8	(1)
stream sediment	0.727251	15.397	38.994	-29.5	(2)
stream sediment	0.717451	15.022	36.106	-26.7	(2)
stream sediment	0.717702	14.926	35.660	-29.1	(2)
Nagssugtoqidian Mobile Belt (NMB)					
Colville et al., 2011 (1); Reyes et al., 2014 (2)					
Sample Type	**$^{87}Sr/^{86}Sr$**	**$^{206}Pb/^{204}Pb$**	**$^{207}Pb/^{204}Pb$**	**ε_{Nd}**	**Ref.**
stream sediment	0.73140	17.58	15.22	-29.3	(1)
stream sediment	0.73793	16.04	14.94	-33.3	(2)
stream sediment	0.71322	15.07	14.82	-31.5	(1)
stream sediment	0.71206	17.41	15.17	-36.8	(1)

Nagssugtoqidian Mobile Belt (NMB)					
Colville et al., 2011 (1); Reyes et al., 2014 (2)					
Sample Type	**$^{87}Sr/^{86}Sr$**	**$^{206}Pb/^{204}Pb$**	**$^{207}Pb/^{204}Pb$**	**ε_{Nd}**	**Ref.**
stream sediment	0.71245	14.81	14.77	-35.0	(1)
stream sediment	0.71260	16.66	15.12	-35.8	(1)
stream sediment	0.70740	17.01	15.28	-29.0	(1)
stream sediment	0.70797	17.51	15.26	-31.4	(1)
stream sediment	0.71211			-34.0	(1)
stream sediment	0.71324			-29.6	(1)
stream sediment	0.71301	14.48	14.70	-36.4	(2)
stream sediment	0.72224	16.53	15.07	-32.3	(2)
stream sediment	0.72158	18.14	15.33	-34.9	(2)
stream sediment	0.72047	18.00	15.31	-32.9	(2)
stream sediment	0.72246	20.79	15.57	-36.6	(2)
stream sediment	0.71874	17.95	15.30	-32.7	(2)
stream sediment	0.70673	15.90	15.09	-27.9	(1)
stream sediment	0.70709	16.38	15.18	-23.3	(1)
stream sediment	0.71363	17.13	15.19	-32.3	(1)
stream sediment	0.70476	16.92	15.37	-26.2	(2)
stream sediment	0.70656	17.37	15.47	-26.6	(2)
stream sediment	0.70499			-30.0	(2)
Disko Island (DI)					
Larsen & Pedersen, 2009 and ref. therein (3)					
Sample Type	**$^{87}Sr/^{86}Sr$**	**$^{206}Pb/^{204}Pb$**	**$^{207}Pb/^{204}Pb$**	**ε_{Nd}**	**Ref.**
rock	0.703314	17.970	15.573	8.47	(3)
rock	0.703320	17.832	15.529	8.27	(3)
rock	0.703265	18.066	15.413	8.70	(3)
rock	0.703214	17.879	15.530	7.67	(3)
rock	0.703399	18.069	15.418	7.78	(3)
rock	0.703464	18.034	15.394	7.57	(3)
rock	0.703319	18.109	15.505	8.88	(3)
rock	0.703243	18.052	15.495	8.11	(3)
rock	0.703352	17.846	15.357	7.74	(3)
rock	0.703297	18.075	15.407	8.34	(3)
rock	0.703466	17.747	15.308	7.55	(3)
rock	0.703333	17.939	15.437	7.33	(3)
rock	0.70572	18.823	15.307	-3.12	(3)
rock	0.70379	19.868	15.549	-4.41	(3)
rock	0.702956	18.020	15.470	10.18	(3)
rock	0.703383	17.805	15.343	7.99	(3)
rock	0.703329	17.965	15.388	8.32	(3)
rock	0.70376	20.177	15.574	-4.39	(3)
rock	0.703210	17.733	15.361	9.56	(3)
rock	0.703480	18.105	15.482	6.55	(3)
rock	0.702975	17.938	15.404	9.27	(3)
rock	0.703263	18.024	15.409	7.54	(3)
rock	0.703456	17.926	15.337	7.57	(3)

Disko Island (DI)					
Larsen & Pedersen, 2009 and ref. therein (3)					
Sample Type	**$^{87}Sr/^{86}Sr$**	**$^{206}Pb/^{204}Pb$**	**$^{207}Pb/^{204}Pb$**	**ε_{Nd}**	**Ref.**
rock	0.703433	17.744	15.350	7.38	(3)
rock	0.703027	17.972	15.410	9.29	(3)
rock	0.703147	17.740	15.399	8.46	(3)
rock	0.703372	17.931	15.398	8.30	(3)
rock	0.708931	17.315	15.222	-4.07	(3)
rock	0.705421	18.376	15.463	2.59	(3)
rock	0.703080	17.813	15.393	10.01	(3)
rock	0.703403	17.528	15.308	8.37	(3)
rock	0.703803	16.904	15.190	6.20	(3)
rock	0.703173	17.840	15.411	9.11	(3)
rock	0.704517	17.390	15.237	3.41	(3)
rock	0.703293	17.862	15.421	8.64	(3)
Rinkian Mobile Belt (RMB)					
Kalsbeek et al., 1998 (4)					
Sample Type	**$^{87}Sr/^{86}Sr$**	**$^{206}Pb/^{204}Pb$**	**$^{207}Pb/^{204}Pb$**	**ε_{Nd}**	**Ref.**
Rock	0.74493				(4)
rock	0.79478				(4)
rock	0.83591			-23.58	(4)
rock	0.75406				(4)
rock	0.76366				(4)
rock	0.76966				(4)
rock	0.79134				(4)
rock	0.81033				(4)
rock	0.82301			-25.89	(4)
rock	0.76381			-21.93	(4)
rock	0.78593				(4)
rock	0.83034				(4)
Northern Greenland (NGr)					
Thorarinsson et al., 2011 (5), 2012 (6)					
Sample Type	**$^{87}Sr/^{86}Sr$**	**$^{206}Pb/^{204}Pb$**	**$^{207}Pb/^{204}Pb$**	**ε_{Nd}**	**Ref.**
rock	0.74938	18.559	15.522	3.16	(5)
rock	0.73265				(5)
rock	0.75702	18.572	15.529	3.36	(5)
rock	0.72513	18.616	15.523	3.16	(5)
rock	0.72183				(5)
rock	0.75230	18.527	15.517	2.97	(5)
rock	0.73749	18.559	15.520	2.97	(5)
rock	0.75724	18.469	15.523	3.16	(5)
rock	0.72357	18.572	15.527	3.16	(5)
rock	0.71925				(5)
rock	0.70759	18.653	15.511	2.77	(5)
rock	0.70752				(5)
rock	0.70636	18.525	15.519	2.97	(5)
rock	0.70635				(5)

Northern Greenland (NGr)					
Thorarinsson et al., 2011 (5), 2012 (6)					
Sample Type	**$^{87}Sr/^{86}Sr$**	**$^{206}Pb/^{204}Pb$**	**$^{207}Pb/^{204}Pb$**	**ε_{Nd}**	**Ref.**
rock	0.70476	19.128	15.554		(5)
rock	0.70475				(5)
rock	0.70551	18.491	15.537	0.04	(5)
rock	0.70548	18.492	15.538		(5)
rock	0.70548			0.23	(5)
rock	0.71208	18.532	15.545	-4.25	(5)
rock	0.71189	18.436	15.538		(5)
rock	0.71560	18.511	15.545	-4.64	(5)
rock	0.71484				(5)
rock	0.70935	18.408	15.531	-4.25	(5)
rock	0.70930				(5)
rock	0.70922	18.515	15.540		(5)
rock	0.70874			-4.45	(5)
rock	0.70940	18.434	15.532	-4.45	(5)
rock	0.70962			-4.25	(5)
rock	0.71291	18.421	15.543		(5)
rock	0.71257				(5)
rock	0.71626	18.995	15.584	-2.89	(6)
rock	0.71088	19.087	15.592	-2.11	(6)
rock	0.71362	18.769	15.565	3.75	(6)
rock	0.70442	18.999	15.564	4.33	(6)
rock	0.76565	18.878	15.577	-0.74	(6)
rock	0.89628	18.855	15.568	1.79	(6)
rock	0.72408	18.685	15.567	0.62	(6)
rock	0.73954	18.817	15.558	3.55	(6)
rock	0.75968	18.754	15.550	3.36	(6)
rock	0.72973	18.519	15.560	0.43	(6)
rock	0.74183	18.713	15.571	1.40	(6)
Ellesmere & Axel Heiberg Islands (EI & AHI)					
Dostal & MacRae, 2018 (7); Estrada, 2015 (8); Estrada et al., 2010 (9); Maccali et al., 2018 (10)					
Sample Type	**$^{87}Sr/^{86}Sr$**	**$^{206}Pb/^{204}Pb$**	**$^{207}Pb/^{204}Pb$**	**ε_{Nd}**	**Ref.**
rock	0.706838			0.76	(7)
rock	0.706896			0.94	(7)
rock	0.705882			2.03	(7)
rock	0.706765			1.11	(7)
rock	0.706951			2.22	(7)
rock	0.704725			3.84	(7)
rock	0.707357			-2.13	(8)
rock	0.707350			-2.07	(8)
rock	0.707336			-2.13	(8)
rock	0.707315			-2.22	(8)
rock	0.703992			4.08	(8)
rock	0.704101			4.14	(8)

Ellesmere & Axel Heiberg Islands (EI & AHI)					
Dostal & MacRae, 2018 (7); Estrada, 2015 (8); Estrada et al., 2010 (9); Maccali et al., 2018 (10)					
Sample Type	**$^{87}Sr/^{86}Sr$**	**$^{206}Pb/^{204}Pb$**	**$^{207}Pb/^{204}Pb$**	**ε_{Nd}**	**Ref.**
rock	0.704182			3.80	(8)
rock	0.704095			3.78	(8)
rock	0.704113			3.80	(8)
rock	0.704060			5.11	(9)
rock	0.704150			4.19	(9)
rock	0.703750			1.91	(9)
rock	0.704830			3.02	(9)
rock	0.703690			1.99	(9)
rock	0.703590			5.13	(9)
rock	0.704290			4.06	(9)
rock	0.703870			2.81	(9)
rock	0.704560			2.07	(9)
rock	0.705980			2.48	(9)
rock	0.706270			2.38	(9)
rock	0.704600			4.06	(9)
rock	0.705040			0.20	(9)
surface sediment	0.723207	18.957	15.631	-12.17	(10)
surface sediment	0.722786	18.900	15.591	-13.26	(10)
surface sediment	0.722570	18.919	15.590	-13.30	(10)
surface sediment	0.723917	18.909	15.599	-13.26	(10)
surface sediment	0.723883	18.970	15.614	-13.26	(10)
surface sediment	0.724239	18.914	15.587	-13.97	(10)
surface sediment	0.738823	18.980	15.627	-15.20	(10)
surface sediment	0.724768	18.844	15.601	-12.46	(10)
surface sediment	0.744196	18.968	15.610	-19.49	(10)
Baffin Island (BI)					
McCulloch & Wasserburg, 1978 (11)					
Sample Type	**$^{87}Sr/^{86}Sr$**	**$^{206}Pb/^{204}Pb$**	**$^{207}Pb/^{204}Pb$**	**ε_{Nd}**	**Ref.**
rock	0.761057			-31.7	(11)

8.6. References

(1) Colville, E. J., Carlson, A. E., Beard, B. L., Hatfield, R. G., Stoner, J. S., Reyes, A. V, & Ullman, D. J. (2011). Sr-Nd-Pb isotope evidence for ice-sheet presence on southern Greenland during the Last Interglacial. Science, 333(6042), 620–623. https://doi.org/10.1126/science.1204673

(2) Reyes, A. V, Carlson, A. E., Beard, B. L., Hatfield, R. G., Stoner, J. S., Winsor, K., … Ullman, D. J. (2014). South Greenland ice-sheet collapse during Marine Isotope Stage 11. Nature, 510(7506), 525–528. https://doi.org/10.1038/nature13456

(3) Larsen, L. M., & Pedersen, A. K. (2009). Petrology of the paleocene picrites and flood basalts on disko and nuussuaq, West Greenland. Journal of Petrology, 50(9), 1667–1711. https://doi.org/10.1093/petrology/egp048

(4) Kalsbeek, F., Pulvertaft, T. C. R., & Nutman, A. P. (1998). Geochemistry, age and origin of

metagreywackes from the Palaeoproterozoic Karrat Group, Rinkian Belt, West Greenland. Precambrian Research, 91(3–4), 383–399. https://doi.org/10.1016/S0301-9268(98)00059-X
(5) Thorarinsson, S. B., Holm, P. M., Duprat, H., & Tegner, C. (2011). Silicic magmatism associated with Late Cretaceous rifting in the Arctic Basin-petrogenesis of the Kap Kane sequence, the Kap Washington Group volcanics, North Greenland. Lithos, 125(1–2), 65–85. https://doi.org/10.1016/j.lithos.2011.01.013
(6) Thorarinsson, S. B., Holm, P. M., Duprat, H. I., & Tegner, C. (2012). Petrology and Sr-Nd-Pb isotope geochemistry of Late Cretaceous continental rift ignimbrites, Kap Washington peninsula, North Greenland. Journal of Volcanology and Geothermal Research, 219–220, 63–86. https://doi.org/10.1016/j.jvolgeores.2012.01.011
(7) Dostal, J., & Macrae, A. (2018). Cretaceous basalts of the High Arctic large igneous province at Axel Heiberg Island (Canada): Volcanic stratigraphy, geodynamic setting, and origin. Geological Journal, (August 2017), 1–17. https://doi.org/10.1002/gj.3132
(8) Estrada, S. (2015). Geochemical and Sr–Nd isotope variations within Cretaceous continental flood-basalt suites of the Canadian High Arctic, with a focus on the Hassel Formation basalts of northeast Ellesmere Island. International Journal of Earth Sciences, 104(8), 1981–2005. https://doi.org/10.1007/s00531-014-1066-x
(9) Estrada, S., Henjes-Kunst, F., Melcher, F., & Tessensohn, F. (2010). Paleocene alkaline volcanism in the Nares Strait region: Evidence from volcanic pebbles. International Journal of Earth Sciences, 99(4), 863–890. https://doi.org/10.1007/s00531-009-0432-6
(10) Maccali, J., Hillaire-Marcel, C., & Not, C. (2018). Radiogenic isotope (Nd, Pb, Sr) signatures of surface and sea ice-transported sediments from the Arctic Ocean under the present interglacial conditions. Polar Research, 37(1), 1–13. https://doi.org/10.1080/17518369.2018.1442982
(11) McCulloch, M. T., & Wasserburg, G. J. (1978). Sm-Nd and Rb-Sr Chronology of Continental Crust Formation. Science, 200(June), 1003–1011.